Wave Loading on Bodies in the Free Surface Using Smoothed Particle Hydrodynamics (SPH)

A thesis is submitted to The University of Manchester for the degree of
Doctor of Philosophy in the Faculty of Engineering and Physical
Sciences

2010

Pourya Omidvar

School of Mechanical, Aerospace and Civil Engineering

Contents

List of Figures

List of Tables

Abstract

The University of Manchester

Pourya Omidvar

PhD

Wave loading on bodies in free surface using smoothed particle hydrodynamics (SPH)

2010

This thesis investigates wave loading on bodies in the free surface using smoothed particle hydrodynamics (SPH). This includes wave loading on fixed bodies, waves generated by heaving bodies in still water and the heave response of a body in waves, representing a wave energy device. SPH is a flexible Lagrangian technique for CFD simulations, which in principle applies to steep and breaking waves without special treatment allowing us to simulate highly nonlinear and potentially violent flows encountered in a real sea. However few detailed tests have been undertaken even with small amplitude waves.

This research uses the open-source SPH code SPHysics. First two forms of SPH formulation, standard SPH with artificial viscosity and SPH-Arbitrary Lagrange Euler (ALE) with a Riemann solver, are used to simulate progressive waves in a 2-D tank. The SPH-ALE formulation with a symplectic time integration scheme and cubic spline kernel is found to model progressive waves with negligible dissipation whereas with the standard SPH formulation waves decay markedly along the tank.

We then consider two well-defined test cases in two dimensions: progressive waves interacting with a fixed cylinder and waves generated by a heaving semi-immersed cylinder. To reduce computer time in a simple manner a variable particle mass distribution is tested with fine resolution near the body and coarse resolution further away, while maintaining a uniform kernel size. A mass ratio of 1:4 proved effective but increasing to 1:16 caused particle clumping and instability. For wave loading on a half-submerged cylinder the agreement with the experimental data of Dixon *et al.* (1979) for the root mean square force is within 2%. For more submerged cases, the results show some discrepancy, but this was also found with other modelling

approaches. For the heaving cylinder, SPH results for the far field wave amplitude and vertical force on the cylinder show good agreement with the data of Yu and Ursell (1961). The variable mass distribution leads to a computer run time speedup of nearly 200% in these cases on a single CPU. The results of the vertical force and wave amplitude are shown to be quite sensitive to the value of the slope limiter in the Riemann solver for the 2-D heaving cylinder problem.

A heaving 2-D wedge or 3-D cone whose oscillatory vertical motion is prescribed as the elevation of a focused wave group is a precise test case for numerical free-surface schemes. We consider two forms of repulsive boundary condition (Monaghan & Kos, 1999, and Rogers et al., 2008) and particle boundary force (Kajtar and Monaghan, 2009) for the 2-D wedge case, comparing the result with the experimental data of Drake et al. (2009). The repulsive boundary condition was more effective than the particle boundary force method. Variable particle mass with different kernel sizes was then tested for 2-D problems for mass ratios of 1:4, 1:16 and 1:4:16 with satisfactory results without particle clumping and instability. For the 3-D cone case, SPH reproduces the experimental results very closely for the lower frequency tested where there is no separation from the bottom surface of the body but for the higher frequencies the magnitudes of force minima were underestimated. The mass ratios of 1:8 and 1:8:27 in two and three nested regions are tested for the 3-D cone problem where a computer run time speedup of nearly 500% is achieved on 16 processors for the mass ratio of 1:8.

Finally, the floating body of a heaving wave energy device known as the Manchester Bobber is modelled in extreme waves without power take-off. The results for a single float are in approximate agreement with the experiment.

Declaration

No portion of the work referred to in the thesis has been submitted in support of an application for another degree or qualification of this or any other university or other institute of learning.

Copyright statement

I. The author of this thesis (including any appendices and/or schedules to this thesis) owns certain copyright or related rights in it (the "Copyright") and s/he has given The University of Manchester certain rights to use such Copyright, including for administrative purposes.

II. Copies of this thesis, either in full or in extracts and whether in hard or electronic copy, may be made only in accordance with the Copyright, Designs and Patents Act 1988 (as amended) and regulations issued under it or, where appropriate, in accordance with licensing agreements which the University has from time to time. This page must form part of any such copies made.

III. The ownership of certain Copyright, patents, designs, trade marks and other intellectual property (the "Intellectual Property") and any reproductions of copyright works in the thesis, for example graphs and tables ("Reproductions"), which may be described in this thesis, may not be owned by the author and may be owned by third parties. Such Intellectual Property and Reproductions cannot and must not be made available for use without the prior written permission of the owner(s) of the relevant Intellectual Property and/or Reproductions.

IV. Further information on the conditions under which disclosure, publication and commercialisation of this thesis, the Copyright and any Intellectual Property and/or Reproductions described in it may take place is available in the University IP Policy[1], in any relevant Thesis restriction declarations deposited in the University Library, The University Library's regulations[2] and in The University's policy on presentation of Theses.

---

[1] http://www.campus.manchester.ac.uk/medialibrary/policies/intellectual-property.pdf

[2] http://www.manchester.ac.uk/library/aboutus/regulations

List of publications

1. Omidvar P. Stansby P. K. and Rogers B. D. (2010), “Wave body interaction in 2D using Smoothed Particle Hydrodynamics (SPH) including variable particle mass”, *Accepted for publication.*

2. Omidvar P. Stansby P. K. and Rogers B. D. (2010), “SPH for a 2-D and 3-D heaving body using variable mass particle distribution” *Proceeding of 5th International SPHERIC Workshop*; UK: 282-288.

3. Westphalen J. Greaves D. M. Hunt-Raby R. Williams C. K. Taylor P. H. Hu Z. Z. Omidvar P. Causon D. M. Mingham C. G. Stansby P. K. Rogers B. D. (2010) “Numerical Simulation of Wave Energy Converters using Eulerian and Lagrangian CFD Methods”, *20th International Society of Offshore and Polar Engineers Conference*; China.

4. Westphalen J. Greaves D. M. Hu Z. Z. Omidvar P. and Causon D M. (2010), “Numerical Simulation of Wave-Structure Interaction wave energy conversion applications using Eulerian and Lagrangian CFD Methods”, *3rd International Conference and Exhibition on Ocean energy*; Spain.

5. Omidvar P. Stansby P. K. and Rogers B. D. (2009), “SPH for free-surface flow around a heaving oscillating cylinder using variable particle mass distributions: 2-D investigations” *Proceeding of 4th International SPHERIC Workshop*; France: 347-352.

6. Omidvar P. Stansby P. K. and Rogers B D. (2009), “Investigation of surface waves interacting with a fixed cylinder and generated by a heaving cylinder using Smoothed Particle Hydrodynamics (SPH)” *Proceeding of 33rd IAHR Congress: Water Engineering for Sustainable Environment*; Canada: 7447-7454.

7. Westphalen J. Greaves D. M. Williams C. K. Taylor P. H. Causon D. M. Mingham C. G. Hu Z. Z. Stansby P. K. Rogers B.D. and Omidvar P. (2009), “Extreme wave loading on offshore wave energy devices using CFD: a Hierarchical Team Approach”, *8th European Wave and Tidal Energy Conference*; Sweden.

8. Omidvar P. Rogers B. D. and Stansby P. K. (2008), “Investigation of wave loading on a partially submerged cylinder using SPH”, *Proceeding of 3rd International SPHERIC Workshop*: Switzerland; 245-248.

9. Omidvar P. Rogers B. D. and Stansby P. K. (2008), “Wave loading on a partially and half-submerged circular cylinder using SPH”, *4th Young Coastal Scientist and Engineering Conference*; UK.

Acknowledgements

This thesis thanks to the following people for their kind, generosity and scientific supports:

- I would like to express my appreciation and sincere gratitude to my supervisors **Professor Peter K Stansby** and **Dr Benedict D Rogers** for their excellent supervision, scientific hints, guidance and generously supports throughout this PhD.

- I would like to thank the Engineering and Physical Sciences Research Council (EPSRC) for the financial support of this research and **Professor Peter K Stansby** for arranging this fund. I am also grateful to **Professor Peter K Stansby** for his patient, sincere endeavour and supports throughout my PhD.

- My special acknowledgements to **Dr Benedict D Rogers** for his continuous support, assistance and encouragement throughout regular meetings and discussions. He assisted me with enhancement of my skills such as presentations, writing academic papers, critical analysis of research problems.

- I also take this opportunity to thank **Professor Moncho Gómez-Gesteira** (University of Vigo, Spain) and **Dr Mark Cotton** (University of Manchester) who examined this thesis.

- I thank all the professors and academic and support staff in the School of Mechanical, Aerospace & Civil Engineering, the University of Manchester. The members of the SPH and Hydrodynamics- expert group for their continuous support throughout weekly meetings. **Dr Simon Hood** for his excellent technical supports.

- Many thanks to **Dr Tim Stallard**, **Mr Armando Alexandre** (Armando) and **Mr Samuel Weller** (Sam) for their generous supports, constructive suggestions and providing data for the validation of one chapter of this thesis.

- I will not forget all PhD students who shared the office with me. **Dr Renato Vacondio** (Renato) for his excellent company at different workshops and conferences, friendly and useful discussions during his stay in Manchester. **Vahid**, **Mansoor**, **Roberto**, **Maurice**, **Athanasios**, **Imdad, Waqar**, **Mehdy** and **Hossein** for cheering me up in the office.

- I am grateful to my close relatives (my sister **Elmira** and uncle **Reza**) and friends (**Mahan** and **Mahyar**) who offered me their encouragement and love which were sources of energy and motivation for me throughout this research.
- Finally, my infinite gratitude goes to my parents, my dearest father and mother, for their unconditional love along with their continuous support and encouragement.

Nomenclature and Glossary

Symbol	**Definition**
A	Cone and Bobber amplitude
a	Wave amplitude
B	$\frac{\rho_w c_s^2}{\gamma}$
BPs	Boundary particles
c	Speed of sound
Cr	Courant number
D	Diameter
d	Water depth
$d^/$	Body axis depth
$\mathbf{F}$	Total Force
F	flux
f	Particle force
F_{rms}	Root mean square force
$\mathbf{g}$	Gravity
h	Smoothing length
$\mathbf{i}$, $\mathbf{j}$, $\mathbf{k}$	Unit vectors
k	Wave number
L	Wave length
L_0	Deep-water wave length
L_ϑ	Transport operation
M	Mass of a body
m	Mass of a particle
m_c	Counter mass
m_f	Mass of a single Bobber
$\mathbf{n}_{ij}$	$(\mathbf{r}_i - \mathbf{r}_j) \,/\, \lvert\mathbf{r}_i - \mathbf{r}_j\rvert$
P	Pressure
$P(\xi)$	Function to ensure particles experience a constant repulsive force
q	$\mathbf{r}_{ij}/h$
$\mathbf{r}$	Coordinate vector
$R(\psi)$	Repulsive function

Symbol	**Definition**
R_A	Wave amplitude ratio
R_x	Global relative error
$S_n(\sigma)$	Power spectrum
s	Wavemaker or body stroke
T	Period
t	Time
T_p	Peak period
T_t	Tension force
u, v,w, U, V,W	Components of velocity vector
$u_\perp$	Normal velocity
$\mathbf{v}$	Velocity vector
W	Kernel function
WPs	Water particles
x, y, z, X, Y, Z	Coordinate directions
Δ	Initial particle spacing
Δ_b	Distance between any two adjacent boundary
Π	Artificial viscosity
Φ	Arbitrary function
Ω	Domain of interest in the interpolation of function Φ
Ω_I	Rotational velocity
β	Beta limiter
δ_ε	Dirac function
δt	Time step
$\varepsilon(z, u_\perp)$	Depth function
$\zeta(x)$	Sponge-layer function
μ	Viscosity
σ	Frequency
σ_F	Force coefficient
ρ	Density
ρ_w	Reference density
υ	Kinematic viscosity
ω	Volume of a particle

Term	Description
Artificial viscosity	Artificial viscosity is a common way proposed by Monaghan (1992) to model the effect of viscosity in the Standard SPH equation
HLL	Harten-Lax-van Leer is a solution for a Riemann problem
HLLC	Harten-Lax-van Leer-Contact is a solution for a Riemann problem
Kernel function	is an interpolating function used in SPH
ISPH	Incompressible SPH
MUSCL	Monotone Upstream-centred Schemes for Conservation Laws is a second order extension of the Godunov upwind method
Particles	interpolation points where properties of the fluid can be calculated
Smoothing length	is analogous to an average cell size in Eulerian methods and characterises the spatial discretisation of the problem in SPH.
SPH-ALE	Smoothed Particle Hydrodynamics-Arbitrary Lagrange Euler
Tensile instability	is an instability in SPH when negative pressures cause particle attractions
WCSPH	Weakly Compressible SPH
XSPH	is a term added to the position equation to keep the particles orderly in the absence of viscosity

Chapter 1

Introduction

1.1 Background

Renewable energy sources have become a key component to meet the world's future energy demands due to the recent climate changes. Renewable energy can be produced from different sources such as using wind turbines, wave energy devices and tidal stream turbines. In principle, useful wave energy devices can provide a concentrated source of renewable energy to make a substantial contribution to energy consumption. For example, the Manchester Bobber is considered as such a device, which is a heaving point absorber comprising of a float with hemispherical base generating oscillatory shaft motion.

For the case of multiple heaving wave energy devices the flow field is potentially complex since each device is moving and there is a need to study the basic behaviour to enable the design for such a complex problem. Modelling multiple heaving wave energy devices which involve complex interactions of wave breaking, reflection and diffraction processes can help to understand their behaviour in real seas. Moreover, generating energy from waves with a heaving device can place them under extreme loading conditions, especially for cases where flow is particularly violent. At the moment, no large body of knowledge or understanding of the behaviour of such devices under these conditions exists, hence there is still much work to be undertaken to improve their potential performance.

The offshore flow field with various arrangements of fixed/floating devices can involve complex interactions of physical processes making its experimental investigation very difficult. Furthermore, investigation of the fixed/floating bodies in extreme waves must be evaluated through physical experimentation and sea trials. On the other hand, linear, or second-order, wave diffraction theory is the standard approach for such structures of large dimensions but does not represent highly nonlinear effects associated with extreme waves.

Computational Fluid Dynamics (CFD), which has had many successes in other areas of engineering, e.g. turbomachinery, aeronautics and combustion, is an alternative approach for modelling heaving wave energy devices and understanding their behaviour in real seas by solving the Navier-Stokes and continuity equations. The benefits of using CFD are well known where design cases may be set up and analysed in relatively short time and the input conditions may be precisely controlled which is particularly important for extreme waves. The desired flow field can be generated allowing us to study integrated effects like forces and responses. However, in order to conduct proper analysis, the accuracy of predictions, numerical convergence and computational efficiency are important and need to be quantified.

The implementations of CFD in engineering applications are most of the time based on the Eulerian description. In this method, one can focus on flows at a fixed spatial point $\mathbf{x}$ at time t and any flow variable ϕ is expressed as $\phi(\mathbf{x}, t)$. This description has been studied for over fifty years and is clearly understood. Most of commercial codes have been developed by using finite difference, finite element and finite volume approaches. However, the Eulerian approach is less well suited to complex problems such as large deformations and complex free-surface flow. Simulating free-surface flow with most Eulerian CFD methods is potentially very difficult as explicit treatment of the free surface is required.

Another description of study of CFD is the Lagrangian method where one can follow the history of an individual fluid parameter through the time. In the Lagrangian methods, any flow variable is expressed as $\phi(\mathbf{x}_0, t)$, where the point vector $\mathbf{x}_0$ of the particle at the reference time $t = 0$. Meshless and particle methods are based on the Lagrangian approach and can be used in complex problems described above.

This work is a part of a joint project between the Universities of Plymouth Manchester, Oxford and Manchester Metropolitan funded by EPSRC looking at the suitability of different Computational Fluid Dynamics (CFD) schemes to model heaving wave energy devices and to understand their behaviour in real seas.

1.2 Smoothed Particle Hydrodynamics (SPH)

Simulating free-surface flow with most Eulerian CFD methods can be difficult as explicit treatment of the free-surface is required. Smoothed particle hydrodynamics (SPH) is a flexible Lagrangian and meshless technique for CFD simulations initially developed by Lucy (1977) and Gingold and Monaghan (1977) in astrophysics. In this method, each particle carries an individual mass, position, velocity, internal energy and any other physical quantity. The Lagrangian nature of SPH would lead this method to be well suited to problems with large deformations and distorted free surfaces. Simplicity, robustness and relative accuracy in comparison with other numerical methods are the main advantages of using SPH (Monaghan, 2005). Moreover, the major advantage of using SPH is in dealing with free-surface problems where there is no need for special treatments for the free surface in order to simulate highly nonlinear and potentially violent flows. This method has been successfully applied to a range of free-surface problems which involve breaking and splashing up, e.g. Monaghan & Kos (1999), Monaghan & Kos (2000) and Dalrymple and Rogers (2006).

Advantages and disadvantages

SPH method has some advantages in comparison with the Eulerian methods as follows:

- There is no need to construct a mesh in SPH, therefore in some problems such as breaking waves SPH is easier to be used and gives better results.
- Complex problems related to physical phenomena can be investigated with SPH (such as free surface, voids, Lagrangian phenomena, etc).
- The SPH method can handle fully nonlinear, multiple-connected free-surface problems and extend computations beyond wave breaking.
- The equations used in SPH are quite simple in comparison with other particle methods and Eulerian techniques.

However, SPH has some disadvantages as follows:

- The computational cost is one of the disadvantages of SPH, the time step is much smaller than other methods due to using explicit integration scheme, the use of weakly compressible formulation and avoiding particle penetration.
- Wall treatment may be very difficult and complicated in some problems.
- Parallel computing is more complicated (particles constantly need to be re-grouped in common neighbourhoods).

Although the SPH method has the above drawbacks, it was found to be an attractive and well suited method for free-surface problems and complex environmental flows, since the equations used in SPH are simple to be implemented in comparison with other particle methods (Idelsohn and Oñate, 2005).

1.3 Study objectives

The main objective of this project is to investigate the effect of waves on offshore wave energy devices using the SPH method, especially in extreme conditions. However, first, it is important to study wave propagation in channel, surface waves interacting with a fixed body or generated by a heaving body which would enable us to lead towards simulation of Manchester Bobber wave energy device in waves.

Therefore, the objectives of this research can be summarised as:

- Investigation of wave propagation generated by paddle motion in an intermediate deep and weakly compressible water tank.
- Study of wave loading on fixed and partially submerged bodies.
- To use the SPH method for investigation of surface waves generated by forced-motion bodies.
- Techniques to reduce the computer time in the SPH simulations.
- To extend the knowledge behind the fluid-structure interactions to simulate a floating Manchester Bobber in extreme focused waves using NewWave theory (Taylor and Williams, 2004).

1.4 Outline of the thesis

This chapter is followed by a review of the literature to examine recent advances in meshless and particle methods and in particular the SPH method in Chapter 2, which also includes the recent applications of SPH in free-surface flow and fluid-structure problems. In Chapter 3, the theoretical and mathematical overviews of the SPH method are presented followed by different SPH formulations, two forms of different boundary conditions, time stepping method, kernel functions and all equations used to simulate the problems in later chapters.

The simulation of a vertical plate moving in a 2-D channel and wave propagation in an intermediate deep and weakly compressible water tank, using different SPH equations and kernel functions, are presented in Chapter 4. Then, surface waves interacting with a fixed cylinder or generated by a heaving semi-immersed cylinder are presented in two dimensions.

In order to reduce computer time a variable particle mass distribution is presented in Chapter 5 with fine resolution near the body and coarse resolution further away, paying careful attention to avoid tensile instability with the interpolating kernel function and to obtain hydrostatic pressure in still water conditions. The variable mass distribution of particles will be then used for progressive waves interacting with a fixed cylinder and the simulations of the waves generated by a heaving semi-immersed cylinder.

A heaving wedge or cone with oscillatory vertical motion is a challenging test case for numerical free-surface schemes and will be investigated in Chapter 6, looking carefully at the calculation of the forces on a moving body and the surface elevations around it. The use of variable particle mass distribution for the heaving cone test case with different kernel size will be also explained in Chapter 6. The motion of Manchester Bobber in focus waves will be then investigated in Chapter 7.

All the SPH results will be compared with either the available experimental data or analytical solutions. Finally, the thesis will finish with conclusions and recommendations in Chapter 8.

Chapter 2

Bibliographic investigation

2.1 Introduction

The aim of this literature survey is to examine recent advances in meshless methods and in particular Smoothed Particle Hydrodynamics (SPH). The survey reviews different types of meshless methods, describing advantages and disadvantages, followed by a description of the origins of the SPH method, different SPH formulations and SPH for fluid dynamics. Moreover, the recent applications of SPH in free-surface flow problems will be shown including wave impacts with rigid bodies.

2.2 Meshless methods

Free-surface flow in fluid mechanics problems is a good illustration of complexity where the free surface can be joined in one or broken in multiple locations in a domain which is unknown and may change in time. These types of problems need a complex algorithm to connect the nodes which are close to each other in one particular time step and may be far from each other in the next time step. Therefore, introducing a set of nodal points or particles, without any mesh construction can be an efficient way to overcome these difficulties (Oñate *et al.*, 1996).

Meshless methods are a class of algorithm that define the nodal shape functions which depend only on the node positions and the evaluation of the nodal connectivity bounded in time (Idelsohn and Oñate, 2005). Meshless methods have the advantages of handling very large nonlinear deformations as well as providing accurate representation of geometric objects where controlling the accuracy and nodes can be added (h-adaptivity).

The followings are some examples of meshless methods:

- Vortex methods where the Navier-Stokes equations are introduced in vorticity formulation was originally proposed by Chorin (1973, 1978). In these methods the fluid vorticity field is the principal variable for computations obtained from an integral of vorticity as it is eliminated by the curl operator while pressure is not explicitly solved (Barba *et al.,* 2005). The vortex method has two subjects (a) point-vortex method which is approximated by continuous differentiations instead of Lagrangian finite differencing consequently leading this method to be singular numerically and unstable (Chorin, 1973), (b) The vortex blob method where the numerical computation sheet is discretised into a number of discrete vortex whose strength and location are such that the no-slip condition is satisfied at the corresponding control points on the body surface leading the model to be stable. The vortex method has a wide and efficient application in the investigation of problems involving areas of high vorticity e.g. simulation of flows around cylindrical bodies (Smith and Stansby, 1988) and complex flows involving large scale separation and turbulence (Dutta, 1988). However, it suffers from loss of accuracy for the calculation of unsteady flows due to the Lagrangian deformation of the particle field (Barba *et al.,* 2005). The usefulness and limitations of the method are discussed in details by Sarpkaya (1989).
- The Dissipative Particle Dynamics (DPD) method is a mesoscopic simulation technique first devised by Hoogerbrugge and Koelman (1992) in order to simulate microscopic hydrodynamic phenomena in order to tackle hydrodynamic time and space scales beyond those available with Molecular Dynamics (MD) in which the particles move according to Newton's laws. The main objective of using DPD was to simulate macroscopic non-Newtonian flow properties of the fluid due to its microscopic structure, e.g. modelling the rheological properties of concrete (Sims and Martys, 2004), porous flow (Hoogerbrugge and Koelman, 1992), colloidal suspensions (Koelman and Hoogerbrugge, 1993), or multicomponent flows (Coveney and Novik, 1997). This method however does

not conserve energy which leads the DPD system not to sustain a temperature gradient (Español, 1997).

- Diffuse Elements Method (DEM) proposed by Nayroles *et al.* (1992) uses the collection of nodes and a boundary description to formulate the Galerkin equations, which is a class of method for converting a continuous operator problem such as differential equations to a discrete problem, where the interpolation functions are polynomials fitted to the nodal values by a weighted least-square approximation. This method is more precise in the evaluation of the derivations of the reconstructed functions. However, this method still needs some kind of "auxiliary grid" to compute numerically the integral expressions derived from the Galerkin approach (Oñate *et al.*, 1996 and Nayroles *et al.*, 1992) which limits the applications for complex problems, e.g. free-surface flow (Arefmanesh *et al.*, 2005). This method has a successful application in heat conduction (Liu *et al.*, 1995).

- Atluri and Zhu (1998) proposed the Meshless Local Petrov-Galerkin (MLPG) method. This method is based on a local weak form over a local sub domain which can be any simple geometry such as circles, rectangles, or ellipses centred at the field node in question in two dimensions. MLPG can solve all the weak forms locally and various trial and test functions can be chosen and combined together for solving one problem. This method has been applied to solid mechanics field by Gu and Liu (2001), e.g. to analyse the static and free vibration of thin plates, and has a few application in CFD, e.g. Lin and Atluri (2001) to solve the lid-driven cavity flow problem. More recent application of MLPG was attempted by Ma (2005) in investigation of nonlinear water wave problems. Application of MLPG may cause some instabilities especially for flows with with a Reynolds number more than 400 (Wu *et al.*, 2005).

- Reproducing Kernel Method (RKM) developed by Liu *et al.* (1995) is a meshless and multiple-scale method based on reproducing kernel and wavelet analysis. In this method one can develop a new type of shape functions using an integral window transform. The window transform function is translated and dilated around the domain. This will help to replace the need to define elements and providing refinements. This method can create the ability to analyse a specific frequency range in dynamic problems reducing the CPU cost. This method was applied to large deformation structural dynamics (Liu *et al.*, 1995) and strain localisation (Li and Liu, 2000).

- Finite Point-set Method (FPM) was originally introduced by Tiwari & Kuhnert (2003) for numerical investigation of pure incompressible Navier-Stokes equations and is based on a moving least squares approach where particles are defined as interpolation points without any associated mass. In this method, particles can be added to or removed from the simulation and there is no need to calculate the gradient of kernel, importantly the boundaries can be solved analytically. This method is suitable to handle free-surface flow and two-phase flow (Kuhnert and Tiwari, 2007), however, it is time consuming since 6×6 matrices in 2D and 10×10 matrices in 3D should be solved and inversed for every particle every time step. Moreover, this method is non-conservative in addition to difficulties to reproduce the hydrostatic conditions in free-surface problems (Vacondio and Mignosa, 2009).

- Meshless Finite Element Method (MFEM) is similar to the finite element method with a special shape function whose domain is divided into spherical polyhedral elements (Idelsohn *et al.*, 2003). In this method the shape function depends only on the node positions and the space is divided into elements with continuity of the shape functions but with discontinuity of the derivatives. In MFEM the shape function is applied to each polyhedral element where it is applied to all the domain in the natural element method. Moreover, the evaluation of the node connectivities is bounded in time, which depends on the total number of nodes in the domain (Idelsohn and Oñate, 2005). This method was applied to fluid–structure interaction by Idelsohn *et al.* (2003) and to a number of electromagnetic cases(see Xuan *et al.*, 2004 and Ho *et al.*, 2005).

- Moving Particle Semi-implicit method (MPS) is a meshless method for the simulation of incompressible free-surface flows first developed by Koshizuka and Oka (1996). The MPS method is similar to the Smoothed Particle Hydrodynamics (SPH) method which both provide approximations on the basis of integral interpolants. However, the solutions are obtained through a semi-implicit prediction-correction process and there is no calculations of kernel gradient in MPS. Since the first introduction of this method, MPS has been successfully used in a wide range of applications such as nuclear engineering (Koshizuka *et al.*, 2001) and coastal engineering (Gotoh and Sakai, 1999; Gotoh *et al.*, 2005; Khayyer and Gotoh, 2009). Non conservation of momentum and spurious pressure fluctuation can be classified as the disadvantages of this method, which have been only recently addressed in Khayyer and Gotoh (2009).

- Smoothed particle hydrodynamics (SPH), sometimes called the free Lagrange method (Oñate *et al.* 1996), is described by a set of disordered points or particles first developed by Lucy (1977) and Gingold & Monaghan (1977) in order to investigate the non-axisymmetric phenomenon in astrophysics such as the formulation and evolution of galaxies. Since then, SPH has been widely used in many areas of solid and fluid mechanics, etc. as one of the most efficient computational techniques. In this method each particle has an individual mass, position, velocity, internal energy and other quantities. There is no need to construct a mesh in SPH (Monaghan, 1992), therefore, in some problems such as breaking waves, SPH is easier to use and gives better results. Also, the equations used in SPH are quite simple in comparison with other particle methods and Eulerians. Moreover, by using the SPH algorithms, the boundaries can be described by sets of computational boundary particles interacting with fluid particles (Monaghan, 2005). This advantage of the SPH method including conservation of linear and angular momentum can be extended for floating body problems. However, the computational cost is one of the disadvantages of SPH, the time step is much smaller than other methods due to using explicit integration scheme and avoiding particle penetration.

To conclude, there are numerous particle and meshless methods, with their own advantages and drawbacks, to simulate engineering problems. Here, the SPH method was found to be an attractive method and the best choice for the free-surface problems and complex environmental flows, since first the equations used in SPH are simple to be implemented in comparison with other particle methods (Idelsohn and Oñate, 2005). The most attractive feature of SPH methods in a large-deformation analysis is its general robust behaviour. SPH has been also successfully applied to wide range of fluid mechanics and particularly in free-surface problems e.g. see Monaghan (1994), Monaghan & Kos (1999) and Monaghan & Kos (2000). Moreover, the major advantage of using SPH is that no treatment of the free surface is required which combined with its Lagrangian nature enables one to model highly nonlinear and potentially violent flows.

2.3 Smoothed Particle Hydrodynamics (SPH)

2.3.1 Origins of SPH

Smoothed Particle Hydrodynamics (SPH) is a meshless and flexible Lagrangian technique in Computational Fluid Dynamics (CFD) simulations initially developed by Lucy (1977) and Gingold & Monaghan (1977) in order to investigate the non-axisymmetric phenomenon in astrophysics.

As Monaghan (2005) notes, this method has some attractive advantages in terms of pure advection, which is treated exactly. In this method the particle resolution depends on time and space suited for astrophysical and many geometrical problems. Moreover, for the problems involving more than one material where each material is described by its own set of particles, interface problems are found to be trivial in SPH in comparison with other methods e.g. finite difference schemes. For the complex problems such as fragments, drops or stars, the SPH method has a computational advantage as the simulation can be done only for the active part of the problem consequently leading to reduction in storage and calculations. Simplicity, robustness and relative accuracy in comparison with other numerical methods are other advantages of using SPH whereas the close similarity between SPH and molecular dynamics enables this method to become one of the most attractive numerical methods. The SPH method can handle fully nonlinear, multiply-connected free-surface problems and extend computations beyond wave breaking, which need complex treatments in other grid-based methods, e.g. Volume of Fluid (VoF).

However, the computational cost is one of the disadvantages of SPH because the time step is much smaller than other methods as explicit integration schemes are used. Besides, wall treatments may be difficult and complicated in some problems. On the other hand, although the interpolation method used in SPH is simple and SPH gives reasonable results for the first-order gradients, for higher order derivatives special techniques are required. For example, just developing accurate and robust second-order operators has been a non-trivial task (Schwaiger, 2007).

The initial development of SPH by Lucy (1977) and Gingold & Monaghan (1977) was for calculation of derivatives that did not require a structured computational mesh for the simulation of astrophysics problems. Since then, the SPH method has been used in many areas such as the simulation of binary stars (Benz 1988 & 1990, Monaghan 1992), cloud fragmentation and collisions (Durisen *et al.*, 1986) as well as the formation of galaxies (Monaghan & Lattanzio 1991, Berczik 2000), and even the evolution of the universe (Monaghan, 1990). Besides, SPH has been widely implemented in computational fluid and solid mechanics due to its relatively strong ability to interpolate complicated physical effects into the SPH formulation. Impact problems (Johson *et al.*, 1996, Libersky & Petscheck, 1991 and 1993), impacts of solids simulation (Benz and Asphaug, 1994) and metal forming (Bonet and Kulasegaram. 2000) are the illustrations of using SPH in solid mechanics. SPH investigation of multi-phase flows (Monaghan and Kocharyan, 1995), heat conduction (Chen *et al.*, 1999), underwater explosions (Swegle and Attaway, 1995), free-surface flows (Monaghan, 1994, Monaghan & Kos, 1999 and Monaghan & Kos, 2000), etc., are other examples of implementing SPH in fluid mechanics.

2.3.2 SPH for Fluid Dynamics

Classical SPH

Monaghan has been trying to develop SPH method in the computational fluids area since the 1980s (referring to his SPH papers). The method relies on a local interpolation around each particle and is the heart of SPH in order to derive the SPH formulations. The interpolation method allows one to express any function in terms of its value at a set of disordered points (particles) which can be constructed by using a kernel which is differentiable (Monaghan, 1992). This is called the standard SPH formulation which suffers from several weaknesses such as accuracy, stability and a correct treatment of boundary conditions (Marongiu *et al.*, 2008). In order to remedy partially the lack of stability artificial viscosity was introduced by Monaghan (1992), which was proposed to conserve total linear and angular momentum, to stabilise the numerical algorithm and handle high Mach number shocks (Monaghan, 1992). However, the artificial viscosity may cause some problems involving velocity shear (e.g. differentially rotating disks) by giving a very large effective shear viscosity or velocity divergence (Cha and Whitworth, 2003). Moreover, sometimes the artificial viscosity permits particle penetration in SPH (Monaghan, 1989). Also, as discussed later, the standard SPH formulation cannot deal with the propagation of waves in a long and intermediate depth channel. An overview of classical SPH is presented by Monaghan (1992) and Gómez-Gesteria *et al.* (2010). Details of standard SPH formulation and artificial viscosity will be addressed in Chapter 3.

Variational and momentum aspects of SPH

Both Bonet & Lok (1999) and Vila (1999) showed how to derive SPH formulations for the derivation of the stress forces in terms of an internal energy function in a variational approach. This new formulation simultaneously expresses and relates the equations used for density and employed for the equilibrium of particles in which first-order completeness was enforced, meaning that first-order polynomials are reproduced exactly. Their work is followed by showing the conservation of linear and angular momentum in the absence of external forces. Bonet & Lok (1999) also presented separate and mixed corrections to the gradient and kernel functions with the standard SPH equations, which provide a much improved interpolation, especially near the domain boundary, but fail to satisfy the rotational invariance conditions where the kernel gradients are no longer equal and opposite. Moreover, the forces between the particles are proportional to the kernel gradient. The failure to satisfy rotational invariance conditions leads to failure to satisfy conservation principles. On the other hand, the improvements to the SPH method by Bonet & Lok (1999) were followed by a number of illustrations for free-surface flow such as a water bubble and a breaking dam comparing with the normal SPH algorithm. These illustrations, however, did not conduct detailed investigations into the accuracy and pressure. The non-conservation issue of Bonet & Lok's (1999) correction to the kernel functions was investigated by Vaughan *et al.* (2008). They enforced the mass conservation by employing the summation interpolant (an equation that can be used to approximate an integral using disordered points) for the density.

Godonov-type SPH

An alternative approach to maintaining stabilities to the artificial viscosity is based on a contact interaction between SPH particles described by a Riemann solution for normal and tangential discontinuities, which are achieved by using artificial viscosity for the shock tube problem, introduced by Parshikov *et al.* (2000). The velocity and stresses at the contact surface determined by an approximate Riemann solution is inserted in the SPH approximations instead of mean values between velocities and stresses of contacting basic and surrounding particles. They demonstrated their two-dimensional axisymmetrical code for elastoplastic media where computations were compared with test data for perforation of steel plate by a lead projectile without using the artificial viscosity.

An alternative way of using Godunov method was presented by Cha and Whitworth (2003). The Godunov method Particle Hydrodynamics method (GPH), which is based on Lagrangian hydrodynamics, was computed by using a Riemann solver to calculate numerical flux. The GPH method is a Godunov-type upwind scheme which converts a multidimensional problem into one-dimensional Riemann problem by calculating all hydrodynamical interactions between particles on the line joining the particles. They used different SPH formulations and replaced the artificial viscosity with a Riemann solver by using the resultant pressure of the Riemann solver. They showed the stability of GPH for different wavelengths and various test by performing von Neumann stability analysis without any particle penetration and velocity shear. For the momentum equation, Parshikov *et al.* (2000) and Cha and Whitworth (2003) are identical but Parshikov *et al.* (2000) also perform a similar correction for the continuity and thermal energy equations.

Vila (1999) used an Arbitrary Lagrange Euler (ALE) scheme together with the SPH method linking the finite volume method into the hybrid method, in particular upwind scheme like the Godunov method in a conservative form. He introduced a new formulation with a Godunov type finite difference method followed by the review of some results concerning the classical approximation of Eulerian equations and presenting a new concept for use of variable smoothing length. Besides describing the Riemann solver approach to the SPH method, in order to reduce numerical diffusion and improve accuracy, Vila (1999) presented a higher-order extension of the methods based on the MUSCL technique of van Leer (Toro, 2001) which is a second-order extension of the Godunov upwind method where the piecewise constant approximation of Gudunov's scheme is replaced by reconstructed states and derived from averaged states obtained from the previous time step. Following the work by Vila (1999), Marongiu *et al.* (2008 and 2009) showed that using SPH-ALE method can increase stability and produce pressure fields with much less numerical noise. A full description of Vila's SPH-ALE method and MUSCL technique will be discussed in Chapter 3.

Incompressible SPH

In the original simulation of water flows using SPH, fluid is considered slightly compressible since incompressibility is approximated through a stiff equation of state. For the weakly compressible SPH, a large value for the speed of sound should be chosen in order to keep the corresponding density fluctuation as small as possible which leads to a smaller time step (Shao and Lo, 2003). Following the work done by Cummins and Rudman (1999) and based on the approach by Koshizuka *et al.* (1995) for the Moving Particle Semi-Implicit (MPS) method, Shao & Lo (2003) presented a strictly incompressible SPH (ISPH) method to simulate Newtonian and non-Newtonian flows with free surfaces. Shao & Lo (2003) showed the solution for the incompressible mass conservation and Navier–Stokes equations using a prediction–correction temporal scheme (explained in Chapter 3) without considering incompressibility in the prediction step, where the incompressibility is satisfied by implicitly projecting the particle density onto a divergence-free space through a pressure Poisson equation. This ISPH formulation preserves the linear momentum while it does not generally preserve angular momentum which can influence results especially when the method is applied in the simulation of violent free surface flows (such as the wave breaking and post-breaking). Khayyer *et al.* (2008) used the CSPH approach proposed by Bonet and Lok (1999) and the ISPH method by Shao and Lo (2003) to introduce a Corrected ISPH (CISPH) formulation ensuring the preservation of angular momentum.

Xu *et al.* (2009) have recently tested the accuracy and stability of three existing projection-based ISPH methods for Taylor-Green and vortex spin-down flows. They showed that ISPH based on keeping a divergence-free velocity field (Cummins and Rudman, 1999), and ISPH based on keeping density invariance (Shao and Lo, 2003) may cause instabilities and numerical noise. However, the combination of a divergence-free velocity field and density invariance provides accurate and stable results with less numerical noise.

It is worth mentioning that in ISPH, the CFL (Courant-Friedrichs-Lewi) condition is based on fluid velocity rather than speed of sound which leads to a bigger time step. However, the complexities of solving the pressure Poisson equation is considerable where the total amount of work during each time step is greatly increased as a result.

Choice for SPH formulation

Having described the different SPH formulations above, Vila's approach of using SPH-ALE method is the best choice of wave propagation in a channel without dissipation (for more details see Guilcher *et al.*, 2007). SPH-ALE is more stable and produces pressure fields with much less numerical noise while the conservation principles are satisfied.

2.4 Free-surface flow with SPH

There is a great deal of industrial interest in free-surface flow investigations to study coastal and offshore hydrodynamics. For example, flooding (O'Connor *et al.*, 2004), dam breaks (Stoker, 1957), wave forces (Dixon *et al.*, 1979), the Manchester Bobber offshore wave energy device developed at the University of Manchester, etc. can be classified into this area of research in mechanical and civil engineering.

Simulating free-surface flow with most Eulerian CFD methods is potentially difficult as explicit treatment of the free surface is required. On the other hand, one of the main advantages of the SPH method is that it can deal with such a complex problem where no special treatment of the free surface is needed, which combined with its Lagrangian nature suits it to the simulation of highly nonlinear and potentially violent flows.

Monaghan (1994) gave some examples of SPH application to a breaking dam, a bore, simulation of a wave maker and propagation of waves towards a beach. His approach was based on the observation that real fluids such as water are compressible, but with a speed of sound which is very much greater than the speed of bulk flow. He modelled boundaries by using boundary particles which impose forces on the fluid. This idea is based on the fact that real boundaries are produced by atoms or molecules which exert a force on the fluid. He also described the simulation of a wave generator with the moving particles. His results show that SPH can be used to simulate free surfaces without any difficulty where the particles are moved with a correct velocity. He also showed that the boundary particles give a satisfactory representation of boundaries, however it needed more corrections in order to conserve angular momentum (Robinson *et al.*, 2007).

Monaghan and Kos (1999) extended their approach numerically and experimentally to investigate a solitary wave propagating onto and over a dry beach and returning after striking a vertical wall. They showed that the solitary wave in experiment, which collapses onto the beach and the jets up the wall and splashes, can be successfully modelled with SPH. The SPH simulations reproduce the shape and position of the surface in a fairly good agreement but the velocity field was not detailed. The SPH method was concluded to be useful for studying wave problems.

Dalrymple and Rogers (2006) also showed waves on a beach including some improvements such as sub-grid scaling to handle turbulence, following Colagrossi and Landrini (2003), Shepard filtering to reinitialise the density of each water particle in order to avoid unphysical behaviour at the free surface due to slight density variations being magnified by the equation of state. Their results are fairly satisfactory, however more comparisons with other numerical models and experimental data were needed.

Following the work of Vila (1999), Guilcher *et al.* (2007) presented the capability of the SPH method to simulate the propagation of water waves in a tank using the ALE Riemann solver approach in SPH and renormalisation of the kernel function. They showed that the standard SPH method is not able to model wave propagation in a long and deep tank and the use of Riemann solvers and renormalization techniques brings significant improvements to the standard SPH scheme such as using a bigger Courant number and simulating waves without dissipation.

Other examples of implementing the SPH method in free-surface problems are modelling of underwater landslide generated waves by Panizzo and Dalrymple (2004), Analysing green water overtopping by Gómez-Gesteira *et al.* (2005), modelling dam break behaviour over a wet bed by Crespo *et al.* (2008), weakly compressible and incompressible investigation of dam break and free-surface flow Issa (2005) and Lee *et al.* (2008), etc.

As explained, use of the SPH method to simulate free-surface problems is still developing but has been applied successfully so far. In the present work, an investigation into the propagation of waves in an intermediate depth and long channel will be demonstrated for different SPH formulations and kernel functions. It is shown that a Riemann solver for each particle-particle interaction is the best choice of SPH approaches because, first, pressure fields can be predicted satisfactorily and, second, the standard SPH formulation may cause propagating waves to decay in the channel (also see Guilcher *et al.*, 2007 and Rogers and Dalrymple, 2008). This enables one to establish a good numerical model for further investigations of bodies in waves.

2.5 Interaction of waves with rigid bodies with SPH

One of the most important topics, which is still mainly at the research and development stage, is the application of SPH to fixed/floating bodies in waves and the ocean. There are still many knowledge gaps for floating devices such as understanding the behaviour of fixed/floating bodies in linear and extreme waves.

The SPH method can be used in order to investigate the interactions between structures, such as fixed, floating and heaving, and water waves. Investigation of the impact of a dam break with a structure, overtopping, moving wedge, floating bodies are good illustrations of using the SPH method to study the interactions between structures and waves.

2.5.1 Impact of waves with fixed objects

Monaghan *et al.* (2003) used SPH to study numerically the impact between a rigid body and water and compared the results with their experiments for a rectangular box. As the box enters the water, a vigorous spray projects fluid beyond the box, then, as the water heaves up, it falls back on the upper surface of the box and initiates a solitary wave. They also presented the formulation for the motion of a rigid body and boundary forces in SPH. The SPH simulation technique reproduced the qualitative features of the entire process and gave satisfactory results compared to the experiments but with a small number of particles, which may not be adequate for many situations.

Gómez-Gesteira and Dalrymple (2004) investigated the impact of a single wave generated by a dam break with a tall stationary structure with a three-dimensional version of the SPH method. They used the method to analyse the propagation of a dam-break wave and the force it exerts on a tall structure located in a region with vertical boundaries, which include two parallel layers of fixed boundary particles placed in a staggered manner. Then they compared it with experimental results to show that the velocity field at a given position point was reproduced perfectly with the model. They used the 3D version of model to reproduce a three-dimensional phenomenon, i.e., the collision of a wave with a structure and its passing around the obstacle and the reconstruction of the wave after passing the structure. In their paper, they used one particle resolution and never showed the convergence study of the model. They added in the summary that the SPH can be used successfully to study three-dimensional wave problems like those related to the collision between waves and structures.

Two-dimensional SPH simulations of wedge water entries was investigated by Oger *et al.* (2006) using a variable smoothing length. They showed a new technique based on a particle sampling method and designed to evaluate fluid pressure on solid boundaries, then extended it to the capture of freely moving body dynamics in a fluid/solid coupling approach. They mentioned that there is no need for high accuracy everywhere in the fluid domain but only in a given area. They proposed a new set of SPH formulations and their results near a boundary showed some satisfactory agreement with analytical and experimental ones. The enhanced SPH scheme extended to the test of the impact of a free-falling wedge whose vertical linear motion was the only degree of freedom, showing a fair agreement when compared to analytical and experimental results. Using variable smoothing length may cause some difficulties such as having extra terms in the SPH equations to deal with time and space (Nelson and Papaloizou, 1994).

Shao *et al.* (2006) investigated the simulation of wave overtopping over a fixed horizontal deck and the regular/irregular waves overtopping of a sloping seawall. The computations are validated against the experimental and numerical data and a good agreement by an incompressible SPH model. They used an algorithm implemented by enforcing the constant particle density in the pressure projection in order to solve the incompressible problems. The comparison between the numerical results and experiment show a good agreement. Incompressible SPH uses a bigger time step for the simulations in comparison with weakly compressible SPH but the model calculates the pressure by solving a Poisson equation with the result that the total amount of work during each time step is greatly increased.

2.5.2 Interaction of waves with free-motion objects

Maruzewski *et al.* (2010) used high performance computing to model a sphere impacting with a free surface for different resolutions. They presented different smoothing lengths and showed that the wet surface does not cover the bottom half of the sphere for the biggest smoothing length (82000 particles and a smoothing length of 0.09m). However, the results for a large number of particle (1235000 particles and a smoothing length of 0.025) is in agreement with the experimental data of Laverty (2003) but it is expensive in terms of CPU cost requiring super computers. The CPU cost could be cheaper if either the particle refinement (Lastiwka *et al.*, 2005) or variable smoothing length (Bonet and Rodriguez-Paz, 2005) was used.

Rogers *et al.* (2008) studied floating bodies in the surf zone using the SPH method. They used the SPHysics code with a Riemann solver to present results for *a)* a floating box in the surf zone under the forcing action of periodic waves, and *b)* a comparison with experiments for the movement of a caisson breakwater in 2D. Their results for the floating box appear to give sensible behaviour with box eventually sliding back and forth on the bed with each wave without any comparison with experiments. However, the simulation of the caisson breakwater was in a good agreement with the experimental data but the horizontal force on the block was noisy which has been recently improved upon in later work by using an improved static-dynamic friction model (Rogers *et al.*, 2010).

SPH simulation of floating body forces by regular waves was presented by Monenti *et al.* (2008). The comparison between their experimental measurements and SPH results were promising, however wave crests were underestimated. They explained that the accuracy of the results could be improved by increasing the number of degrees of freedom for the floating body. They also used the mirror particle technique for the boundaries which are difficult address for complex geometries.

Doring *et al.* (2004) presented the SPH simulation of floating bodies in waves. They used the standard SPH equations to investigate wedge water entry and wave interaction with a box. Their results for wedge water entry were compared with the available experimental data of Petterson *et al.* (1998) in terms of the vertical and angular acceleration time history which were in promising agreements. They also showed waves entering a floating box which was initially located at a distance from the free surface. The results for the floating box are promising in relation to our consideration of validation work.

Campbell and Vignjevic (2009) investigated extreme wave loading on offshore structures using coupled Finite Element-SPH. They first showed the equilibrium of two floating objects. These results were promising in comparison with other CFD methods but they obtained a different phase and amplitude for a rectangular box. They also showed wave loading on 3-D structures without any validation.

As explained, there is limited knowledge of the impact of waves with fixed, forced and free-motion objects in the literature. In this work, an investigation of fixed/heaving bodies will be presented in two and three dimensions. Furthermore, to circumvent the need for a simulation with an extremely large number of particles, variable distributions of particle mass will be used thereby avoiding complicated issues related to particle refinement (Lastiwka *et al.*, 2005) or variable smoothing length (Bonet and Rodriguez-Paz, 2005).

2.6 Résumé

The work presented herein uses the meshless Smoothed Particle Hydrodynamics (SPH) in order to investigate fixed/heaving bodies in waves. The major advantage of using SPH is that no treatment of the free-surface is required which combined with its Lagrangian nature allows us to simulate highly nonlinear and potentially violent flows. The desired flow field can be generated allowing us to study integrated effects like forces and responses. However, in order to conduct proper analysis, the accuracy of predictions, numerical convergence and computational efficiency are important and need to be quantified.

Further to the advantages of meshless methods, the increasing popularity and suitability of SPH to fluid mechanics, particularly in free-surface flow, offers good prospects for simulating wave energy devices. Previously conducted research efforts on the simulation of wave impact on fixed/heaving objects are very limited in relation to the capabilities of the SPH method.

Here, it will first aim to compare different SPH formulations and kernel equations for wave propagation. This will enable one to choose effectively the best alternatives for modelling fixed/heaving objects in waves. Moreover, a new method will be demonstrated to avoid simulations with extremely large number of particles, especially in 3D problems.

Chapter 3

The SPH methodology

The Smoothed Particle Hydrodynamics (SPH) method is a meshless and Lagrangian solver which can be used for free-surface hydrodynamics problems. In this chapter, theoretical and mathematical details of the SPH method are introduced.

3.1 Definition of particles

Here, SPH is used as a technique to obtain approximate numerical solutions of the equations of fluid dynamics by replacing the fluid with a set of particles. Mathematically, the SPH particles are expressed as interpolation points where properties of the fluid can be calculated. On the other hand, and in a physical sense, the fluid can be discretised by a finite number of macroscopic volumes of fluid, which are defined in a continuum mechanics formalism. In SPH each fluid particle i is characterised by a mass m_i, density ρ_i, pressure P_i, velocity v_i and volume ω_i updated at each time step. Much of the basic material mentioned herein was developed in Gingold and Monaghan (1977) and Lucy (1977), and can be found in summary in Monaghan (1992, 2005).

3.2 Mathematical formulation

3.2.1 Basics of the method

The basis of the Smoothed Particle Hydrodynamics method (SPH) uses an integral interpolation of a function Φ, defined over a domain of interest Ω, allowing Φ to be estimated in terms of its values in the surrounding domain. The value of Φ at the location $\mathbf{r}$ can be written as a convolution product of the function Φ:

$$\Phi(\mathbf{r}) = \int_{\Omega} \Phi(\mathbf{r}')\delta_{\varepsilon}(\mathbf{r} - \mathbf{r}')d\mathbf{r}', \tag{3.1}$$

where the summation is obtained by integrating over the whole domain Ω and $d\mathbf{r}$ is a differential volume element. The Dirac function δ_{ε} is approximated by a smoothing function $W(\mathbf{r}\text{-}\mathbf{r}')$ called the smoothing kernel. Therefore $\Phi(\mathbf{r})$ is weighted integral interpolation of the function Φ at the point $\mathbf{r}$, denoted $< \Phi(\mathbf{r}) >$:

$$\Phi(\mathbf{r}) \approx < \Phi(\mathbf{r}) >= \int_{\Omega} \Phi(\mathbf{r}')W(\mathbf{r} - \mathbf{r}')d\mathbf{r}'. \tag{3.2}$$

A Taylor series around $\mathbf{r}$ can be used for $\Phi(\mathbf{r})$ in order to determine the accuracy of the above equation

$$\Phi(\mathbf{r}') = \Phi(\mathbf{r}) + (\mathbf{r}' - \mathbf{r}).\nabla\Phi(\mathbf{r}) + O\left(| \mathbf{r} - \mathbf{r}' |^2\right), \tag{3.3}$$

where $\nabla\Phi(\mathbf{r})$ is the first derivative of Φ. The combination of Equations (3.2) and (3.3) gives (Monaghan, 2005)

$$< \Phi(\mathbf{r}) >= \Phi(\mathbf{r}) \int_{\Omega} W(\mathbf{r} - \mathbf{r}')d\mathbf{r}' + \nabla\Phi(\mathbf{r}). \int_{\Omega} (\mathbf{r}' - \mathbf{r})W(\mathbf{r} - \mathbf{r}')d\mathbf{r}' + O\left(| \mathbf{r} - \mathbf{r}' |^2\right). \tag{3.4}$$

On the other hand, if the kernel function W is spherical, i.e.

$$W(\mathbf{r} - \mathbf{r}') = W(| \mathbf{r} - \mathbf{r}' |) \tag{3.5}$$

then the terms of the order $O\left(| \mathbf{r}' - \mathbf{r} |\right)$ in Equation (3.4) will vanish. Meanwhile, the order of $| \mathbf{r}' - \mathbf{r} |$ is generally similar to the order of the smoothing length, h, therefore Equation (3.4) becomes (Monaghan, 1992)

$$< \Phi(\mathbf{r}) >= \Phi(\mathbf{r}) \int_{\Omega} W\left(| \mathbf{r} - \mathbf{r}' |\right) d\mathbf{r}' + O(h^2). \tag{3.6}$$

Moreover, since

$$\int_{\Omega} W(\mathbf{r}-\mathbf{r}')d\mathbf{r}' = 1, \tag{3.7}$$

thus

$$< \Phi(\mathbf{r}) >= \Phi(\mathbf{r}) + O(h^2). \tag{3.8}$$

this equation shows that the leading-error is proportional to h^2 and leads to a second-order accuracy in space for SPH discretisations (Ellero *et al.*, 2002) . Thus

$$\Phi(\mathbf{r}) = \int_{\Omega} \Phi(\mathbf{r}')W(\mathbf{r}-\mathbf{r}')d\mathbf{r}' + O(h^2). \tag{3.9}$$

3.2.2 Transition to a discrete domain

The transition to a discrete domain is obtained by approximating the integral of the Equation (3.9) by a summation

$$\Phi(\mathbf{r}) = \sum_j \frac{m_j}{\rho_j}\Phi_j W(\mathbf{r}-\mathbf{r}_j), \tag{3.10}$$

where Φ_j denotes the value of Φ at the point occupied by particle j. The summation sign includes all particles j that constitute the fluid domain and the volume element $d\mathbf{r}'$ is replaced by the particles volume m_j/ρ_j.

Thus, the value of the quantity Φ relative to the particle i located at the point $\mathbf{r}_{ij}$ can then be written as the following

$$\Phi_i = \sum_j \frac{m_j}{\rho_j}\Phi_j W_{ij}, \tag{3.11}$$

where

$$W_{ij} = W(\mathbf{r}_i - \mathbf{r}_j), \tag{3.12}$$

and $\mathbf{r}_{ij}$ is the distance between particle i and j which is

$$\mathbf{r}_{ij} = \mathbf{r}_i - \mathbf{r}_j. \tag{3.13}$$

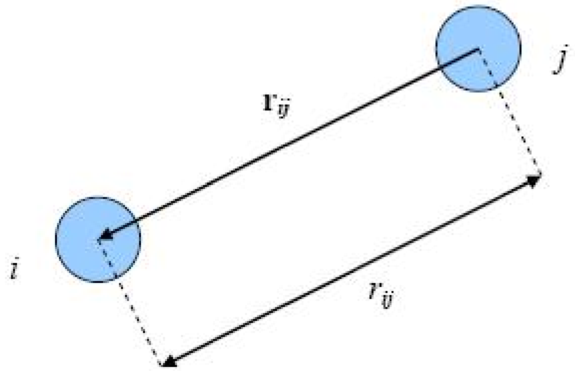

Figure 3.1: Definition of the particle vector $\mathbf{r}_{ij}$

3.2.3 Gradients

Basic formulation

The differentiable form of the interpolation of the function Φ according to Equation (3.11), leads the kernel function to be also differentiable. Therefore, one can write the gradient of the scalar field Φ relative to the particle as

$$(\nabla\Phi)_i = \sum_j \frac{m_j}{\rho_j}\Phi_j \nabla_i W_{ij} \tag{3.14}$$

where the quantity $\nabla_i W_{ij}$ denotes the gradient of kernel taken with respect to i-coordinates as

$$\nabla_i W_{ij} = \left(\frac{\partial}{\partial x_i}\mathbf{i} + \frac{\partial}{\partial y_i}\mathbf{j} + \frac{\partial}{\partial z_i}\mathbf{k}\right) W_{ij}, \tag{3.15}$$

where **i**, **j** and **k** are unit vectors in their coordinate directions. One can understand that it is not necessary to use a grid to evaluate the gradient of a scalar field since it is a function of the kernel gradient which is analytically known.

Other formulations

According to the following mathematical expressions

$$\rho\nabla(\Phi) = \nabla(\rho\Phi) - \Phi\nabla\rho, \tag{3.16}$$

$$\nabla(\Phi) = \rho\nabla(\frac{\Phi}{\rho}) - \frac{1}{\rho}\Phi\nabla\rho, \tag{3.17}$$

and by considering Equation (3.14), two forms of the gradient of a scalar field are obtained:

$$(\nabla\Phi)_i = \frac{1}{\rho_i}\sum_j m_j(\Phi_j - \Phi_i)\nabla_i W_{ij}, \tag{3.18}$$

$$(\nabla\Phi)_i = \rho_i\sum_j m_j(\frac{\Phi_i}{\rho_i^2} + \frac{\Phi_j}{\rho_j^2})\nabla_i W_{ij}. \tag{3.19}$$

There are several forms of scalar field gradients in the literature (see Monaghan, 1992). Equation (3.18) has the well-known feature of presenting the zero gradient of a constant field of Φ. Similar expressions can be used for the the divergence of a vector field and tensors (Vila, 1999, and Monaghan, 2005).

3.3 The kernel function

3.3.1 Fundamental properties: axioms

As mentioned before, an interpolation kernel over the whole domain Ω must satisfy the following

$$\int_\Omega W(\mathbf{r} - \mathbf{r}')d\mathbf{r}' = 1, \tag{3.20}$$

where $W > 0$. Here, the smoothing length, h, which is similar to an average cell size in Eulerian codes, is defined in order to characterise the spatial discretisation of the problem. The above equation can be written in the discretised form of

$$\sum_j W(\mathbf{r} - \mathbf{r}_j)\frac{m_j}{\rho_j} = 1. \tag{3.21}$$

One the other hand, when the parameter h (the smoothing length) tends to zero, the kernel function must tends to the Dirac distribution

$$\lim_{h\to 0} W(\mathbf{r} - \mathbf{r}') = \delta_\varepsilon(\mathbf{r} - \mathbf{r}'). \tag{3.22}$$

Moreover, the kernel function must be at least once differentiable and its derivative

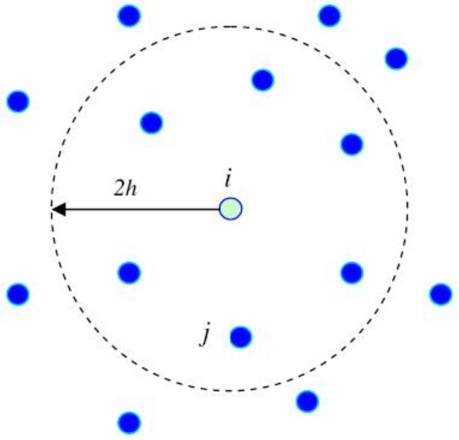

Figure 3.2: Neighbours of particle i within the kernel

must be continuous in order to avoid large fluctuations which affect the solutions (Gingold & Monaghan, 1982 and Issa, 2005).

3.3.2 The smoothing length

The smoothing length, which is analogous to an average cell size, characterises the spatial discretisation of the problem in SPH. In SPHysics, the optimum value of the smoothing length is found to be $h = 1.3\triangle$ (e.g. see Rogers *et al.*, 2010) where $\triangle$ is the initial particle spacing and the summation Equation (3.10) is restricted to particles j, which are considered as the nearest neighbours of particle i within the kernel (Figure 3.2).

Quinlan *et al.* (2006) investigated the truncation error for the approximation of the kernel function which depends on both the smoothing length h and the ratio of particle spacing to smoothing length $\triangle/h$. For one dimensional analysis they showed that reducing h and keeping constant $\triangle/h$ leads to a decrease of error as h^2 until a limiting discretisation error, which is independent of h, is reached. If h is kept constant while reducing $\triangle/h$, where the number of neighbours per particle is increased, the error will decrease depending on the rate of the kernel function's smoothness. Quinlan's *et al.* (2006) numerical investigations indicated that the results are also true for three dimensions.

3.3.3 Kernel formulations

Generally, a kernel function can be written as

$$W_{ij} = \frac{\varpi}{h^{\kappa}} f\left(\frac{\mathbf{r}_{ab}}{h}\right), \tag{3.23}$$

where ϖ and κ are the normalisation contact and the number of dimensions, respectively. ϖ is employed in order to ensure the condition of (Equation 3.20) in the continuous domain. Concerning the function *f*, several formulations are available in the literature. The second order (quadratic) kernel function is defined as

$$W_{ij} = \frac{\varpi}{h^{\kappa}} \begin{cases} \frac{3}{16}q^2 - \frac{3}{4}q + \frac{3}{4} & q \leq 2 \\ 0 & q \geq 2 \end{cases}, \tag{3.24}$$

where q denotes the ratio $\mathbf{r}_{ij}/h$, and $\frac{\varpi}{h^{\kappa}}$ is $\frac{2}{\pi h^2}$ and $\frac{5}{4\pi h^3}$ in 2D and 3D, respectively (Monaghan and Lattanzio, 1985). The advantage of using a second-order kernel are the simplicity and cheap computational cost. However, it is not suitable for physical processes needing higher-order interpolation to capture important effects.

Monaghan (1992) defined the third-order kernel based on spline function as

$$W_{ij} = \frac{\varpi}{h^{\kappa}} \begin{cases} 1 - \frac{3}{2}q^2 + \frac{3}{4}q^3 & 0 \leq q \leq 1 \\ \frac{1}{4}(2-q)^3 & 1 \leq q \leq 2 \\ 0 & q \geq 2 \end{cases}, \tag{3.25}$$

where the term ϖ/h^{κ}can be

$$\frac{2}{3}, \frac{10}{7\pi^2}, \frac{1}{\pi^3}$$

in one, two and three dimensions, respectively. The cubic spline kernel has a maximum in its gradient at the particle centre which can lead to tensile instability, and has to be corrected, according to Monaghan (2000), in order to avoid particle clumping. (see section 3.3.4) but it approximates the Gaussian kernel very closely while it has a compact support, meaning that interactions are zero for $q > 2$. Also, the second derivative of the cubic spline kernel is continuous.

In the same way, a fourth and fifth order spline kernels are defined in the literature (see Morris *et al.*, 1997). Using higher order kernel may have a disadvantage of expensive computational cost in comparison with the cubic spline kernel (Morris *et al.*, 1997).

3.3.4 Tensile instability

A one-dimensional von Neumann analysis of the SPH method was conducted by Swegle and Attaway (1995). They have found that the SPH method suffers form a tensile instability when negative pressures which attract particles occur. The instability does not result from the numerical time integration algorithm, but rather from an effective stress resulting from a non-physical negative modulus produced by the interaction between the constitutive relation and the kernel interpolation. In other words the nature of original particle differential equations is changed by the kernel interpolation in spatial discretisation. The condition of the criterion for stability is deducted as (Monaghan, 2000)

$$W_{ij}^{''}.\tau > 0, \tag{3.26}$$

where $W_{ij}^{''}$ is the second derivative of the kernel function and τ is the particle stress, negative in compression and positive in tension. Both derivation of above relation are independent of the viscous term modelling and the temporal integration scheme. Generally, it has been proved that a more universal instability criterion can be obtained by considering the system potential energy. The tensile instability is inherent to the cubic and quintic kernels. However, more recent research by Robinson *et al.* (2008) suggest that the cause of tensile instability is due to the behaviour in the frequency domain.

Since the cubic kernel is used for most problems of this research an assessment of tensile instability is needed, especially at the interface of different particle size introduced in Chapter 5.

3.3.5 Removing tensile instability

Kernel improvement

As mentioned in the previous session, tensile instability occurs when the first derivative of either the cubic or quintic kernels goes to zero with q. To overcome this issue other types of kernel can be implemented. However, as described later, the cubic kernel is found to be the best choice of kernel function for propagation of waves in a channel.

Artificial pressure

Monaghan (2000) revealed that the kernel instability can be removed if the repulsive force is written in terms of the kernel. The pressure gradient term present in the momentum Equation (3.34) is thus modified according to

$$\frac{P_j}{\rho_j^2} + \frac{P_i}{\rho_i^2} \longrightarrow \frac{P_j}{\rho_j^2} + \frac{P_i}{\rho_i^2} + Cf_{ij}^{\kappa} \tag{3.27}$$

where the function f_{ij} is defined as

$$f_{ij} = \frac{W_{ij}}{W_{\Delta}} \tag{3.28}$$

and n must be positive and C is determined from a dispersion relation (Monaghan, 2000 and Issa, 2005) according to the pressure and density of particle i or j. Δ corresponds to the initial spacing of particles. Monaghan (2000) also showed that for the fluid dynamics, where $h = 1.3\Delta$ and $\kappa = 4$, the repulsive force increases by a factor of ~ 23 as r_{ij} decreases from Δ to zero. The tensile instability is only palliated by this correction but the instability is still there.

3.4 SPH governing equations

3.4.1 Governing conservation equations

The basic governing equations of weakly compressible flow are based on the following two fundamental physical conservation laws

- Conservation of mass
- Conservation of momentum

Therefore, the rates of change of velocity, density and position are expressed by the Euler equations in the following Lagrangian form:

$$\frac{d\rho}{dt} = -\rho\nabla.\mathbf{v}, \tag{3.29}$$

$$\frac{d\mathbf{v}}{dt} = -\frac{1}{\rho}\nabla P + \mathbf{g}, \tag{3.30}$$

$$\frac{d\mathbf{r}}{dt} = \mathbf{v}. \tag{3.31}$$

where $\mathbf{v}$ is the velocity, ρ is the density, P is the pressure and $\mathbf{g}$ is the body force per unit mass. In general, P can be described as a function of ρ.

The SPH version of these equations are described in the next sections.

3.4.2 Standard SPH formulation

SPH continuity equation

The SPH continuity equation can be obtained in two ways as shown below:

- Equation (3.9) is used to find the natural formulation of the continuity equation, where Φ corresponds to the density ρ (Monaghan, 2005)

  $$\rho_i = \sum_j m_j W_{ij}, \tag{3.32}$$

- In the classic Lagrangian formulation, the continuity equation can be written as

  $$\frac{d\rho}{dt} = -\rho\nabla\mathbf{v} = -\nabla(\rho\mathbf{v}) + \nabla\rho.\mathbf{v}, \tag{3.33}$$

  where the operator d/dt denotes a Lagrangian derivative. Using Equation (3.11) leads the SPH form of continuity to be deduced as

  $$\frac{d\rho_i}{dt} = \sum_j m_j \mathbf{v}_{ij}.\nabla_i W_{ij}, \tag{3.34}$$

  with $\mathbf{v}_{ij} = \mathbf{v}_i - \mathbf{v}_j$ (Monaghan, 2005).

From a compressible point of view, since the number of the particles is constant the mass of the system is conserved according to Equations (3.32) and (3.34) , therefore the mass of each particle is constant throughout the calculations. From an incompressible point of view, velocity divergence is not identically zero and therefore both equations are not exactly conservative (Issa, 2005). Moreover, because the kernel gradient should be calculated for momentum equation (see section 3.4.2), using Equation (3.34) can be a best choice since the kernel gradient can be calculated in one subroutine.

SPH momentum equation

The momentum conservation equation in a continuum field is

$$\frac{d\mathbf{v}}{dt} = -\frac{1}{\rho}\nabla P + \mathbf{g}, \tag{3.35}$$

where P and $\mathbf{g}$ refer to pressure and external forces, respectively.

Gingold and Monaghan (1982) obtained the original form of SPH momentum equation by converting the acceleration equation into the SPH as

$$(\nabla P)_i = \sum_j m_j \frac{P_j}{\rho_j}.\nabla_i W_{ij}, \tag{3.36}$$

such that

$$\frac{d\mathbf{v}_i}{dt} = -\frac{1}{\rho_i}\sum_j m_j \frac{P_j}{\rho_j}.\nabla_i W_{ij} + \mathbf{g} \tag{3.37}$$

However, symmetrisation of pressure gradient can be achieved by rewriting the term $\nabla P/\rho$ as

$$\frac{\nabla P}{\rho} = \nabla\left(\frac{P}{\rho}\right) + \frac{P}{\rho^2}\nabla\rho. \tag{3.38}$$

Hence, using SPH interpolation rules, the above equation becomes (Monaghan, 2005)

$$\frac{d\mathbf{v}_i}{dt} = -\sum_j m_j\left(\frac{P_j}{\rho_j^2} + \frac{P_i}{\rho_i^2}\right).\nabla_i W_{ij} + \mathbf{g}. \tag{3.39}$$

Artificial Viscosity

Artificial viscosity is a common way proposed by Monaghan (1992) to model the effect of viscosity in SPH. The artificial viscosity, Π_{ij}, is added to the momentum equation as

$$\frac{d\mathbf{v}_i}{dt} = -\sum_j m_j \left(\frac{P_j}{\rho_j^2} + \frac{P_i}{\rho_i^2} + \Pi_{ij} \right) .\nabla_i W_{ij} + \mathbf{g}, \tag{3.40}$$

where $\frac{d\mathbf{r}_i}{dt} = \mathbf{v}_i$.

$$\Pi_{ij} = \begin{cases} \frac{-\lambda_{vis} \bar{c}_{ij} \mu_{ij}}{\bar{\rho}_{ij}} & \mathbf{v}_{ij}\mathbf{r}_{ij} < 0 \\ 0 & \mathbf{v}_{ij}\mathbf{r}_{ij} > 0 \end{cases}, \tag{3.41}$$

with

$$\mu_{ij} = \frac{h\mathbf{v}_{ij}\mathbf{r}_{ij}}{r_{ij}^2 + \iota^2}, \tag{3.42}$$

$$\bar{c}_{ij} = \frac{c_i + c_j}{2}, \tag{3.43}$$

$$\bar{\rho}_{ij} = \frac{\rho_i + \rho_j}{2}. \tag{3.44}$$

$\iota^2 = 0.01h^2$ and λ_{vis} is a free parameter that can be changed according to each problem. Here, c_i and c_j are the speed of sound of particle i and j, respectively.

Monaghan (1997) introduced a new artificial viscosity in order to handle shocks in high Mach numbers. This artificial viscosity is defined as

$$\Pi_{ij} = -\frac{K\upsilon_{sig}(i,j)\mathbf{v}_{ij}}{\bar{\rho}_{ij}} . \frac{\mathbf{r}_{ij}}{r_{ij}}, \tag{3.45}$$

where

$$\upsilon_{sig}(i,j) = c_i + c_j - 2\mathbf{v}_{ij}.\frac{\mathbf{r}_{ij}}{r_{ij}}, \tag{3.46}$$

and K is an arbitrary constant. The new artificial viscosity is not taken to the account in this investigation since the problems studied here are not with high Mach numbers.

Laminar Viscosity

The simplified laminar viscosity introduced by Morris (1997) is given by

$$\left(\nu_0 \nabla^2 \mathbf{v}\right)_i = \sum_j m_j \left(\frac{4\nu_0 \mathbf{r}_{ij}\mathbf{v}_{ij}}{(\rho_i + \rho_j)\left(\mid \mathbf{r}_{ij} \mid^2 + \iota^2 \right)} \right) .\nabla_i W_{ij}, \tag{3.47}$$

where υ_0 is the kinematic viscosity of laminar flow ($= 10^{-6} m^2/s$) and is added to the momentum equation as

$$\frac{d\mathbf{v}}{dt} = -\frac{1}{\rho}\nabla P + \mathbf{g} + \nu_0 \nabla^2 \mathbf{v},. \tag{3.48}$$

Position of particles

The position of particle i can be obtained by considering the definition of the velocity as (Monaghan, 2005):

$$\frac{d\mathbf{r}_i}{dt} = \mathbf{v}_i. \tag{3.49}$$

XSPH method

It is efficient to obtain the particle position according to the XSPH method since it keeps the particle orderly in the absence of viscosity. Therefore, the above equation is corrected

$$\frac{d\mathbf{r}_i}{dt} = \mathbf{v}_i + \underbrace{\varrho \sum_j \frac{m_j\left(\mathbf{v}_j - \mathbf{v}_i\right)}{\bar{\rho}_{ij}} W_{ij}}_{corrective\ term}, \tag{3.50}$$

where

$$\bar{\rho}_{ij} = \frac{\rho_i + \rho_j}{2} \qquad and \qquad 0 \leq \varrho < 1. \tag{3.51}$$

Here, the particle equation is modified with an average velocity characteristic of the neighbourhood of particle i. XSPH has the capability of increasing dispersion in the simulation of nearly incompressible flows in order to avoid situations where particles clump together due to numerical viscosity. Thus, particles stay more ordered (Monaghan, 1992, 1994 & 1995).

There are two velocities when the XSPH method is used, one results from the momentum equation and the second corresponds to r.h.s of Equation (3.50). Therefore, the velocity used in the continuity equation (Equation 3.34) must be the corrected velocity in order to ensure the consistency of Navier-Stokes equations (Issa, 2005).

It was proved by Colagrossi and Landrini (2003), and Panizzo (2004) that, just as the local velocities are averaged in the XSPH term, the averaging of the densities helps ensure that the free surfaces are smooth and physically acceptable. It can be one of the reasons that Shepard filtering (see Dalrymple and Rogers, 2006) is used.

3.4.3 Arbitrary Lagrange Euler (ALE) formulation in SPH

Vila (1999) used an Arbitrary Lagrange Euler (ALE) method together with the SPH method linking the finite volume method into the hybrid method, in particular upwind scheme like the Godunov method. Use of SPH-ALE is an alternative to artificial viscosity which solves a Riemann problem between each particle pair.

Conservative Riemann Formulation

In Vila's (1999) paper, he derived the SPH equations in ALE by starting from the following PDE in conservative form was stated

$$L_{\vartheta} + divF(r, t, \Phi) = S, \tag{3.52}$$

where Φ is the vector of conserved variables, the subscript ϑ is a regular vector field, F is a flux vector, S represents source terms and L_{ϑ} is the transport operator given by:

$$\Phi \to L_{\vartheta}(\Phi) = \frac{\partial \Phi}{\partial t} + \sum \frac{\partial}{\partial r}(\mathbf{v}\Phi). \tag{3.53}$$

Therefore in 1-D

$$\frac{\partial \Phi}{\partial t} + \frac{\partial (u\Phi)}{\partial x} + \frac{\partial F}{\partial x} = S, \tag{3.54}$$

which is

$$\frac{\partial \Phi}{\partial t} + \Phi\frac{\partial u}{\partial x} + u\frac{\partial \Phi}{\partial x} + \frac{\partial F}{\partial x} = S, \tag{3.55}$$

or in turn

$$\frac{D\Phi}{Dt} = -\left[\Phi\frac{\partial u}{\partial x} + \frac{\partial F}{\partial x}\right] + S. \tag{3.56}$$

Vila (1999) defined the particle approximation as

$$\Pi^h(f) = \sum_j \omega_j(t) f_j W(\mathbf{r} - \mathbf{r}_j), \tag{3.57}$$

which is equivalent to Equation (3.11)

$$f(\mathbf{r}) = \sum_j \frac{m_j}{\rho_j} f_j W(\mathbf{r} - \mathbf{r}_j) = \Pi^h(f), \tag{3.58}$$

where the volume of each particle is

$$\omega_i(t) = \frac{m_i}{\rho_i}. \tag{3.59}$$

(note Π^h here is not the same as artificial viscosity in Equation (3.40)).

He also showed the gradient of a function as

$$\nabla \Pi^h(f)_i = \sum_j \omega_j(t) f_j \nabla W_{ij}, \tag{3.60}$$

For symmetrical formulation designed to give equal and opposite reactions between interacting particles, this is replaced by

$$\nabla \Pi^h(f)_i = \sum_j \omega_j(t)(f_i + f_j) \nabla W_{ij}, \tag{3.61}$$

The particles move along the paths given by the particle velocities.

The definition of the particle approximation and derivatives (Equations 3.57 and 3.61) in now substituted into Equation (3.52) and then the equations of conservation become

$$\frac{d\mathbf{r}_i}{dt} = \mathbf{v}_i, \tag{3.62}$$

$$\frac{d\omega_i}{dt} = \omega_i \nabla \mathbf{v}_i, \tag{3.63}$$

$$\frac{d}{dt}(\omega_i \Phi_i) + \omega_i \sum_j \omega_j \left(F(\mathbf{r}_i, t, \Phi_i) + F(\mathbf{r}_j, t, \Phi_j) \right) . \nabla W_{ij} = \omega_i S_i. \tag{3.64}$$

Here, the definition of conserved variables and fluxes in given by

$$\Phi = \begin{bmatrix} \rho \\ \rho u \\ \rho w \end{bmatrix}, \qquad F_x = \begin{bmatrix} 0 \\ P \\ 0 \end{bmatrix} \qquad F_z = \begin{bmatrix} 0 \\ 0 \\ P \end{bmatrix}, \tag{3.65}$$

to derive the conventional SPH equations. Thus Equation (3.64) becomes

$$\frac{d}{dt}\left(\omega_i \rho_i\right) = 0, \tag{3.66}$$

$$\frac{d}{dt}\left(\omega_i \rho_i \mathbf{v}_i\right) + \omega_i \sum_j \omega_j \left(P_i + P_j\right) . \nabla W_{ij} = \omega_i S_i, \tag{3.67}$$

if the value of $\omega_i \rho_i = m_i$ is taken constant then the above equations become similar to standard SPH equations.

Consider now the gradient of the kernel defined as

$$\nabla_i W_{ij} = \frac{\partial W}{\partial q} \nabla_i q, \tag{3.68}$$

$$\nabla_i W_{ij} = \frac{\partial W_{ij}}{\partial x_i}\mathbf{i} + \frac{\partial W_{ij}}{\partial z_i}\mathbf{k} = \frac{\partial W}{\partial q}\left(\frac{\partial q}{\partial x_i}\mathbf{i} + \frac{\partial q}{\partial z_i}\mathbf{k}\right), \tag{3.69}$$

where $q = \mathbf{r}_{ij}/h$ and $r_{ij} = |\mathbf{r}_i - \mathbf{r}_j|$ so that

$$\frac{\partial q}{\partial x_i} = \frac{1}{h}\frac{\partial r_{ij}}{\partial x_i} \tag{3.70}$$

and

$$\nabla_i W_{ij} = \frac{\partial W_{ij}}{\partial x_i}\mathbf{i} + \frac{\partial W_{ij}}{\partial z_i}\mathbf{k} = \frac{1}{h}\frac{\partial W_{ij}}{\partial q}\frac{\mathbf{r}_i - \mathbf{r}_j}{|\mathbf{r}_i - \mathbf{r}_j|} = -D\theta_{ij}\mathbf{n}_{ij}, \tag{3.71}$$

where

$$\mathbf{n}_{ij} = \frac{(\mathbf{r}_i - \mathbf{r}_j)}{|\mathbf{r}_i - \mathbf{r}_j|}, \tag{3.72}$$

is the unit vector joining points i and j (Figure 3.3) and

$$D\theta_{ij} = D\theta(\mathbf{r}_{ij}). \tag{3.73}$$

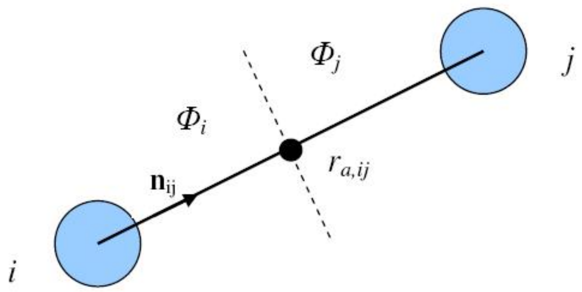

Figure 3.3: One dimension Riemann problem between interacting points

Hence, the governing conservation Equation (3.64) can be written as

$$\frac{d}{dt}\left(\omega_i \Phi_i\right) - \omega_i \sum_j \omega_j \left(F_i + F_j\right).\mathbf{n}_{ij} D\theta_{ij} = \omega_i S_i. \tag{3.74}$$

The interactions between the particles i and j are computed along the direction $\mathbf{n}_{ij}$ connecting r_i with r_j. All features are introduced naturally at $r_{a,ij} = \frac{r_i + r_j}{2}$, and the conservation law related to the direction $\mathbf{n}_{ij}$ becomes:

$$\frac{\partial \Phi}{\partial t} + \frac{\partial}{\partial r}\left(F\left(\mathbf{r}_{ij}, t, \Phi\right).\mathbf{n}_{ij}\right) = S_i. \tag{3.75}$$

In accordance with Godunov-type methods, it is natural therefore to replace:

$$\left(F\left(\Phi_i\right) + F\left(\Phi_j\right)\right).\mathbf{n}_{ij}$$

by a numerical flux of finite difference scheme, $2N\left(\mathbf{n}_{ij}, \Phi_i, \Phi_j\right)$, which is required to satisfy

$$\begin{array}{ll} (1) & N(n,u,u) = F(u).\mathbf{n} \\ (2) & N(n,u,w) = -N(-n,w,u)' \end{array} \tag{3.76}$$

To formulate a Riemann solver, the 2-D Eulerian equation can be considered in the conservative form and in the absence of source terms with a regular vector transport field v^0 as given by Vila (1999)

$$L_{v^0} + \sum \frac{\partial}{\partial r}\left(F_E^l(\Phi) - \mathbf{v}^{0,l}\Phi\right) = 0, \tag{3.77}$$

where l denotes the coordinates and the fluxes are given by

$$F_{E,x}(\Phi) = \begin{bmatrix} \rho u \\ P + \rho u^2 \\ \rho u w \end{bmatrix} \qquad F_{E,z}(\Phi) = \begin{bmatrix} \rho w \\ \rho u w \\ P + \rho w^2 \end{bmatrix}, \tag{3.78}$$

Thus, Equation (3.77) written as

$$\frac{\partial}{\partial t}(\Phi) + \frac{\partial \left(u^0 \Phi\right)}{\partial x} + \frac{\partial \left(w^0 \Phi\right)}{\partial z} + \frac{\partial}{\partial x}\left(F_{E,x}(\Phi) - u^0 \Phi\right) + \frac{\partial}{\partial z}\left(F_{E,z}(\Phi) - w^0 \Phi\right) = 0, \tag{3.79}$$

is better written as

$$\frac{\partial}{\partial t}(\Phi) + \frac{\partial}{\partial x}\left(F_{E,x}(\Phi)\right) + \frac{\partial}{\partial z}\left(F_{E,z}(\Phi)\right) = 0. \tag{3.80}$$

or more fully as

$$\frac{\partial}{\partial t}\begin{bmatrix} \rho \\ \rho u \\ \rho w \end{bmatrix} + \frac{\partial}{\partial x}\begin{bmatrix} \rho u \\ P + \rho u^2 \\ \rho u w \end{bmatrix} + \frac{\partial}{\partial z}\begin{bmatrix} \rho w \\ \rho u w \\ P + \rho w^2 \end{bmatrix} = 0, \tag{3.81}$$

which is the more recognisable 2-D Eulerian conversation law excluding source terms.

Incorporating the one-dimensional Riemann problem

Vila (1999) also noticed that conservative formulation by the SPH method leads to the appearance of one-dimensional Riemann problems between pairs of neighbouring points. Thus, the Riemann problem has to be solved between particle i and j in one-dimensional set of conservation laws (see Figure 3.3, whose initial condition is discontinuous at the mid-point (Marongiu, 2008)):

$$\begin{cases} \frac{\partial}{\partial t}(\Phi) + \frac{\partial}{\partial x}\left(F_E(\Phi).\mathbf{n}_{ij} - \mathbf{v}^0_{a,ij}(x_{ij}, t).\mathbf{n}_{ij}\Phi\right) = 0 \\ \Phi(x,0) = \begin{cases} \Phi_i & x < 0 \\ \Phi_j & x > 0 \end{cases} \end{cases}, \tag{3.82}$$

Since a Lagrangian calculation is performed, the transport field $\mathbf{v}^0(x,t)$ must be treated in order to apply the technique developed for shock-capturing techniques. Therefore, if we consider the classical Riemann problem for the Eulerian equations (which does not include the effect of the velocity field $\mathbf{v}^0$)

$$\begin{cases} \frac{\partial}{\partial t}(\Phi) + \frac{\partial}{\partial x}\left(F_E(\Phi).\mathbf{n}_{ij}\right) = 0 \\ \Phi(x,0) = \begin{cases} \Phi_i & x < 0 \\ \Phi_j & x > 0 \end{cases} \end{cases}, \tag{3.83}$$

which has the exact solution (to the "non-moving Riemann" problem) of $\Phi_{E,a,ij} = \Phi_{E,a,ij}\left(\frac{x}{t}; \Phi_i, \Phi_j\right)$. The solution of the above is given by

$$\begin{cases} \Phi_E = \left(\frac{x+X^0(t)}{t}; \Phi_i, \Phi_j\right) \\ X^0(t) = \int_0^t \mathbf{v}^0(x_{a,ij}, T).\mathbf{n}_{ij} dT \end{cases}, \tag{3.84}$$

which is the solution to the "moving Riemann" problem. The solution to $\Phi_{a,ij}$ can be obtained using any of the techniques developed for approximate Riemann solvers available in the literature. The approximation solution will be given later in sections 3.4.3 and 3.4.3.

System of discrete conservation laws

The flux between the particles can be evaluated with the solution $\Phi_{a,ij}$

$$\begin{cases} \lambda^0_{ij} = \mathbf{v}^0_{ij}(x_{ij}, t).\mathbf{n}_{ij} \\ \Phi^\lambda_{a,ij} = \Phi_{ij}\left(\lambda^0_{ij}\right) = \Phi_{a,ij}\left(\lambda^0_{ij}, \Phi_i, \Phi_j\right) \\ \mathbb{N}_{a,ij}\left(\Phi_i, \Phi_j\right) = F_{a,ij}\left(\Phi^\lambda_{a,ij}\right) - \mathbf{v}^0_{ij} \otimes \Phi^\lambda_{a,ij} \\ N_{a,ij}\left(n_{ij}, \Phi_i, \Phi_j\right) = \mathbb{N}_{a,ij}\left(\Phi_i, \Phi_j\right).\mathbf{n}_{ij} \end{cases}, \tag{3.85}$$

where λ^0_{ij} is the projection of the local velocity field onto the direction vector $\mathbf{n}_{ij}$ between each particle, subscript a denotes the result from the approximate Riemann solver, and $N_{a,ij}$ is the flux between each particles.

The terms in the above equation can be written more fully as

$$\mathbf{v}^0_{ij} \approx \frac{1}{2}\left(\mathbf{v}^0_i + \mathbf{v}^0_j\right) = \frac{1}{2}\left[\left(u_i\mathbf{i} + w_i\mathbf{j}\right) + \left(u_j\mathbf{i} + w_j\mathbf{j}\right)\right], \tag{3.86}$$

$$\lambda^0_{ij} = \mathbf{v}^0_{ij}.\mathbf{n}_{ij} = \frac{\left(u_i + u_j\right)\left(x_i + x_j\right) + \left(w_i + w_j\right)\left(z_i + z_j\right)}{2\left|\mathbf{r}_i - \mathbf{r}_j\right|}, \tag{3.87}$$

$$\Phi^{\lambda}_{a,ij} = \Phi_{ij,i}\left(\lambda^{0}_{ij}\right) = \Phi_{a,ij}\left(\lambda^{0}_{ij}, \Phi_i, \Phi_j\right) = \begin{bmatrix} \rho_{a,ij} \\ (\rho\mathbf{v})_{a,ij} \end{bmatrix} \tag{3.88}$$

$$\mathbb{N}_{a,ij}\left(\Phi_i, \Phi_j\right) = F_{a,ij}\left(\Phi^{\lambda}_{a,ij}\right) - \mathbf{v}^{0}_{ij} \otimes \Phi^{\lambda}_{a,ij} \tag{3.89}$$

with

$$N_{a,ij}\left(n_{ij}\Phi_i, \Phi_j\right) = \mathbb{N}_{a,ij}\left(\Phi_i, \Phi_j\right).\mathbf{n}_{ij} = \begin{bmatrix} \rho_{a,ij}\left(\mathbf{v}_{a,ij} - \mathbf{v}^{0}_{ij}\right) \\ P_{a,ij} + \rho_{a,ij}\mathbf{v}_{a,ij}\left(\mathbf{v}_{a,ij} - \mathbf{v}^{0}_{ij}\right) \end{bmatrix}. \tag{3.90}$$

The particle approximation of conservation Equations (3.64) and (3.74) become

$$\frac{d}{dt}\left(\omega_i\Phi_i\right) + \omega_i\sum_j \omega_j 2\mathbb{N}_{a,ij}\left(\Phi_i, \Phi_j\right).\nabla W_{ij} = \omega_i S_i, \tag{3.91}$$

$$\frac{d}{dt}\left(\omega_i\Phi_i\right) - \omega_i\sum_j \omega_j 2\mathbb{N}_{a,ij}\left(\Phi_i, \Phi_j\right).\mathbf{n}_{ij} D\theta_{ij} = \omega_i S_i. \tag{3.92}$$

Thus, the governing equations become

$$\begin{cases} \frac{d\mathbf{r}_i}{dt} = \mathbf{v}_i \\ \frac{d\omega_i}{dt} = \omega_i \nabla.\mathbf{v}_i \\ \frac{d}{dt}\left(\omega_i\rho_i\right) + \omega_i\sum_j \omega_j 2\rho_{a,ij}\left(\mathbf{v}_{a,ij} - \mathbf{v}^0\right)\nabla W_{ij} = 0 \\ \frac{d}{dt}\left(\omega_i\rho_i\mathbf{v}_i\right) + \omega_i\sum_j \omega_i 2\left[P_{a,ij} + \rho_{a,ij}\mathbf{v}_{a,ij} \otimes \left(\mathbf{v}_{a,ij} - \mathbf{v}^{0}_{ij}\right)\right]\nabla W_{ij} = \omega_i S. \end{cases} \tag{3.93}$$

where the Kronecker product is defined in 2-D as:

$$\mathbf{v}_{a,ij} \otimes \left(\mathbf{v}_{a,ij} - \mathbf{v}^0\right) = \begin{bmatrix} u_{a,ij}\left(u_{a,ij} - u^0\right) & w_{a,ij}\left(u_{a,ij} - u^0\right) \\ u_{a,ij}\left(w_{a,ij} - w^0\right) & w_{a,ij}\left(w_{a,ij} - w^0\right) \end{bmatrix}. \tag{3.94}$$

Here and opposite to the standard SPH equations, $\frac{d}{dt}(\omega_i\rho_i) = \frac{d}{dt}(m_i) \neq 0$, so that the mass of particles are not constant.

Definition of the Riemann problem

The Riemann problem includes a discontinuity located at x_0 in space where

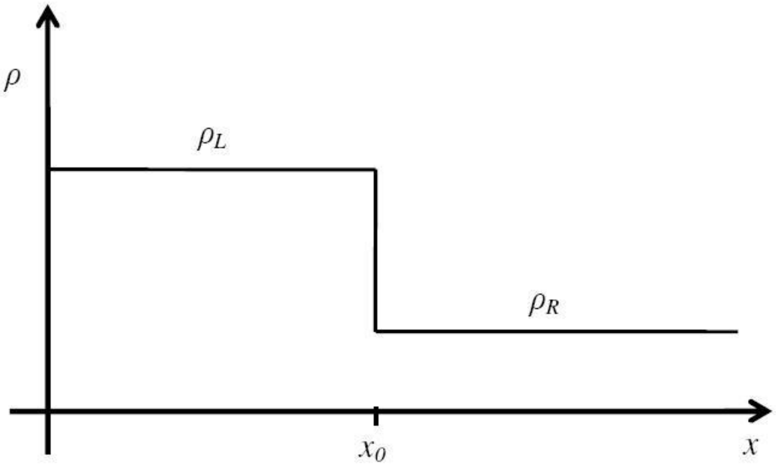

Figure 3.4: Initial discontinuity in density in 1-D

$$\Phi(x,t) = \begin{cases} \Phi_L & x \le x_0 \\ \Phi_R & x > x_0 \end{cases}, \tag{3.95}$$

where the subscripts L and R denote left and right states, respectively (Toro, 2001). For instance, Figure (3.4) shows a simple discontinuity in density.

Figure (3.5) clearly shows the structure of the solution of the Riemann problem, which is defined as all the states from left to right regions, on the x-t plane for one-dimension where a shock wave propagates to the right while a rarefaction wave propagates to the left (Figure 3.5.a). A possible wave pattern in solution of the Riemann problem can be displayed as a single line for shock propagation to the right and rarefaction wave spreading out to the left (Figure 3.5.b). However, the unknown region between the left and right waves is divided by the middle wave into two sub-regions star and specified a region called star region. The middle wave is always a contact discontinuity while the left and the right waves are either the shock or rarefaction waves depending on the initial conditions (see Toro, 1997).

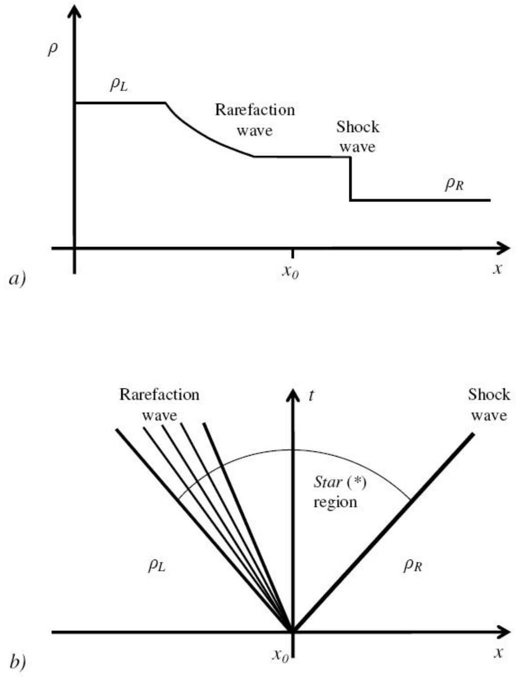

Figure 3.5: $a)$ Propagation of initial discontinuity at time $t = t_1$, $b)$ Evolution of discontinuity in density

Solution of the Riemann problem

There is no exact closed-form solution to the Riemann problem for ideal gases, or for much simpler models such as the isentropic and isothermal equations hence approximate Riemann solvers have been a large area of research (Toro, 2001). The Harten-Lax-van Leer (HLL) Riemann solver approach is based on estimating the smallest and largest signal velocities in the solution of the Riemann problem. In this approach, intermediate waves such as contact discontinuities are ignored. The Harten-Lax-van Leer-Contact (HLLC or HLL for contact wave) approximate Riemann solver is a modification of the basic HLL scheme to account for the influence of intermediate waves (Toro, 2001). Considering the following conservation law in 1-D

$$\frac{\partial \mathbf{\Phi}}{\partial t} + \frac{\partial \mathbf{F}}{\partial x} = 0, \qquad (3.96)$$

where the vector of conserved variables and fluxes are given by

$$\mathbf{\Phi} = \begin{bmatrix} \rho \\ \rho u \end{bmatrix} \qquad and \qquad \mathbf{F} = \begin{bmatrix} \rho \\ \rho u^2 + P \end{bmatrix}. \qquad (3.97)$$

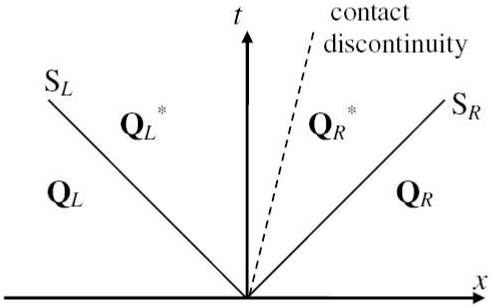

Figure 3.6: Evolution of the wave system for Riemann problem with contact surface

Recalling equation (3.64), the initial state now is considered as

$$\Phi(x,0) = \begin{cases} \mathbf{Q}_L & x < 0 \\ \mathbf{Q}_R & x > 0 \end{cases}, \tag{3.98}$$

where L and R denote the left and right states, respectively. Figure (3.6) shows the evolution of the wave system for Riemann problem with contact surface where the left and right initial states $\mathbf{Q}_L$ and $\mathbf{Q}_R$ are separated by a star region which also contains a contact discontinuity between the states $\mathbf{Q}_L^*$ and $\mathbf{Q}_R^*$.

Initial estimation of pressure and velocity in the star region are computed from linear theory

$$\begin{aligned} P^* &= \tfrac{1}{2}\left(P_L + P_R\right) + \tfrac{1}{2}\left(u_L + u_R\right)\left(\hat{\rho}\hat{c}\right), \\ u^* &= \tfrac{1}{2}\left(u_L + u_R\right) + \tfrac{1}{2}\left(P_L + P_R\right)/\left(\hat{\rho}\hat{c}\right), \end{aligned} \tag{3.99}$$

where $\hat{\rho} = \frac{1}{2}\left(\rho_L + \rho_R\right)$ and $\hat{c} = \frac{1}{2}\left(c_L + c_R\right)$. Here, c is the local speed of sound. The value of velocities at left and right states are then obtained by projecting onto the the line $\mathbf{r}_{ij}$. For example in 2-D for the left (L) state:

$$\begin{bmatrix} u_L \\ w_L \end{bmatrix} = \begin{bmatrix} \cos\theta & \sin\theta \\ -\sin\theta & \cos\theta \end{bmatrix} \begin{bmatrix} u_i \\ w_i \end{bmatrix}, \tag{3.100}$$

where $\cos\theta = \frac{x_{ij}}{r_{ij}}$ and $\sin\theta = \frac{z_{ij}}{r_{ij}}$.

In the star region, the fluid properties are defined as

$$\begin{cases} P_L^* = P_R^* = P^*, \\ u_L^* = u_R^* = u^* = S^*, \\ v_L^* = v_L, \quad w_L^* = w_L, \\ v_R^* = v_R, \quad w_R^* = w_R. \end{cases}$$

The left and right wave speed and fluxes are given by

$$S_L = u_L - c_L \Upsilon_L \tag{3.101}$$

$$S_R = u_R + c_R \Upsilon_R \tag{3.102}$$

$$\mathbf{F}_L^* = \mathbf{F}_L + S_L \left(\mathbf{Q}_L^* - \mathbf{Q}_L \right) \tag{3.103}$$

$$\mathbf{F}_R^* = \mathbf{F}_R + S_R \left(\mathbf{Q}_R^* - \mathbf{Q}_R \right) \tag{3.104}$$

where

$$\Upsilon_K = \begin{cases} 1 & P^* \leq P_K \qquad \text{Rarefaction} \\ \sqrt{1 + \frac{\gamma+1}{2\gamma} \left(\frac{P^*}{P_K} - 1 \right)} & P^* > P_K \qquad \text{Shock} \end{cases}, \tag{3.105}$$

K=R, L for right and left states, respectively. The fluid property states within the star region are therefore:

$$\mathbf{Q}_K^* = \rho_K \left(\frac{S_K - u_K}{S_K - S^*} \right) \begin{bmatrix} 1 \\ S^* \\ v_K \\ w_K \end{bmatrix}. \tag{3.106}$$

Thus the solution is given by

$$\mathbf{Q}^{HLLC} = \begin{cases} \mathbf{Q}_L & x/t < S_L \\ \mathbf{Q}_L^* & S_L < x/t < S^* \\ \mathbf{Q}_R^* & S^* < x/t < S_R \\ \mathbf{Q}_R & S_R \end{cases}, \tag{3.107}$$

while the fluxes are given by

$$\mathbf{F}^{HLLC} = \begin{cases} \mathbf{F}_L & x/t < S_L \\ \mathbf{F}_L^* & S_L < x/t < S^* \\ \mathbf{F}_R^* & S^* < x/t < S_R \\ \mathbf{F}_R & S_R \end{cases}. \tag{3.108}$$

where the value of velocities at the mid point, $\mathbf{v}_{a,ij}$, are obtained from inverse projection. For example in 2-D

$$\begin{bmatrix} u_{a,ij} \\ w_{a,ij} \end{bmatrix} = \begin{bmatrix} \cos\theta & -\sin\theta \\ \sin\theta & \cos\theta \end{bmatrix} \begin{bmatrix} u^{HLLC} \\ w^{HLLC} \end{bmatrix}. \tag{3.109}$$

Higher order extension for the Riemann problem

The MUSCL (Monotone Upstream-centred Schemes for Conservation Laws) is a second order extension of the Godunov upwind method, which is necessary in order to avoid massive dissipation. In this method, the piecewise constant approximation of Godunov's scheme is replaced by reconstructed states and derived from averaged states obtained from the previous time-step. For each particle, using a slope limiter (β-limiter), reconstructed left and right states are obtained and used to calculate fluxes at the mid-points. These fluxes can, in turn, be used as input to a Riemann solver, following which the solutions are averaged and used to advance the solution in time (Vila, 1999 and Toro, 2001). Defining the gradient constructed variable differences as

$$\begin{cases} \triangle\Phi_i = \nabla\Phi_i . \frac{1}{2} r_{ji} \\ \triangle\Phi_j = \nabla\Phi_j . \frac{1}{2} r_{ij} \end{cases}, \tag{3.110}$$

the left and right Riemann states either side of the midpoint are then defined by

$$\begin{cases} \Phi_i^L = \Phi_i + \overline{\triangle\Phi_i} \\ \Phi_j^R = \Phi_j - \overline{\triangle\Phi_j} \end{cases}, \tag{3.111}$$

where $\overline{\triangle\Phi_i}$ and $\overline{\triangle\Phi_j}$ are given by

$$\overline{\triangle\Phi_i}, \overline{\triangle\Phi_j} = \begin{cases} \max & \left[0, \min\left(\beta\triangle\Phi_i, \triangle\Phi_j\right), \min\left(\triangle\Phi_i, \beta\triangle\Phi_j\right)\right] & \triangle\Phi_j > 0 \\ \min & \left[0, \max\left(\beta\triangle\Phi_i, \triangle\Phi_j\right), \max\left(\triangle\Phi_i, \beta\triangle\Phi_j\right)\right] & \triangle\Phi_j < 0 \end{cases}, \tag{3.112}$$

If either $\overline{\triangle\Phi_i}$ or $\overline{\triangle\Phi_j}$ is found to have a value greater than $\frac{1}{2}\left|\Phi_i-\Phi_j\right|$, then $\overline{\triangle\Phi_i}$ and $\overline{\triangle\Phi_j}$ are further limited to $\frac{1}{2}\left|\Phi_i-\Phi_j\right|$. This is done to ensure that the values of $\Phi_i^L$and Φ_j^R always lie between the values of Φ_i and Φ_j. The left and right states are used as the discontinuous states for the individual Riemann problem between particles i and j. For a full description an understanding of Riemann solvers, the reader is referred to Toro (2001). As is well known for Riemann solvers and higher-order schemes, results can be sensitive to the choice and value of the limiter (Rogers, 2001).

3.4.4 Equation of State

In weakly compressible SPH, pressure is calculated by the equation of state of Tait defined as the following in fluid dynamics (Batchelor, 1967)

$$P_a = B\left[\left(\frac{\rho_a}{\rho_w}\right)^{\gamma} - 1\right], \tag{3.113}$$

where

$$B = \frac{\rho_w c_s^2}{\gamma}, \tag{3.114}$$

ρ_w and c_s are the reference density and numerical speed of sound, respectively. The choice of $\gamma = 7$ makes pressure very sensitive to density variation. Therefore, when the particles are approaching each other, their pressure increase dramatically and consequently the particles will repel each other through the pressure gradient. Through this equation, when density equals the reference density, pressure goes to zero. It consequently ensures the zero pressure condition relative to a free surface (Issa, 2005).

This equation also implies that the fluid is compressible, and that there is a speed of sound $c_s^2 = \partial P/\partial\rho$ set (by changing the value of B) to be at least ten times the maximum wave velocity to be modelled (Monaghan, 1992).

3.5 Time integration

3.5.1 Time step

Determination of time step depends on some conditions as the followings

Internal and external forcing terms

This condition is applied to ensure that the particles do not get very close to the neighbours during their movement when they experience external and internal forces

$$\delta t_{forces} = \min \sqrt{\left(\frac{h}{\mid f_i \mid}\right)}, \tag{3.115}$$

where f_i denotes internal or external forces associated to particle i per unit mass (Monaghan, 1999).

Combination of CFL and viscous conditions

The combination of CFL and viscous conditions gives

$$\delta t_{CV} = \min_i \left(\frac{h}{c_s + \mu_i}\right), \tag{3.116}$$

where

$$\mu_i = \max_j \left(\frac{h\mathbf{v}_{ij}\mathbf{r}_{ij}}{\mathbf{r}_{ij}^2}\right). \tag{3.117}$$

Final time step choice

The final time step denoted δt is then expressed as

$$\delta t = Cr \min(\delta t_{forces}, \delta t_{CV}), \tag{3.118}$$

where Cr is the Courant number.

3.5.2 Time integration schemes

Generally, the continuity, momentum and position equations can be written as

$$\begin{cases} \frac{d\rho_i}{dt} = G_i \\ \frac{d\mathbf{v}_i}{dt} = \mathbf{F}_i \\ \frac{d\mathbf{r}_i}{dt} = \mathbf{H}_i \end{cases}, \tag{3.119}$$

where G, $\mathbf{F}$ and $\mathbf{H}$ corresponds to the r.h.s of each equation. There are several methods used in order to obtain parameters such as predictor-corrector scheme and symplectic scheme.

Predictor-Corrector scheme

In this method, the second order scheme in time is used in order to update the values of parameters at the time level *n+1*. First, the accelerations term at the time level $n + \frac{1}{2}$ are calculated

$$\begin{cases} \rho_i^{n+\frac{1}{2}} = \rho_i^n + \frac{\Delta t}{2} G_i^n \\ \mathbf{v}_i^{n+\frac{1}{2}} = \mathbf{v}_i^n + \frac{\Delta t}{2} \mathbf{F}_i^n \\ \mathbf{r}_i^{n+\frac{1}{2}} = \mathbf{r}_i^n + \frac{\Delta t}{2} \mathbf{H}_i^n \end{cases}, \tag{3.120}$$

calculating $P^{n+1/2}$ using $\rho^{n+1/2}$.

These values are then corrected using forces at the half step

$$\begin{cases} \rho_i^{n+\frac{1}{2}} = \rho_i^n + \frac{\Delta t}{2} G_i^{n+\frac{1}{2}} \\ \mathbf{v}_i^{n+\frac{1}{2}} = \mathbf{v}_i^n + \frac{\Delta t}{2} \mathbf{F}_i^{n+\frac{1}{2}} \\ \mathbf{r}_i^{n+\frac{1}{2}} = \mathbf{r}_i^n + \frac{\Delta t}{2} \mathbf{H}_i^{n+\frac{1}{2}} \end{cases}, \tag{3.121}$$

and finally the values are calculated at the end of time step as

$$\begin{cases} \rho_i^{n+1} = 2\rho_i^{n+\frac{1}{2}} - \rho_i^n \\ \mathbf{v}_a^{n+1} = 2\mathbf{v}_i^{n+\frac{1}{2}} - \mathbf{v}_i^n \\ \mathbf{r}_a^{n+1} = 2\mathbf{r}_i^{n+\frac{1}{2}} - \mathbf{r}_i^n \end{cases}, \tag{3.122}$$

and the updated pressure at the time *n+1*, P^{n+1} is calculated from (3.113) by using the value of density at the time n+1, ρ^{n+1}.

Time integration in the absence of dissipation (symplectic)

Because the SPH algorithm reduces the original continuum partial differential equations to sets of ordinary differential equations, any stable time stepping algorithm for ordinary differential equations can be used. A symplectic integrator (see Monaghan, 2005 and Leimkuhler *et al.*, 1997) can be used to preserve the properties of the Lagrangian equations when there is no dissipation. This method is often known as kick-drift-kick form of time stepping where the kick is the change in velocity by the force and drift is the change in coordinate moving with initial velocity. In this case, first, the value of density and position acceleration are calculated at the middle of time step as

$$\begin{cases} \rho_i^{n+\frac{1}{2}} = \rho_i^n + \frac{\Delta t}{2} G_i^n \\ \mathbf{r}_i^{n+\frac{1}{2}} = \mathbf{r}_i^n + \frac{\Delta t}{2} \mathbf{H}_i^n \end{cases}, \tag{3.123}$$

then $P^{n+\frac{1}{2}}$ is calculated from $\rho^{n+\frac{1}{2}}$. Second, $\mathbf{F}_i^{n+\frac{1}{2}}$ is obtained by a sweep over the particles and finally

$$\begin{cases} \mathbf{v}_i^{n+1} = \mathbf{v}_i^{n+\frac{1}{2}} + \frac{\Delta t}{2} \mathbf{F}_i^{n+\frac{1}{2}} \\ \mathbf{r}_i^{n+1} = \mathbf{r}_i^{n+\frac{1}{2}} + \frac{\Delta t}{2} \mathbf{v}_i^{n+1} \end{cases}. \tag{3.124}$$

Now G_i^{n+1} is calculated using $\mathbf{v}_i^{n+1}$ and $\mathbf{r}_i^{n+1}$ and then pressure is calculated form ρ^{n+1} .

3.6 Boundary conditions

For modelling bodies in SPH there must be some form of boundary condition at a solid wall to prevent particles crossing the impermeable boundary. There are now several techniques available in the literature, e.g. using ghost particles (Colagrossi and Landrini, 2003), using stationary particles (Shao and Lo, 2003), dynamic boundary conditions (Gómez-Gesteira & Dalrymple, 2004 and Crespo *et al.*, 2007), using repulsive forces (Monaghan and Kos, 1999 and Rogers *et al.*, 2008), a flux-based boundary conditions (De Leffe *et al.*, 2009) or particle boundary force (Kajtar and Monaghan, 2009). Each have their own advantages and disadvantages, for example, techniques such as the ghost particles method become unwieldy when there are corners or surfaces of higher curvature (this has been improved recently by Colagrossi *et al.*, 2009). The technique of using stationary water particles to represent the solid body can create very large unphysical boundary layers which can only be overcome using very small $\triangle$ (initial particle spacing) with the obvious penalties in terms of computational cost (Rogers and Dalrymple, 2008). The dynamic boundary condition of Gómez-Gesteira and Dalrymple (2004) and Crespo *et al.* (2007) has recently been improved with the implementation of the correction proposed by Hughes and Graham (2010). In this work, the following two boundary conditions will be used.

3.6.1 Repulsive boundary condition

In this work, the repulsive boundary condition, developed by Monaghan and Kos (1999) and modified by Rogers *et al.* (2008) is used due to the ease of implementation for complex boundaries and particle feedback interactions. In this case, the boundary exerts forces on the fluid particles and the force experienced by a water particle, acting normal to the wall, is given by

$$\mathbf{f} = \mathbf{n}.R(\psi)P(\xi)\varepsilon(z, u_{\perp}), \tag{3.125}$$

where $\mathbf{n}$ is the unit normal, $R(\psi)$ is the repulsive function of the distance ψ, which is the perpendicular distance of the particle from the wall, and is expressed as

$$R(\psi) = A\frac{1}{\sqrt{q}}\left(1 - q\right), \tag{3.126}$$

where the coefficient A is

$$A = \frac{1}{h}0.01c_i^2. \tag{3.127}$$

The function $P(\xi)$ is chosen so that a water particle experiences a constant repulsive force as it travels parallel to the wall

$$P(\xi) = \frac{1}{2}\left[1 + \cos\left(\frac{2\pi\xi}{\Delta b}\right)\right], \tag{3.128}$$

where ξ is the projection of interpolation location ξ_i onto the chord joining the two adjacent boundary particles and Δb is the distance between any two adjacent boundary particles.

Finally, the function $\varepsilon(z, u_{\perp})$ is a modification to Monaghan and Kos's (1999) original suggestion and adjusts the magnitude of the force according to the local water depth and velocity of the water particle normal to the boundary

$$\varepsilon(z, u_{\perp}) = \varepsilon(z) + \varepsilon(u_{\perp}), \tag{3.129}$$

where

$$\varepsilon(z) = \begin{cases} 0.02 & z \geq 0 \\ \mid \frac{z}{d} \mid +0.02 & -d \leq z < 0\ , \\ 1 & \mid \frac{z}{d} \mid > 1 \end{cases} \tag{3.130}$$

and

$$\varepsilon(u_\perp) = \begin{cases} 0 & u_\perp > 0 \\ \frac{|20u_\perp|}{c_s} & \mid 20u_\perp \mid < c_s\ , \\ 1 & \mid 20u_\perp \mid > c_s \end{cases} \tag{3.131}$$

in this case, z is the elevation above the local still-water level d,$u_\perp$is the velocity of the water particle projected onto the normal expressed by

$$u_\perp = (\mathbf{v}_{WP} - \mathbf{v}_{BP}).\mathbf{n}, \tag{3.132}$$

where the subscripts WP and BP refer to water and boundary particles, respectively (Monaghan & Kos, 1999 and Rogers *et al.*, 2010). Unless stated, repulsive boundary conditions are used in our investigations.

3.6.2 Particle boundary Force

The particle boundary force proposed by Kajtar and Monaghan (2009) is another type of boundary condition where there is no need to calculate normals as the repulsive boundary condition, which makes the boundary conditions easy to be implemented. The force/mass on fluid particle j due to boundary particle k is expressed as

$$\mathbf{f}_{jk} = \frac{1}{\gamma_f} \left(\frac{V_{max}^2}{r_{jk} - \iota} \right) \frac{\mathbf{r}_{jk}}{r_{jk}} W_{jk} \frac{2m_k}{m_j + m_k}, \tag{3.133}$$

where V_{max} is the estimated maximum speed, W_{jk} is the 1D Wendland kernel, m is the particle mass , ι is chosen in order to prevent particle penetration and the factor γ_f is used to ensure that by changing the space of boundary particles the force on the fluid is invariant.

3.6.3 Moving boundaries

For modelling moving boundaries, in theory, all boundary particles experience an equal and opposite force to the repulsive force that they exert on surrounding fluid particles. By summing the contributions exerted on the boundary particles for an entire body, the force and hence motion of the floating body can be evaluated (Rogers *et al.*, 2010). Herein, following the technique of Monaghan *et al.* (2003) for modelling the floating body using the repulsive boundary particle technique the objects are treated as rigid bodies. The force on each boundary particle is computed by summing up the contribution from all the surrounding water particles within the surrounding kernel. Hence, boundary particle k experiences a force per unit mass given by

$$\mathbf{f}_k = \sum_{i \in WPs} \mathbf{f}_{ki}, \tag{3.134}$$

where f_{ki} is the force per unit mass exerted by water particle i on boundary particle k. By the principle of equal and opposite action and reaction, the force exerted by a water particle on each boundary particle is given by

$$m_k \mathbf{f}_{ki} = -m_i \mathbf{f}_{ik}. \tag{3.135}$$

This is useful since during the simulation we only actually compute the repulsive force, $\mathbf{f}_{ik}$, exerted by the boundary particle k on water particle i. Hence, using the equation below, we can estimate the force exerted on the moving body. For the floating body, we use the equations of basic rigid body dynamics. The total force on the body is then calculated as

$$\mathbf{f}_{total} = \sum_{k \in BPs} m_k \mathbf{f}_k. \tag{3.136}$$

For the floating body, we use the equations of basic rigid body dynamics. The equations of motion of the body in the translational and rotational degrees of freedom are given by

$$M \frac{d\mathbf{V}}{dt} = \sum_{k \in BPs} m_k \mathbf{f}_k, \tag{3.137}$$

$$I \frac{d\mathbf{\Omega}_I}{dt} = \sum_{k \in BPs} m_k \left(\mathbf{r}_k - \mathbf{R}_0 \right), \tag{3.138}$$

where I is the moment of inertia, $\mathbf{V}$ is the velocity of the object, $\mathbf{\Omega}_I$ is the rotational velocity of the object whose direction is perpendicular to the object motion and $\mathbf{R}_0$

is the position of the centre of mass. Equations (3.137)and (3.138)are integrated in time to predict the values of $\mathbf{V}$ and $\mathbf{\Omega}_I$ or the beginning of the next timestep. Each boundary particle that describes the moving body has a velocity given by

$$\mathbf{v}_k = \mathbf{V} + \mathbf{\Omega}_I \times (\mathbf{r}_k - \mathbf{R}_0) \tag{3.139}$$

The boundary particles within the rigid body are then moved by integrating Equation (3.139) in time. It can be shown that this technique conserves both linear and angular momentum (Monaghan *et al.*, 2003).

3.7 Summary

In this chapter, the theoretical and mathematical features of the SPH method were shown. Most of the formulations and features of SPH presented in this chapter are essential to be used in the following chapters for solving numerical problems for this thesis. The next chapters will present 2-D investigations of wave propagation in intermediate depth and weakly compressible water, wave loading on a submerged and fixed cylinder and generated by a heaving cylinder. Moreover, The 3-D investigation of a heaving cone and Manchester Bobber wave energy device will be also presented in the following chapters.

Chapter 4

Investigation of wave propagation and wave-body interaction in 2D

4.1 Introduction

In this chapter, the numerical results for various two-dimensional test cases are simulated for wave propagation with and without body interaction in a channel.

First the solution for flow due to vertical plate moving in a channel is compared with an analytical solution and other numerical simulations. This will be followed by an investigation of wave propagation in an intermediate depth and weakly compressible water tank using different SPH formulations and kernel functions. The comparison between the experimental data of Dixon *et al.* (1979) and SPH results for wave loading on a fixed, partially submerged cylinder will be presented with a careful attention to the force along each direction exerted by fluid particles to the body in still water. Finally, surface waves generated by a 2-D heaving cylinder of different wave period and stroke will be compared with the experimental data of Yu and Ursell (1961).

4.2 Wavemaker theory

A wavemaker is any device whose prescribed motion produces surface waves in a channel or basin with a free surface. A piston type wavemaker is a classical example of wavemakers which can be located in one end of a long rectangular water tank oscillating at a prescribed frequency (Dean and Dalrymple, 2000). Consider a piston wavemaker with a stroke, s, which has a horizontal displacement and velocity of the boundary wall described as:

$$X_{paddle} = \frac{\mathrm{s}}{2} \sin \sigma t \tag{4.1}$$

$$U_{paddle} = \frac{\mathrm{s}}{2} \sigma \cos \sigma t, \tag{4.2}$$

where T is a wave period and σ is wave frequency defined as

$$\sigma^2 = gk \tanh kd. \tag{4.3}$$

Here, d is the water depth and k is wave number inversely related to wavelength, defined as

$$k = \frac{2\pi}{L}, \tag{4.4}$$

where L denotes the value of wave length given at depth d by

$$L = L_0 \tanh kd, \tag{4.5}$$

where L_0 is deep-water wave length expressed by:

$$L_0 = \frac{gT^2}{2\pi}. \tag{4.6}$$

The main objective of this part of research is to investigate wave propagation in intermediate deep and weakly compressible water where

$$\frac{\pi}{10} < kd < \pi.$$

More information about wavemaker theory can be found in Dean & Dalrymple (2000).

4.3 Numerical Solution

Here to ensure clarity of which SPH formulation is being used and investigated, we repeat the specific equations being solved.

4.3.1 Standard SPH formulation

Recalling Equation (3.34), the standard SPH equations are expressed as:

$$\begin{cases} \frac{d\mathbf{r}_i}{dt} = \mathbf{v}_i \\ \frac{d\rho_i}{dt} = \sum\limits_j m_j \mathbf{v}_{ij}.\nabla_i W_{ij} \\ \frac{d\mathbf{v}_i}{dt} = -\sum\limits_j m_j \left(\frac{P_j}{\rho_j^2} + \frac{P_i}{\rho_i^2} + \Pi_{ij} \right).\nabla_i W_{ij} + \mathbf{g} \end{cases} , \tag{4.7}$$

where $\mathbf{r}_i$, $\mathbf{v}_i$ P_i and ρ_i denote position, velocity, pressure and density of particle i, respectively. Here

$$\Pi_{ij} = \begin{cases} \frac{-\lambda_{vis}\bar{c}_{ij}\mu_{ij}}{\bar{\rho}_{ij}} & \mathbf{v}_{ij}\mathbf{r}_{ij} < 0 \\ 0 & \mathbf{v}_{ij}\mathbf{r}_{ij} > 0 \end{cases} , \tag{4.8}$$

with $\mu_{ij} = \frac{h\mathbf{v}_{ij}\mathbf{r}_{ij}}{r_{ij}^2+\iota^2}$, $\bar{c}_{ij} = \frac{c_i+c_j}{2}$, $\bar{\rho}_{ij} = \frac{\rho_i+\rho_j}{2}$, where $\iota^2 = 0.01h^2$ and λ_{vis} is a free parameter that can be changed according to each problem, which is 0.05 for our simulations. Here, c_i and c_j are the speed of sound of particle i and j, respectively.

4.3.2 The SPH-ALE scheme

As described in the previous chapter, Vila (1999) proposed the following formulations in an Arbitrary-Lagrangian Eulerian (ALE) form in SPH by recalling Equation (3.93):

$$\begin{cases} \frac{d\mathbf{r}_i}{dt} = \mathbf{v}_i \\ \frac{d\omega_i}{dt} = \omega_i \nabla.\mathbf{v}_i \\ \frac{d}{dt}(\omega_i\rho_i) + \omega_i \sum\limits_j \omega_j 2\rho_{a,ij}\left(\mathbf{v}_{a,ijj} - \mathbf{v}^0\right)\nabla W_{ij} = 0 \\ \frac{d}{dt}(\omega_i\rho_i\mathbf{v}_i) + \omega_i \sum\limits_j \omega_i 2\left[P_{a,ij} + \rho_{a,ij}\mathbf{v}_{a,ij} \otimes \left(\mathbf{v}_{a,ij} - \mathbf{v}_{ij}^0\right)\right]\nabla W_{ij} = \omega_i S \end{cases} , \tag{4.9}$$

where subscript a denotes the result from the approximate Riemann solver, superscript *0* denotes the field value (i.e. the value at the particle itself). The interaction between each particle pair is solved as a 1-D Riemann problem, so that the solution at the mid-point $\mathbf{r}_{a,ij}$ is $\mathbf{v}_{a,ij}$, P_a, ρ_a a for velocity, pressure and density, respectively. In the code SPHysics , this Riemann problem is solved using an HLLC approximate

Riemann solver using MUSCL-based upwinding with a general β-limiter described in full detail in the previous chapter.

In addition to the above formulations, the symplectic time stepping (Leimkuhler *et al.*, 1997 and Monaghan, 2005), repulsive boundary conditions (Monaghan and Kos, 1999 and Rogers *et al.*, 2008), second-order (Monaghan and Lattanzio, 1985) and third-order (Monaghan, 1992) kernel functions will be used.

4.4 Flow due to a vertical plate moving in a channel

For flow due to a vertical plate moving in a channel, one can consider a semi-infinite channel of water depth d initially set at rest. Then at $t = 0$ the plate at $x = 0$ instantaneously starts moving with uniform velocity U or uniform acceleration where the impulsive motion leads to a jet of water travelling up the face of the plate. Peregrine (1972) showed that the free surface evaluation caused by a vertical plate with zero gravity, which is singular at origin, can be expressed analytically by

$$z = -\frac{2Ut}{\pi} \ln\left[\tanh\left(\frac{\pi x}{4d}\right)\right], \tag{4.10}$$

where t is very small time and $U = 1m/s$.

The numerical simulation is conducted in a channel of length 2m and depth 0.5m where the total number of particles for the initial particle spacing of 0.01m and 0.005m are 10,200 and 41,000, respectively. For this problem, the cubic kernel and repulsive boundary condition are used.

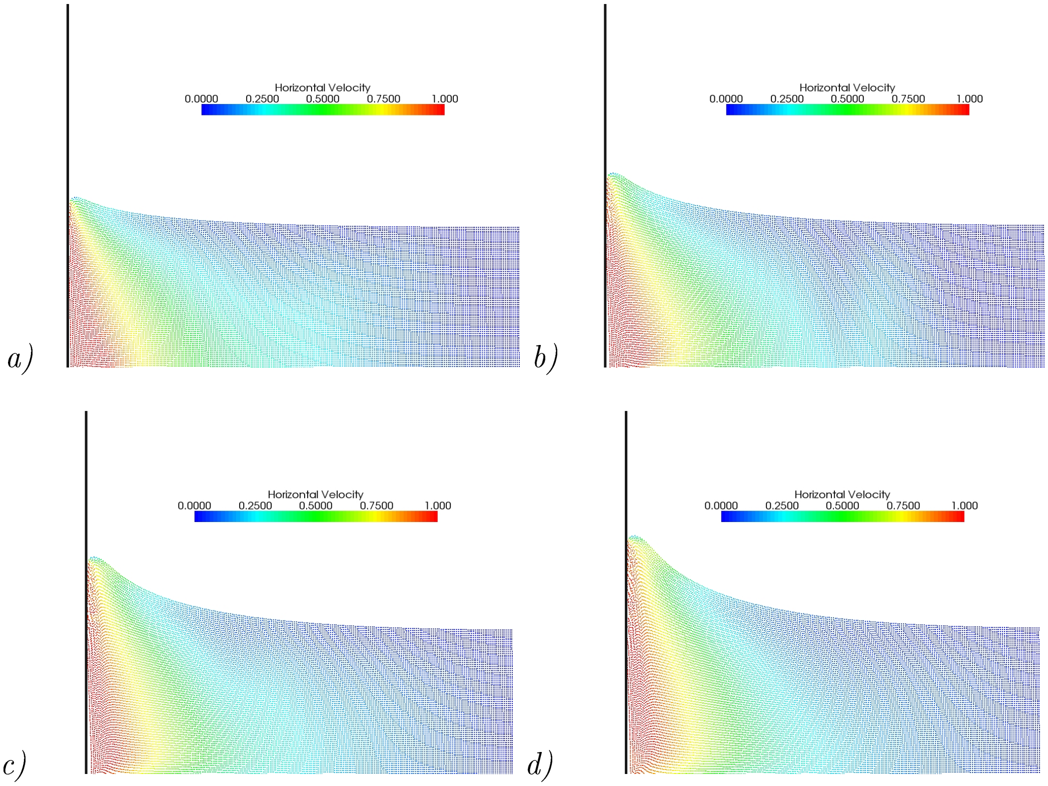

Figure 4.1: Particle distribution for flow due to a vertical plate moving in a channel using standard SPH formulation and cubic kernel function after *a)* t=0.04s *b)* t=0.08s *c)* t=0.12s *d)* t=0.16s, $\triangle = 0.005m$

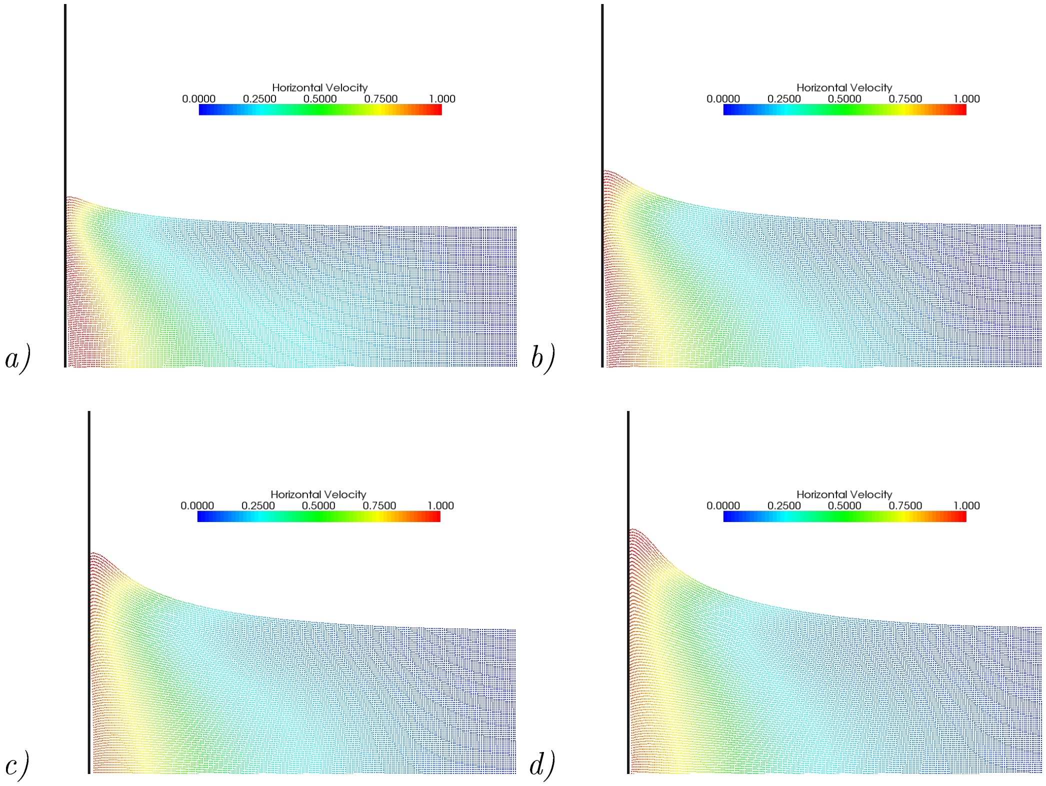

Figure 4.2: Particle distribution for flow due to a vertical plate moving in a channel using SPH-ALE formulation and cubic kernel function after *a)* t=0.04s *b)* t=0.08s *c)* t=0.12s *d)* t=0.16s, $\triangle = 0.005m$

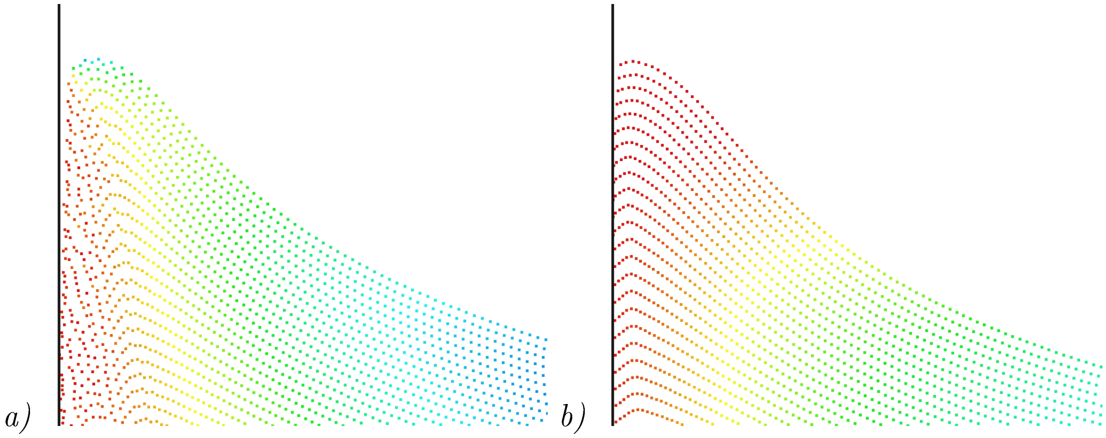

Figure 4.3: Horizontal velocity for particles for flow due to a vertical plate moving in a channel using standard SPH formulation and cubic kernel function after t=0.16s *a)* Standard SPH *b)* SPH_ALE, $\triangle = 0.005m$, (same colour scale as Figure (4.2))

Figures (4.1) to (4.2) show distribution of particles, coloured according to their horizontal velocity, for flow due to a vertical plate moving in a channel using different SPH formulations (Standard SPH & SPH-ALE) after *a)* t=0.04s *b)* t=0.08s *c)* t=0.12s *d)* t=0.16s in the absence of the gravity. According to Figure (4.3), it is clear that using the standard SPH formulation causes a separation from the wall in comparison with the SPH-ALE formulation and consequently a discrepancy in the magnitude of the horizontal velocity at the free surface near the paddle.

Figures (4.4) and (4.5) display the comparisons between the surface profiles for different SPH formulations, the incompressible SPH (ISPH) data of Xu (2009) and analytical solution for flow due to a vertical plate after *a)* t=0.4s *b)* t=0.8s *c)* t=0.12s *d)* t=0.16s, using different initial particle spacing, $\triangle$. The comparisons are in good agreements for positions of $X - X_{paddle} > 0.05m$ however for $X - X_{paddle} < 0.05m$ there is a discrepancy due to the way we defined the free surface which does not work perfectly near the wall (see Appendix A) whereas ISPH uses a different surface particle identification. Furthermore, as mentioned before, the original formulation proposed by Peregrine (1972) is singular at the origin which is also the reason for having a discrepancy at the wavemaker. It is worth mentioning that Peregrine's idea is based on potential flow whereas here the simulation is based on the no-slip boundary conditions.

For this problem, it is difficult to draw any conclusion for the best choice of SPH formulation for free-surface problems, however, it seems the standard SPH formulation underestimates velocity at the free surface near the paddle.

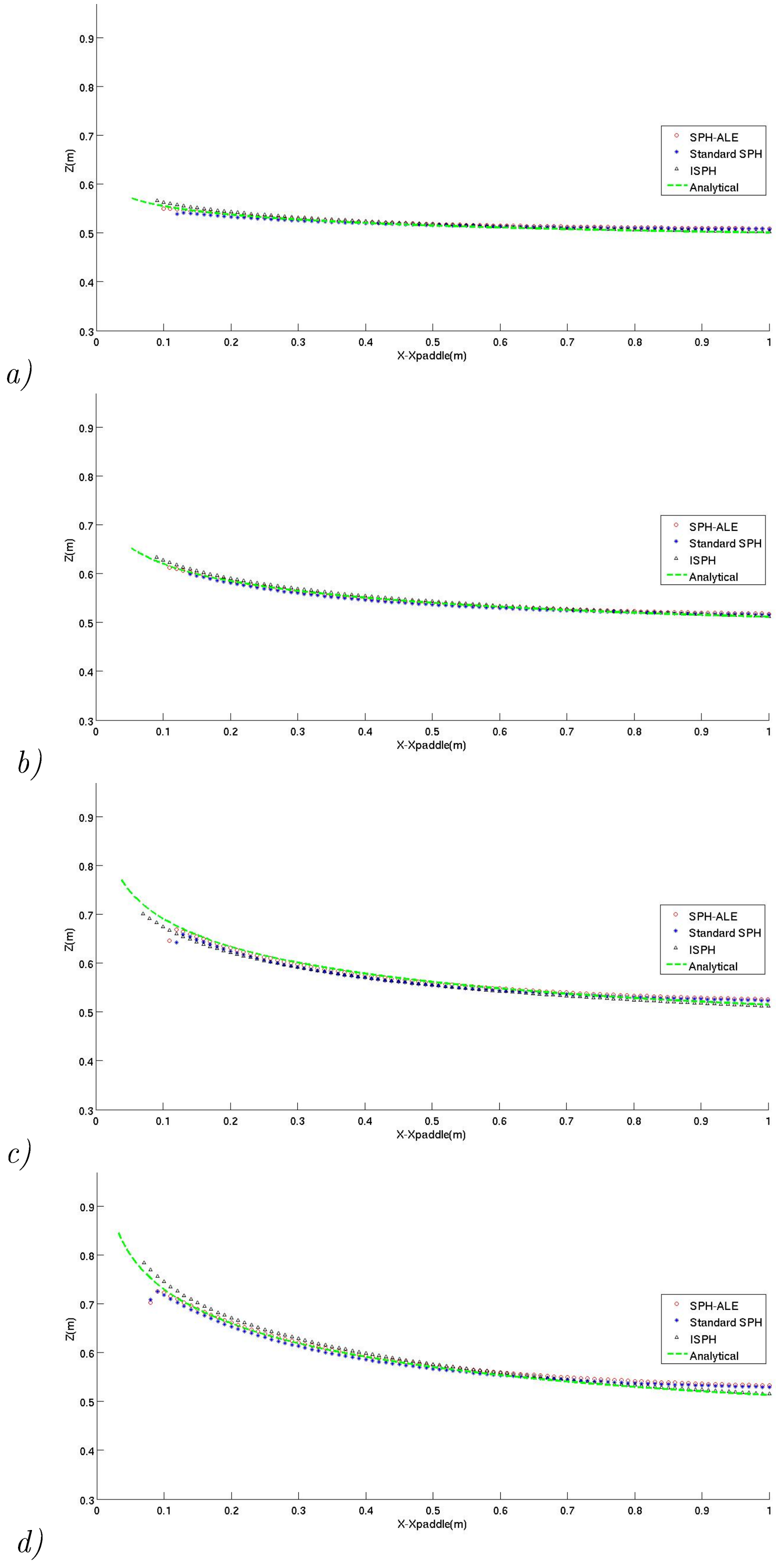

Figure 4.4: Comparison between the surface profiles for different SPH formulations, ISPH and analytical solution for flow due to vertical plate after *a)* t=0.04s *b)* t=0.08s *c)* t=0.12s *d)* t=0.16s, $\triangle = 0.01m$

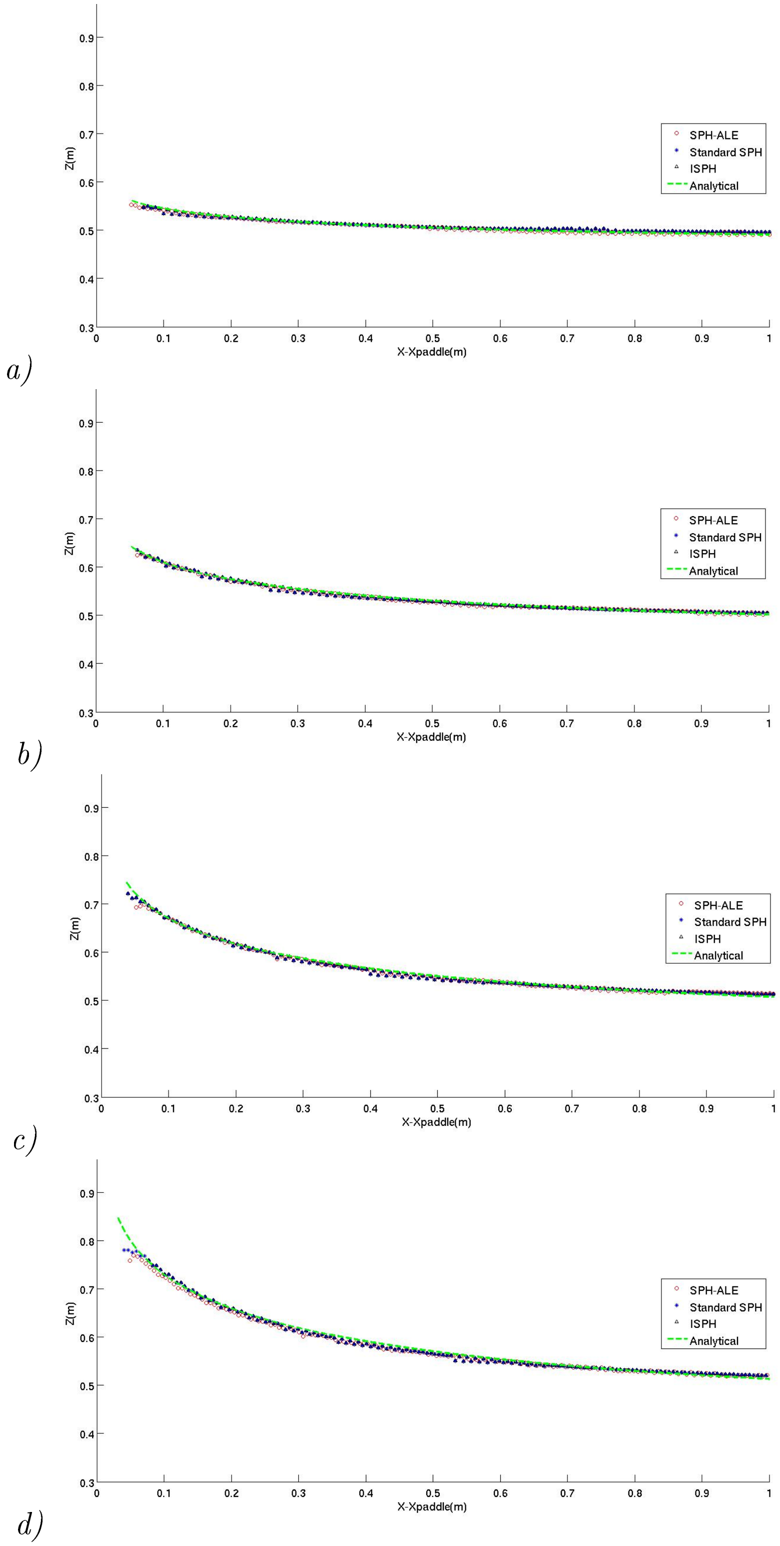

Figure 4.5: Comparison between the surface profiles for different SPH formulations, ISPH and analytical solution for flow due to vertical plate after *a)* t=0.04s *b)* t=0.08s *c)* t=0.12s *d)* t=0.16s, $\triangle = 0.005m$

4.5 Absorption of waves at the boundary in SPH

4.5.1 Theory of Sponge layer proposed by Larsen and Dancy (1983)

Generating waves inside the computational domain may causes reflections at boundaries. These reflections may also lead to standing waves which cause unphysical behaviour of waves at the boundaries. Larsen and Dancy (1983) proposed the use of a so-called “sponge layer” in Finite Difference Scheme (FDS) to damp waves at the boundaries in the interval $x > x_s$. The original equation of sponge layer is expressed by

$$\zeta(x) = \begin{cases} \exp\left[(\chi^{\frac{-x}{\Delta}} - \chi^{\frac{-x_s}{\Delta}}) \ln \alpha \right] & x > x_s \\ 1 & 0 \leq x \leq x_s \end{cases}, \tag{4.11}$$

where α is a constant depending on the number of grid lines in the layer (suggested to be $\alpha = 2$ or $\alpha = 5$, Δ is the grid spacing and

$$\chi = 1 + r_{sponge} + \exp\left(-\frac{1}{r_{sponge}} \right), \tag{4.12}$$

where $r_{sponge} = 1$.

Due to the differences between the SPH method and FDS, the value of the constant α should be changed in order to get a sufficient damp at the boundary in the SPH simulations. Here, we propose two values as $\alpha = 1.001$ or $\alpha = 1.01$. Figure (4.6) shows the function $\zeta(x)$ versus the length of the sponge layer for two different values of α.

4.5.2 Absorption of waves with a lower order of Riemann solver approximation

An alternative way to damp waves at the boundary is to change the order of the Riemann solver approximation from second to first by gradually decreasing the value of β-limiter described in the previous chapter, i.e. from $\beta = 1$ to $\beta = 0$ since the first order Riemann solver is known to be highly viscous.

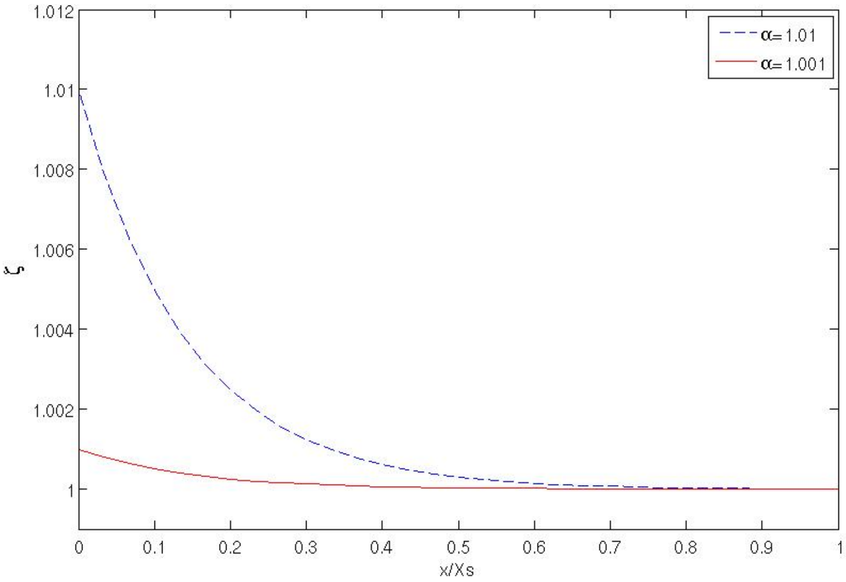

Figure 4.6: Values of $\zeta(x)$ for different values of α

4.6 Creating linear waves with a paddle

The investigation of wave propagation in intermediate, deep and weakly compressible water is conducted in this section, using the standard SPH and SPH-ALE formulation. The numerical domain of length 40m and height 1m is shown in Figure (4.7) where waves of 2s period are generated with a paddle at the left boundary and absorbed by a sponge layer of length 3m, at the right boundary. The water particles are initially in a still condition and then the paddle starts moving in a horizontal direction producing regular and linear waves. The total number of particles for the initial particle spacing of 0.04m and 0.02m are 25,500 and 102,000, respectively.

4.6.1 Simulation of wave propagation using standard SPH formulation

Figures (4.8) and (4.9) show the wave propagation using the standard SPH equations for different initial particle spacing, each at two sample times. It is clearly shown that using standard SPH formulation will cause dissipation in progressive waves. Figure (4.10) displays the comparison of surface profile using the standard SPH formulation and analytical solution for $\triangle = 0.02m$ at $a)$ t=10s, $b)$ t=15s which is

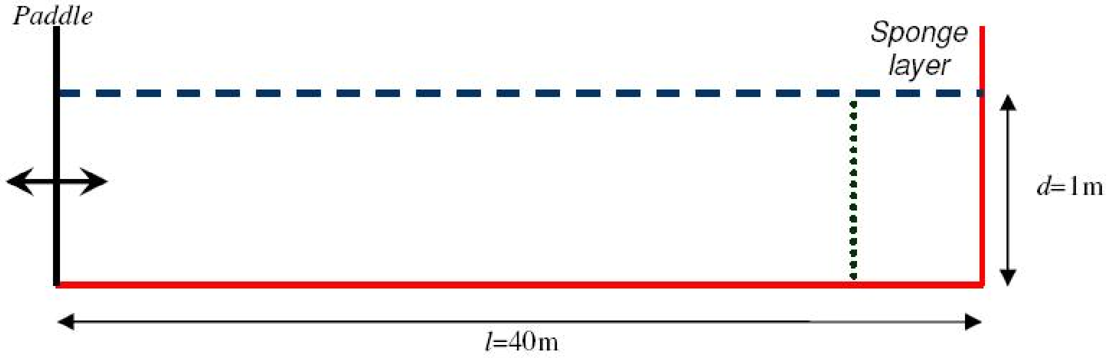

Figure 4.7: Schematic of surface wave generated by a paddle

in good agreement in terms of phase for the first three waves but underestimates the wave magnitude as the waves propagate along the tank.

4.6.2 Simulation of wave propagation using SPH-ALE formulation and second-order kernel

Figure (4.11) displays the pressure distributions for waves generated by a paddle using SPH-ALE and 2nd-order quadratic kernel at *a*) t=10s, *b*) t=15s where the waves are clearly seen to dissipate along the channel, which is also shown in Figure (4.12) for the surface profile comparison of SPH with the analytical solution. The reason can be due to the kernel gradient which is linear and first order. The wave dissipation can be improved by using the 3rd-order cubic kernel, which approximates the Gaussian kernel closely.

4.6.3 Simulation of wave propagation using SPH-ALE formulation and cubic spline kernel

Using the SPH-ALE formulation and cubic kernel leads the waves to propagate along the channel without any dissipation. The pressure distributions for two sample times are shown in Figure (4.13) where waves produced by the paddle propagate towards the end of the tank without any dissipation and absorbed by the sponge layer which is located 3m from the right boundary.

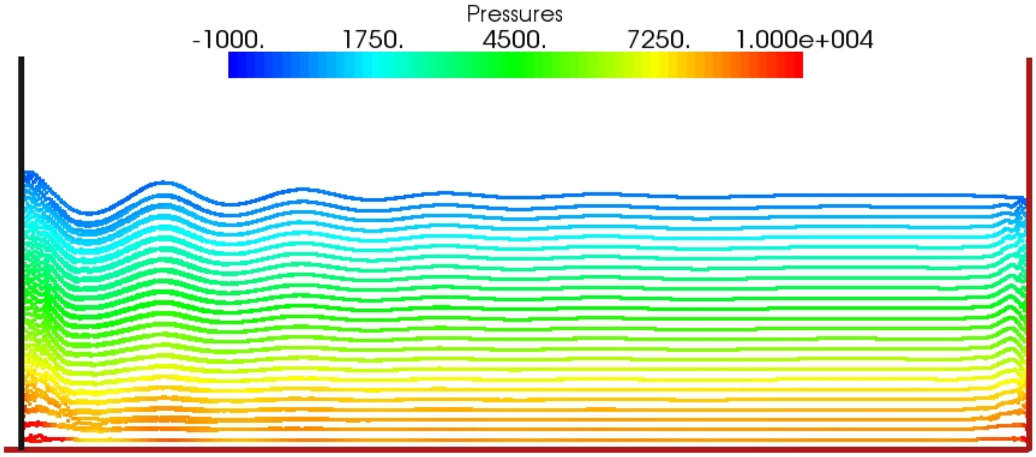

a)

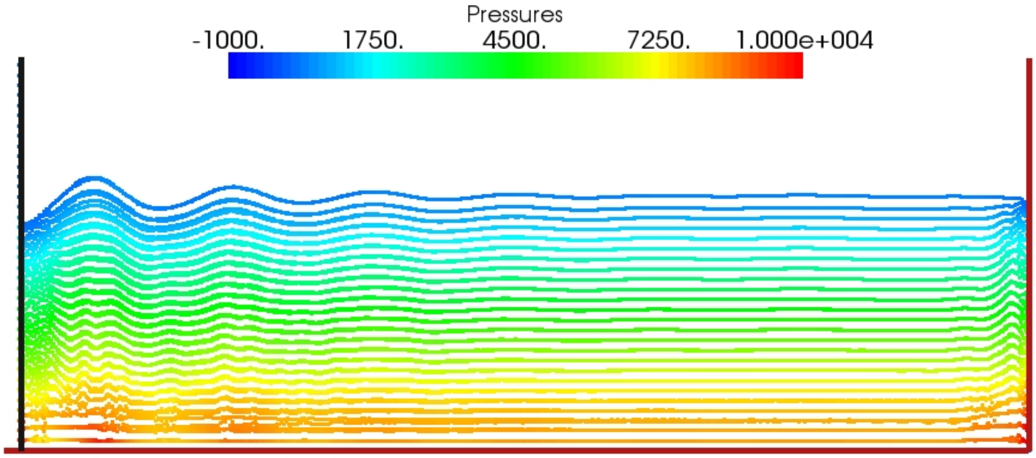

b)

Figure 4.8: Pressure distributions for waves generated by a paddle using standard SPH formulation and cubic kernel at *a)* t=10s, *b)* t=15s, $\triangle = 0.04m$. Note distorted scale

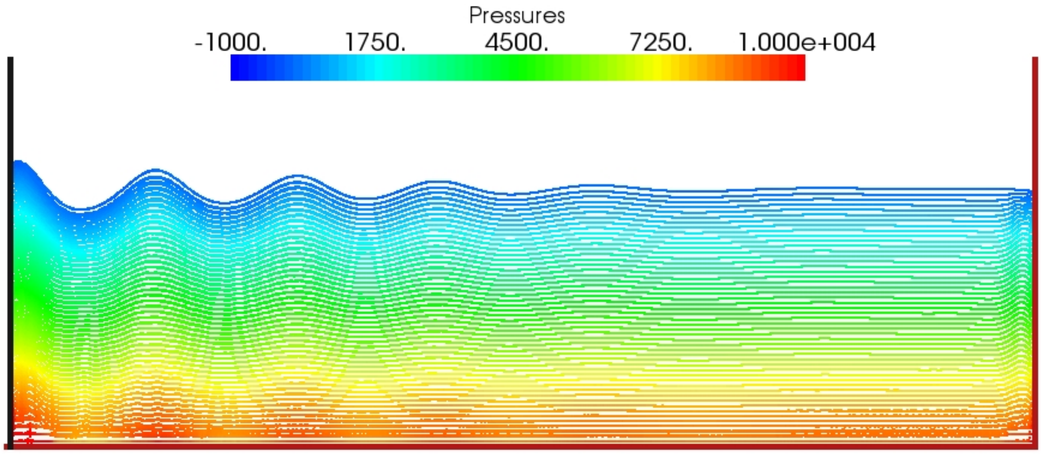

a)

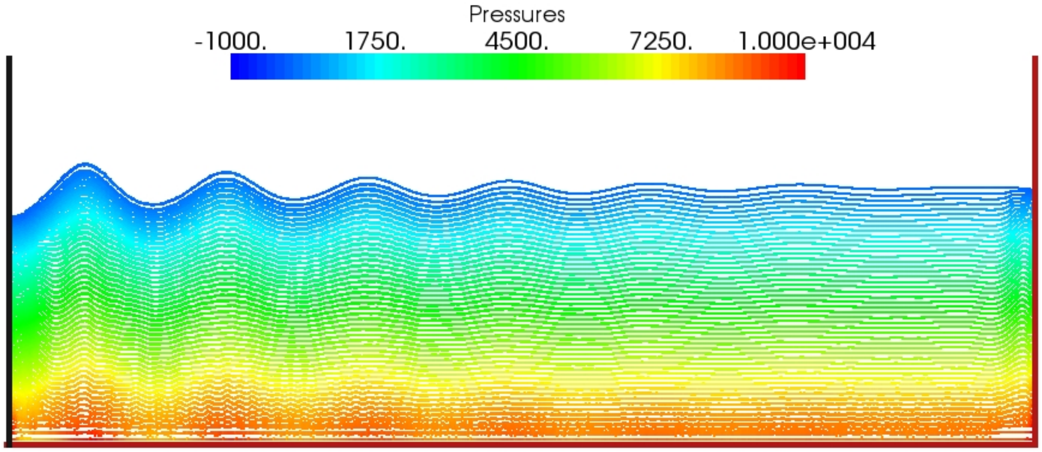

b)

Figure 4.9: Pressure distributions for waves generated by a paddle using standard SPH formulation and cubic kernel at *a)* t=10s, *b)* t=15s $\triangle = 0.02m$. Note distorted scale

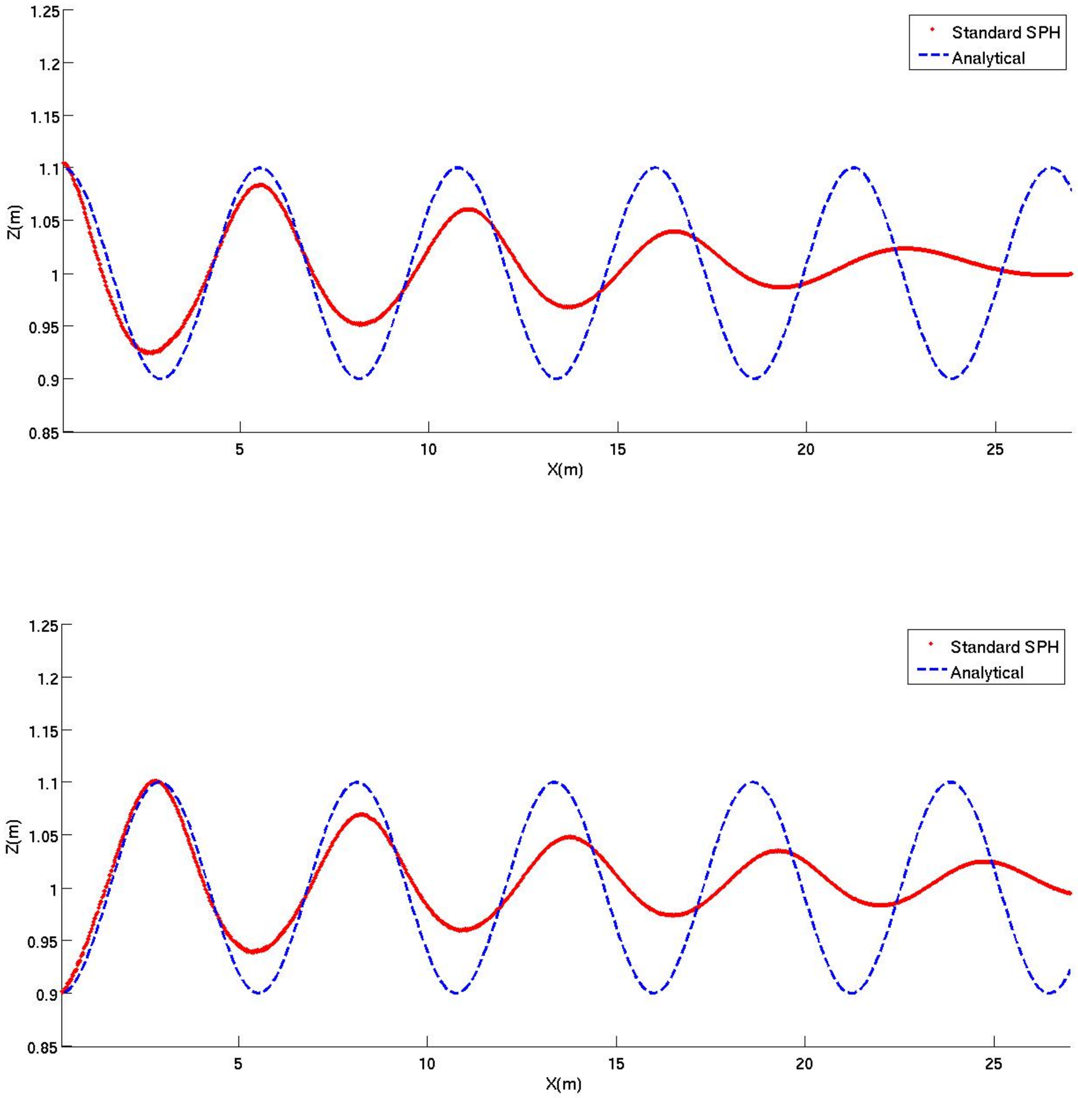

a)

b)

Figure 4.10: Surface profiles for waves generated by a paddle using and standard SPH formulation and cubic kernel at *a)* t=10s, *b)* t=15s, $\triangle = 0.02m$

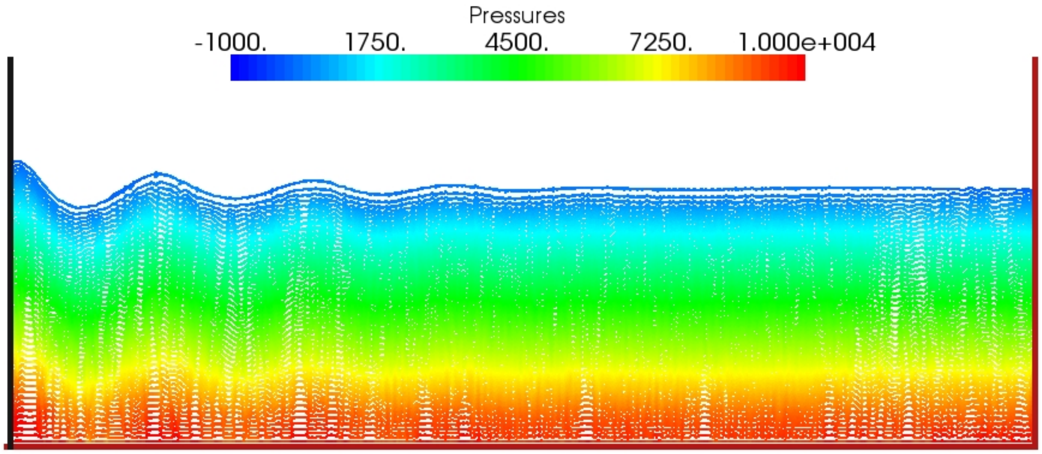

a)

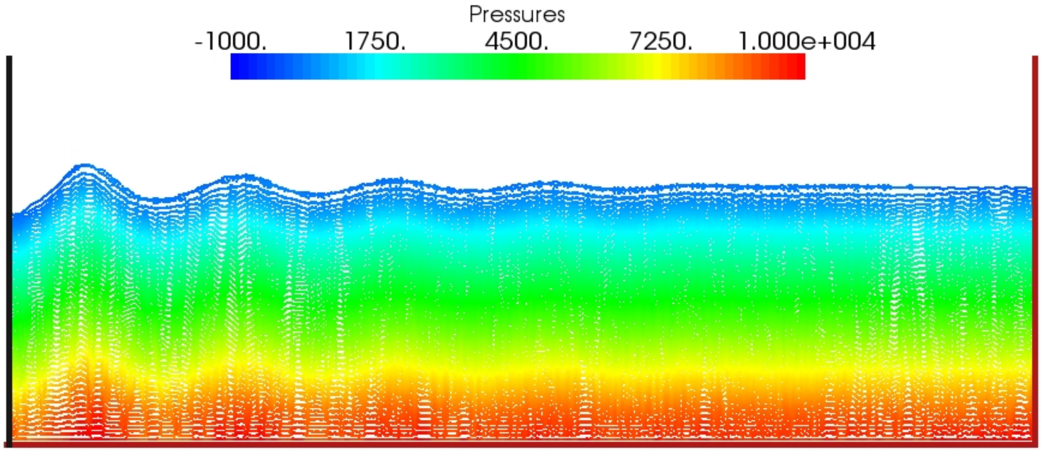

b)

Figure 4.11: Pressure distributions for waves generated by a paddle using SPH-ALE and 2nd-order quadratic kernel at *a)* t=10s, *b)* t=15s, $\triangle = 0.02m$. Note distorted scale

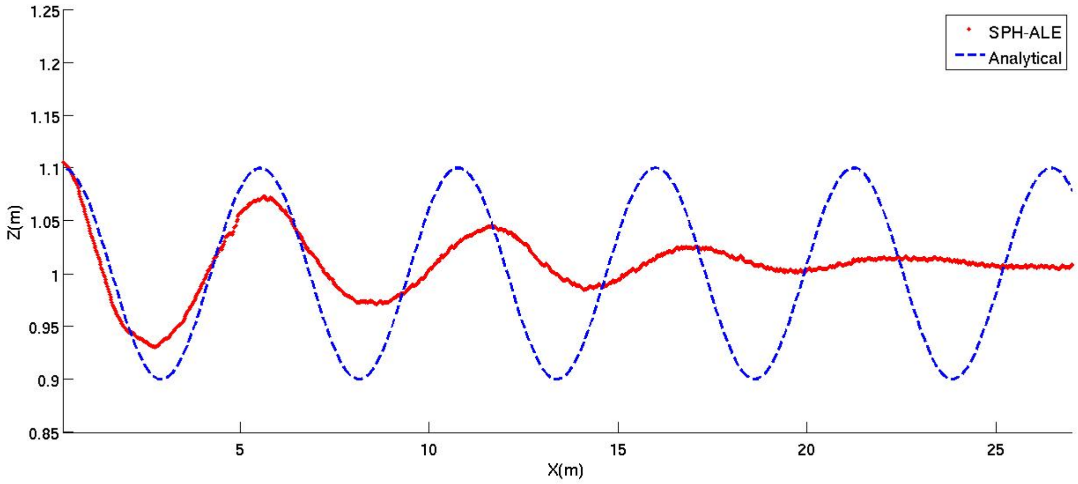

a)

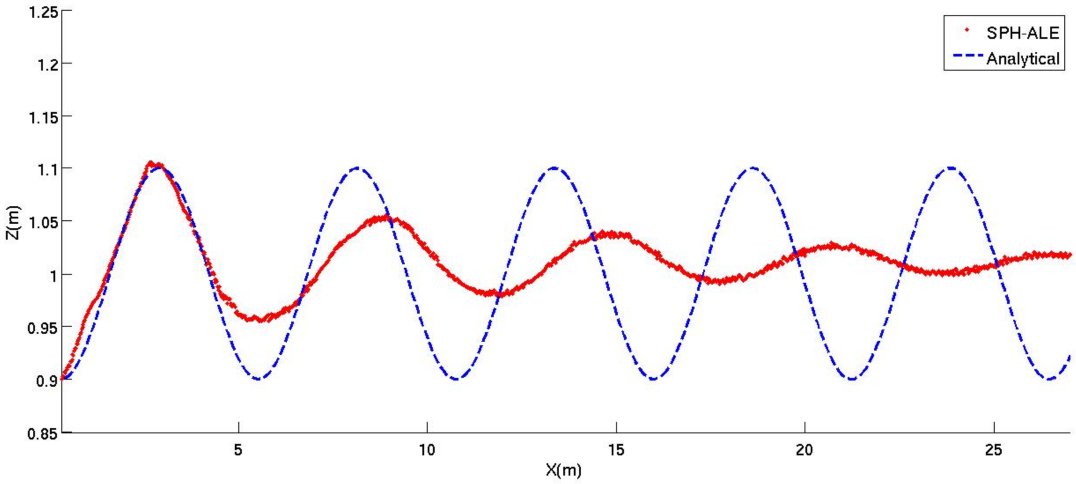

b)

Figure 4.12: Surface profiles for waves generated by a paddle using SPH-ALE and 2nd-order kernel at *a)* t=10s, *b)* t=15s, $\triangle = 0.02m$

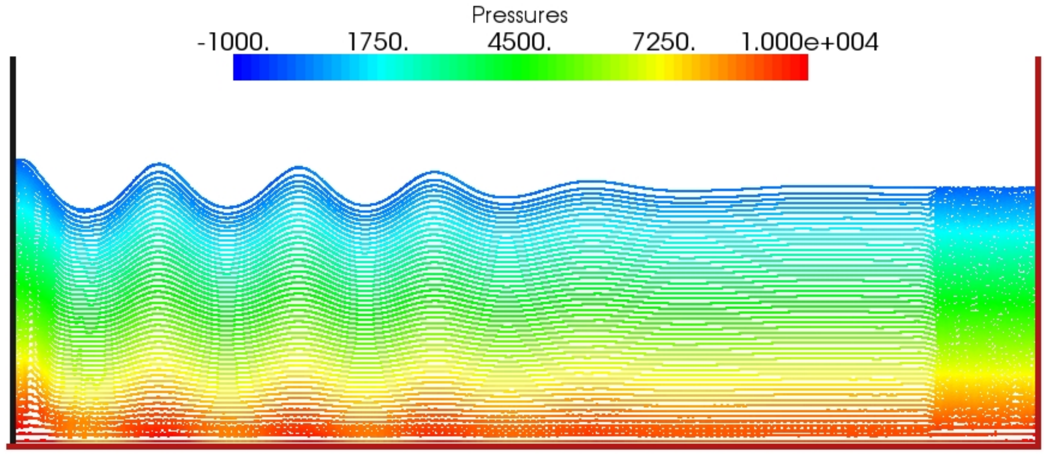

a)

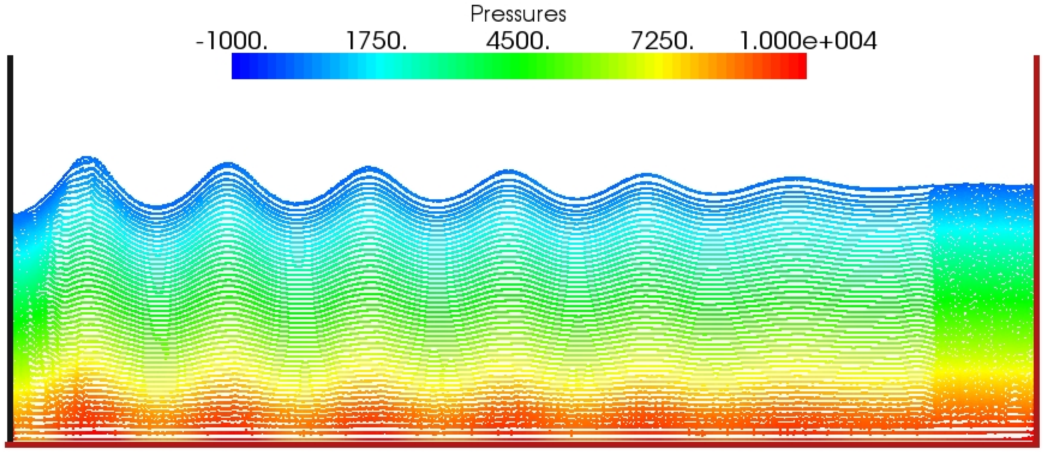

b)

Figure 4.13: Pressure distributions for waves generated by a paddle using SPH-ALE and 3rd-order cubic kernel at *a)* t=10s, *b)* t=15s, $\triangle = 0.02m$. Note distorted scale

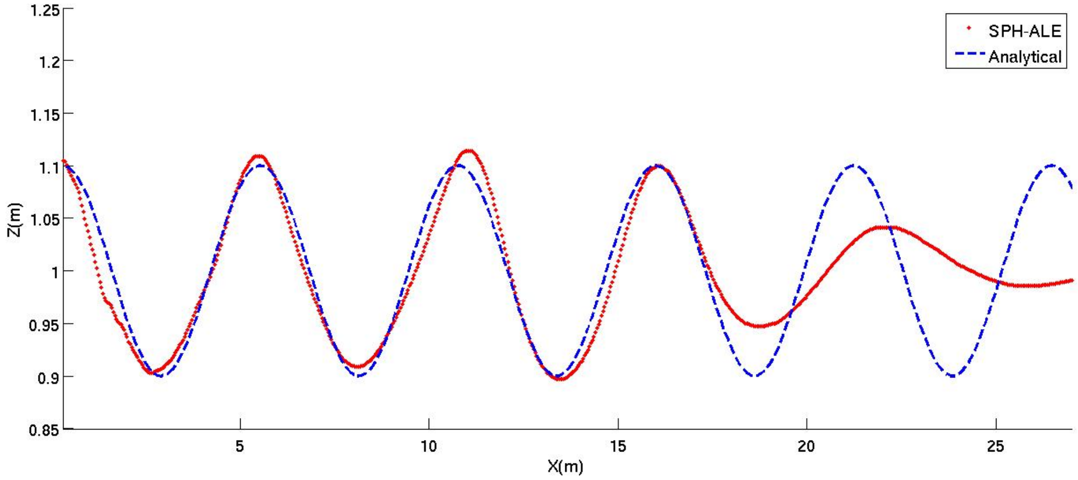

a)

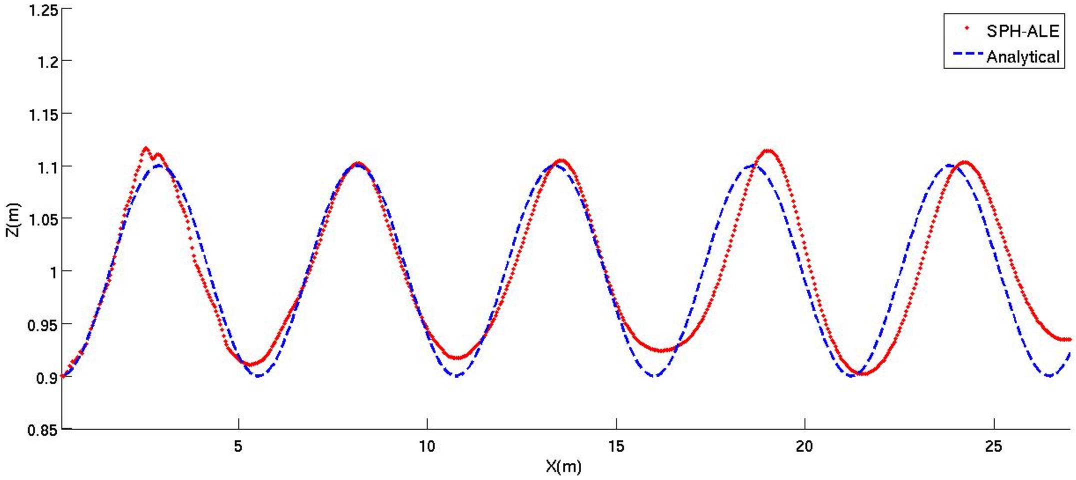

b)

Figure 4.14: Surface profiles for waves generated by a paddle using SPH-ALE and 3rd-order cubic kernel at *a)* t=10s, *b)* t=15s, $\triangle = 0.04m$

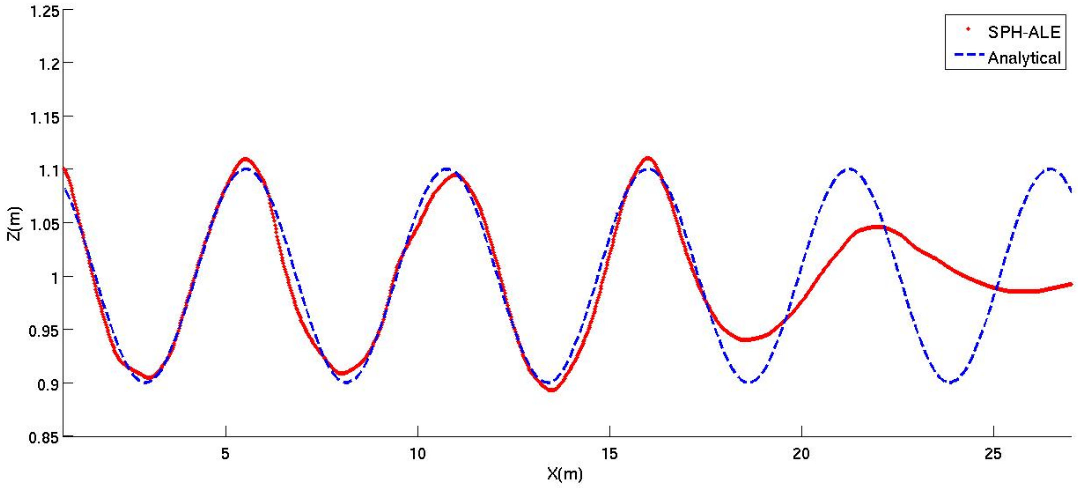

a)

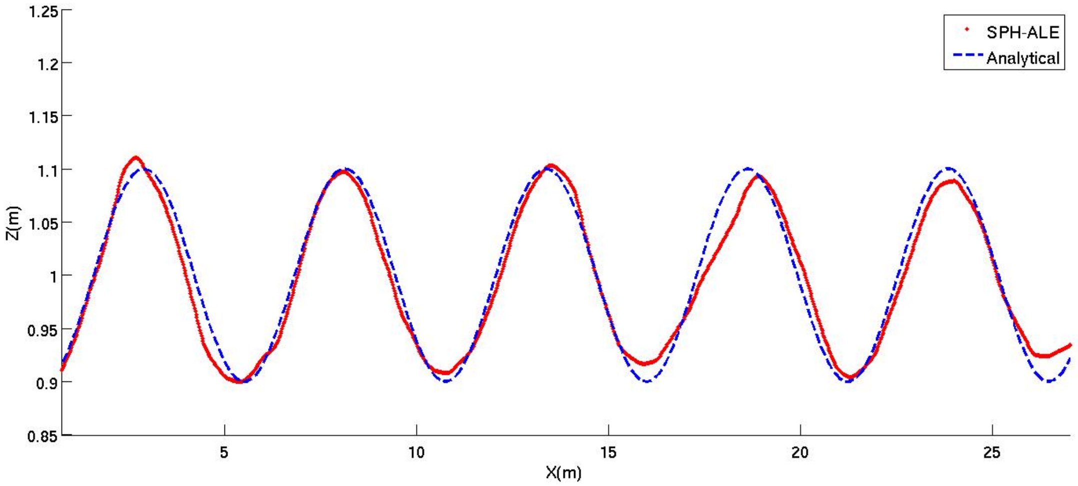

b)

Figure 4.15: Surface profiles for waves generated by a paddle using SPH-ALE and 3rd-order cubic kernel at *a)* t=10s, *b)* t=15s, $\triangle = 0.02m$

The surface profile produced by the SPH-ALE formulation can also predict the linear wave theory, shown in Figures (4.14) and (4.15) for two different initial particle spacing, in terms of magnitude and phase.

In comparison with the use of artificial viscosity in the standard SPH formulation, the upwinding provided by the Riemann solver is found to be more stable and give better results than the standard SPH. Moreover, according to Guilcher *et al.* (2007), higher values for λ_{vis} in Equation (4.8) leads to an increased damping, whereas lower values for λ_{vis} causes instabilities near the wavemaker. Furthermore, the pressure distribution in SPH-ALE is more uniform whereas the artificial viscosity creates some noise in the simulations. The reason may be found in the momentum equation (Equation 4.7) where any error in density may lead to fluctuations in momentum equation, due to the $1/\rho^2$ term, whereas in the original SPH-ALE of Vila (1999) this will not happen.

The cubic kernel is used for all the following simulations in this thesis.

4.7 Fixed cylinder in still water

The first step of studying bodies in waves is to investigate the vertical and horizontal forces in still water and examine if the right force values can be obtained along each direction. A tank of 5m length and 2m height is chosen and a half-submerged circular cylinder of 1m diameter is located in the middle of channel. Here, the initial particle spacing is $\triangle$=0.02m.

Figure (4.16) and Figure (4.17) show the particles distribution initially and at t=5s, respectively. As seen in the figures the particles reorganise their positions, especially around the body, and remain symmetric to the centre of the tank. Figure (4.18) indicates the variation in time of the horizontal force and vertical force minus the exact buoyancy component divided by buoyancy component in still water where the values for the dimensionless forces become zero. However, the magnitude of the vertical force for the first second of time is varying as particles reorganise themselves around body. Similar results can be obtained using different cylinder submergence depths.

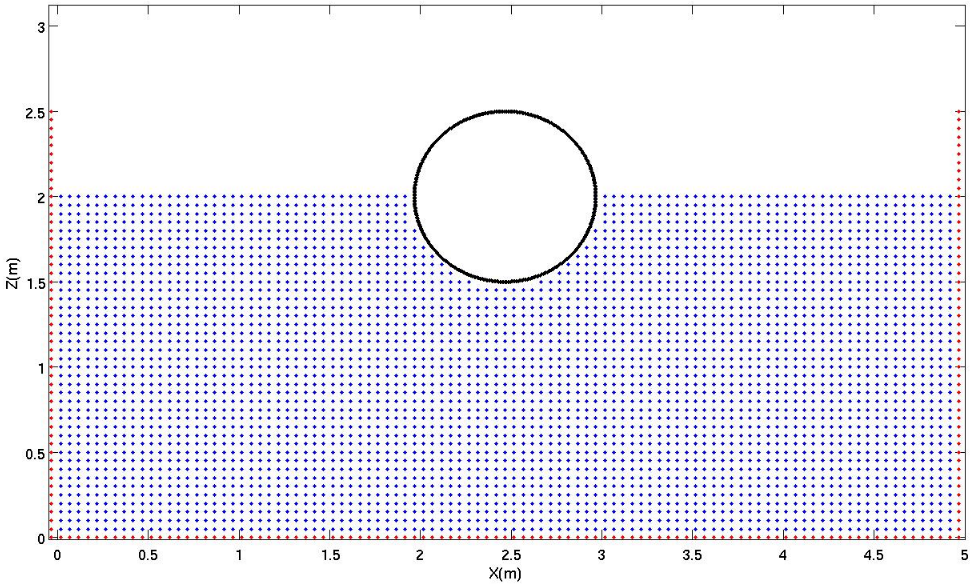

Figure 4.16: Particle distribution of still water at t=0

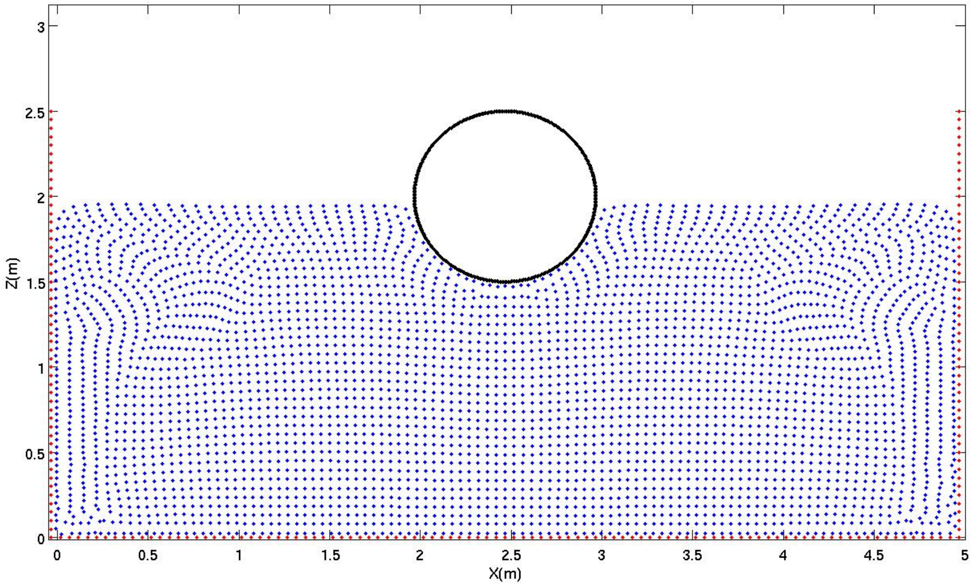

Figure 4.17: Particle distribution of still water at t=5s

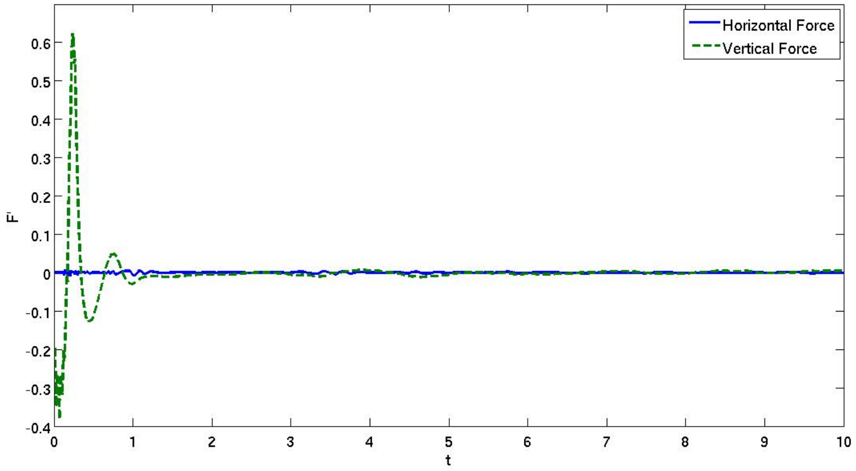

Figure 4.18: Normalised horizontal and vertical forces versus time for still water problem

4.8 Wave loading on a partially submerged and fixed cylinder

Wave forces on partially submerged, fixed cylinders in two dimensions measured by Dixon *et al.* (1979) are used for comparison for different wave amplitude and cylinder submergence.

4.8.1 Experimental data for progressive wave loading on a cylinder

The experiment data of Dixon *et al.* (1979) are used in order to validate the SPH results for a fixed and partially submerged cylinder. Dixon *et al.* (1979), first, presented the theory of wave forces followed by a modification of vertical force theoretical formulation. Then, the force on a circular cylinder was calculated using linear wave theory for different water levels. In this work, we use their wave frequency and various wave amplitudes and axis depths. Table (4.1) shows their results, which will be used here, for different relative axis depths and relative amplitudes. The relative amplitude and axis depth are the ratio between the amplitude and axis depth, and the cylinder diameter, respectively. These experiments were done for the relative wave length (wave length divided by the diameter of cylinder) of 15.62.

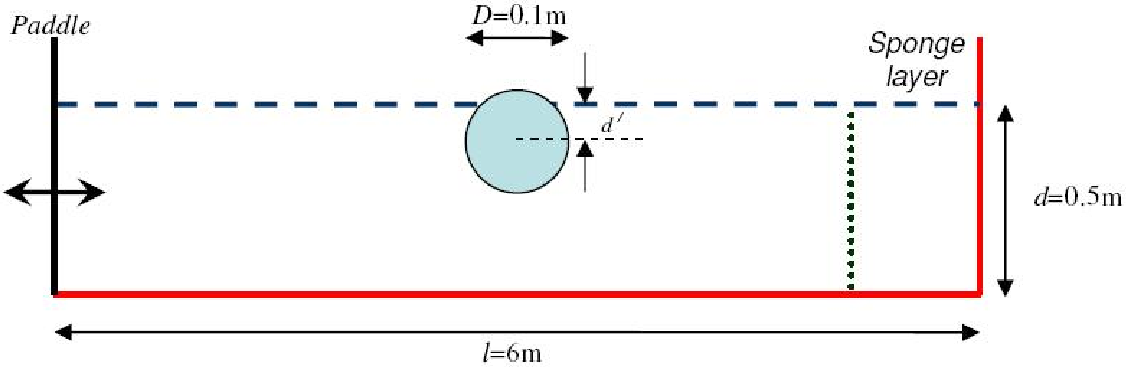

Figure 4.19: Schematic figure of the wave loading on a partially submerged cylinder

Relative amplitude	Relative axis depth	C_M	Experimental F_{rms}	Theoretical F_{rms}
0.10	0.00	1.86	0.062	0.063
0.50	0.00	1.73	0.264	0.284
0.20	-0.10	1.81	0.112	0.115
0.20	-0.20	1.72	0.101	0.099
0.20	-0.30	1.78	0.087	0.074
0.30	-0.40	1.31	0.118	0.116
0.30	-0.50	1.25	0.089	0.093

Table 4.1: Force coefficients and Root-Mean-Square relative forces for different test cases (after Dixon *et al*, 1979)

4.8.2 SPH results for progressive wave loading on a cylinder

Figure (4.19) shows the schematic of the SPH domain where waves of 1s period are generated with a paddle at the left boundary and absorbed by a sponge layer of length 1m at the right boundary. The sponge layer is implemented by changing the order of the Riemann solver approximation from second to first by gradually decreasing of the value of β-limiter in Equation (4.9), i.e. from β-limiter=1 to β-limiter=0. A cylinder with a diameter of 0.1m is located in the middle of the channel that is 6m in length and 0.5m in depth, and the axis depth below mean water level, d', varies. The initial particle spacing is $\triangle$=0.02m. Figure (4.20) shows the particle distributions at two sample times. The wave propagation near the cylinder has clearly been altered by the presence of the cylinder. Since the simulations are single phase (i.e. only water particles) the compressibility of air around the cylinder is not taken into account. The zoomed images of the particle distributions are presented

Relative amplitude	Relative axis depth	SPH F_{rms}	Experimental F_{rms}
0.10	0	0.075	0.062
0.50	0	0.259	0.264
0.20	-0.1	0.115	0.112
0.20	-0.2	0.120	0.101
0.20	-0.3	0.109	0.087
0.30	-0.4	0.149	0.118
0.30	-0.5	0.179	0.089

Table 4.2: Comparison of SPH dimensionless *rms* force, normalised by submerged buoyancy force, with experiment for different relative wave amplitude (a/D) and axis depth ($d^{/}/D$)

in Figure (4.21).

In order to compare the forces obtained by the SPH method with the experimental data, the dimensionless root mean square (rms) vertical force is calculated as

$$F_{rms} = \sqrt{\frac{1}{n}\sum_{k=1}^{n} F_k^2}, \tag{4.13}$$

where F_{rms} is the root mean square force, F_k is the total vertical force component at each time steps (evaluated by summing the force contribution from nearby fluid particles) divided by the weight of water displaced by a totally submerged cylinder in still water, and n is the number of timesteps.

Table (4.2) shows the comparisons of dimensionless *rms* force between the SPH results and the experimental data presented by Dixon *et al.* (1979) for different relative axis depths and relative amplitudes. The relative amplitude and axis depth are defined as the ratio between the amplitude and axis depth to the cylinder diameter, respectively. As shown in the table, one can see that the experimental and SPH results are in reasonable agreement especially for the half submerged cylinder. The results show promising agreement for the more submerged cylinder cases, but with a discrepancy that might be due to problems with the experimental data as discussed in Westphalen *et al.* (2009). The convergence test will be shown in Section (5.5).

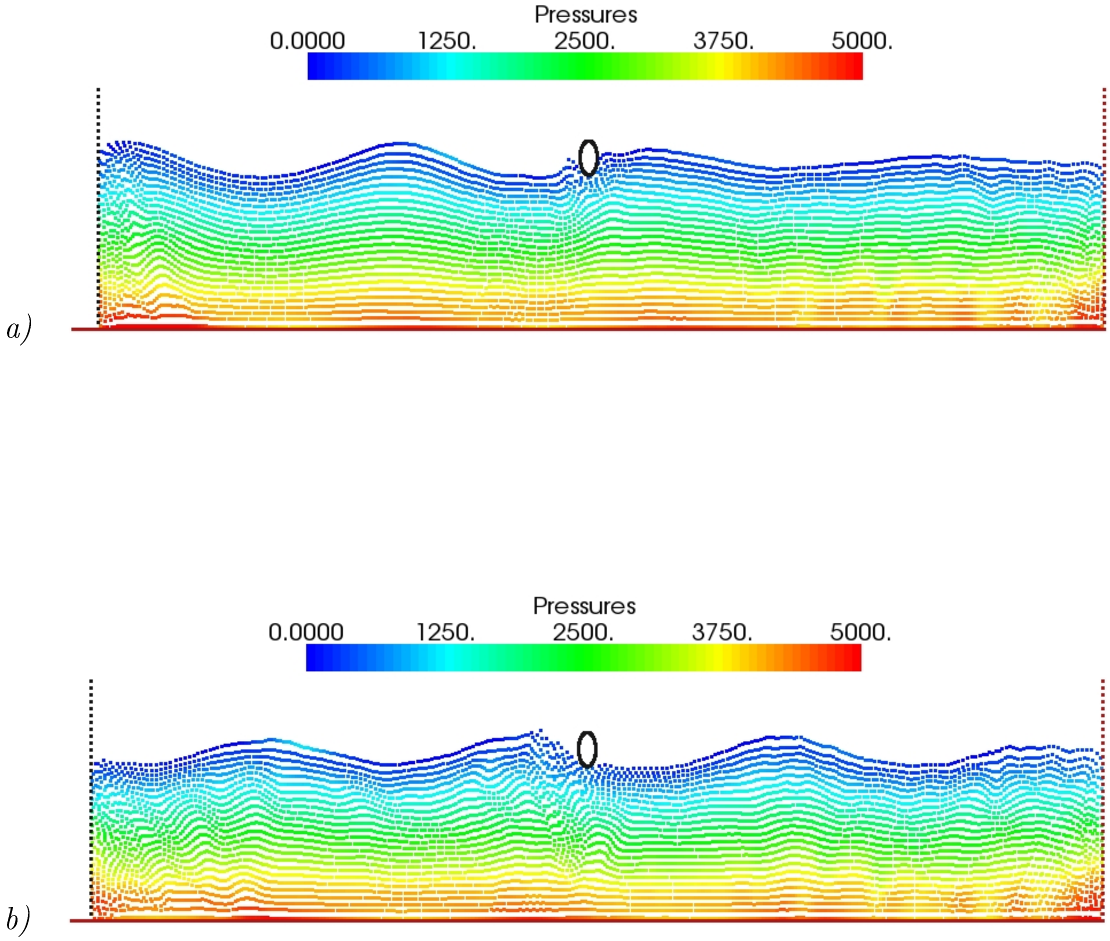

Figure 4.20: Particles for half submerged cylinder with relative amplitude of 0.5 at *a)* t=5s, *b)* t=7.5s

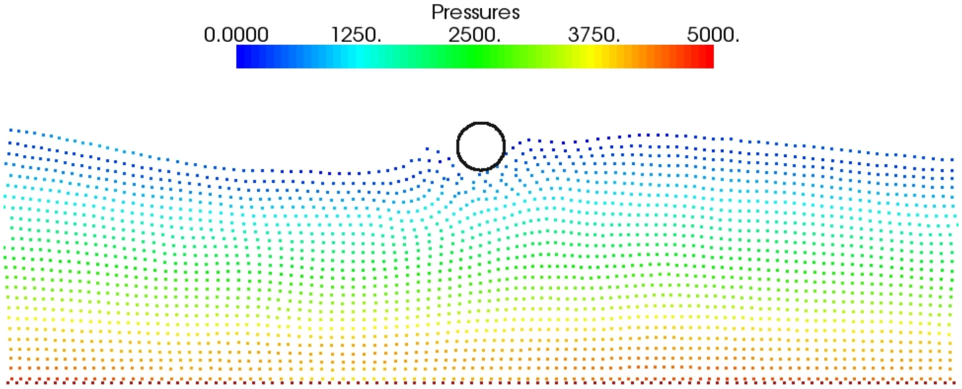

a)

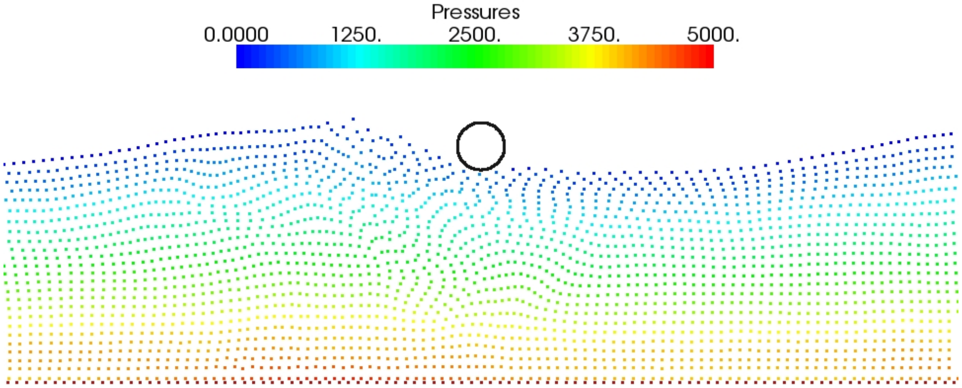

b)

Figure 4.21: Particles for half submerged cylinder with relative amplitude of 0.5 at *a)* t=5s, *b)* t=7.5s, zoomed figures

4.9 Surface waves generated by a heaving cylinder

Here, surface waves generated by a 2-D heaving cylinder of different wave period and stroke will be compared with the experimental data of Yu and Ursell (1961).

4.9.1 Experimental data for heaving cylinder

Yu and Ursell (1961) measured surface waves generated by a heaving cylinder. In their paper, they also presented linearised theory for this problem where a half submerged cylinder is forced to oscillate vertically in still water in a channel of infinite length. They derived theoretical formulations for the surface wave motion and force coefficient of a heaving cylinder. Experimentally, they performed measurements in a channel of length 30m with the cylinder at mid length. Their comparisons between theoretical and experimental wave amplitudes, using the ratio:

$$\mathrm{R_A} = \frac{\text{Wave amplitude at infinity}}{\text{Amplitude of motion of cylinder}}, \tag{4.14}$$

were in good agreement although the experimental values were in general a few percent lower than the theoretical values. Here, we validate our results using the experimental values of the amplitude ratio for different wave periods. For our numerical simulations, the wave amplitude at infinity is an amplitude of a wave which is far from the boundaries and the body to avoid the physical effects (e.g. for a wave with a period of 0.76s the third wave is considered to be at infinity). Table (4.3) shows the experimental amplitude ratio for different wave periods and cylinder strokes.

Cylinder stroke (cm)	Wave period (s)	Experimental R_A
1.23	0.69	0.610
1.23	0.76	0.543
1.23	0.84	0.514
1.23	0.93	0.451
0.91	0.50	0.810
0.93	0.45	0.852

Table 4.3: Experimental amplitude ratio for different wave periods and cylinder strokes (after Yu and Ursell, 1961)

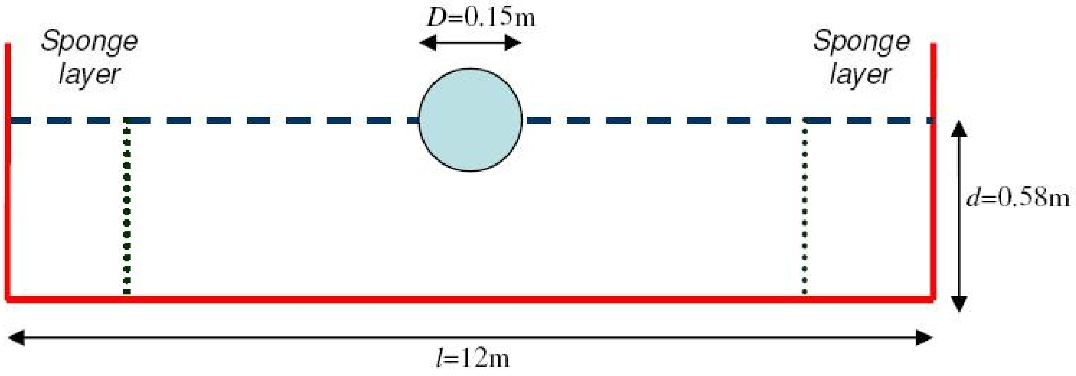

Figure 4.22: Schematic of surface wave generated by a heaving cylinder

4.9.2 SPH results for surface waves generated by a heaving cylinder

The numerical domain is shown in Figure (4.22) where waves are generated by a heaving cylinder at the centre of the channel and propagate towards both ends of the channel, which is 12m in length and 0.58m in depth. Waves are absorbed by sponge layers of length 1.5m at the boundaries. As for the fixed cylinder, the sponge layer can be implemented on both sides of the tank by changing the order of the Riemann solver approximation from second to first by gradually decreasing the value of the β-limiter in Equation (4.9), i.e. from β-limiter=1 to β-limiter=0. The cylinder is initially half submerged and then starts oscillating in a vertical direction in simple harmonic motion with small amplitude. The initial particle spacing and the diameter of cylinder are $\triangle$=0.02m and D=0.15m, respectively. The stroke of the cylinder is small in the experiment in order to simulate the small-amplitude wave of the theory, and yet was large enough to generate waves with height which could be measured accurately. Figure (4.23) shows pressure distributions for a heaving cylinder with a stroke of 1.23cm and a period of 0.76s. Also, the zoomed images of the particle distributions are presented in Figure (4.24) for two sample times. It is clear from the Figures (4.23) and (4.24) that waves generated by the heaving cylinder travel along the channel without any dissipation and absorbed by the sponge layer.

The comparisons of the surface profile between the linear theoretical free surface for the present wave period and depth and our SPH results at t=10s are presented in Figures (4.25) and (4.26) for different wave periods, where the agreement is close. Note that the domain length is chosen to be 16m for the period of 0.84s.

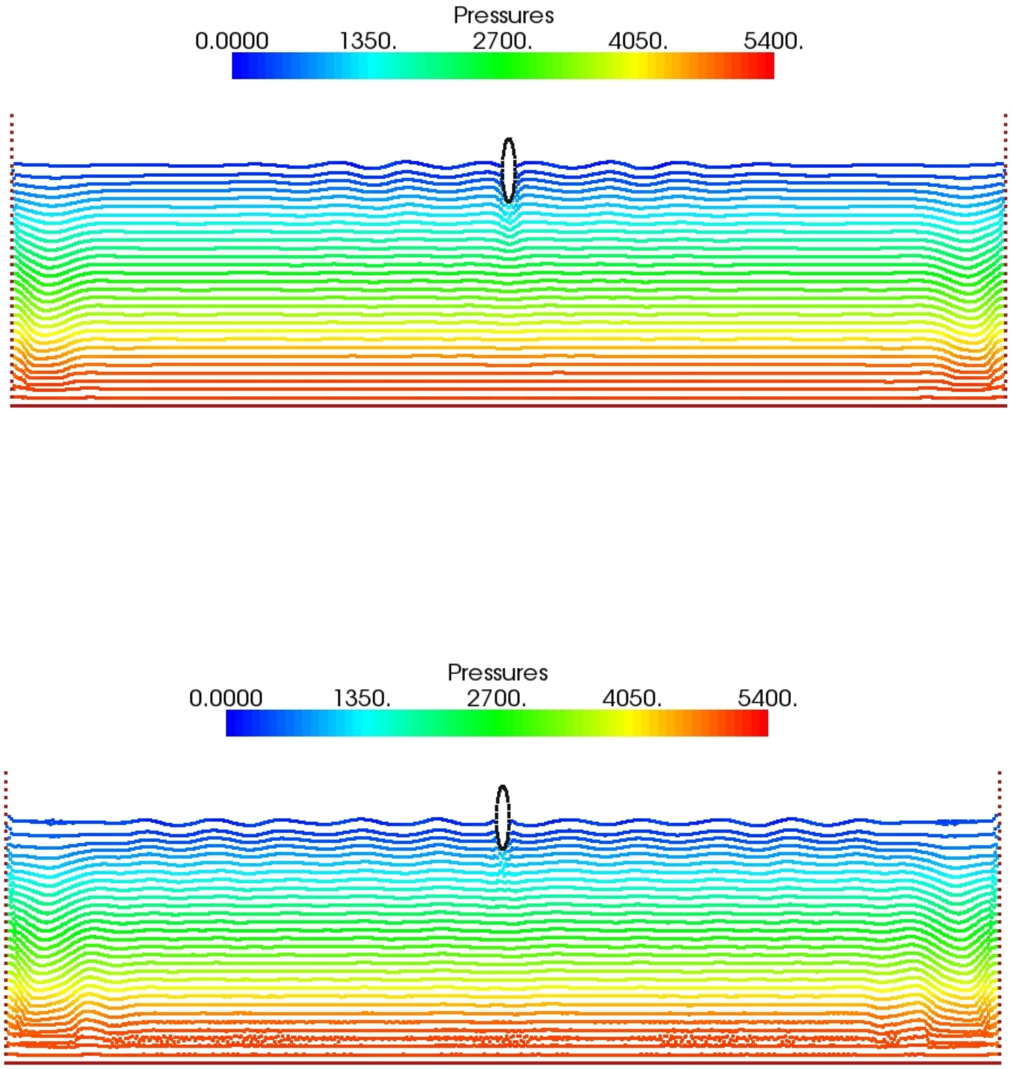

a)

b)

Figure 4.23: Pressure distributions for a heaving cylinder with the stroke of 1.23cm and a period of 0.76s at *a)* t=5s, *b)* t=10s. Note distorted scale

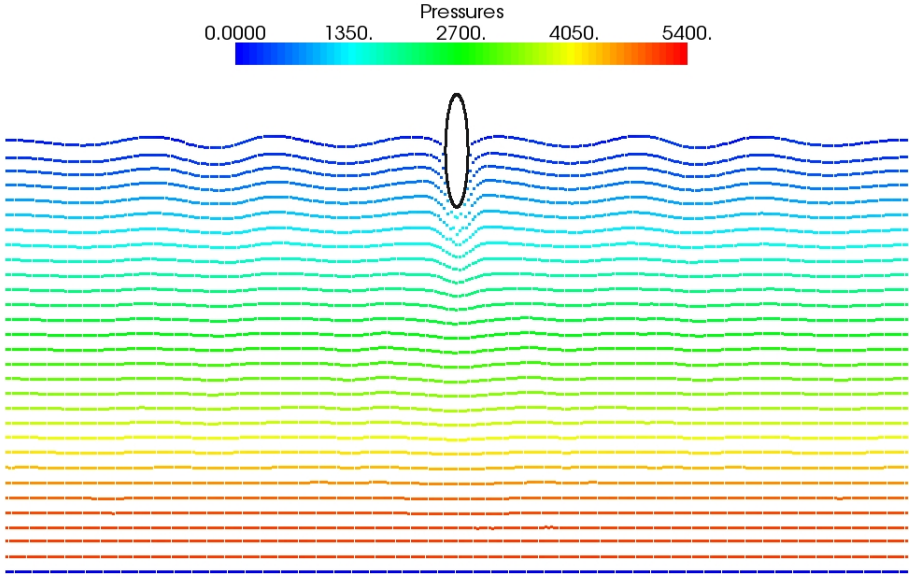

a)

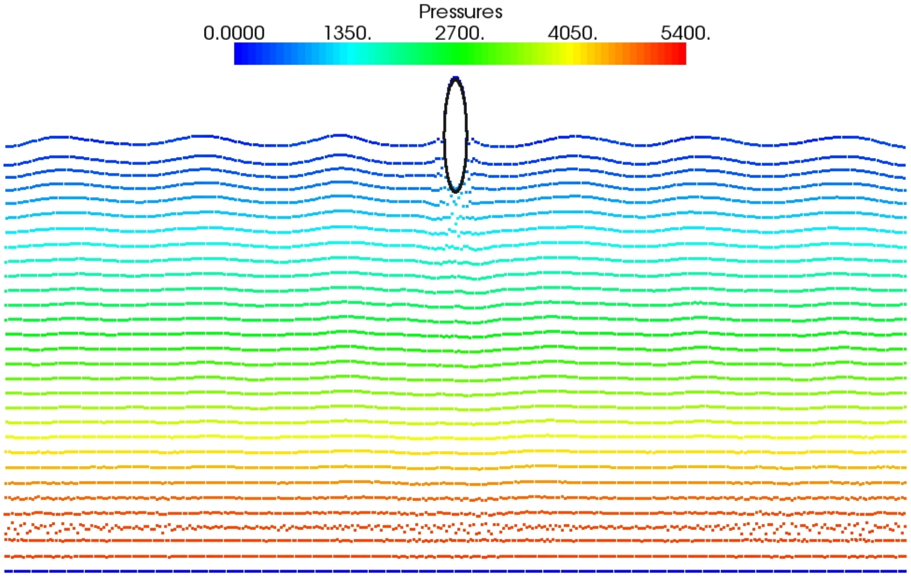

b)

Figure 4.24: Pressure distributions for a heaving cylinder with the stroke of 1.23cm and a period of 0.76s at *a)* t=5s, *b)* t=10s. Note distorted scale

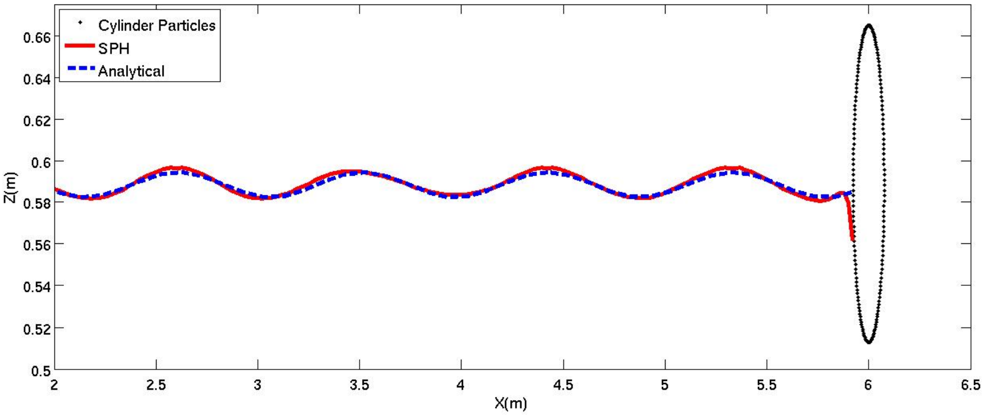

Figure 4.25: Comparison of surface profile between analytical and SPH results for a heaving cylinder with the stroke of 1.23cm and a period of 0.76s at t=10s

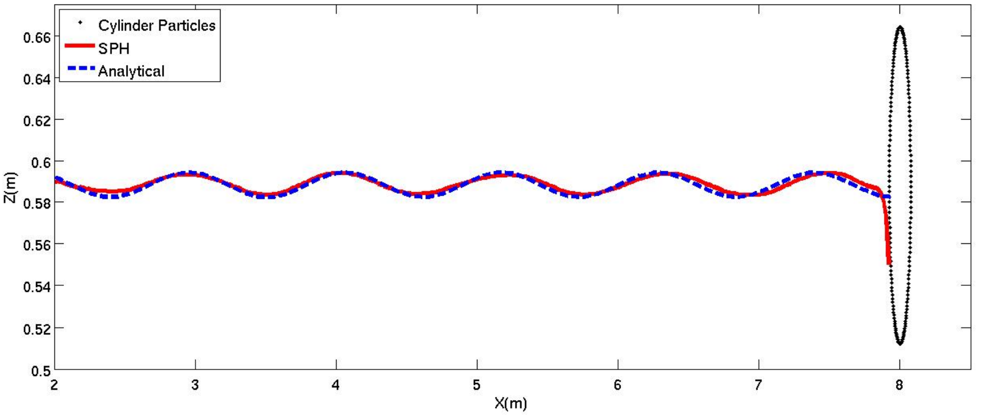

Figure 4.26: Comparison of surface profile between analytical and SPH results for a heaving cylinder with the stroke of 1.23cm and a period of 0.84 at t=10s

Cylinder stroke (cm)	Wave Period T(s)	SPH Coarse R_A ($\triangle$=0.02m)	SPH Finer R_A ($\triangle$=0.01m)	Experimental R_A
1.23	0.69	0.63	0.60	0.610
1.23	0.76	0.58	0.53	0.543
1.23	0.84	0.49	0.51	0.514
1.23	0.93	0.42	0.44	0.451
0.91	0.50	0.87	0.83	0.810
0.93	0.45	0.89	0.84	0.852

Table 4.4: Comparison of SPH wave amplitude with experiments for different wave periods and cylinder strokes

As suggested by Yu and Ursell (1961) to compare with the experimental data, we use the amplitude ratio, R_A theoretically defined at infinity, Equation (4.14), at three wavelengths from the cylinder. This avoids nonlinear affects around the cylinder.

The SPH amplitude ratio for a heaving cylinder with the stroke of 1.23cm and a period of 0.76s is $R_{A,SPH} = 0.58$, which is close to the experimental value $R_{A,Exp} = 0.543$. Table (4.4) shows that the experimental and SPH results for the amplitude ratio with different wave periods and cylinder strokes are in good agreement. Using finer resolution shows an improved agreement in all cases, however using finer resolution needs a large number of particles, increasing computer time.

This is not trivial in SPH as it is computationally expensive, hence achieving this efficiently will be the topic of the next chapter.

4.10 Summary

In this chapter, first, the analytical results for a plate moving horizontally in a channel were compared with two forms of SPH formulations and the ISPH data of Xu (2009). The results found to be in a good agreement with the ISPH data and analytical solutions.

An investigation into wave propagation in a long tank of intermediate deep was conducted using the standard and SPH-ALE formulations with different kernel functions. It was shown that using the SPH-ALE formulation and cubic kernel would give the best results, comparing the results with the linear wave theory.

Moreover, surface waves interacting with a fixed cylinder and generated by a heaving cylinder were investigated using the SPH method. The SPH method was successfully used to predict wave propagation in a channel applied to loading a partially submerged and fixed circular cylinder for various wave amplitudes and axis depths. For the half- submerged cylinder the agreement with the experimental data for root mean square force is within 2%. For the submerged cylinder, the results also show promising agreement.

We also compared our SPH results and available experimental data for surface waves generated by a heaving cylinder for different cylinder strokes and wave periods, which were in a very good agreement. We also presented the comparisons of the surface profile between the linear theoretical free-surface where the agreement was close. However, obtaining a more accurate answer for the free-surface profile in 2D and capturing the entire three dimensional flow fields would require a large number of particles. This may be difficult and time consuming for capturing the entire three dimensional flow fields. In the following chapters, variable particle mass will be defined in order to avoid expensive CPU cost.

Chapter 5

Variable particle mass for 2-D wave body interaction

5.1 Introduction

Efficient computing of the free-surface motion, in particular to capture highly nonlinear waves, would require a simulation with a large number of particles which is extremely time consuming in SPH. In this chapter, after the description of the numerical setup, first the need for variable particle mass will described. Then, the variable mass distribution of particles is employed to simulate the still water problem for different mass ratios, looking carefully at the kernel instability and hydrostatic pressure. Finally variable mass distribution of particles will be employed for wave loading on a fixed, partially submerged cylinder of Dixon *et al.* (1979) and for the heaving cylinder case of Yu and Ursell (1961) described in the previous chapter.

5.2 Numerical setup

In this chapter, the SPH-ALE formulation of Vila (1999) are used for all the simulations using an HLLC approximate Riemann solver and MUSCL-based upwinding as described in Chapter 3. In Chapter 4 the cubic kernel function (Monaghan, 1992) was found to be the best choice of kernel function (see Section 4.6.3). The symplectic

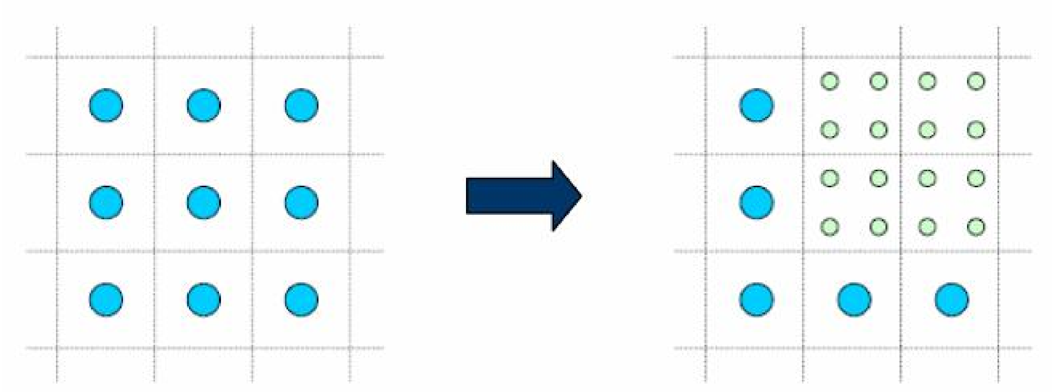

Figure 5.1: Replacing a particle with a mass m with four lighter ones with a mass $m/4$

time stepping method (Leimkuhler *et al.*, 1997 and Monaghan, 2005) is used. Moreover, in order to prevent a water particle crossing a solid boundary, the repulsive boundary condition described in Section (3.6.1) is used.

5.3 The need for variable particle mass

To reduce the particle number, previous SPH studies have recommended using variable smoothing lengths (Bonet and Rodriguez-Paz, 2005) or particle refinement (see Nelson & Papaloizou, 1994 and Lastiwka *et al.*, 2005). There can be conservation issues using particle refinement and there are extra terms to deal with time and space varying smoothing lengths. Here, instead of variable smoothing length or particle refinement, a pre-defined variable mass distribution is used with refined particles in a selected area (i.e. around the circular cylinder) where a heavier particle with a mass of m is replaced typically with four lighter ones with a mass $m/4$ (Figure 5.1). Here, the value of the smoothing length is kept constant at the original value of the larger particles.

Since the cubic kernel is used without changing the smoothing length, an assessment of tensile instability at the interface of different particle size is needed. To circumvent this, there are some techniques suggested in the literature to overcome the kernel instability such as using other kernel formulations and adding an artificial pressure (Monaghan, 2000). The cubic kernel function, which approximates the Gaussian kernel function, is found to be the best choice for propagation of waves in a channel (see Chapter 4), but this is well known to have kernel instability issues. Monaghan

(2000) demonstrated that the kernel instability can be virtually removed if a pressure correction is used. In the SPH-ALE formulation, this is achieved by replacing the pressure P_a in the ALE scheme in Equation (4.9) with

$$P_a + C f_{ij}^{\kappa}, \tag{5.1}$$

where $\kappa > 4$, $C = C_i + C_j$ and

$$f_{ij} = \frac{W_{ij}}{W_{\triangle}}, \tag{5.2}$$

where $\triangle$ is the initial particle spacing in the neighbourhood of particle i. The kernel instability correction is activated depending on the mass of two interacting particles. Here C_i and C_j have no direct physical meaning but represent instead a numerical correction for the well-known tensile instability issue mentioned above where the kernel gradient tends to zero as $r_{ij} \rightarrow 0$. In the formulation used here, the decreasing kernel gradient leads to a reduction in the pressure experienced between particles in Equation (3.93), soC_i and C_j enable recovery of this pressure

5.4 Assessing still water with variable mass distribution of particles

Before using this scheme for dynamic problems, it is important to assess the prediction of still-water conditions. The numerical domain for an example still-water problem is shown in Figure (5.2) where the lighter particles are initially located in region 2 while the heavier particles are in region 1. The channel is 2m in length and water depth is 1m. The box of lighter particles is symmetric about the central vertical axis.

Here, we use an investigation of hydrostatic pressure to determine appropriate values of C_i and C_j, where the mass ratio of 1:4 (since it is easier to be implemented), shown in Figure 5.1), is used. Figure (5.3) displays the comparison between the exact and SPH hydrostatic pressure at t=5s where $C_i = 0.01P_i$ and $C_j = 0.2P_j$; pressures are in acceptable agreement. There is a discrepancy near the bed ($z \rightarrow 0$) where there is a noticeable error due to a lack of a complete kernel support. This region is not

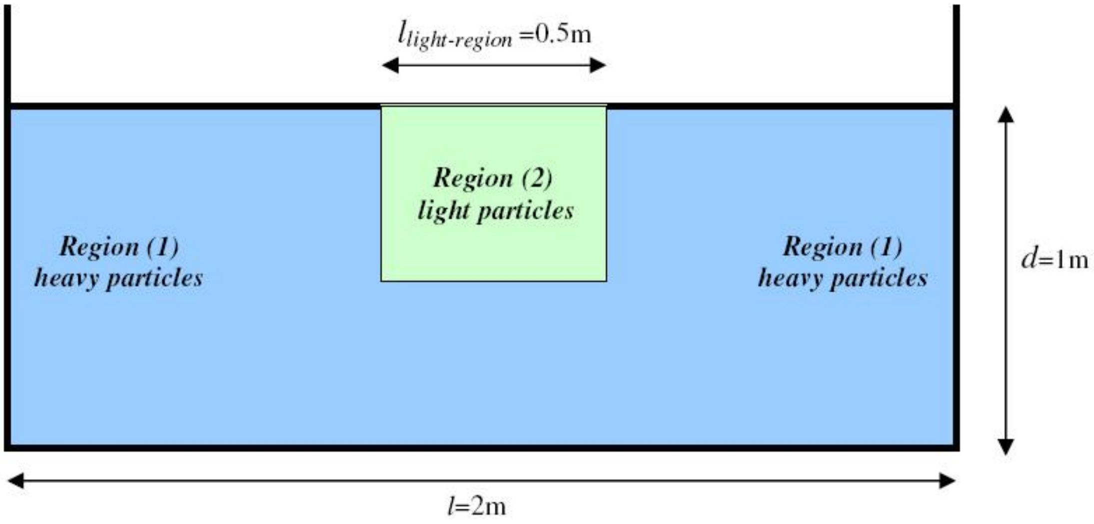

Figure 5.2: Schematic of still water problem using variable distribution of particles

important in our simulations and so no remedy is attempted. However, these C_i and C_j values lead to particle clumping at the interface of lighter and heavier particles.

Results with an increased value of $C_i = 0.05P_i$ keeping $C_j = 0.2P_j$ are shown in Figure (5.4). There is a very small pressure error at the interface of two regions which is simply due to the introduction of the small artificial pressure to the momentum equation. The particle clumping (an example is shown later) still occurs with the value of $C_i = 0.05P_i$.

Figure (5.5) shows that as the value of C_i increases to $0.1P_i$ the pressure error will grow at the interface while the particle clumping exists at some part of the interface.

Increasing the value of C_i to $0.15P_i$ avoids particle clumping at the interface of the lighter and heavier particles but Figure (5.6) shows that this significantly affects the pressure at the interface. Here, the maximum error in pressure profile can be estimated as 10%, which occurs at the lower interface of light and heavy particle regions shown in Figure (5.2).

To examine the degree of clumping, Figure (5.7) shows the dependence of the ratio of minimum particle spacing to initial particle spacing on C_i, where $C_j = 0.2P_j$ for all cases. At t=5s the value of 50% for $\left[\frac{\min(r_{ij})}{\triangle}\right]$describes the particle spacing in the lighter mass region where the initial particle spacing is half the initial particle spacing in the heavier mass region. This plot shows the particle clumping signifi-

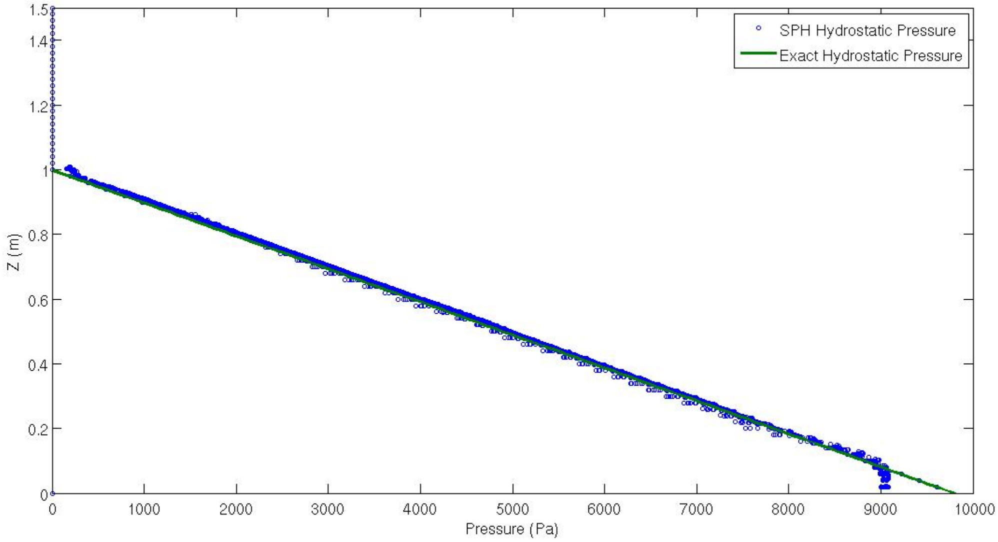

Figure 5.3: Comparisons between the exact and SPH hydrostatic pressure for $C_i = 0.01P_i$ and $C_j = 0.2P_j$ at t=5s

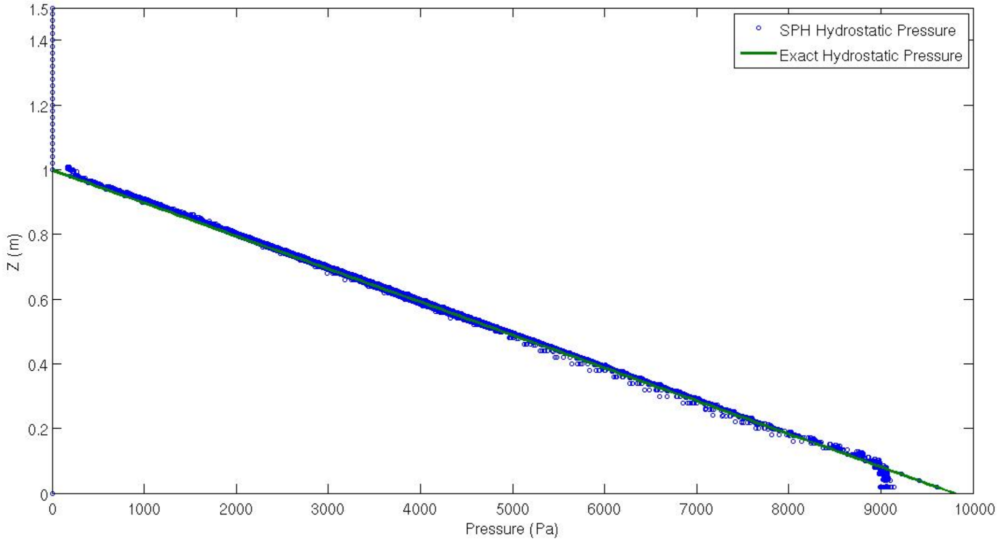

Figure 5.4: Comparisons between the exact and SPH hydrostatic pressure for $C_i = 0.05P_i$ and $C_j = 0.2P_j$ at t=5s

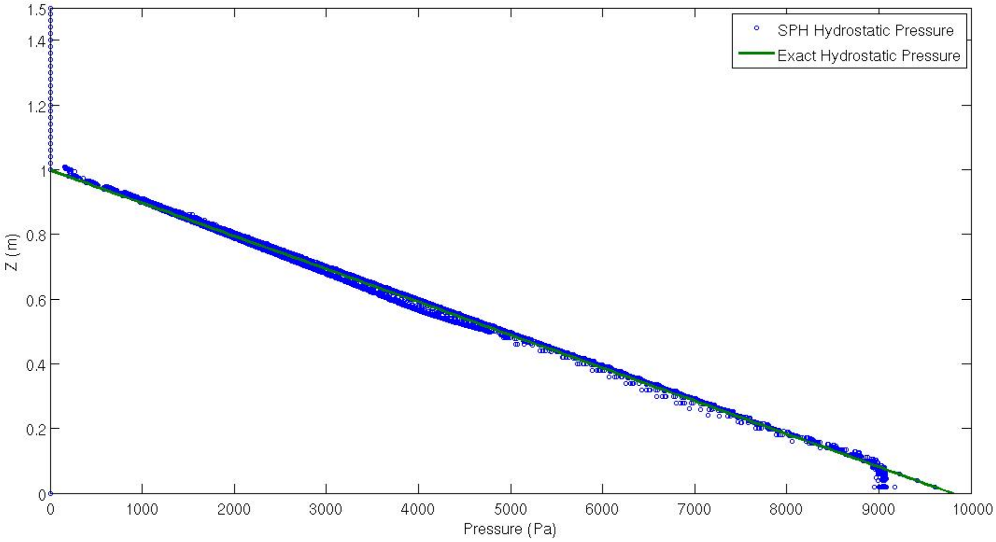

Figure 5.5: Comparisons between the exact and SPH hydrostatic pressure for $C_i = 0.1P_i$ and $C_j = 0.2P_j$ at t=5s

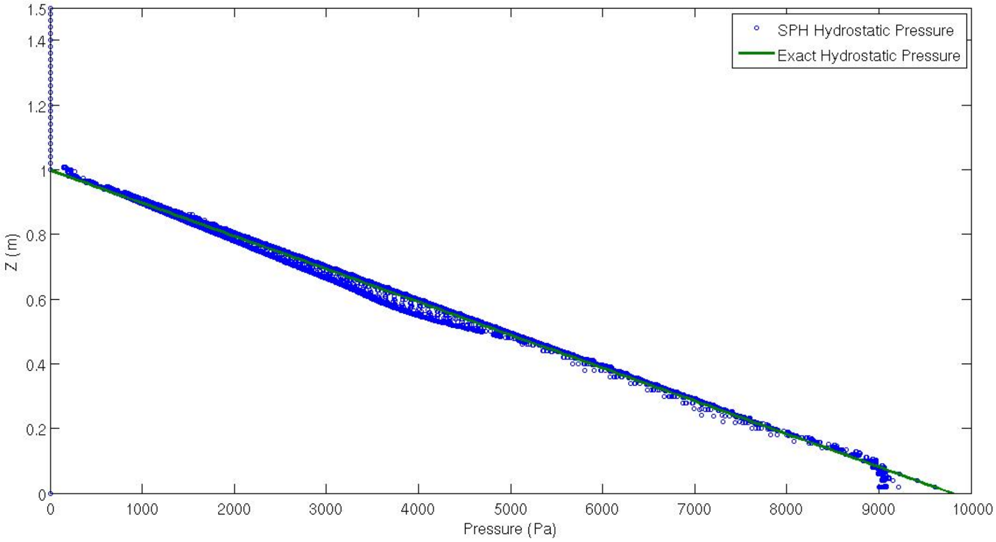

Figure 5.6: Comparisons between the exact and SPH hydrostatic pressure for $C_i = 0.15P_i$ and $C_j = 0.2P_j$ at t=5s

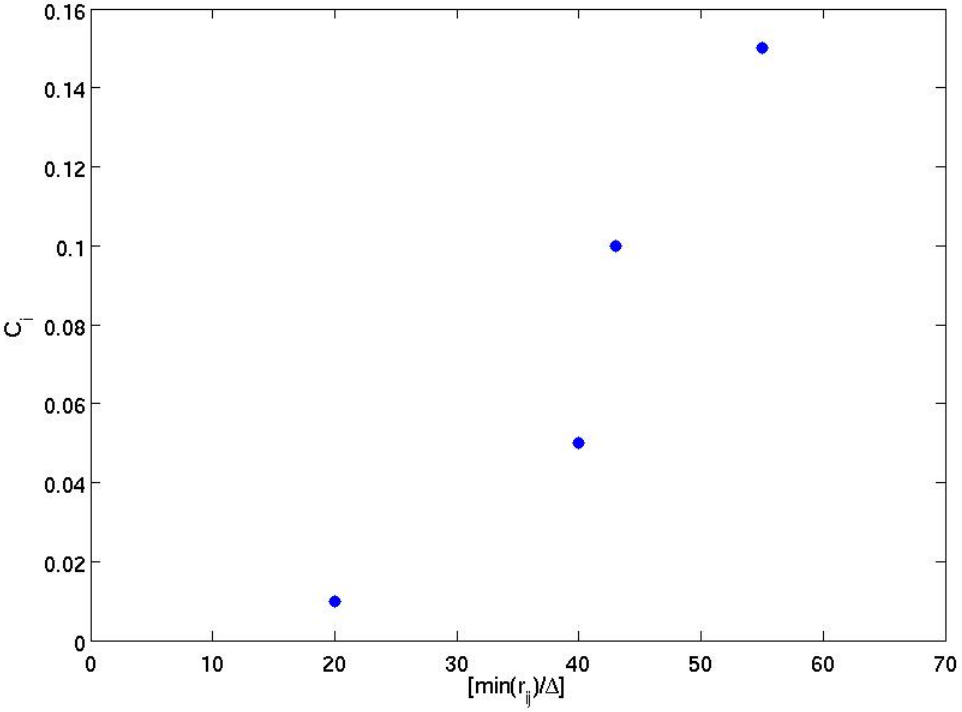

Figure 5.7: Percentage of minimum particle spacing over initial particle spacing versus C_i where $C_j = 0.2P_j$

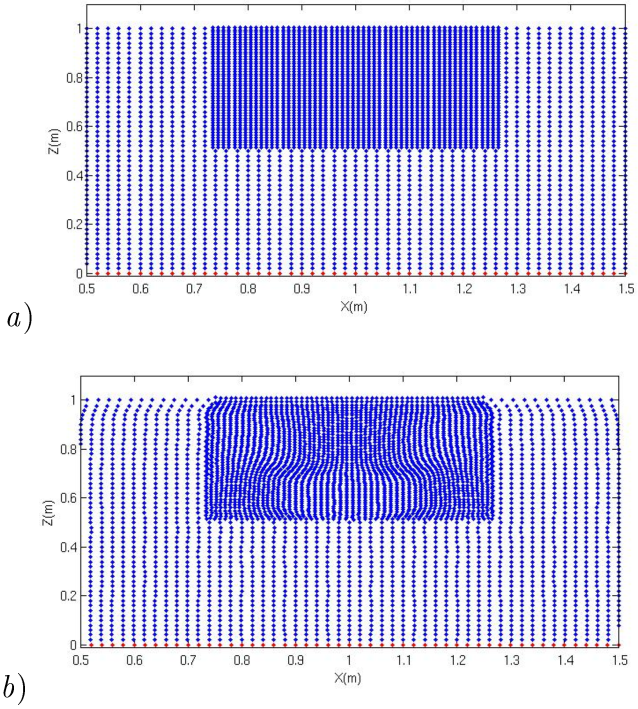

Figure 5.8: Particle distribution for still water problem for the mass ratio of 1:4 at *a*) t=0 and *b*) t=10s with the initial particle distance of 0.02m

cantly increases (i.e. $\left[\frac{\min(r_{ij})}{\triangle}\right]$ decreases) at the interface region when the value of C_i decreases. By examining Figure (5.7) and comparing with the hydrostatic pressure distributions in Figures (5.3) to (5.6), we can see that choosing the value of $C_i = 0.1P_i$ produces minimum clumping (i.e. marginally less than 50%) while still producing accurate hydrostatic pressure in Figure (5.6) in the area of interest. We use $C_i = 0.1P_i$ and $C_j = 0.2P_j$ in our simulations.

The next step of this section is to assess still water with variable mass distribution of particles. Figures (5.8) to (5.11) display different plots of particles in still water, initially and after 10s, where the variable mass distribution of particles is used.

Figure (5.8) shows the particle configuration where the mass ratio of 1:4 is used. The particles stay stable and symmetric about the vertical axis after 10 seconds without any clumping or unphysical mixing at the interface, thus preserving the still-water condition. At the free surface, there is some very small movement or deformation due to lack of kernel completeness.

The stability of the particles can be also assessed using a diagonally-slanted distribution shown in Figure (5.9). The mass ratio is kept 1:4 and a particle in the

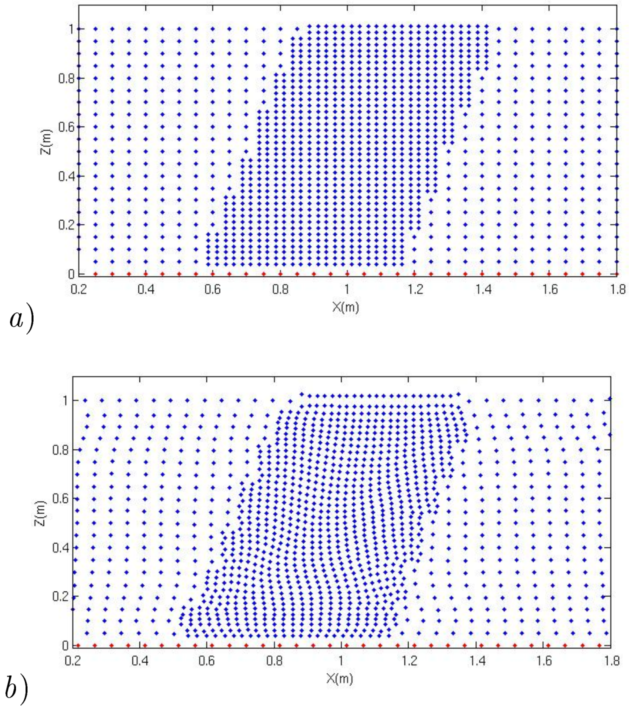

Figure 5.9: Particle distribution for still water problem for the mass ratio of 1:4 at *a*) t=0 and *b*) t=10s with the initial particle distance of 0.05m

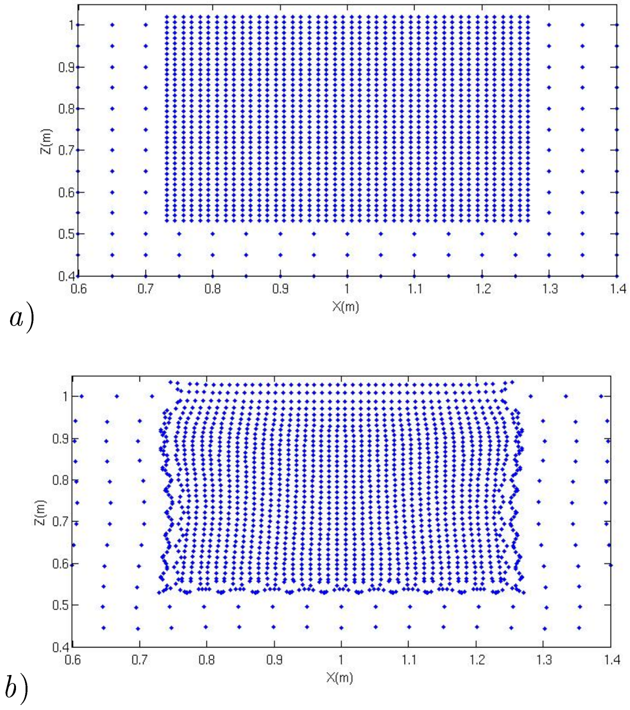

Figure 5.10: Particle distribution for still water problem for the mass ratio of 1:16 at *a*) t=0 and *b*) t=10s with the initial particle distance of 0.05m

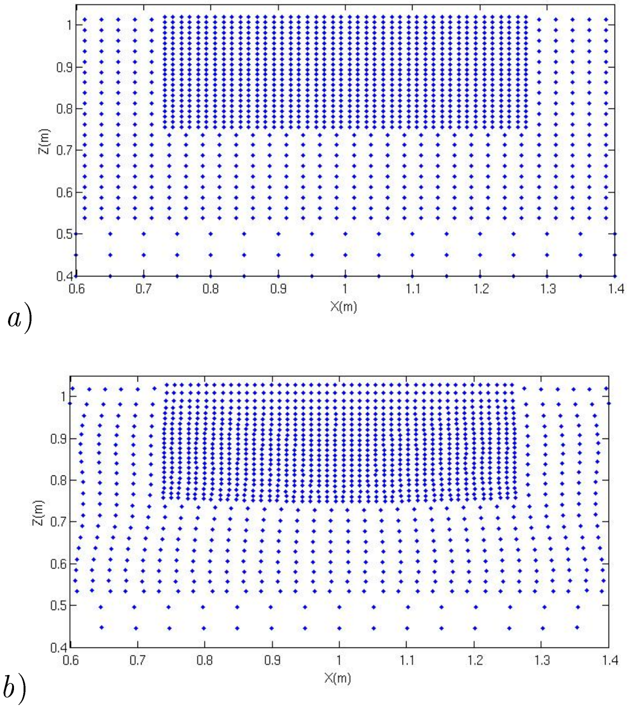

Figure 5.11: Particle distribution for still water problem for the mass ratio of 1:4:16 at *a*) t=0 and *b*) t=10s with the initial particle distance of 0.05m

diagonally-slanted region can be replaced by four lighter particles according to Figure (5.1). Figure (5.9) proves that lighter particles do not move or mix due to the irregular interface so that the particles remain close to the original position. However, better results can be achieved using a finer resolution. For the above problems the time step (Courant number, Cr=0.2) is half of the original time step (Cr=0.4).

Employing the mass ratio of 1:16 is the next step to check the limitation of mass ratio for the cubic kernel function. Figure (5.10) shows particle clumping at the interface of the regions after 10s due to the tensile instability since the initial distance between the lighter particles and therefore kernel gradient is far smaller than for the mass ratio of 1:4, shown in Figure (5.8). Adding more artificial pressure may cause other numerical issues such as a significant error in hydrostatic pressure.

However, if the domain of interest is divided into three regions and the mass distribution of particles decreases in steps, first from m to $m/4$ and then from $m/4$ to $m/16$, clumping of particles at the interface does not occur (Figure 5.11). The reason may be due to the artificial pressure (Equation 5.1) added to the momentum equation which increases gradually across different regions. Moreover, gradual di-

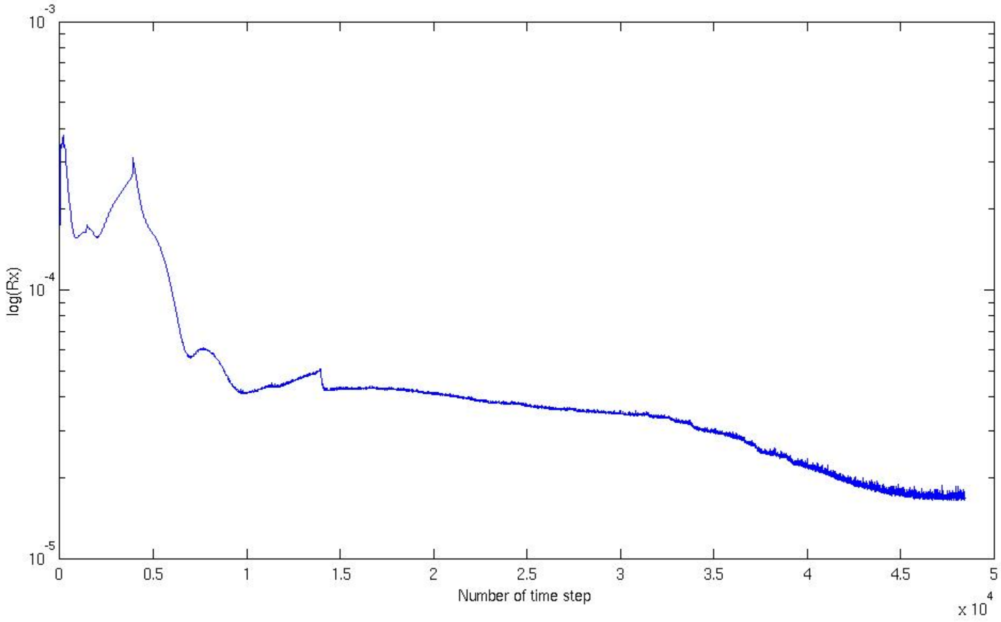

Figure 5.12: An example error of the horizontal particle positions for diagonally-slanted mass distribution

minishing of the kernel gradient from one region to another may cause the particle stress between the particles to decrease slowly across different regions. Here, the time step (Cr=0.1) is a quarter of the original time step (Cr=0.4) for the uniform coarse distribution of particles. Having three regions of mass distribution, however, may influence the CPU cost in some problems since first a smaller time step would be used and second there are more particles interacting within the lighter particle kernels than for the problem illustrated in Figure (5.8). This case shows that a pre-defined nested distribution of particles possibly has a more expensive CPU cost.

In order to assess the convergence of the method in still water one can define a global relative error (GRE) R_x (Zhou *et al.*, 2001) which is

$$R_x = \sqrt{\sum_{i \in WPs} \left(\frac{x_i^n - x_i^{n-1}}{x_i^n} \right)^2}, \tag{5.3}$$

where n denotes the time step and x_i is the position of particle along the x-direction. Figure (5.12) displays the error of the horizontal particle positions for diagonally-slanted mass distribution (shown in Figure 5.9). We consider the simulation to have reached steady state when $R_x < 4 \times 10^{-5}$. This is an arbitrary value to examine particle motion in still water chosen when the particles are not moving (Zhou *et al.*, 2001).

As a result, investigation of using variable mass distribution of particles demonstrates that variable mass distribution of particles can successfully be implemented for still water when the mass ratio is 1:4. Similar results may be obtained using a ratio of 1:3. On the one hand, using the cubic kernel function may lead the particles to clump at the interface and on the other hand, the cubic kernel was found to be the best choice for wave propagation with uniform particle mass.

In the next sections, a variable mass distribution will be used for a pre-selected area where high resolution is desirable, for example around the cylinders described in the previous chapters.

5.5 Investigation of wave loading on a partially submerged and fixed cylinder using variable mass distribution of particles

In this case, the variable particle mass is used around the fixed and partially submerged cylinder of Section (4.8), where the cylinder is located at the middle of a tank with a 6m length and 0.5m depth (Figure 4.19) and waves of 1s period are generated with a paddle at the left boundary and absorbed by a sponge layer of length 1m at the right boundary. The initial particle spacing is $\triangle$=0.02m.

Figure (5.13) displays the initial distribution of particles where the lighter particles are located near the cylinder, where high resolution and consequently more particles are needed.

Figure (5.14) shows the particle distributions at two sample times where the lighter particles are located around the cylinder. The waves appear to have passed from one region to another without loss of form at the interface and the wave propagation near the cylinder is altered by the presence of the cylinder. Moreover, there is no mixing between the particles with different masses at the interface.

In Figures (5.15) to (5.17) the SPH time histories of normalised vertical force over one wave period are compared with the experimental data for two relative axis

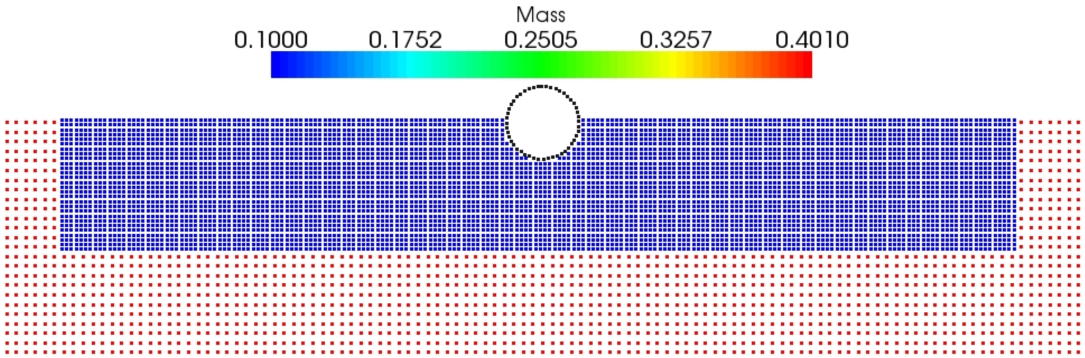

Figure 5.13: Initial distribution of particles near cylinder according to the mass

depths ($a/D = 0.5$ and $d^{/}/D = 0$ and $a/D = 0.2$ and $d^{/}/D = -0.3$ and three different resolutions: coarse uniform distribution $\triangle$=0.02m(Figure 5.15), fine uniform distribution $\triangle$=0.01m (Figure 5.16) and variable mass distribution (Figure 5.17).

It is clearly shown that the SPH results agree with the physical experiment in terms of phase, however, the vertical force is slightly noisy. Noisy force profiles are typical in many SPH simulations, e.g. see Delorme *et al.* (2007). Also, we can see that during the second half of the wave period for half-submerged cylinder, there is some discrepancy between the experimental and numerical forces but it should be noted that similar behaviour was exhibited by a finite volume code (Westphalen *et al*, 2009). This discrepancy shown in Figure (5.15) for the second half of the period of half-submerged cylinder has taken place when the wave is falling below the cylinder (Figure 5.14.a), where the number of water particle interactions is less.

In Figure (5.15), for a smaller wave amplitude ($a/D = 0.2$ and $d^{/}/D = -0.2$) the results for vertical force are noisy when using a coarse resolution. However, the results for a finer resolution ($\triangle$=0.01m) demonstrate the convergence of wave loading on a submerged cylinder using uniform mass distribution of particles (Figure 5.16), which is also demonstrated for the variable mass distribution in Figure (5.17).

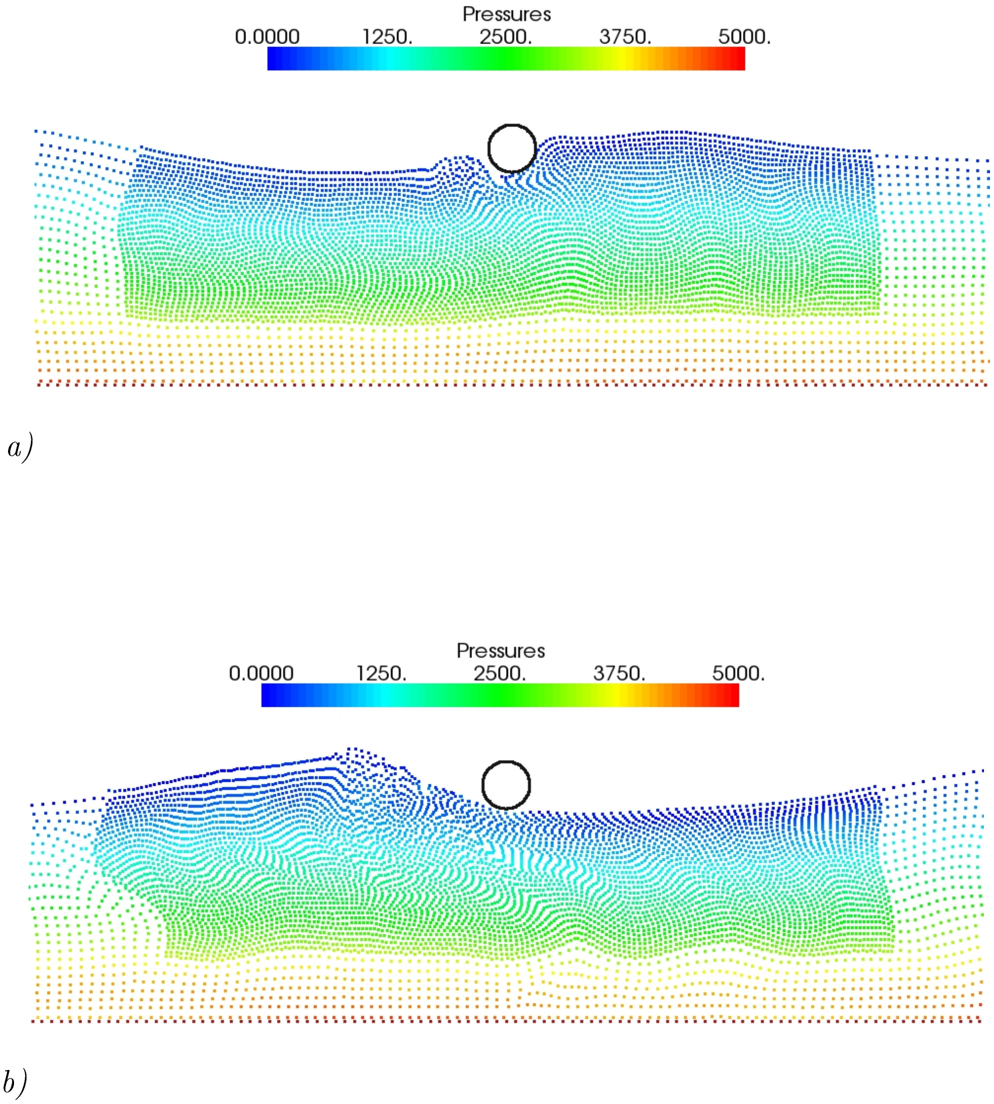

Figure 5.14: Particles for half submerged cylinder with relative amplitude of 0.5 at *a*) t=5s, *b*) t=7.5s) using variable mass distribution of particles

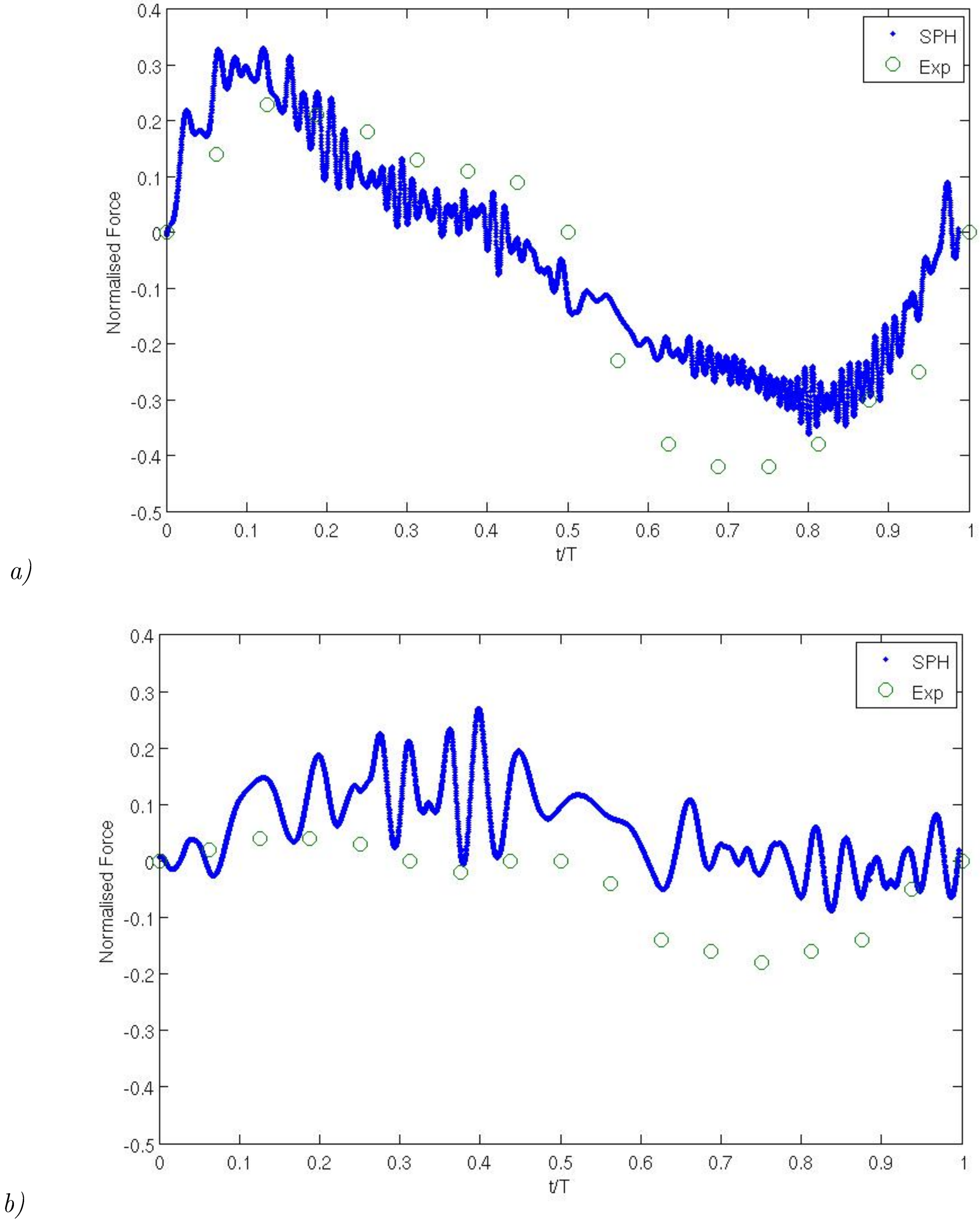

Figure 5.15: Normalised vertical forces on fixed cylinder using coarse and uniform resolution ($\triangle$=0.02m) for *a*) $a/D = 0$ and $d^{/}/D = 0.5$ *b*) $a/D = 0.2$ and $d^{/}/D = -0.3$

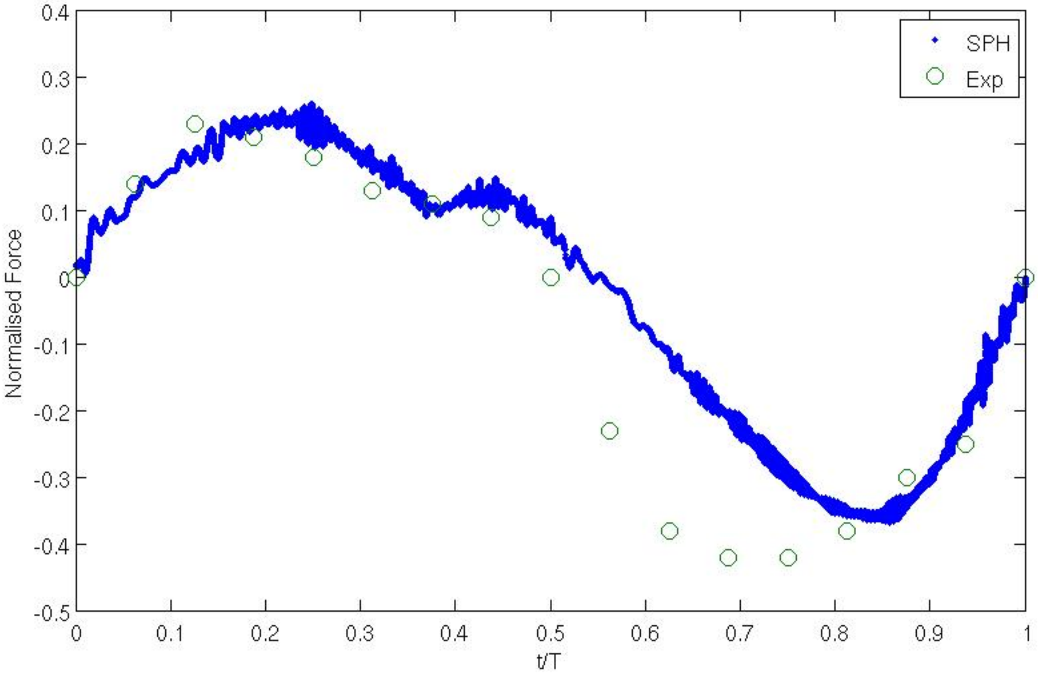

a)

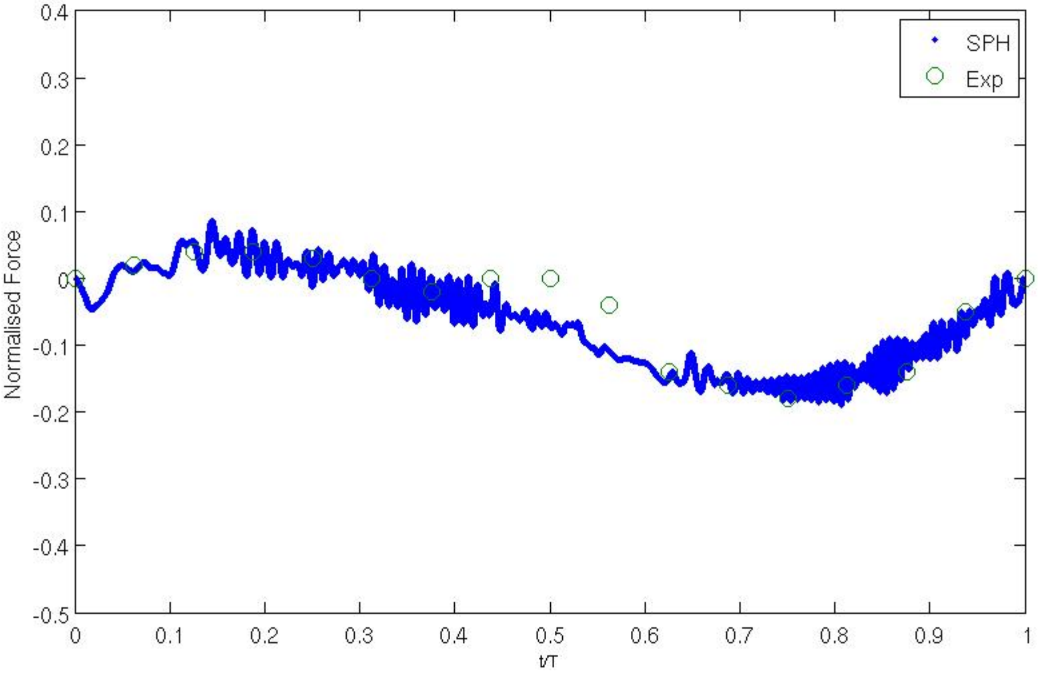

b)

Figure 5.16: Normalised vertical forces on fixed cylinder using fine and uniform resolution ($\triangle$=0.01m) for *a)* $a/D = 0.5$ and $d^{/}/D = 0$, *b)* $a/D = 0.2$ and $d^{/}/D = -0.3$

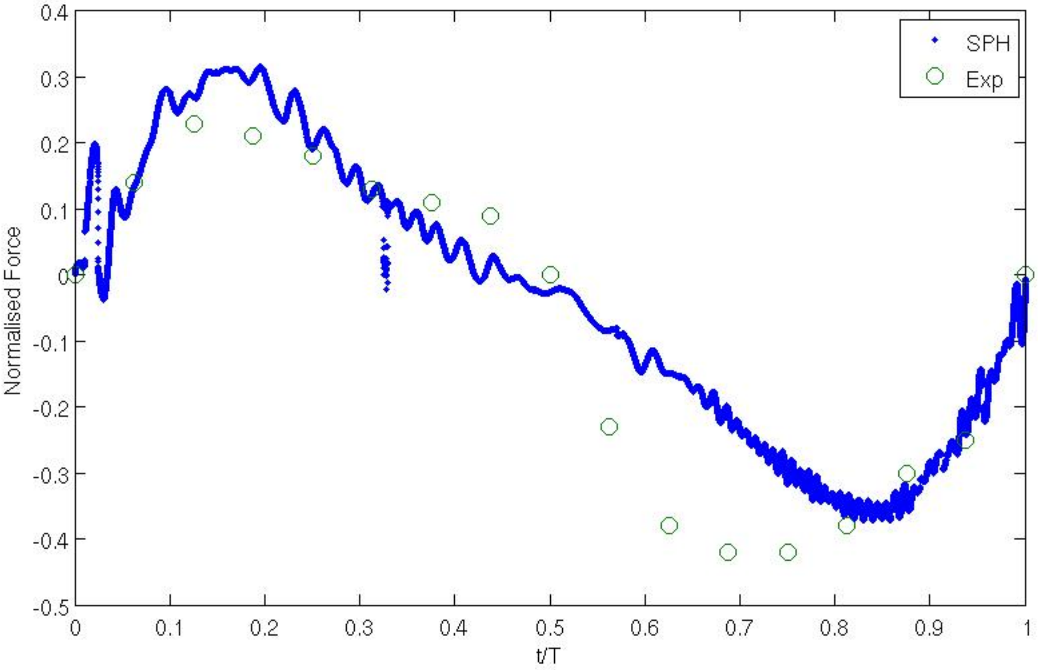

a)

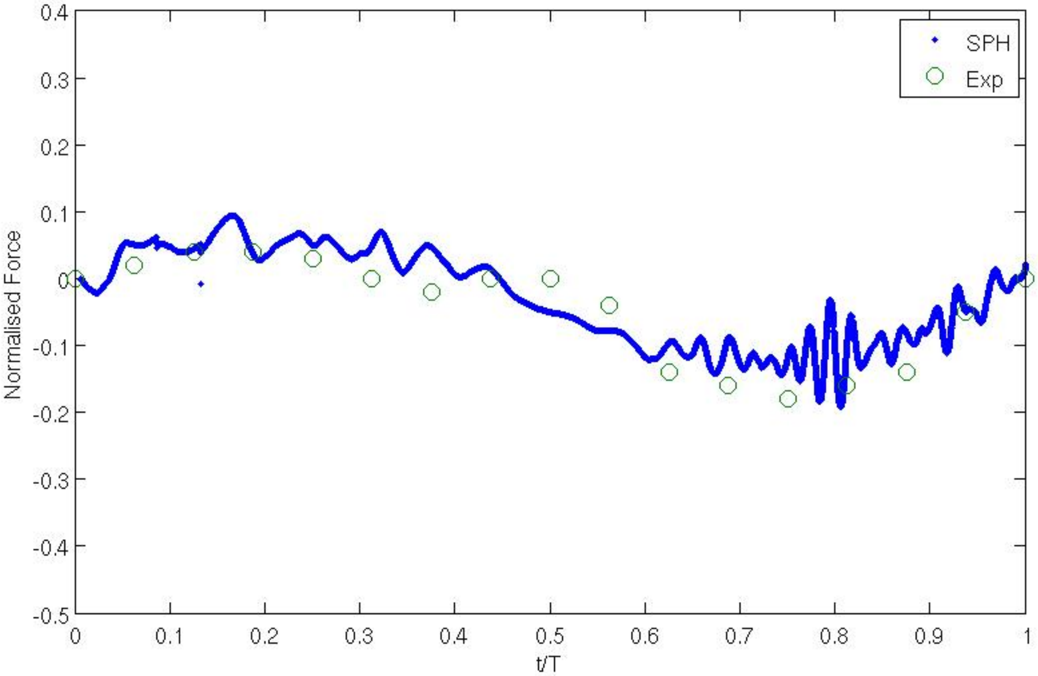

b)

Figure 5.17: Normalised vertical forces on fixed cylinder using variable particle mass distribution ($\triangle_{coarse}$=0.02m) for *a)* $a/D = 0.5$ and $d^/ /D = 0$, *b)* $a/D = 0.2$ and $d^/ /D = -0.3$

Numerical Model	Uniform coarse distribution of particles	Uniform fine distribution of particles	Variable mass Distribution of particles
Number of Particles	7800	30240	11900
CPU cost	15 hours	3 days	1 day

Table 5.1: Comparison of using different particle resolutions for wave loading on a half submerged and fixed cylinder

Table (5.1) demonstrates the CPU costs of different techniques on a single processor for wave loading on a half submerged and fixed cylinder, which proves the efficiency of using variable mass distribution, that is using the mixed mass achieves virtually comparable accuracy but with fewer particles and hence a reduced CPU cost of only 1 day.

5.6 Variable mass distribution of particles around the heaving cylinder

Here, the variable mass distribution is employed to the heaving cylinder test case described in Section (4.9), where the cylinder with a diameter of D=0.15m is located in channel in 12m length and 0.58m depth (Figure 4.22). The cylinder is initially set to be half submerged in still water and starts oscillating in the vertical direction to generate waves with small amplitude towards the boundaries. The waves are then absorbed by the sponge layers at the boundaries. The initial particle spacing is $\triangle$=0.02m.

The area of particles with lighter mass is chosen similar to Figure (5.13) in the previous section, where high resolution is desirable.

Figures (5.18.*a)* and (5.18.*b)* show the case of the heaving cylinder at two different times for the cylinder with the stroke of 1.23cm and a period of 0.76s, where the area of lighter-mass particles is located in the vicinity of the cylinder, which is important for studying the flow pattern around the cylinder. The zoomed figures of the problem are shown in Figure (5.19).

A comparison between the surface profiles for the analytical solution and the combined mass SPH approach for two sample wave periods are shown in Figure (5.20)

Numerical Model	Uniform coarse distribution of particles	Uniform fine distribution of particles	Variable mass Distribution of particles
Number of Particles	18500	71000	22300
SPH R_A	0.58	0.54	0.53
CPU cost	2days	5days	2days and 15 hours

Table 5.2: Comparison of using different particle resolutions for the wave period of 0.76s and the cylinder stroke of 1.23cm

and Figure (5.21). The comparison of SPH and analytical surface profile confirms that using variable mass distribution does not affect the form of the free-surface profile.

Here, for instance, a heaving cylinder with the stroke of 1.23cm and a period of 0.76s, the amplitude ratio of Equation (4.14) (see Section 4.9) can be calculated as $R_{A,SPH} = 0.53$ which also gives us a satisfactory result in comparison with the experimental data of $R_{A,Exp} = 0.543$. The number of particles used in this case was 22300 compared to the 18500 particles used for the uniform coarse resolution results shown in Figure (4.23) which gave $R_{A,SPH} = 0.58$. With a uniformly fine resolution (not shown here), 71000 particles are required needing 5 days of CPU time on a single processor giving $R_{A,SPH} = 0.54$. Using a single-CPU machine, the computation time for the variable mass distribution case was only 2 days and 15 hours for the extra resolution compared to 2 days with the coarse distribution. Therefore, the scheme offers a computational advantage and is hence a more efficient technique to model the wave propagation from the cylinder. Figure (5.22) demonstrates the convergence of the variable mass distribution of particles, where

$$Error = \frac{\mid R_{A,SPH} - R_{A,Exp} \mid}{R_{A,Exp}} \tag{5.4}$$

The results for different techniques are summarised in Table (5.2) for a heaving cylinder with the stroke of 1.23cm and a period of 0.76s.

The comparisons of SPH wave amplitude between uniform coarse and fine distribution of particles and variable mass distribution of particles for different wave periods and cylinder strokes are shown in Table (5.3), which demonstrates satisfactory agreement. Generally, the finer resolution results are in better agreement than the coarse

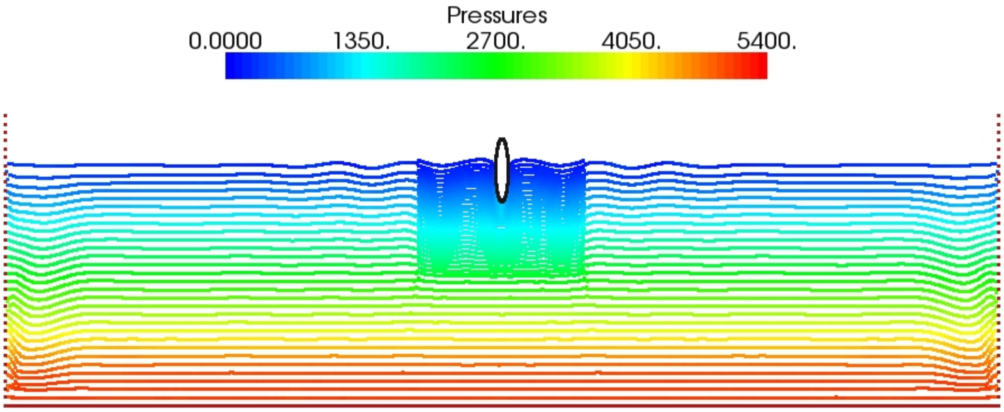

a)

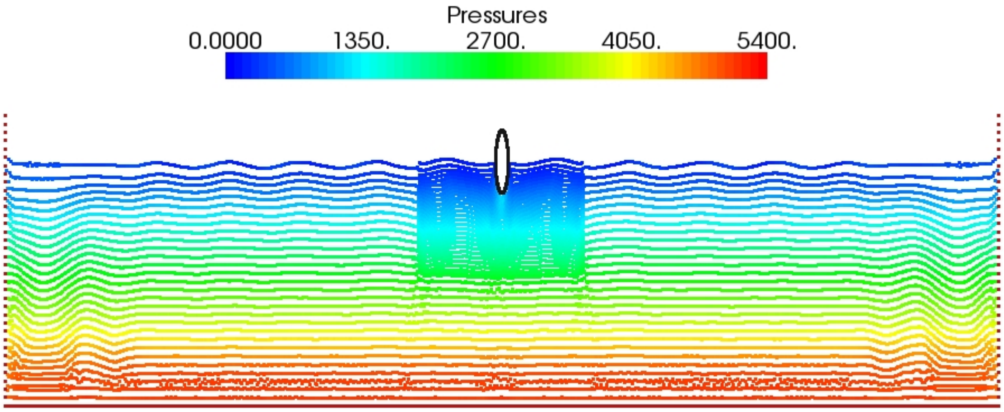

b)

Figure 5.18: Pressure distributions for a heaving cylinder with the stroke of 1.23cm and a period of 0.76s at *a)* t=5s, *b)* t=10s. Note distorted scale

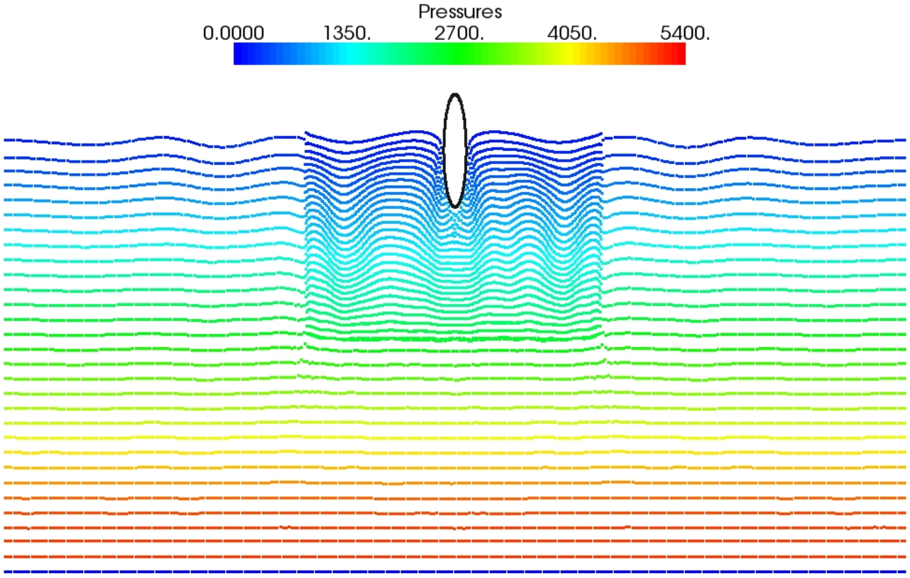

a)

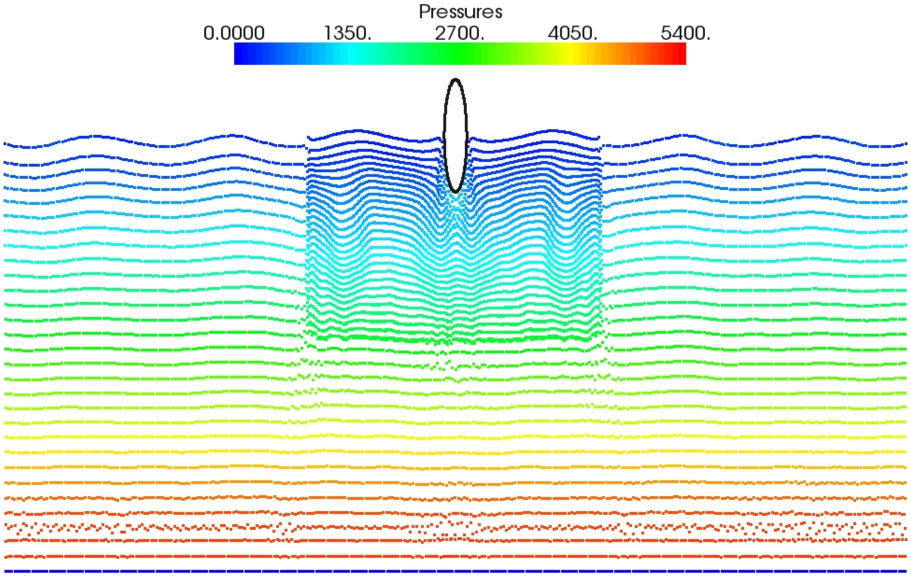

b)

Figure 5.19: Pressure distributions for a heaving cylinder with the stroke of 1.23cm and a period of 0.76s at *a)* t=5s, *b)* t=10s. Note distorted scale

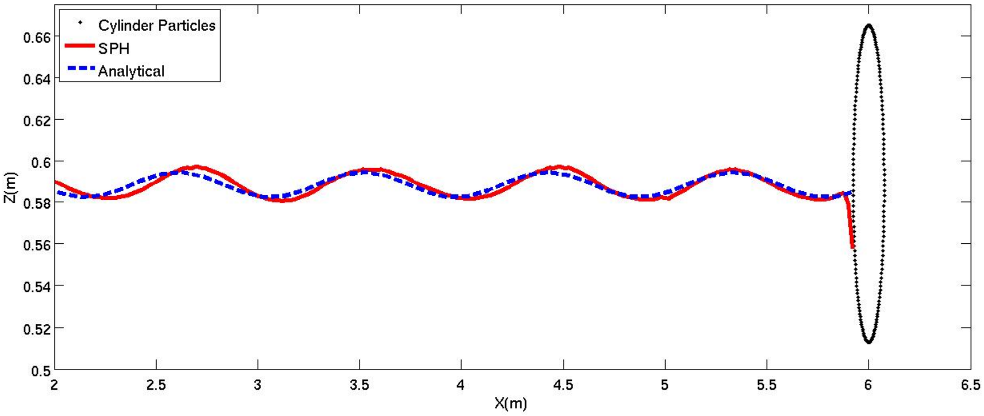

Figure 5.20: Comparison of surface profile between analytical and SPH results for a heaving cylinder with the stroke of 1.23cm and a period of 0.76s at t=10s. Note distorted scale

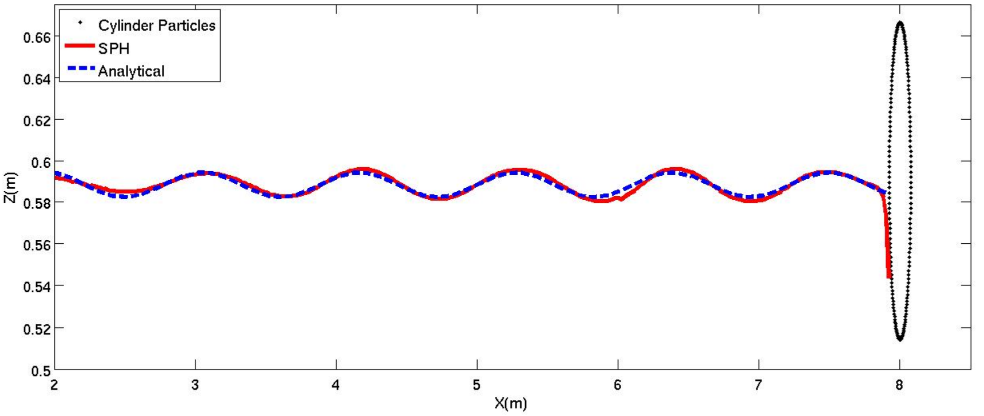

Figure 5.21: Comparison of surface profile between analytical and SPH results for a heaving cylinder with the stroke of 1.23cm and a period of 0.84 at t=10s. Note distorted scale

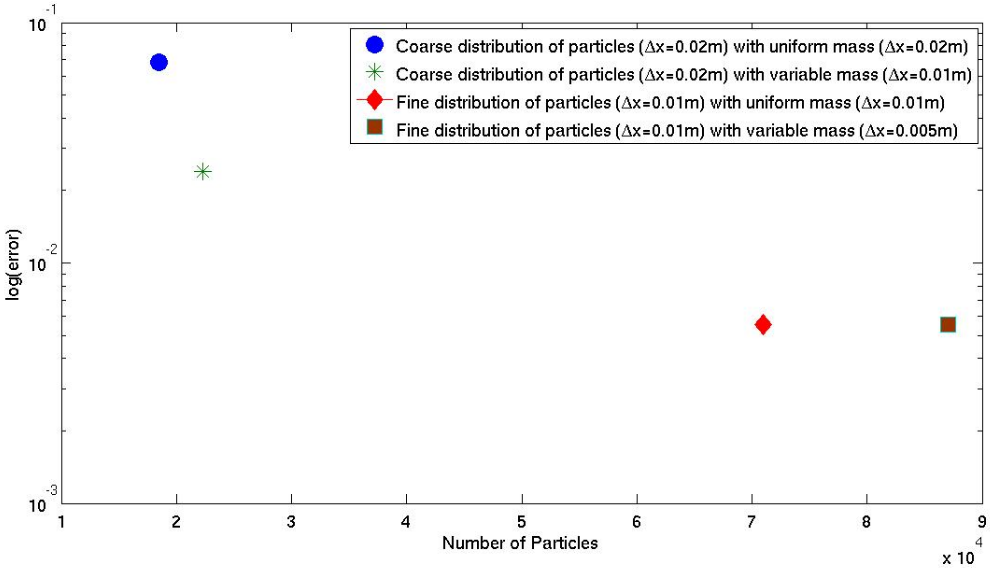

Figure 5.22: Convergence test of a heaving cylinder with the stroke of 1.23cm and a period of 0.76s at t=10s, for the coarse resolution $\triangle$=0.02m and for the fine resolution $\triangle$=0.01m using different mass ratio

resolution as expected, but using variable mass gives a significant improvement in the coarse results but without the computational expense of the finer resolution.

Table (5.4) indicates the comparisons between the theoretical and numerical force coefficient σ_F (defined as the ratio between the maximum vertical force over the product of the maximum acceleration and cylinder mass) for different numerical runs, which are in promising agreement. It shows that using a coarse distribution of particles overestimates the force coefficient. However, if the variable mass distribution of particles is used around the heaving cylinder the results improve. That is due to the larger number of particles used around the cylinder in comparison with uniform coarse distribution of particles. The table also demonstrates the sensitivity of the values to the β-limiter of Equation (3.112) explained in Chapter 3 for different test cases. For instance, the value of the β-limiter (e.g. for the heaving cylinder problem with the stroke of 1.23cm and a period of 0.76s) was chosen as 1.5 for the uniform coarse particle distribution and variable mass distribution of particles. A β-limiter of 1.3 was found to be the best choice for a uniform fine particle distribution. In general, the value of β in the limiter is well known to affect numerical results (for example see Hirsch, 1998), where $\beta = 1$ gives the Minmod limiter which is known to give diffusive results while $\beta = 2$ gives the Superbee limiter which can give unphysically sharp profiles. Previous work in the context of Riemann solvers for the shallow

Cylinder stroke (cm)	Wave Period T(s)	Experimental R_A	Uniform coarse distribution of particles R_A	Uniform fine distribution of particles R_A	Variable particle mass R_A
1.23	0.69	0.610	0.63	0.60	0.62
1.23	0.76	0.543	0.58	0.54	0.53
1.23	0.84	0.514	0.49	0.51	0.52
1.23	0.93	0.451	0.42	0.44	0.43
0.91	0.50	0.810	0.87	0.83	0.84
0.93	0.45	0.852	0.89	0.84	0.82

Table 5.3: Comparison of SPH wave amplitude between uniform distribution of particles and variable mass distribution of particles for different wave periods and cylinder strokes

water equations using a finite volume scheme (for example see Rogers, 2001) has shown similar behaviour where for standing waves in a basin, too small a value of $\beta(\approx 1)$ can lead to decay of free-surface waves, while too large a value $\beta(\approx 1.5)$ can lead to the unphysical behaviour of the wave amplitude increasing with time. Table (5.4) demonstrates that while the results are in reasonable agreement, the results are quite sensitive to the chosen value of β, and that a future improvement would be to identify a suitable alternative to the β-limiter.

Cylinder stroke (cm)	Wave Period T(s)	Theoretical σ_F	Uniform coarse distribution of particles		Uniform fine distribution of particles		Variable mass distribution of particles	
			σ_F	β	σ_F	β	σ_F	β
1.23	0.69	0.58	0.72	1.50	0.65	1.30	0.63	1.50
1.23	0.76	0.59	0.75	1.50	0.68	1.30	0.65	1.50
1.23	0.84	0.61	0.78	1.40	0.73	1.15	0.66	1.40
1.23	0.93	0.63	0.79	1.40	0.71	1.15	0.66	1.40
0.91	0.50	0.72	0.95	1.40	0.91	1.20	0.83	1.43
0.93	0.45	0.70	0.95	1.50	0.92	1.30	0.81	1.55

Table 5.4: Comparison between the theoretical and numerical force coefficient σ_F using different particle resolutions, different wave periods and cylinder strokes

5.7 Summary

In this chapter, variable particle mass distribution was introduced in order to reduce computer time. It was shown that how fine resolution around the body and coarse resolution further away can be used to improve accuracy, while maintaining a uniform kernel size. Variable particle mass distribution avoids the conservation issues with particle refinement suggested by Feldman and Bonet (2007) and dealing with time and space by using variable smoothing length. The method was tested in still water, showing hydrostatic pressure, for different mass ratio where a mass ratio of 1:4 proved effective but increasing to 1:16 caused particle clumping and instability.

The results for variable mass around cylinder in regular waves also showed good agreement for the force history in comparison with the experimental data.

Variable mass distribution of particles was tested for the heaving cylinder problem showing that converged solutions could be obtained with much lower computational costs than with particles of uniform mass. We also show that how the results can be sensitive to the chosen value of β-limiter.

Chapter 6

Surface waves generated by an Oscillating 2-D wedge and 3-D cone

6.1 Introduction

For simulation of wave energy devices, first it is important to be able to calculate the forces on a moving body and the surface elevations around it correctly. In this chapter the SPH method is used to investigate waves generated by a bobbing 2-D wedge and 3-D cone. This will include a summary of the experimental data provided by Drake *et al.* (2009) followed by the simulations of an oscillating 2-D wedge, initially set in still water using two forms of boundary conditions described in Section (3.6): repulsive boundary condition (Monaghan and Kos, 1999 and Rogers *et al.*, 2008) and particle boundary force (Kajtar and Monaghan, 2009). Then, the force comparison between the SPH results and experimental data for 3-D heaving cone will be shown. The use of variable particle size will be shown for 3-D heaving cone, which is used in a pre-selected area and avoids the need for particle refinement.

6.2 Numerical setup

The SPH-ALE formulation (Vila, 1999) are used for all the simulations in this chapter with the cubic kernel function (Monaghan, 1992) and symplectic time stepping method (Leimkuhler *et al.*, 1997 and Monaghan, 2005). Two forms of repulsive boundary condition (Monaghan and Kos, 1999 and Rogers *et al.*, 2008) and particle boundary force (Kajtar and Monaghan, 2009) are also used to simulate the 2-D bobbing wedge. For the 3-D bobbing cone only repulsive boundary condition (Monaghan and Kos, 1999 and Rogers *et al.*, 2008) will be used as it will be shown that the force of Kajtar and Monaghan (2009) produces noisy results. All the formulations are fully described in Chapter 3.

6.3 Experimental data

In this work, we use the experimental data of Drake *et al.* (2009) in order to validate our SPH results. Drake *et al.* (2009) experimentally investigated the motion of a cone, which is forced to oscillate vertically in still water in a wave tank, and compared the results for force and surface elevation with linear and non-linear theory. The cone was located centrally in the tank with a depth of 1.01m. The cone draught was 148 mm, equal to the waterline radius in the case of a right circular cone. The vertical motion of the cone $z(t)$ followed the form of a Gaussian wave packet defined by:

$$z(t) = A \sum_{n=1}^{N} Z(\sigma_n) \cos\left[\sigma_n (t - t_0)\right] \triangle\sigma_n, \tag{6.1}$$

where

$$Z(\omega_n) = \frac{1}{\varsigma\sqrt{2\pi}} \exp\left[-(\sigma_n - \sigma_0)^2 / 2\varsigma^2\right], \tag{6.2}$$

$\varsigma = \sigma_0/2\pi$, $\triangle\sigma_n = 2\sigma_0/N$, central circular frequency $\sigma_n = n\triangle\sigma_n$, A is the largest excursion from the still water level, σ_0 denotes the central frequency of the Gaussian wave packet in rad/s, were given by $\kappa\pi/3$. For our SPH simulation A is chosen to be $+50$mm, the number of frequency components N is 50, and κ is 3, 7 and 9. In accordance with the suggestion of Drake *et al.* (2009), the force results are compared with the experimental data in non-dimensional form as $F/\rho g \pi R^2 A$ where F is the time varying component of the vertical fluid force, ρ is the density of fresh water, g is the acceleration due to gravity, R is the cone radius at the waterline (equal to the draught for a right circular cone). Time is expressed in non-dimensional form by dividing through by the period that corresponds with the central frequency of the wave packet. For example for $\kappa = 3$ the central frequency and corresponding period

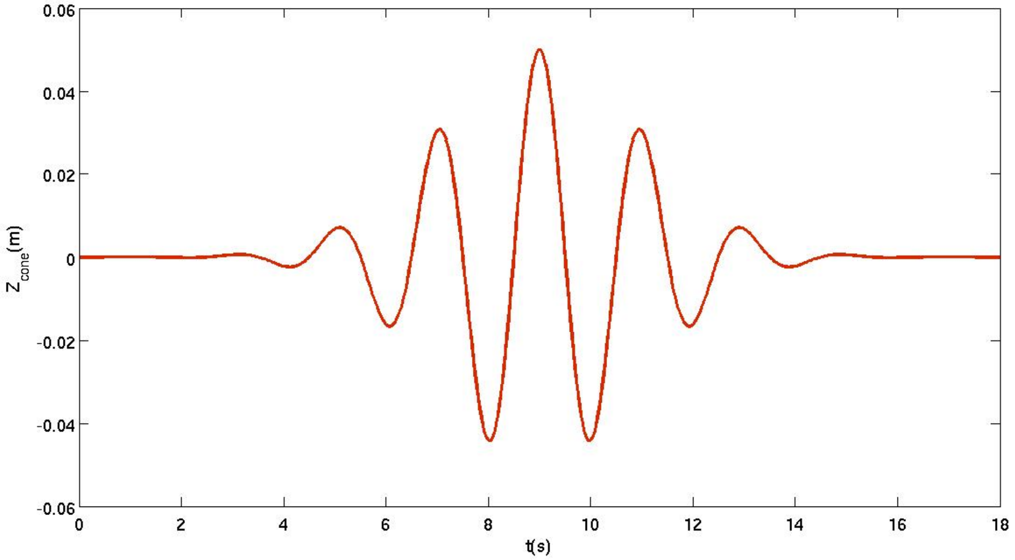

Figure 6.1: Vertical motion of the cone vs time according to Equation (6.1) when $\kappa = 3$ and $A = 0.05m$

are calculated as πHz and 2s, respectively. Figure (6.1) displays the motion of the cone where $\kappa = 3$.

6.4 2-D Heaving wedge

The 2-D numerical domain is shown in Figure (6.2) where waves are generated by a wedge, bobbing according to Equation (6.1) and initially set to have a zero velocity, at the centre of the channel of length 4m and depth 1m, and propagate towards both ends of the channel. Waves are absorbed by sponge layers of length 0.8m at the boundaries implemented as before by changing the order of the Riemann solver approximation from second to first by gradually decreasing the value of the β-limiter in Equation (3.112), i.e. from $\beta =$local value to $\beta = 0$. The initial particle spacing is $\triangle = 0.02$m. Figure (6.3) displays the initial distribution of particles.

6.4.1 Results using repulsive boundary condition

Figure (6.4) shows the pressure for 2-D heaving wedge using the repulsive boundary condition as described in Section (3.6.1), at (a) t=2s, (b) t=3.5s, where κ and A

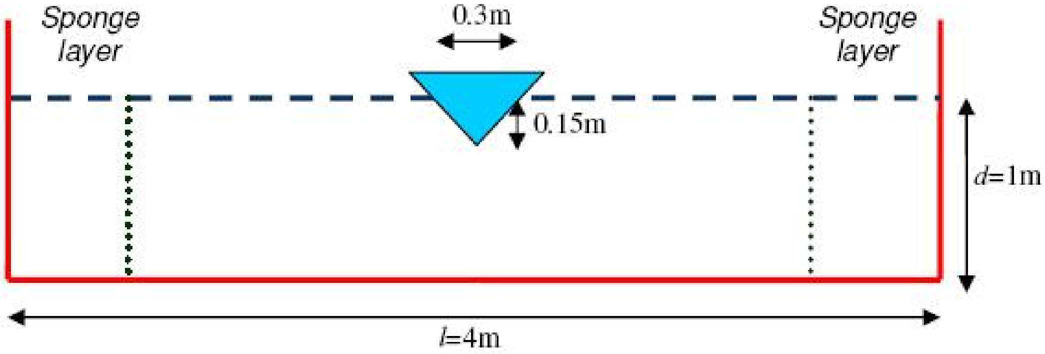

Figure 6.2: Schematic of surface wave generated by a heaving cone

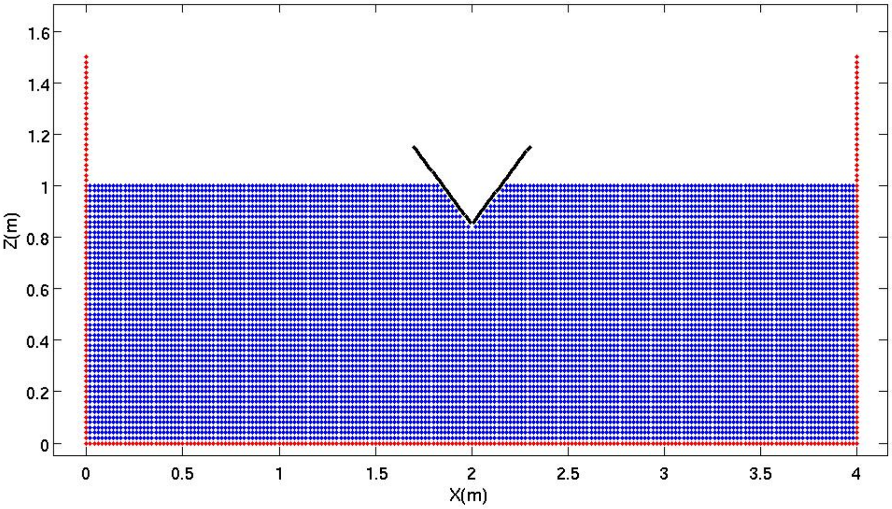

Figure 6.3: Initial particle distribution for 2-D bobbing wedge, $\triangle = 0.02$m

used in Equation (6.1) are chosen to be 9 and +0.05m, respectively. The waves, generated by the Gaussian wave packet motion of the wedge, are clearly seen to propagate towards the walls and be absorbed at the boundary. Figures (6.5) and (6.6) display force comparison between the SPH results and experimental data for 2-D wedge, shifted backward by 2.3s in order to have the maximum excursion at t=0 for two initial particle spacing. The agreement is in a good agreement in magnitude and phase. This simulation takes about one day on single CPU.

6.4.2 Results using particle boundary force

The pressure configurations for two sample times are shown in Figure (6.7) using the particle boundary force of Kajtar and Monaghan (2009) for the wedge particles as described in Section (3.6.2). Similar to the previous case, waves are generated by the heaving wedge and absorbed by the sponge layers at the boundaries. However, there is a particle separation of almost $2\triangle$ from the wedge, which is also shown by Kajtar and Monaghan (2009) . This can be due to the initial force exerted by the wedge particles on the fluid particles, although a normalisation factor of $W(0) = 1.8$ was used and a damping was produced in Equation (3.133) for the first 2500 time step, in order to reach the equilibrium in the similar way to that suggested by Kajtar and Monaghan (2009). The inconsistency is also shown in the force comparison (Figure 6.8 and Figure 6.9) between the SPH results and experiment where the SPH force has some noise, especially when the fluid particles are in rest (a similar problem is seen for the fixed cone in still water). Moreover, since the boundary force needs a normalisation to keep the fluid particles with the distance from the boundary approximately equal to the initial particle spacing, the force on the wedge is oscillatory for the beginning of the simulation (see Kajtar and Monaghan, 2009). It is found that in order to reduce the oscillation in force history, there is a need to give a high viscosity to the simulation, e.g. changing the value of β-limiter to be 0 for the whole simulation, which causes almost complete dissipation of waves in the results.

Figures (6.10) and (6.11) demonstrate the surface profiles for both implementations of particle boundary force and repulsive boundary condition at two sample times. The particle boundary force seems to produce a phase change in the surface profile. This discrepancy is probably due to the unphysical and exaggerated force exerted by the wedge particles on the fluid.

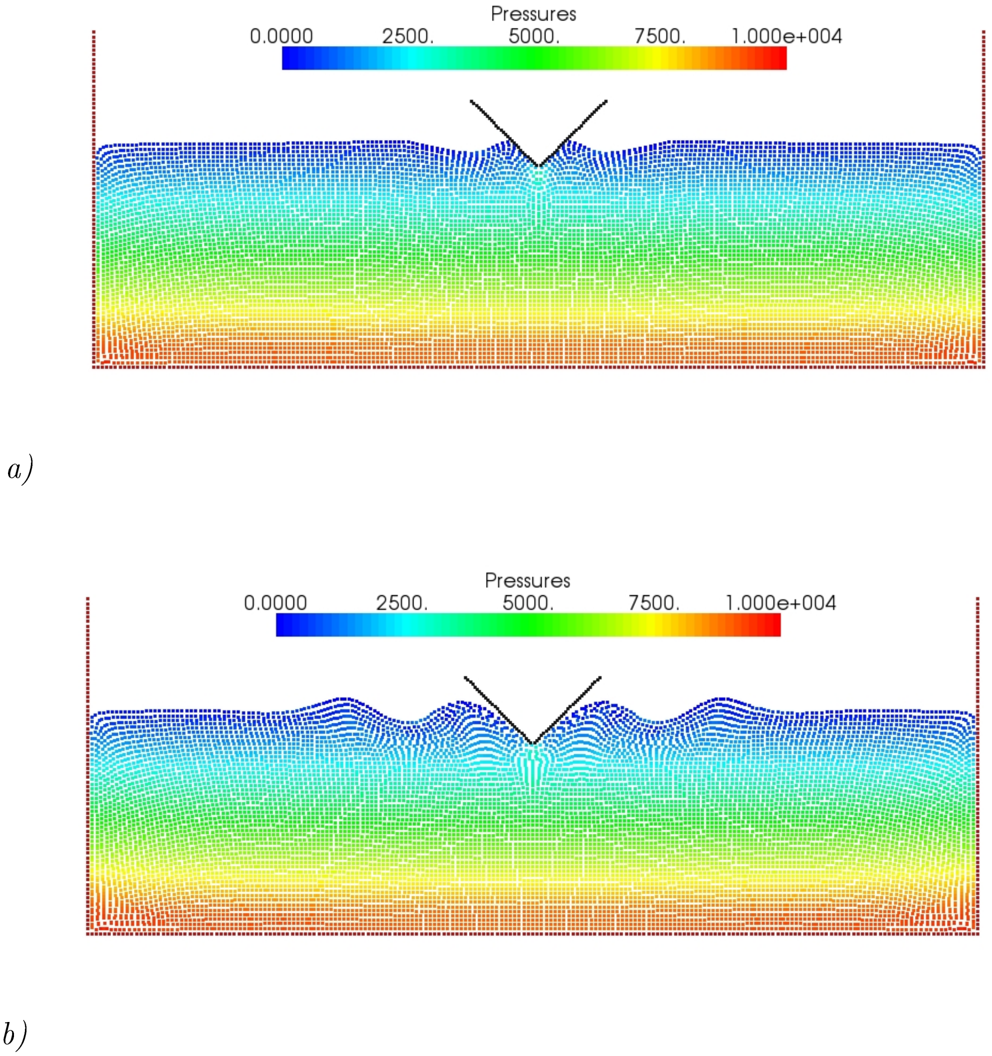

Figure 6.4: Pressure for 2-D bobbing wedge with the central period of 0.66s at *a)* t=2s, *b)* t=3.5s using repulsive boundary condition, $\triangle = 0.02$m

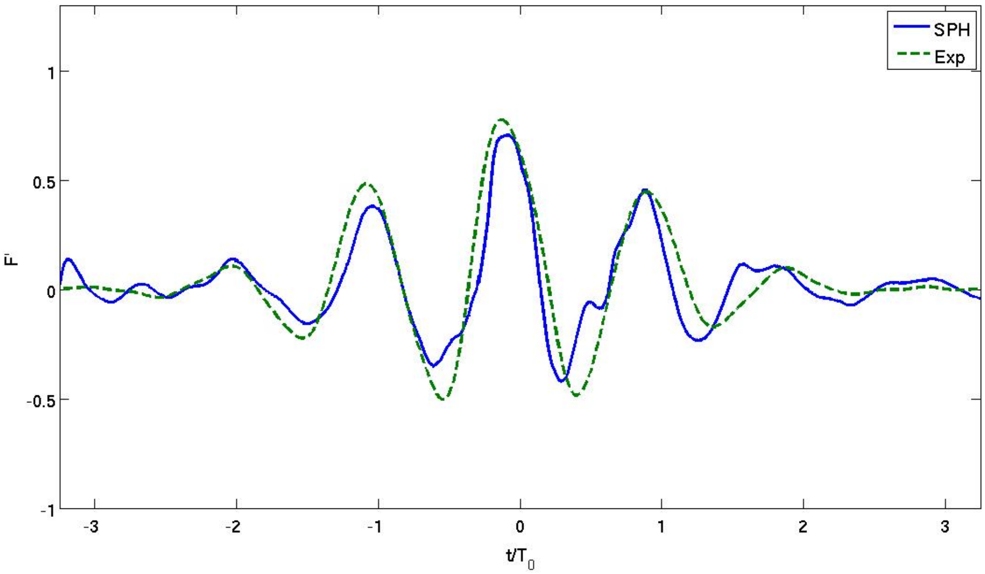

Figure 6.5: Force comparison between the SPH results and experimental data for 2-D wedge using repulsive boundary condition, $\triangle = 0.02$m

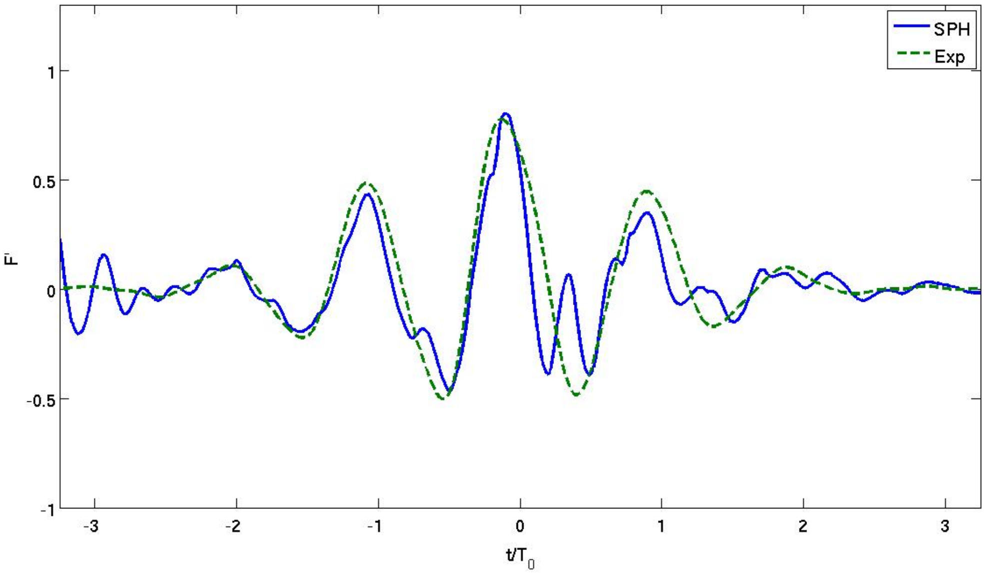

Figure 6.6: Force comparison between the SPH results and experimental data for 2-D wedge using repulsive boundary condition, $\triangle = 0.01$m

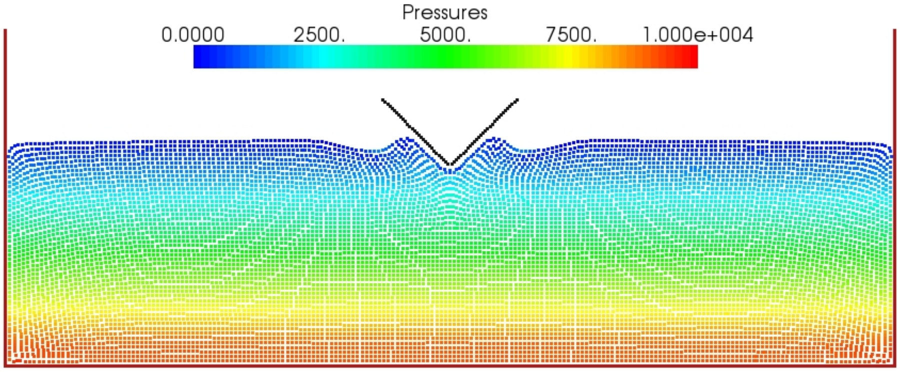

a)

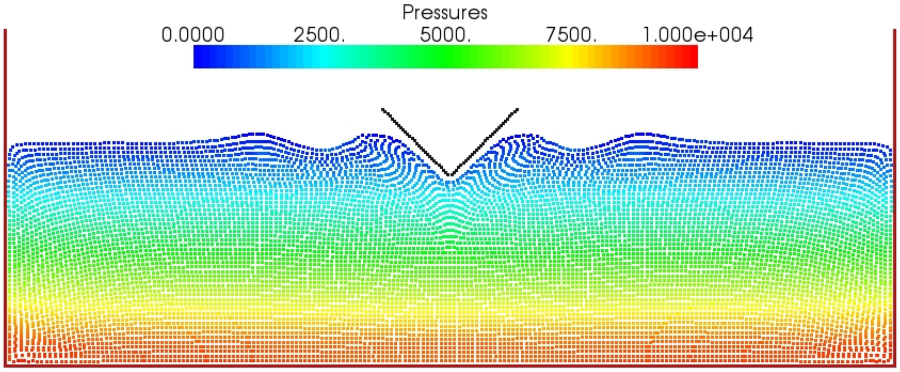

b)

Figure 6.7: Pressure for 2-D bobbing wedge with the central period of 0.66s at *a)* t=2s, *b)* t=3.5s using particle boundary force, $\triangle = 0.02$m

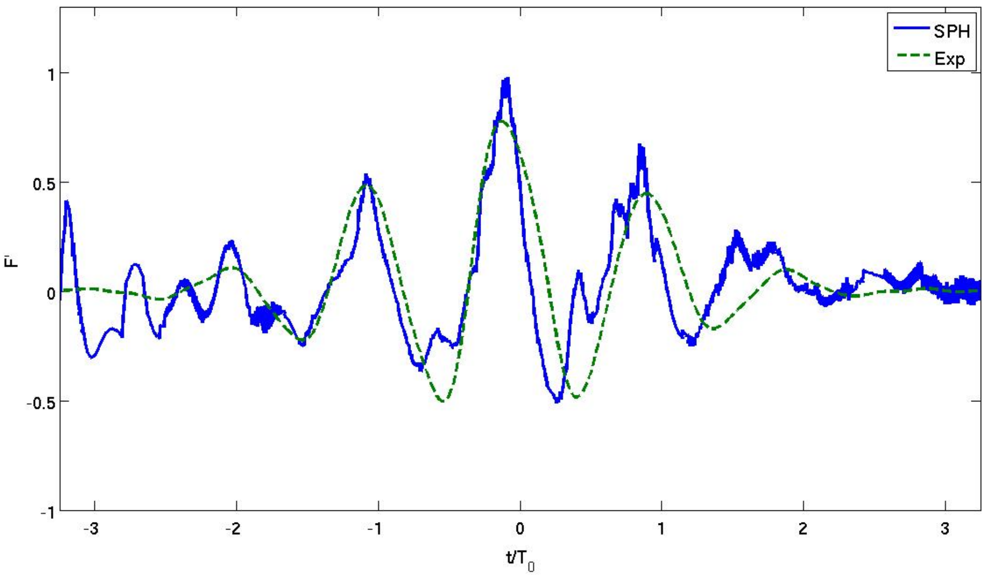

Figure 6.8: Force comparison between the SPH results and experimental data for 2-D wedge using particle boundary force of Monaghan & Kajtar (2009) , $\triangle = 0.02$m

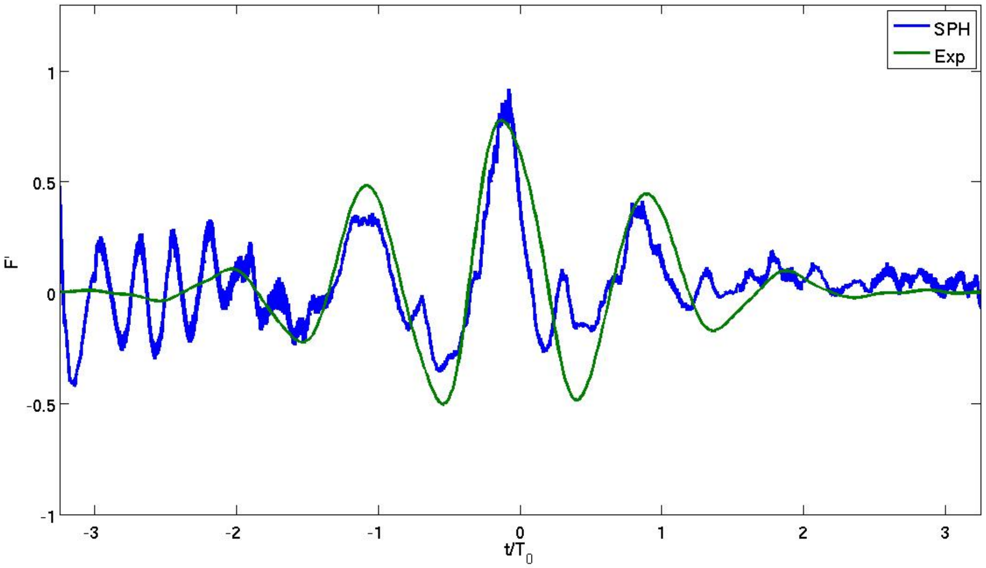

Figure 6.9: Force comparison between the SPH results and experimental data for 2-D wedge using particle boundary force of Monaghan & Kajtar (2009) , $\triangle = 0.01$m

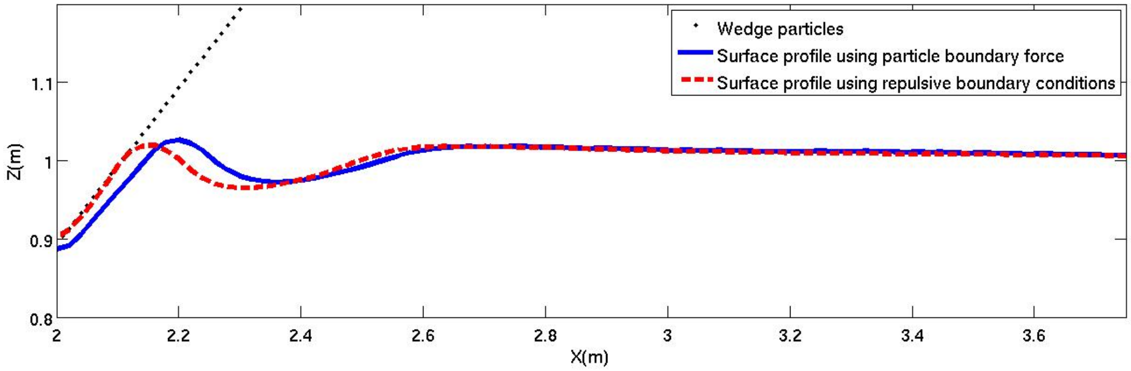

Figure 6.10: Surface profile comparisons using particle boundary force and repulsive boundary condition at t=2s

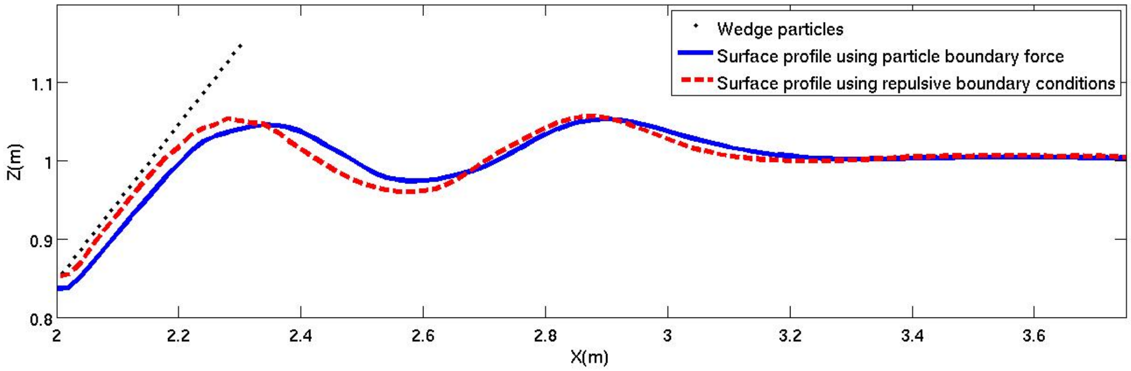

Figure 6.11: Surface profile comparisons using particle boundary force and repulsive boundary condition at t=3.5s

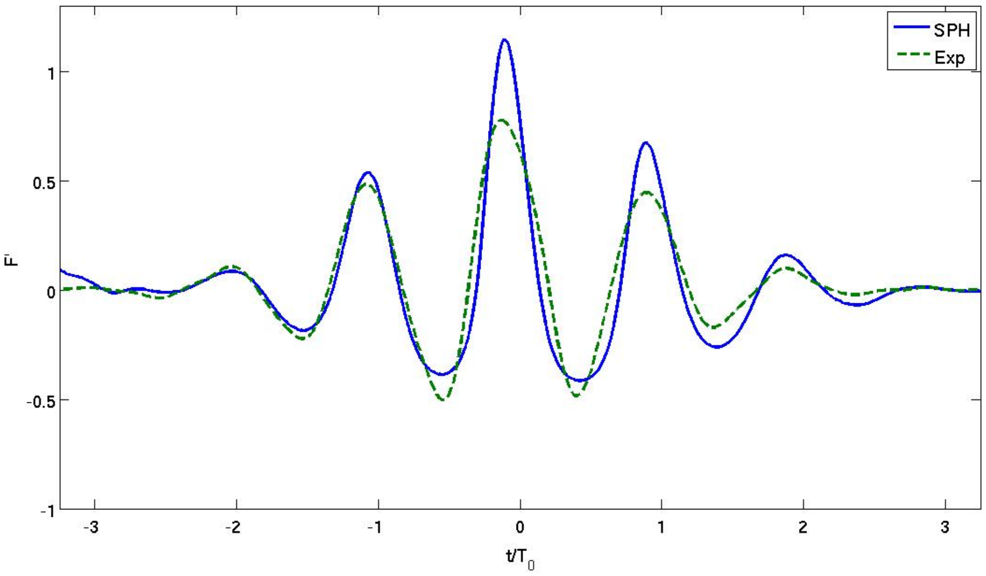

Figure 6.12: Force comparison between the SPH results and experimental data for 3-D cone using coarse resolution ($\triangle = 0.04$m), where $\kappa = 9$ and $A = 0.05m$

6.5 3-D bobbing cone with uniform particle mass distribution

The motion of a 3-D heaving cone is investigated here. The numerical simulation is conducted in a tank 4m in width and length, and 1m in depth. Waves generated by a bobbing cone, which is initially set to have zero velocity, at the centre of the tank propagate towards the boundaries are absorbed by the sponge layer of length 0.8m at the boundaries similar to the 2-D case. The cone draught is 0.15m and is equal to the waterline radius. Figure (6.12) shows the force comparison between the SPH results and experimental data where $\triangle = 0.04$m and with 270,000 particles. The results are in a good agreement in terms of the phase, however, there is an overestimation for peaks and underestimation for troughs. The overestimation of peaks can be solved using a finer resolution, $\triangle = 0.02$m with 2,080,000 particles but the troughs are still underestimated (Figure 6.13). This is possibly due to the compressibility of air which is not taken into account for our mono-phase simulations in addition to the problems with the boundary conditions. Moreover, numerical viscosity is likely to cause excessive damping in the SPH simulations. The simulations of the heaving cone with coarse ($\triangle = 0.04$m) and fine resolutions ($\triangle = 0.02$m) take 1.5 days and 12 days on 16 processors, respectively.

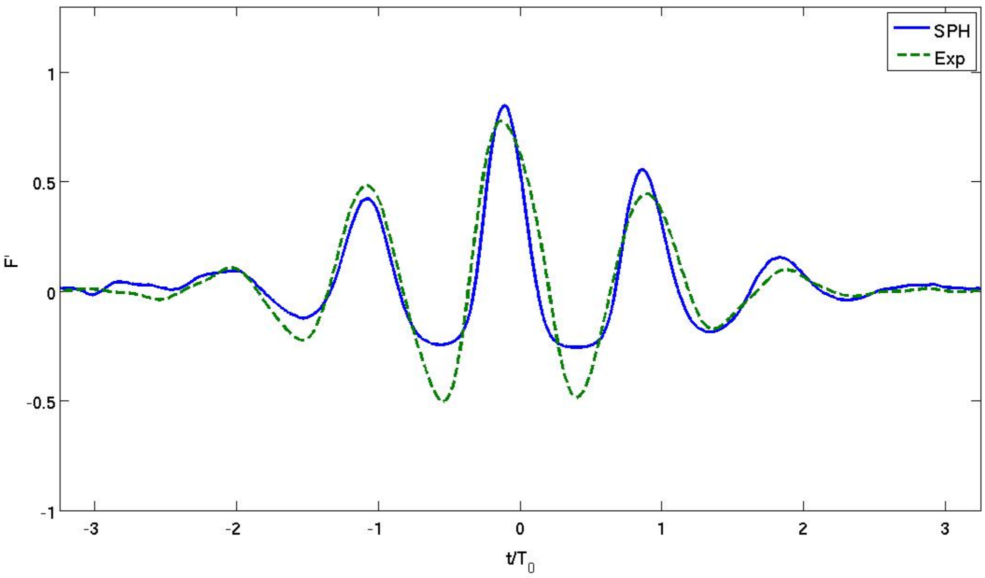

Figure 6.13: Force comparison between the SPH results and experimental data for 3-D cone using coarse resolution ($\triangle = 0.02$m), where $\kappa = 9$ and $A = 0.05m$

6.6 Variable particle mass distribution

To reduce the particle number and consequently the CPU cost, the use of pre-defined variable mass distribution was suggested in Chapter 5 where refined particles are used in a selected area (i.e. here around the cone). A particle with a mass of m is replaced typically with eight lighter ones with a mass $m/8$. In the original proposal for variable particle mass in Chapter 5, the value of the smoothing length was suggested to be constant in order to avoid the complexities of using variable smoothing length and particle refinement. However, for the 3-D simulations, it was found that, for example, using a constant smoothing length of $h = 1.3\triangle$ may lead to almost 400 interactions within the kernel support for the area where refined particles are used, which increases the CPU cost dramatically. Here, we use a different kernel size for different areas as

$$\widetilde{W}_{ij} = \frac{1}{2}\left(W_i + W_j\right) \tag{6.3}$$

where $W_i = W(r_{ij}, h_i)$ and $W_j = W(r_{ij}, h_j)$ (Monaghan, 1992), where the normalisation factor in the cubic kernel function is also chosen according to the kernel size.

Similar to the discussion in the previous chapter, first, it is essential to assess the

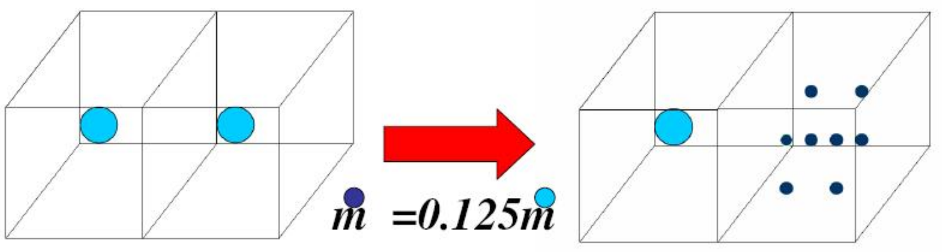

Figure 6.14: Replacing a particle with a mass m with four lighter ones with a mass $m/8$

prediction of still-water conditions in 2-D. Figures (6.15) to (6.17) display different plots of particles in still water, initially and after 10s, where the variable mass distribution of particles is used for different mass ratios in two dimensions.

Figure (6.15) shows the particle distribution where a mass ratio of 1:4 is used initially and after 10s. It is clear that the particles stay stable and symmetric to the vertical axis without any clumping and mixing. There is a movement for the smaller particles located at the interface of the regions where the smoothing length is varying.

The mass ratio of 1:16 is also employed, shown in Figure (6.16). In comparison with what shown for the same problem and constant smoothing length in the previous chapter, there is no clumping between the particles because the kernel size is not constant here. However, since the smoothing length is changed rapidly from h to $h/4$ at the interface of the lighter and heavier particles, there is a movement of particles at the interface.

Finally, employing the mass ratio of 1:4:16 with three different smoothing length (h, $h/2$, $h/4$), where the domain of interest is divided into three regions, is shown in Figure (6.17) for two sample times where the particle stay stable without any clumping and mixing. Moreover, gradual diminishing of the kernel size from one region to another causes the particle moving at the interfaces of regions similar to the previous problems.

As the result, employing variable particle mass with variable smoothing length is successfully applied to the still water for the mass ratio of 1:4, 1:16 and 1:4:16 while similar results are found for the mass ratio of 1:3 and 1:4:9. The CPU costs for the above problems, in comparison with what discussed in the previous chapter for constant smoothing length, is cheaper because the number of particle interactions in the kernels with different sizes are smaller than the kernels with uniform size.

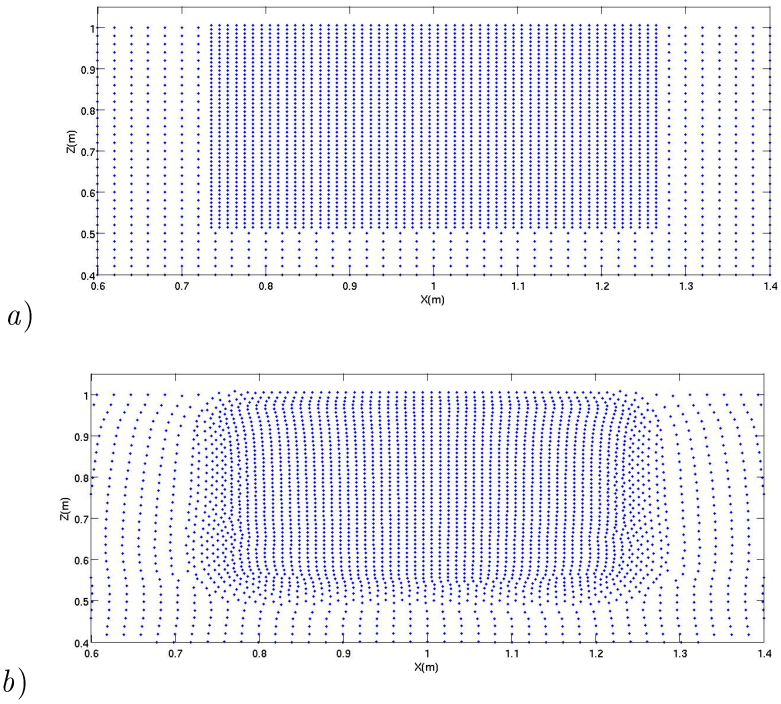

Figure 6.15: Particle distribution for still water problem for the mass ratio of 1:4 at *(a)* t=0 and *(b)* t=10s with the initial particle distance of 0.02m

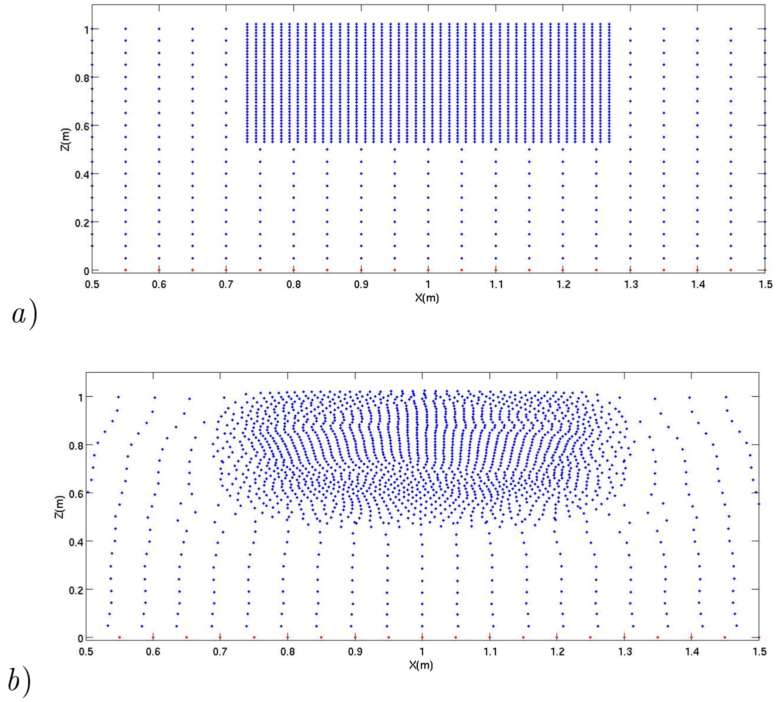

Figure 6.16: Particle distribution for still water problem for the mass ratio of 1:16 at (a) t=0 and (b) t=10s with the initial particle distance of 0.05m

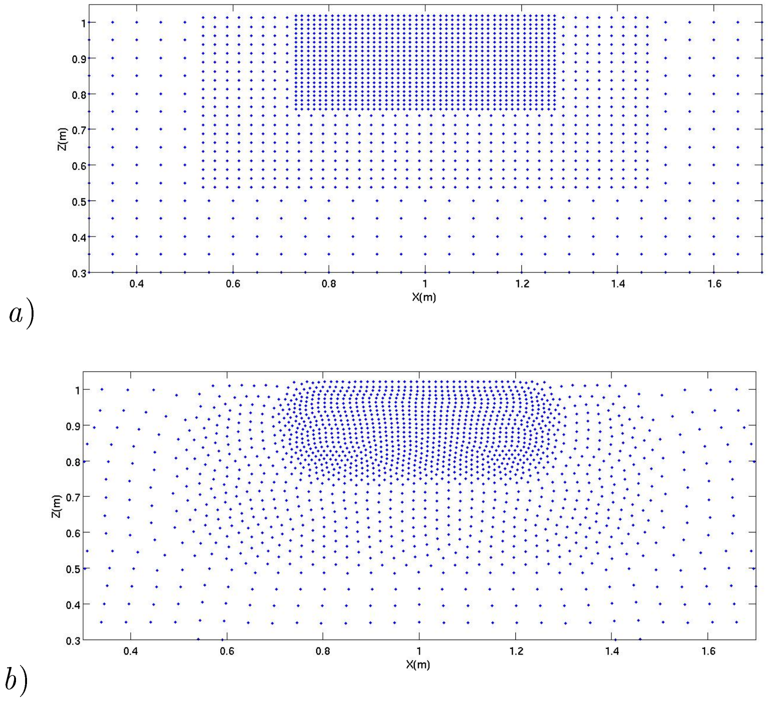

Figure 6.17: Particle distribution for still water problem for the mass ratio of 1:4:16 at (a) t=0 and (b) t=10s with the initial particle distance of 0.05m

6.7 3-D bobbing cone with variable particle mass distribution

Figure (6.18) shows a vertical slice of the problem at t=0 where a particle with mass m is replaced with eight smaller ones of mass $m/8$ an intermediate distance away from the cone and twenty seven lighter ones with the mass $m/27$ close to the cone as three nested regions. The area of lighter particles is chosen according the shape of the cone.

First, it is important to study the cone in still-water conditions before any investigation of dynamic problems. We choose the same numerical domain as the previous section but without the movement of the cone. Figure (6.19) demonstrates the variation of dimensionless vertical force on the cone minus the exact buoyancy force with time in still water using the variable mass distribution of particles. It is shown that the value of the vertical force for the first second is varying as particles reorganise themselves around the body.

Figure (6.20) shows a plot of the particles using mass ratio of 1:8:27 in the compu-

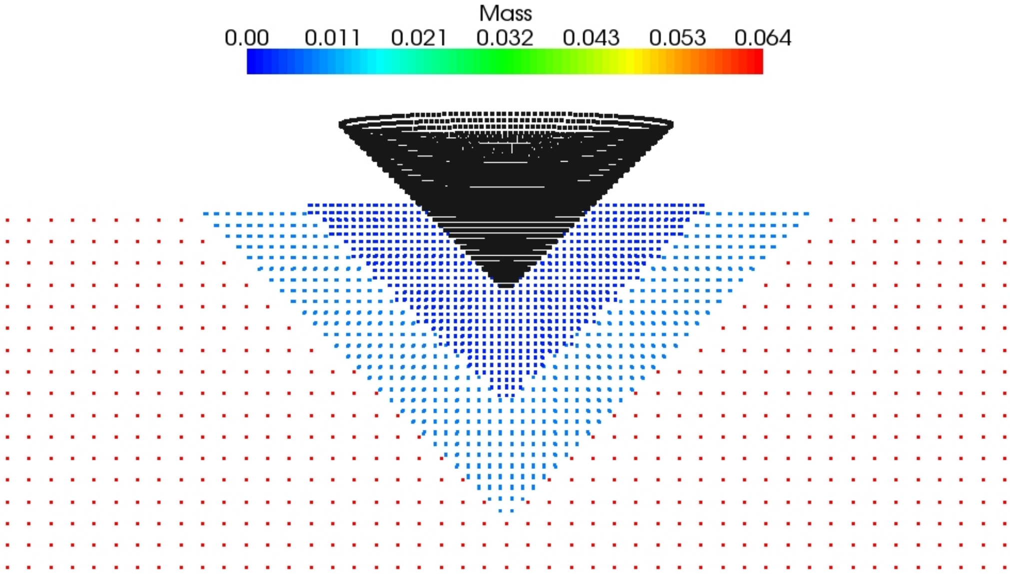

Figure 6.18: Replacing a particle with a mass m with lighter ones with masses $m/8$ and $m/27$ for heaving cone at t=0

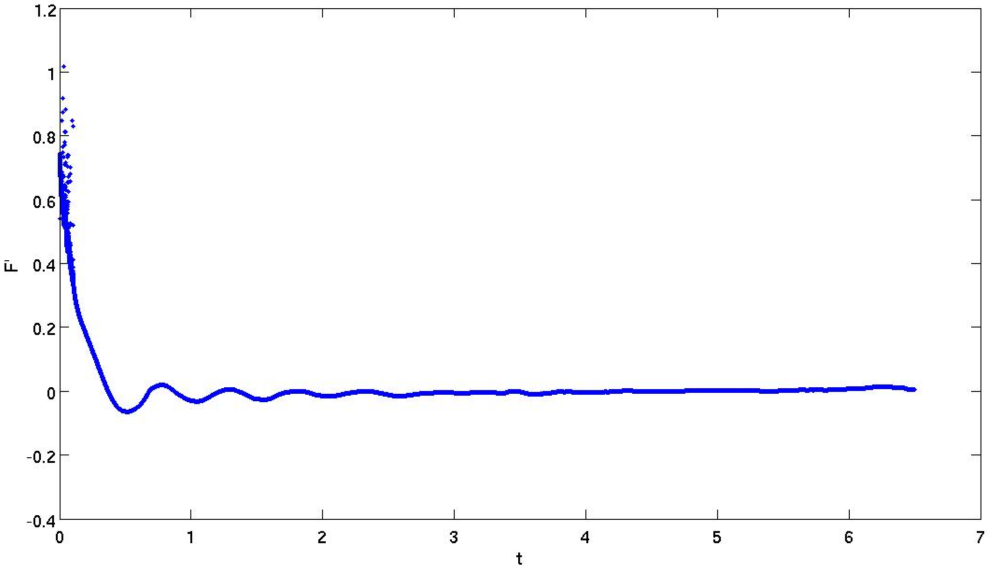

Figure 6.19: SPH Force on the cone in still water using variable mass distribution of particles ($\triangle = 0.04$m)

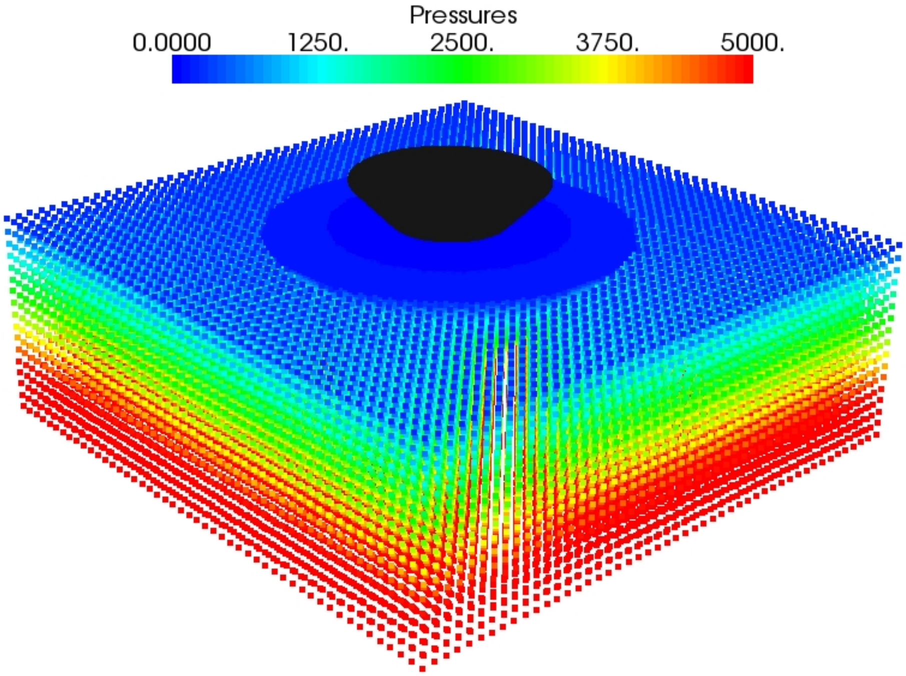

Figure 6.20: Pressure distributions for a heaving cone using the mass ratio of 1:8:27

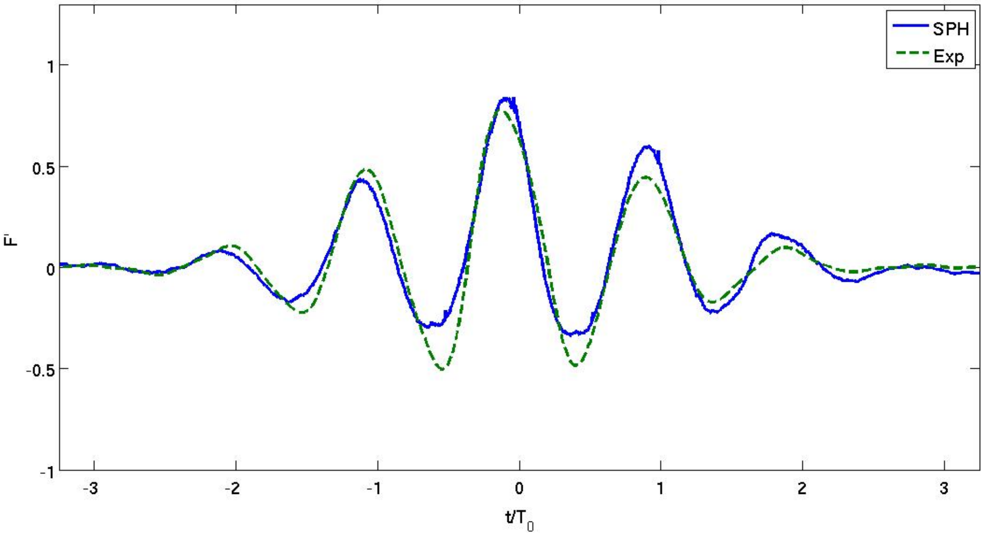

Figure 6.21: Force comparison between the SPH results and experimental data for 3-D cone using the mass ration of 1:8 (2 nested regions), where $\kappa = 9$ and $A = 0.05m$

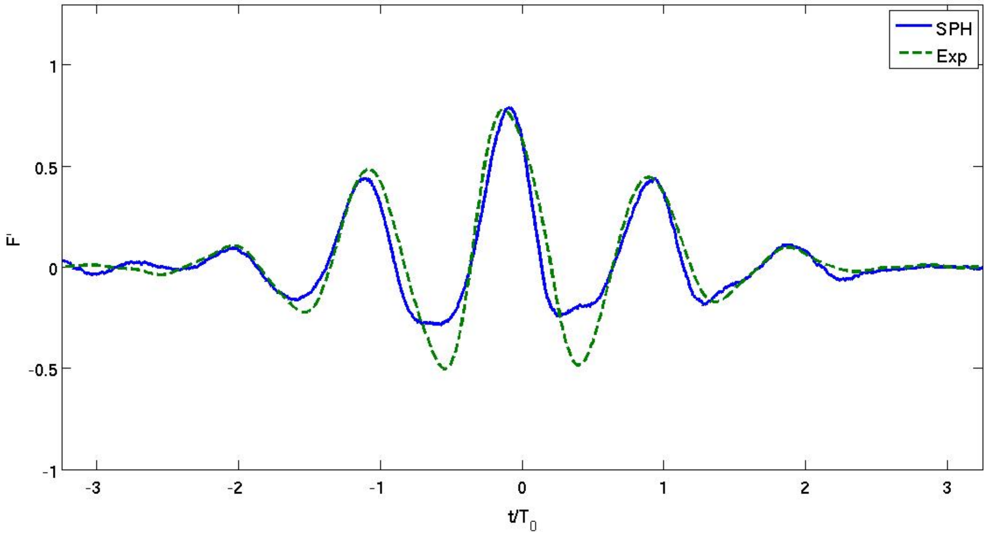

Figure 6.22: Force comparison between the SPH results and experimental data for 3-D cone using the mass ration of 1:8:27 (3 nested regions), where $\kappa = 9$ and $A = 0.05m$

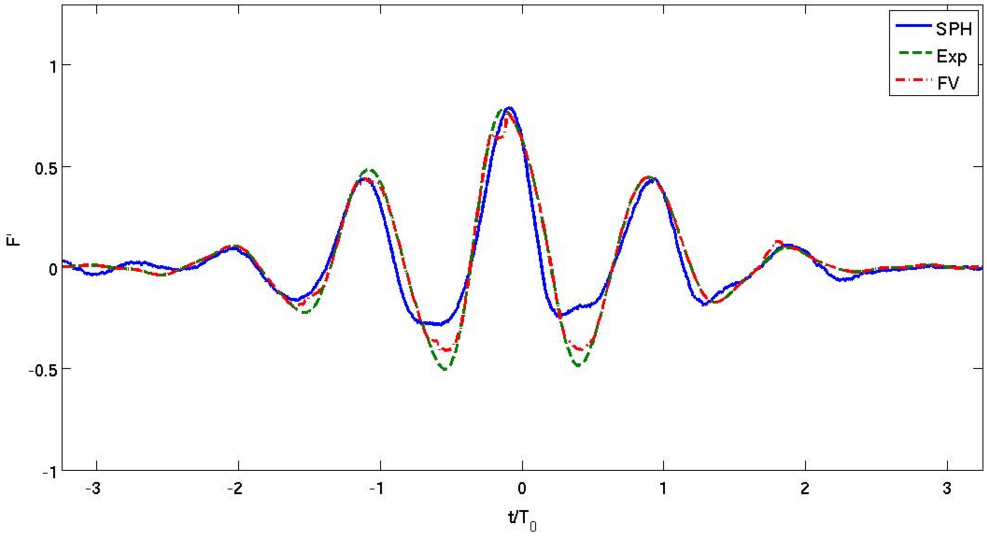

Figure 6.23: Force comparison between the SPH results, experimental data and finite volume data for 3-D cone using the mass ration of 1:8:27 (3 nested regions), where $\kappa = 9$ and $A = 0.05m$

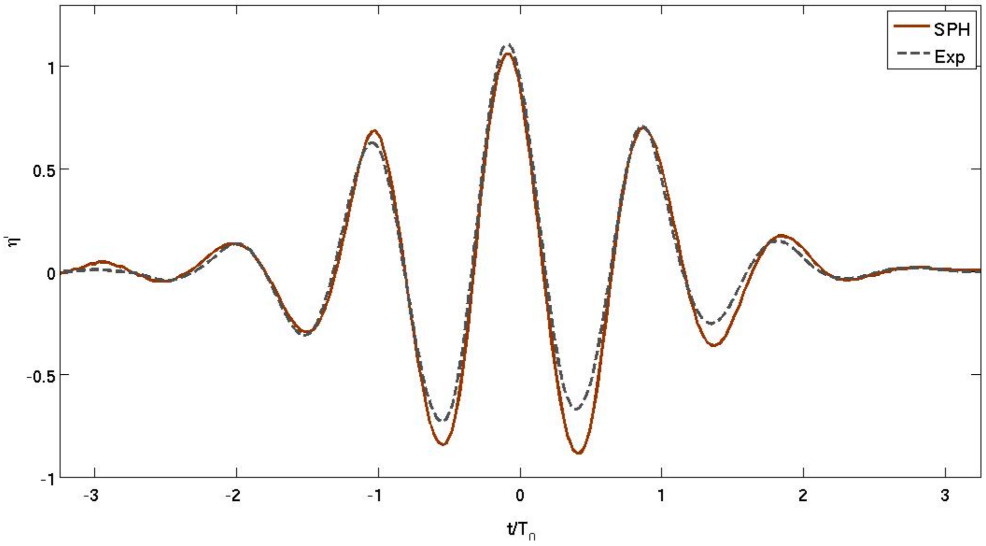

Figure 6.24: Comparison of the relative vertical motion between the SPH results and experimental data using the mass ratio of 1:8:27 (3 nested regions), where $\kappa = 9$ and $A = 0.05m$

tational domain where the hydrostatic pressure distribution is evident.

Figure (6.21) and (6.22) show the comparisons of experimental data for a moving cone with the SPH result using the mass ratio of 1:8 and 1:8:27, respectively. The results are in a good agreement with the experimental data in terms of phase. It can also reproduce the experimental data in the peaks, however, similar to uniform mass distribution explained in the previous section, the SPH results underestimates the force due to the same reasons mentioned in the previous section. The problem with a sharp edge is well known in hydrodynamics where similar behaviour (Figure 6.23) is found for the finite volume code, although less marked (Westphalen *et al.*, 2010).

The relative vertical motion can be defined as the free-surface elevation minus the vertical displacement of the cone. The relative vertical motion can be normalised by dividing by the largest excursion from the still water level, A. Figure (6.24) displays the relative vertical motion comparison between the SPH result and experimental data using the mass ratio of 1:8:27, which is in satisfactory agreement. There is a small discrepancy for the troughs which may be due to the resolution. It is shown in Figure (6.25) that the SPH result produce a better agreement with the experiment in comparison with a FV code (Westphalen *et al*, 2010).

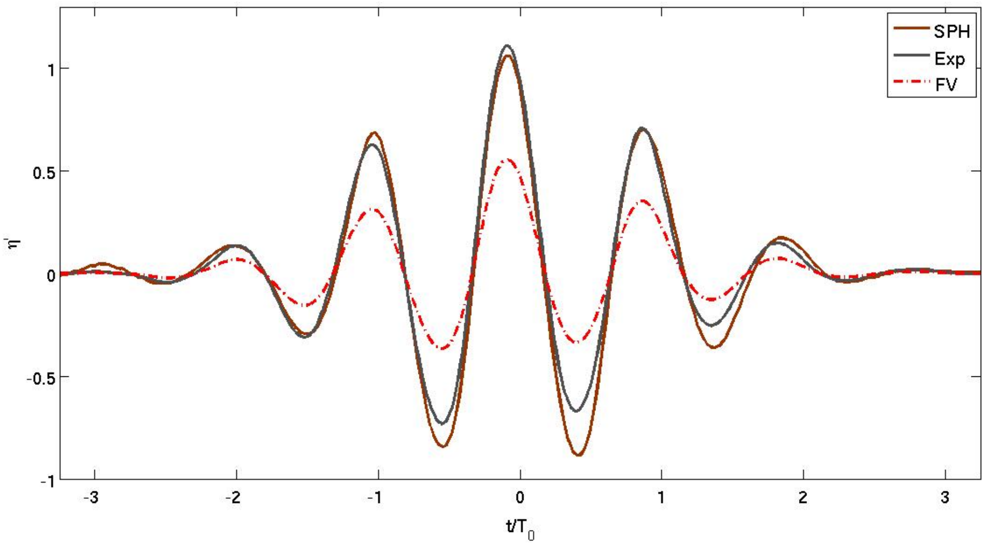

Figure 6.25: Comparison of the relative vertical motion between the SPH results, experimental data and finite volume data using the mass ratio of 1:8:27 (3 nested regions), where $\kappa = 9$ and $A = 0.05m$

Figures (6.26) and (6.27) show the force and surface elevation comparison of SPH and experimental data of Drake *et al.* (2009) where $\kappa = 7$ (Figures 6.26) and $\kappa = 3$ (Figures 6.27). It is shown that since the velocity and the frequency of the cone when $\kappa = 3$ is smaller than other two cases, consequently the motion is slower, the force and surface elevation are in very good agreement, even for the troughs. Moreover, it is found that using $\kappa = 7$ and $\kappa = 9$ would lead to a separation of fluid particles from the body particles when the body moves up (troughs in the force profile), however, since the motion is slower, the separation does not happen when $\kappa = 3$ and hence the troughs are well estimated.

Table (6.1) demonstrates the comparison of CPU costs for different particle resolutions using 16 processors. It is shown that using the nested resolution (mass ratio of 1:8:27) would save the CPU cost to obtain the same result. Therefore, the scheme offers a computational advantage and is hence a more efficient technique to model the wave propagation from the cone.

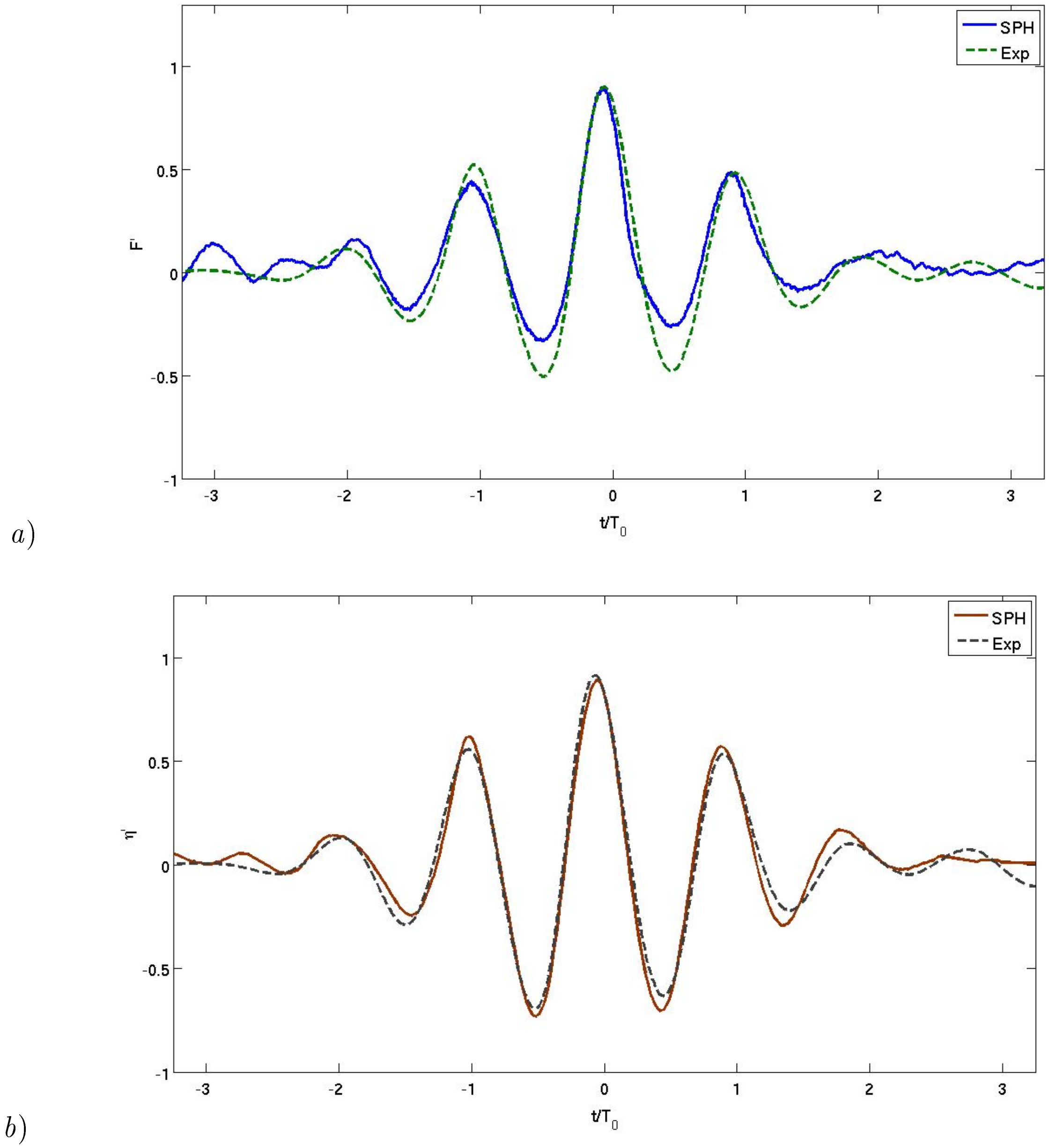

Figure 6.26: *a*) Force *b*) surface elevation comparison between the SPH results and experimental data for 3-D cone using the mass ration of 1:8:27 (3 nested regions), where $\kappa = 7$ and $A = 0.05m$

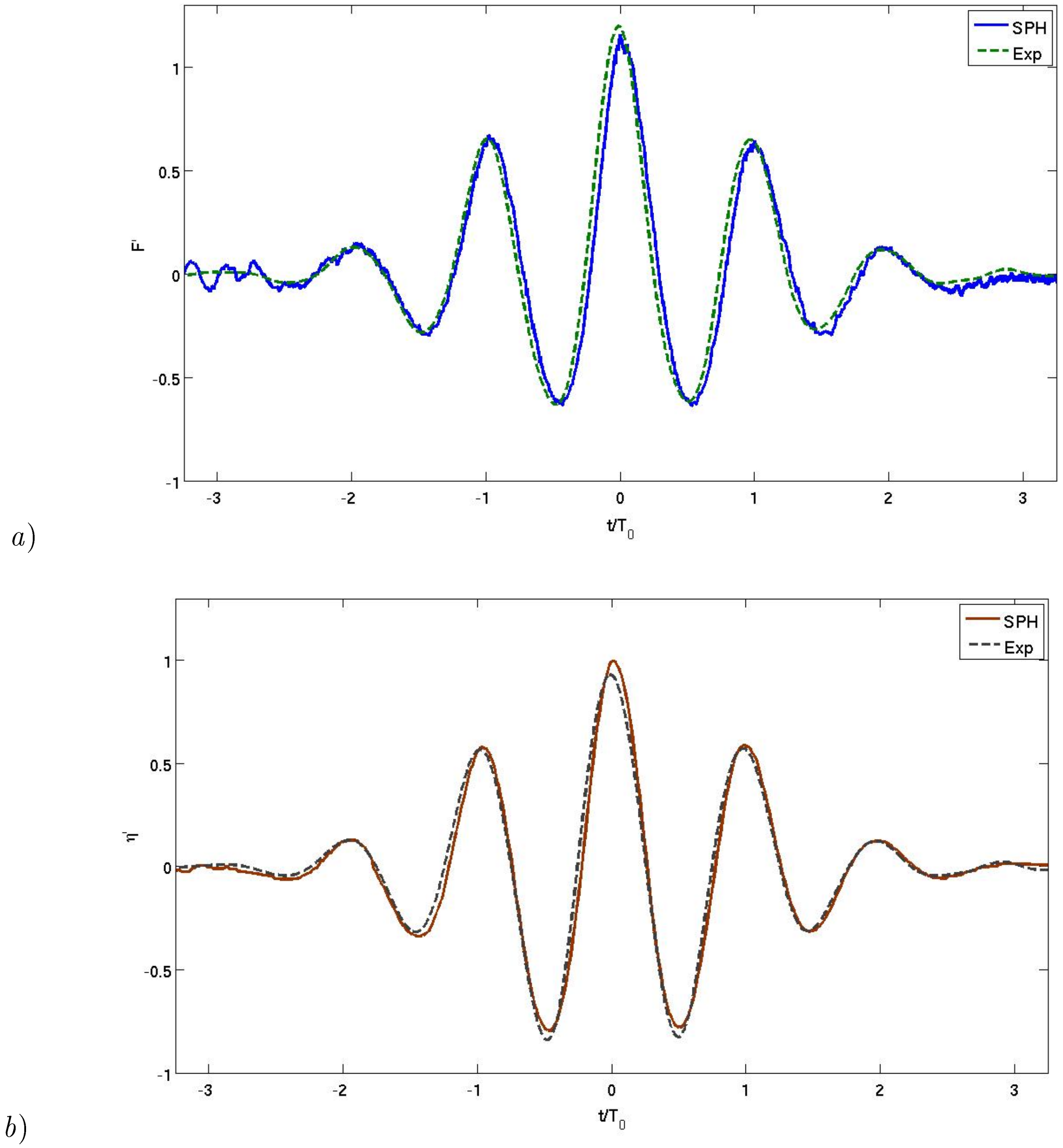

Figure 6.27: *a*) Force *b*) surface elevation comparison between the SPH results and experimental data for 3-D cone using the mass ration of 1:8:27 (3 nested regions), where $\kappa = 3$ and $A = 0.05m$

Numerical Model	Uniform coarse distribution of particles $(\triangle = 0.04m)$	Uniform fine distribution of particles $(\triangle = 0.02m)$	Variable mass, ratio of 1:8 $(\triangle_{finest} = 0.02m)$	Variable mass, ratio of 1:8:27 $(\triangle_{finest} = 0.013m)$
Number of Particles	272,000	2,100,000	283,000	315,000
CPU cost	1.5 days	12 days	2 days	4 days

Table 6.1: Comparison of using different particle resolutions on 16 processors for the simulation of the 3-D cone

6.8 Summary

Surface waves generated by a 2-D wedge and 3-D cone moving as a Gaussian wave packet have been investigated using the SPH method, making comparison with the experimental data. In 2-D the results were in a good agreement with the experimental data in terms of phase. However, the repulsive boundary condition seems to work better and gives better force prediction in terms of magnitude in comparison with the boundary particle force method. For the 3-D cone, the results for the coarse resolution were qualitatively satisfactory. However, in order to improve accuracy, a large increase in the number of particles would be necessary, which increases the CPU cost markedly. In order to reduce computer time a variable particle mass distribution was tested with fine resolution near the body and coarser resolutions further away. Variable particle mass distribution with variable kernel size was first successfully investigated for 2-D still water problems. For 3-D problems two and three level resolutions were tested. It was shown that using such variable mass can be successfully implemented in the 3-D problem improving accuracy with much lower computational costs than with particles of uniform mass. Moreover, the agreement between the SPH results and experimental data was shown for the 3-D cone using different particle mass, where for a lower frequency the comparison is in very good agreement whereas for a higher frequency there is a discrepancy for the troughs which is due to the separation of water particles from the bottom edge of the cone in our mono-phase simulation.

Chapter 7

Manchester Bobber in Focused-wave group

7.1 Introduction

The response of Manchester Bobber wave energy device in extreme waves, based on NewWave theory of Taylor and Williams (2004), is presented in this chapter using the SPH method with uniform and variable particle mass. The concept of NewWave focusing is to generate several waves of different amplitudes and periods which combine to a localised extreme wave, with the maximum possible crest elevation, focused at a specific time and location. The motion of a single heaving device is simulated with one degree of freedom.

7.2 Experimental data

The physical tests were performed in the wavetank of Joule Centre, the University of Manchester by Stallard *et al.* (2009). The tank is 18.5m long, 5m wide with a water depth of 0.5m. The waves are generated using a piston type paddle and absorbed by a curved surface piercing beach at the far end wall. The device is placed 3.5m from the paddles which are located in a water depth of almost 4m. Figure (7.1) shows the physical tank with four floats during an experiment.

Figure 7.1: Physical tank with four floats in extreme waves

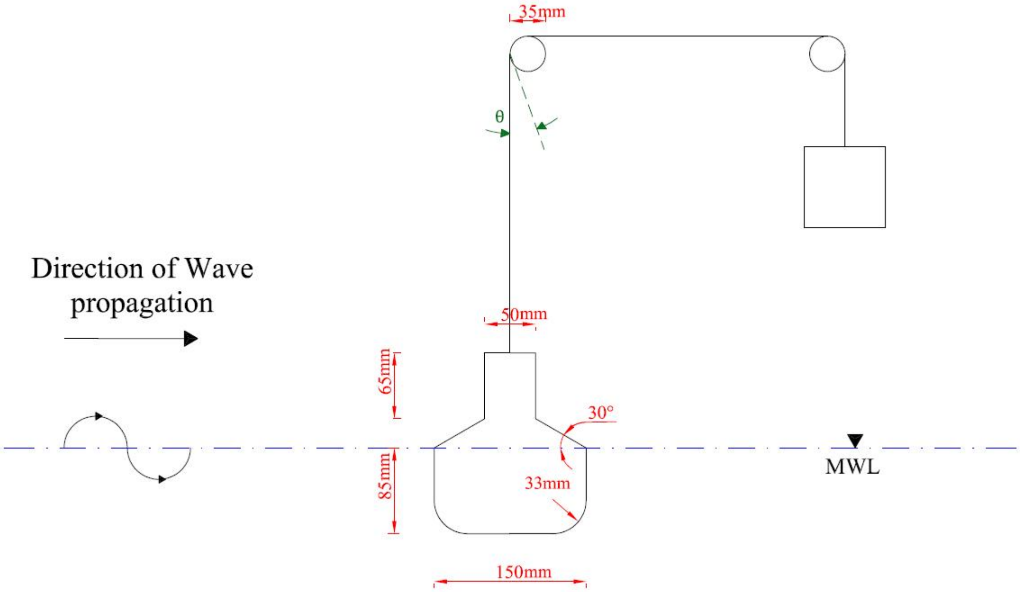

Figure 7.2: A single pulley-supported float at mid-draft with key dimensions

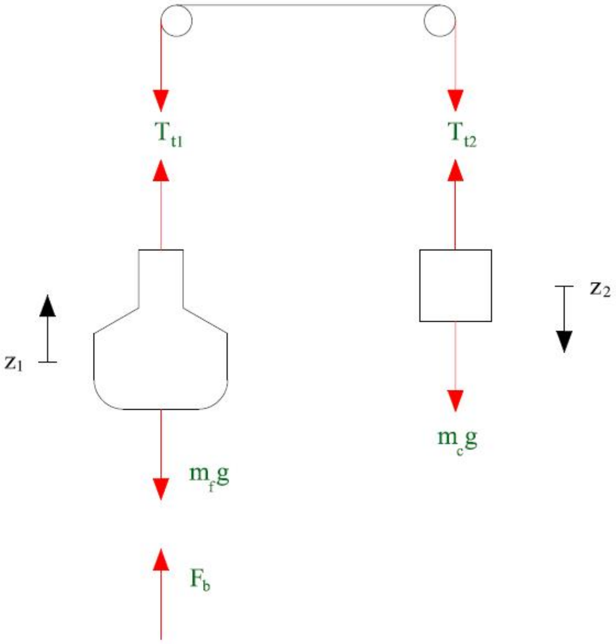

Figure 7.3: Mechanical system of a single float experiment

A pulley-supported float at mid-draft is shown in Figure (7.2) indicating key dimensions.

7.3 Numerical setup

A schematic arrangement of the system can be seen in Figure (7.3) where m_f and m_c are the masses of the float and the counter weight, respectively. The horizontal displacement of the float is restricted due to the vertical cables. The whole system is attached to the superstructure and held by weights at their ends. In the physical experiment the displacements are deduced from the angular displacement of the pulley, σ_p (see Figure 7.2). During all tests no power was taken off the system and the friction in the pulley was compensated to be negligible. The cables are assumed to be stiff, inextensible and always under tension.

First, it is necessary to know the relationship between the two accelerated bodies, float and counter weight where the unknowns are the tension forces T_1 and T_2, where

$T_t = T_{t1} = T_{t2}$, and the acceleration of the system, $\ddot{z}$. The system equation can be written as

$$\ddot{z_1} = \frac{(m_c - m_f)\, g + F_b}{m_c + m_f}, \tag{7.1}$$

$$T_t = -m_c \frac{(m_c - m_f)\, g + F_b}{m_c + m_f} + m_c g, \tag{7.2}$$

where F_b is calculated from the force exerted by the fluid particles on the body particles (Monaghan and Kos, 1999).

Here, a focused wave group based upon the NewWave concept of Tromans *et al.* (1991) and Taylor & Williams (2004) is used to define the paddle motion. A focused wave group contains a range of amplitudes and frequencies which are designed to come into phase at a specific time and location (Hunt-Raby *et al.*, 2010), which interact and constructively interfere to build up a localised extreme wave, larger than any individual wave created at the paddle. Therefore, the focused wave group has distinct properties governed by input amplitude, focus location, focus time, phase, etc.

The surface elevation η of an irregular wave is defined by the sum of harmonics

$$\eta = \sum_{n=1}^{\infty} a_n \cos\left(k_n x - \sigma_n t + \phi_n\right), \tag{7.3}$$

where a_n is the amplitude of the *nth* wave component and k_n, σ_n, ϕ_n are its associated wave number, frequency and phase. The shape of NewWave group can be calculated from any sea spectrum by defining the amplitude a_n for each wave component (Hunt-Raby *et al.*, 2010).

$$a_n = A_N \frac{S_n(\sigma) \triangle\sigma_n}{\sum\limits_n S_n(\sigma) \triangle\sigma_n}, \tag{7.4}$$

where $S_n(\sigma)$ is the power spectrum, $\triangle\sigma_n$ is the frequency step, A_N is the maximum amplitude here defining from the experiments. The Bretschneider spectrum (Bretschneider, 1968) is applied for our simulation. The frequency range of $0.5\sigma_p < \sigma < 3\sigma_p$ is divided into 50 components, N, where σ_p is the frequency at the spectral peak.

Based on Dean and Dalrymple (2000), the *nth* component of piston stroke s_n is given by

$$\frac{s_n}{a_n} = \frac{\sinh(2k_n d) + 2k_n d}{2(\cosh(2k_n d) - 1)}, \tag{7.5}$$

where d is still water depth . The piston position and velocity are thus given by

$$X_{paddle} = \sum_{n=1}^{\infty} - s_n \sin(-\sigma_n t + \phi_n), \tag{7.6}$$

$$U_{paddle} = \sum_{n=1}^{\infty} s_n \sigma_n \cos(-\sigma_n t + \phi_n), \tag{7.7}$$

respectively.

Here, the SPH-ALE formulation (Vila, 1999) is used along with the cubic kernel function (Monaghan, 1992) , symplectic time-stepping method (Leimkuhler *et al.*, 1997 and Monaghan, 2005) and repulsive boundary conditions (Monaghan and Kos, 1999 and Rogers *et al.*, 2008). For more information readers are referred to Chapter 3.

The numerical simulation is investigated in a tank with a length 7m, height 0.5m and width 2m. Focused waves are generated by a motion of paddle according to the NewWave theory of previous section and absorbed by a the sponge layer of length 1.5m at the end of the tank. The float of mass $m_f = 1.58$kg is located at 3.5m from the paddle where all the waves would come to a focus at this point. The maximum amplitude comes to the focus at t=4.6s. The draft (the distance form the float bottom to mean water level) and the peak frequency are chosen to be 85mm and 0.688Hz, respectively. For this case a counter mass of $m_c = 0.4$kg is employed in the float dynamics.

7.4 Results for the Manchester Bobber in focused waves

7.4.1 Manchester Bobber in waves using uniform particle mass

Figure (7.4) displays the particle distributions for waves on a single float at two sample times according to the pressure, where for a better view the wall particles are removed. In Figure (7.4.*b*) focused waves are generated by the paddle motion pass through the device location and are absorbed by the sponge layer at the end of the tank. Figure (7.5) shows a slice of the pressure distribution for the particles with velocity vectors at *a)* t=3.5s, *b)* t=4.6s and *c)* t=5.2s where the motion of the device is clearly altered by the wave propagation. The device experiences the largest wave amplitude at *b)* t=4.6s (Figure 7.5.*b*). All the device dynamics are solved with one degree of freedom where the device motion is limited in the vertical direction.

Figures (7.6) and (7.7) represent the comparison of SPH results and experimental data for the device response using uniform particle mass. The maximum wave amplitude produces the second peak in the device-response profile at t=4.6s or t/T_p=3.2.

The results are in agreement in terms of phase and magnitude. However, the SPH result for the coarse simulations seems to be oscillatory because the number of fluid particles interacting with the device is small (see Figure 7.5) whereas for the finer resolution the response is considerably smoother. Moreover, according to Figures (7.5.*a*) and (7.5.*c*), there are particle separations from the object which would cause the discrepancy in the troughs in Figures (7.6) and (7.7). In order to achieve a smoothed profile of device response, the number of fluid particles around the device has to be considerably more, which is expensive for the SPH simulations. The first and second peaks are reproduced by the SPH results, however, SPH underestimates the third peak, where the reason can be due to the following: First, the experiment was conducted with six degrees of freedom in 3-D whereas here the results are achieved according to the motion of the float in the vertical direction (one degree of freedom). Second, numerical viscosity is likely to cause excessive damping as for the cone. Similar results to the SPH for the third peak have been achieved for the third peak using a finite volume code (Westphalen *et al.*, 2010).

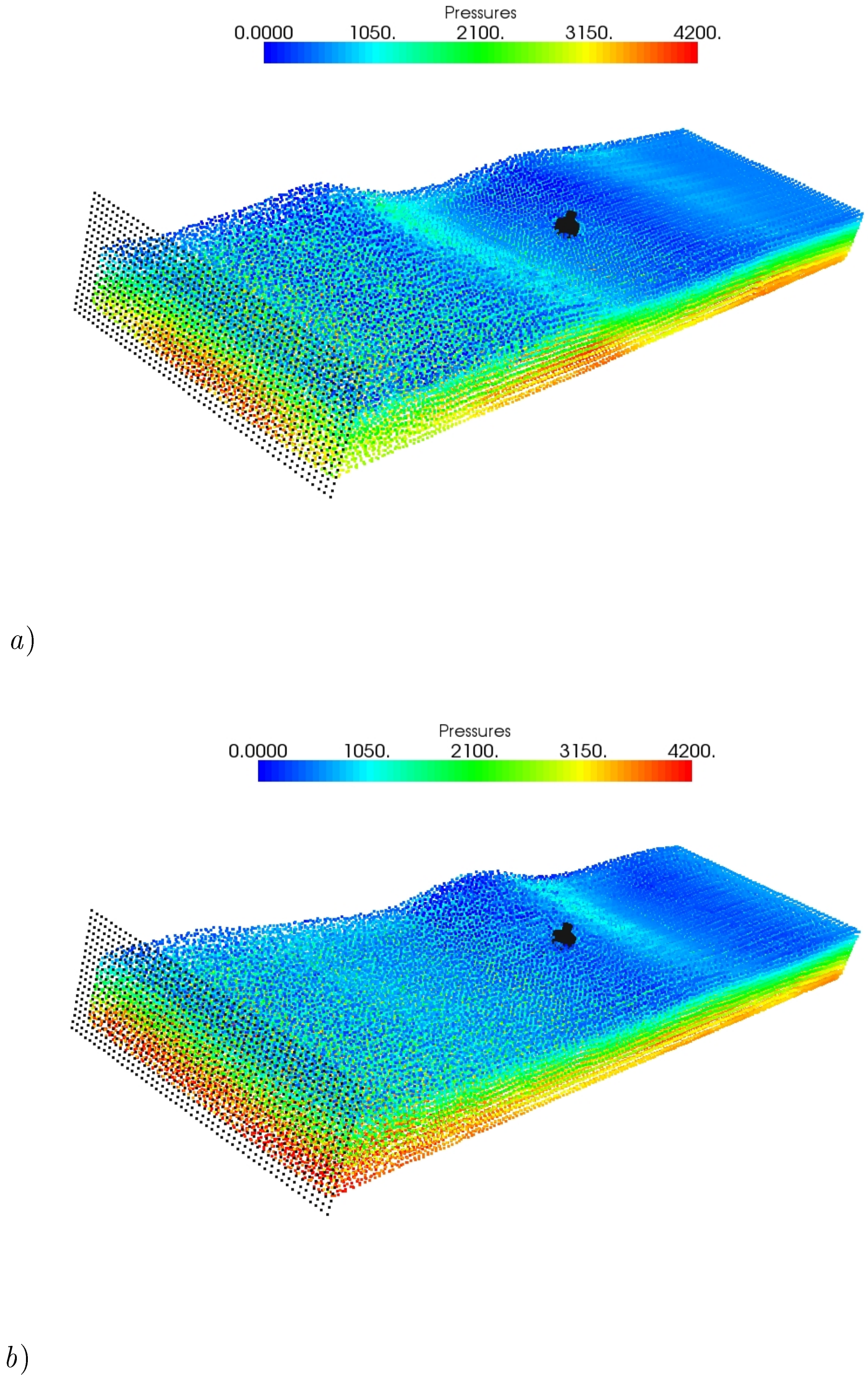

Figure 7.4: Focused waves on a single float at *a)* t=3.5s, *b)* t=4.6s

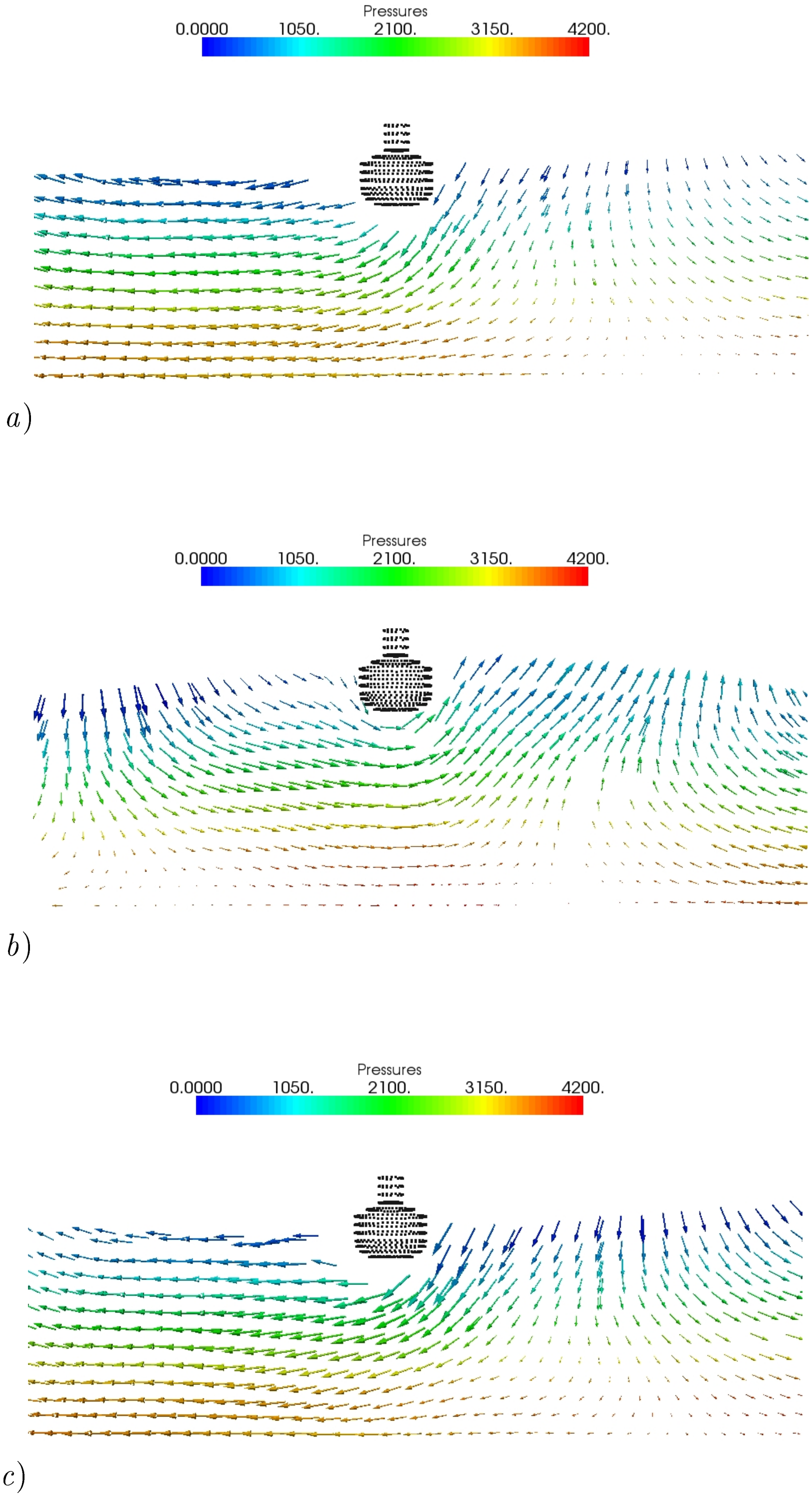

Figure 7.5: A slice of particles with velocity vectors for focused waves on a single float at *a)* t=3.5s, *b)* t=4.6s, *c)* t=5.2s. Note velocity vectors are scaled as 0.3 of the original value

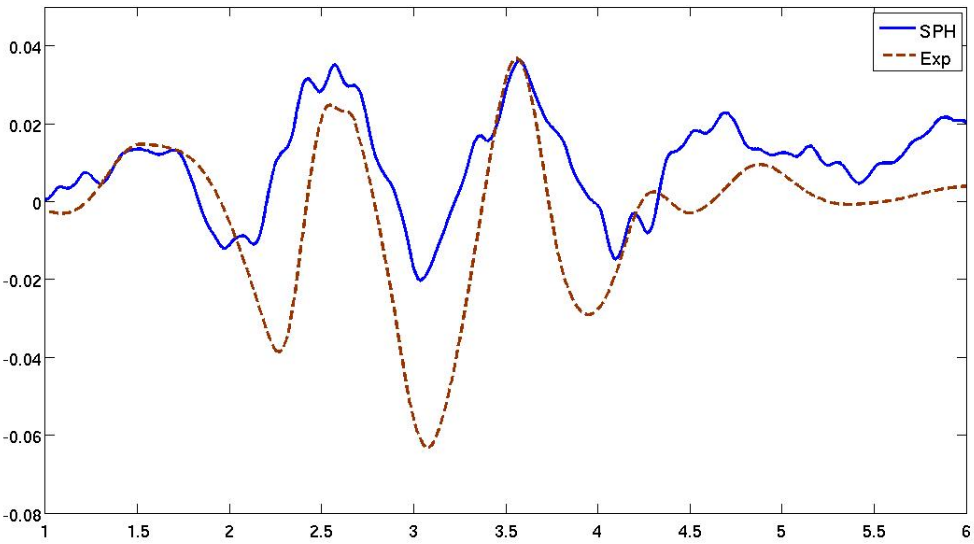

Figure 7.6: Comparison of SPH result and experimental data for the device response using uniform particle mass, ($\triangle = 0.04$m)

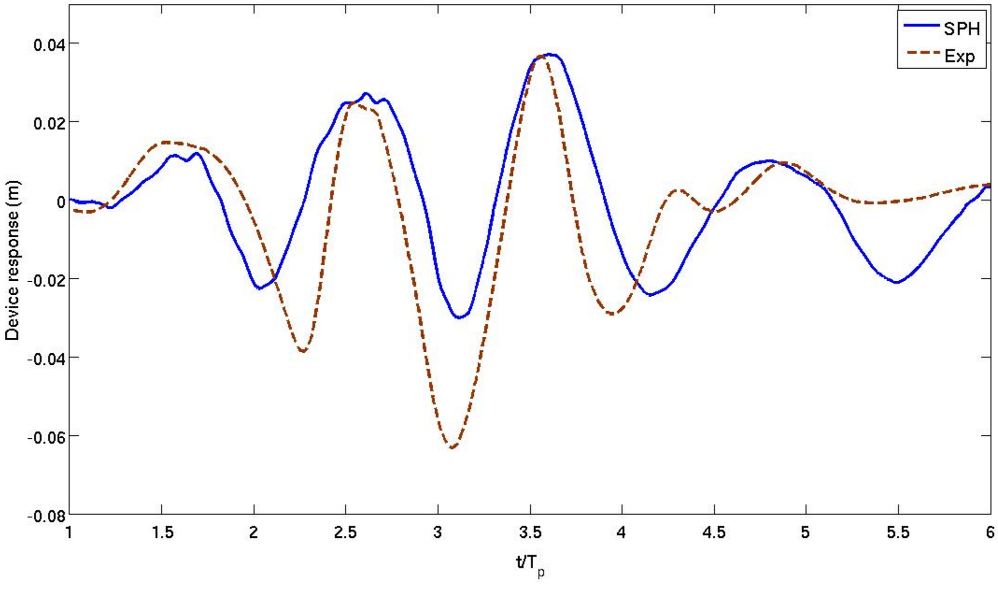

Figure 7.7: Comparison of SPH result and experimental data for the device response using uniform particle mass, ($\triangle = 0.02$m)

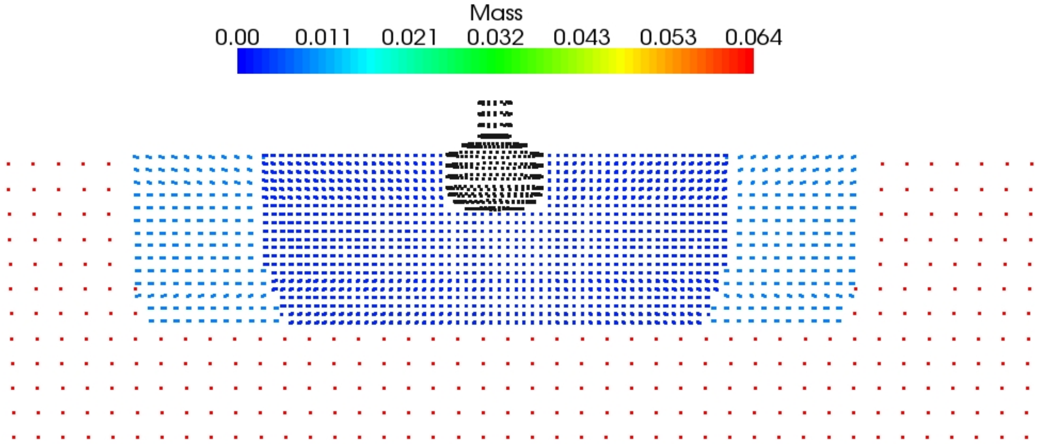

Figure 7.8: Replacing a particle with a mass m with lighter ones with masses $m/8$ and $m/27$ for Bobber at t=0

7.4.2 Manchester Bobber in waves using variable particle mass

Figure (7.8) shows a vertical slice of the problem at t=0 where a particle with mass m is replaced with eight smaller ones of mass $m/8$ an intermediate distance away from the Bobber and twenty seven lighter ones with the mass $m/27$ close to the Bobber as three nested regions. The area of lighter particles is close to the shape of the Bobber. Figures (7.9) shows the float response in focused waves for a mass ratio of 1:8 with two nested regions coloured according to the pressure of particles, where lighter particles are pre-located around the float. It is clearly shown that the waves pass through the nested regions without any problems.

Figure (7.10) displays the particle pressure for a slice of problem at t=4.6s, the time that the highest wave focused on the Bobber, using variable particle mass with mass ratio of 1:8:27. From this figure it is clear that particles travel on the float whereas this was not shown in Figure(7.5) with a uniform coarse distribution. Moreover, the particle velocity vectors are shown in Figure (7.11) for the mass ratio of 1:8:27 at *a)* t=3.5s, *b)* t=4.6s, *c)*t=5.2s (Note that the slice width (0.02m) includes multiple particle into the plane). The figure shows the separation of particles from the bottom of the float which produces a discrepancy in the profile of float response shown in Figures (7.12) and (7.13) .

Figures (7.12) and (7.13) display the comparison of SPH results and experimental

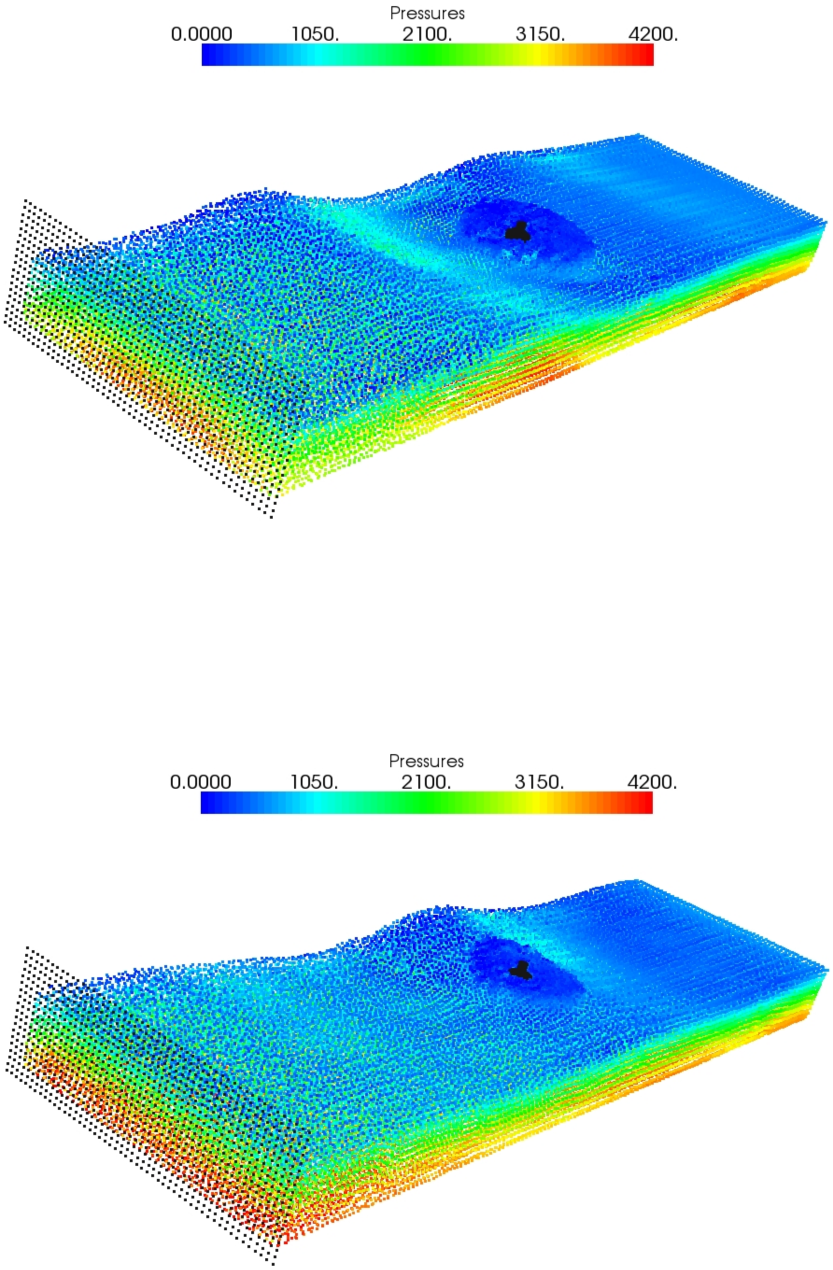

a)

b)

Figure 7.9: Focused waves on a single float at *a)* t=3.5s, *b)* t=4.6s mass ratio of 1:8 with two nested regions, ($\triangle_{finest} = 0.02m$)

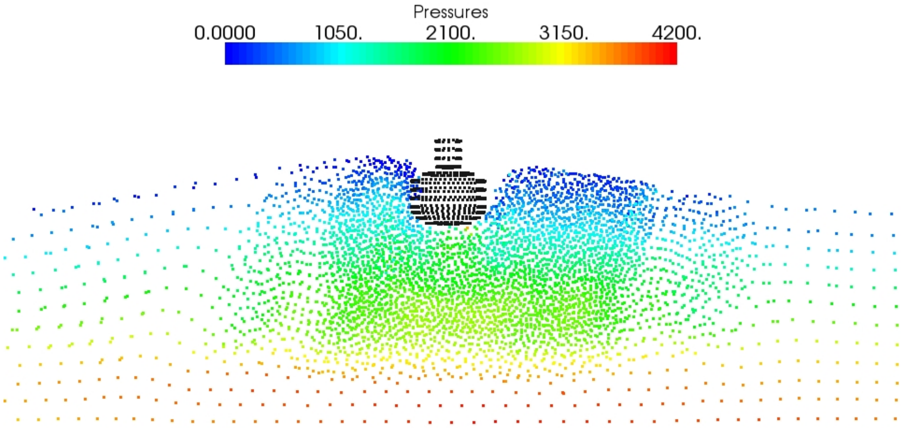

Figure 7.10: A slice of particles for focused waves on a single float at t=4.6s using variable particle mass with mass ratio of 1:8:27, ($\triangle_{finest} = 0.013m$)

Numerical Model	Uniform coarse distribution of particles ($\triangle = 0.04m$)	Uniform fine distribution of particles ($\triangle = 0.02m$)	Variable mass, ratio of 1:8 ($\triangle_{finest} = 0.02m$)	Variable mass, ratio of 1:8:27 ($\triangle_{finest} = 0.013m$)
Number of Particles	118,000	918,000	139,000	185,000
CPU cost	1 day	7 days	1.5 days	4 days

Table 7.1: Comparison of using different particle resolutions on 16 processors for the simulation of the Bobber in focused waves

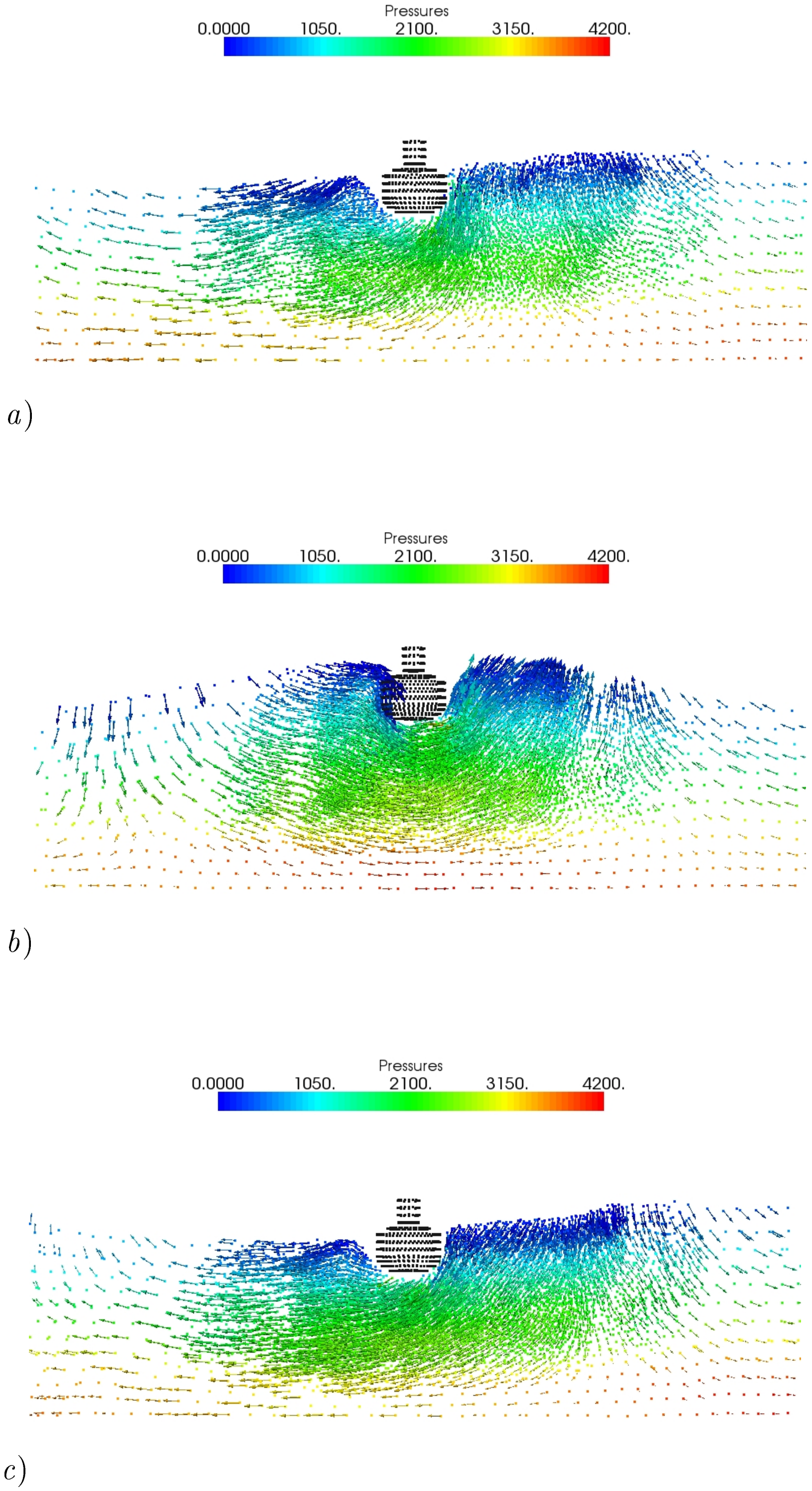

Figure 7.11: A slice of particles with velocity vectors for focused waves on a single float at *a)* t=3.5s, *b)* t=4.6s, *c)* t=5.2s using variable particle mass with mass ratio of 1:8:27, ($\triangle_{finest} = 0.013m$). Note velocity vectors are scaled as 0.2 of the original value

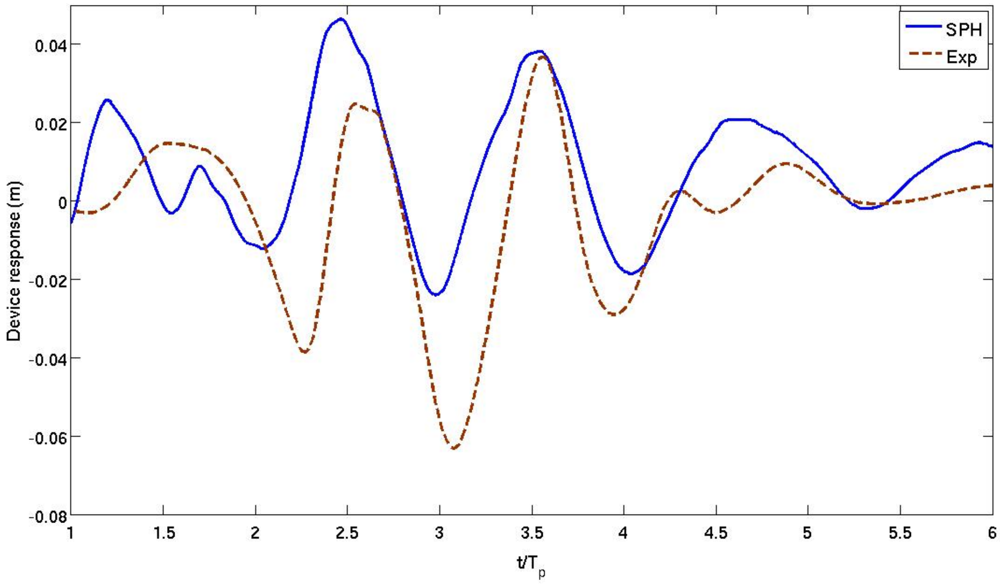

Figure 7.12: Comparison of SPH result and experimental data for the device response using mass ratio of 1:8 with two nested regions, ($\triangle_{finest} = 0.02m$)

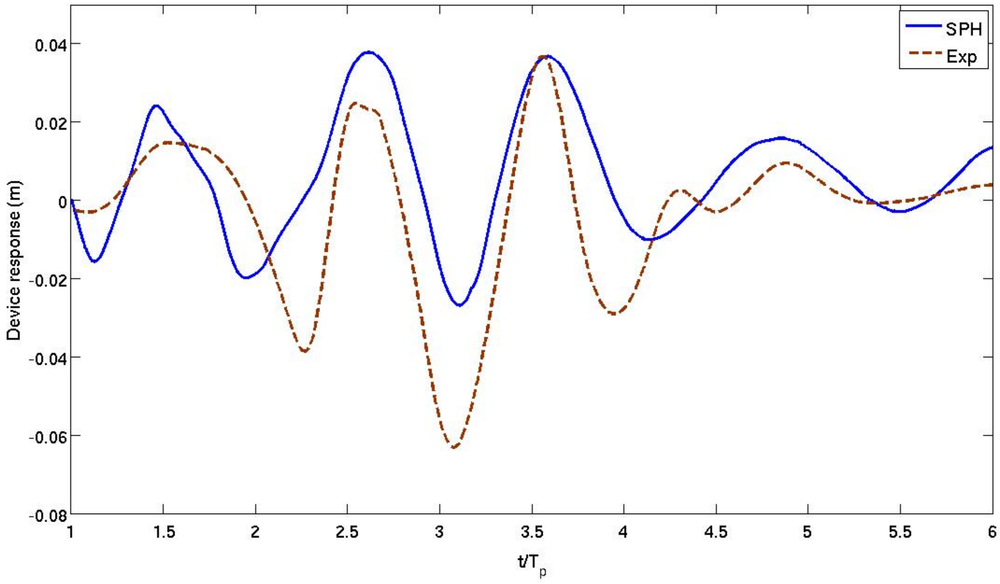

Figure 7.13: Comparison of SPH result and experimental data for the device response using mass ratio of 1:8:27 with three nested region, ($\triangle_{finest} = 0.013m$)

data for the device response using mass ratios of 1:8 and 1:8:27, respectively. Similar results to Figure (7.7) are obtained. As seen in the figures, the third peak is still underestimated due to the reasons explained in the previous section. Results with the 1:8:27 particle distribution are similar to 1:8 but with a slightly smoother response.

Table (7.1) demonstrates the comparison of CPU costs for different particle resolutions using 16 processors. It is clear that using variable mass enables large saving in CPU cost to be made. Furthermore, comparing Figure (7.13) and (7.7), it is clear that there is better agreement for the first two peaks and the first trough with a finer resolution in Figure (7.13) at a fraction of the computational cost, see Table (7.1).

7.5 Summary

The response of a single Manchester Bobber float in extreme wave has been calculated in this chapter using uniform and variable particle mass in three dimensions. The SPH results were in reasonable agreement with the experimental data of Stallard *et al.* (2009) in terms of phase and magnitude. However, since only one degree of freedom is taken into account for the SPH simulation, there is a discrepancy especially for the third peak. It was also shown that using variable particle mass improves accuracy and decreases CPU costs.

Chapter 8

Conclusions and Recommendations

8.1 General conclusions

In this PhD thesis, state-of-the-art Smoothed Particle Hydrodynamics (SPH) was used to present an investigation into surface waves interacting with or generated by structures in two and three dimensions. The major advantage of using SPH is that no special treatment of the free surface is required which is advantageous for simulating highly non-linear flows with possible wave breaking. Furthermore, simplicity, robustness and relative accuracy are other advantages of using SPH for complex problems such as surface waves interacting with structures. The open-source code SPHysics (serial in 2-D and parallel in 3-D) was used and validated for wave-body interactions using different experimental data. The SPH method has been found to be robust enough to simulate various wave-structure interactions.

One drawback of the SPH method is the large computational time associated with the large number of particles desirable for good flow definition, especially in capturing entire three dimensional flow fields. Here, to compute the free-surface motion efficiently, variable mass distribution is employed around the cylinder where surface waves are generated paying careful attention to avoid tensile instability with the interpolating kernel function. This can be done by using particles of small mass and small kernel support in regions where high definition is needed and particles of larger mass elsewhere.

8.2 Detailed Conclusions

8.2.1 Progressive waves in a 2-D tank

The standard SPH and SPH-Arbitrary-Lagrange Euler (SPH-ALE) formulations were first used to study a plate moving horizontally in a 2-D channel where the results were found to be in a good agreement with the ISPH data and analytical solutions. However, SPH-ALE with a Riemann solver gives a better results in comparison with the standard SPH formulation which causes some discrepancy in the horizontal velocity near the paddle.

Wave propagation in an intermediate depth and weakly compressible water tank has been also investigated using the standard and SPH-ALE formulations, and different kernel functions, comparing with linear wave theory. This investigation showed that using standard SPH equations would lead the waves to decay along the tank, however, results for SPH-ALE formulation were successfully compared with the linear wave theory where waves propagate without dissipation. Moreover, the cubic spline kernel was found to be the best choice for propagation of waves in a channel. Therefore, the SPH-ALE formulation and cubic kernel were chosen to investigate wave-body interactions.

8.2.2 Variable particle mass distributions

In order to reduce computer time a variable particle mass distribution is tested with fine resolution near the body and coarse resolution further away. In Chapter 5 variable particle mass was applied to progressive waves loading on a fixed cylinder and waves generated by a heaving cylinder, while maintaining a uniform kernel size, looking carefully at kernel instability and hydrostatic pressure in still water conditions. However, in Chapter 6, it was found that for the 3-D simulations, using a constant smoothing length would lead to a considerable number of interactions in the kernel support for the area where refined particles are used, which increases the CPU cost dramatically. Therefore, variable kernel sizes for different areas were tested for different mass ratios for the 3-D problem improving accuracy with much lower computational costs. Thus, the variable particle mass not only improves the accuracy but also reduces the CPU costs.

8.2.3 Surface waves interacting with a fixed cylinder and generated by a heaving cylinder

Two well-defined test cases, in two dimensions, of progressive waves interacting with a fixed cylinder and waves generated by a heaving semi-immersed cylinder were considered.

The SPH method was successfully used to predict wave propagation in a channel applied to loading a partially submerged and fixed circular cylinder for various wave amplitudes and axis depths. For wave loading on a half-submerged cylinder the agreement with the experimental data of Dixon et al. (1979) for the root mean square force is within 2%. For more submerged cases, the results show some discrepancy, but this was also found with other modelling approaches. For the heaving cylinder, SPH results for far field wave amplitude and cylinder force show good agreement with the data of Yu and Ursell (1961) and linear wave theory for different wave periods and cylinder strokes. The results for variable mass around the cylinder also showed good agreement for the force and surface profile with cheaper CPU costs.

8.2.4 Surface waves generated by a bobbing 2-D wedge and 3-D cone

Surface waves generated by a 2-D wedge and 3-D cone moving as a Gaussian wave packet have been investigated using the SPH method and comparison was made with the experimental data. In 2-D two forms of boundary conditions, repulsive boundary conditions and particle boundary force, were studied and the results were in good agreement with the experimental data in terms of phase. However, the repulsive boundary condition seems to work better and gives better force prediction in terms of magnitude in comparison with the boundary particle force method. For the 3-D cone, the results were qualitatively satisfactory. Using different particle mass techniques with different kernel sizes has been shown to work well, especially for low frequencies, for the 3-D cone simulations improving accuracy with much lower computational costs.

8.2.5 Simulation of the floating body of the Manchester Bobber

The main objective of this PhD thesis was to study extreme waves loading on offshore wave energy devices. The floating body of the Manchester Bobber is considered as such a device which can be placed under extreme loading conditions. Here, it was shown that the SPH method can be used in order to investigate a single Bobber in focused waves, which is based on the NewWave theory of Taylor and Williams (2004). The SPH simulations were shown, using uniform and variable particle mass, for a single float with dynamics modelled in one degree of freedom. The results are in good agreement with the experimental data of Stallard *et al.* (2009), however, some differences in the magnitude of the device motion is observed.

8.2.6 Comparison of SPH results with Finite Volume

This work has been conducted as part of a joint project between the Universities of Plymouth, Manchester, Oxford and Manchester Metropolitan University looking at the suitability of different Computational Fluid Dynamics (CFD) schemes to model heaving wave energy devices and to understand their behaviour in real seas. Table (8.1) demonstrates a summary of the comparisons between SPH results and the Finite Volume (FV) scheme using Volume of Fluid (VoF) method for the different problems discussed in this thesis. For more information about FV results readers are referred to Westphalen *et al.* (2009, 2010). In general SPH performs well, with some discrepancies in the forces for troughs, but SPH is superior in determining the free-surface location.

8.3 Limitation of validation/verification

One of the main objectives of this PhD was to calculate the correct force on bodies with different shapes which can be evaluated by summing the force exerted on the boundary particles for the entire body. Therefore, the correct force magnitude is sensitive to the type of boundary conditions which are not yet solved properly. There are some hints in the literature with advantages and drawbacks. For this work, the repulsive boundary condition is found to be well suited for complex boundaries

Numerical modelling	**SPH-ALE with Riemann solver**	**Finite Volume (CFX) with Volume of Fluid (VoF)**
Progressive waves in 2-D tank	Waves propagate along the channel without any dissipation	Waves decay in the tank
Waves interacting with fixed cylinder	Root mean square force is within 2% of experimental data for half submerged cylinder, SPH overestimates the fully submerged case. The force profile is noisy	CFX well estimates the experiment for half submerged cylinder and overestimates the fully submerged case. The force profile is smoothed
Surface waves generated by 3-D cone	Surface elevation and Force is well estimated. Troughs in force profile are underestimated for higher frequency	Surface elevation and Force is well estimated for lower frequency. For higher frequency troughs in force profile are underestimated and surface elevation is underestimated with a factor of two
Manchester Bobber	For single float with new shape and system with one degree-of-freedom results are in approximate agreement with experiment	For single float with horizontal shape and system with one degree-of-freedom results are in approximate agreement with experiment

Table 8.1: Comparison of SPH results with Finite Volume

and particle interactions. However, for example for the heaving cone problem, the author had some difficulties in choosing the right repulsive and depth functions due to the complexities involved with the shape of the object. On the other hand, since the simulations are single phase (i.e. only water particles) the compressibility of air around the cylinder is not taken into account which could affect the results, especially for the troughs in force profiles.

The numerical results for small waves, e.g. the 2-D heaving cylinder, are found to be very sensitive to the values of the β-limiter in the MUSCL scheme. This can be improved by using other limiters e.g. van Leer limiter (Toro, 2001).

One of the drawbacks of the SPH method involves expensive CPU costs, especially for simulating 3-D problems, in comparison with other numerical methods such as finite volume. Although previous SPH studies and the present work in this PhD have recommended techniques to reduce the particle number but an expensive CPU cost is still a disadvantage of the SPH method. Here, variable particle mass was suggested in order to reduce the CPU costs, however, the use of variable particle mass is limited to the problems without sloshing and breaking, e.g. the dam break problem, where there is no mixing between particles with different masses.

8.4 Recommendations for future research

Alternative boundary conditions

There are several techniques available in the literature for simulating boundaries in the SPH method with their own advantages and drawbacks. For example, techniques such as the ghost particles method (Colagrossi and Landrini, 2003) become unwieldy for complex geometries, the use of stationary water particles (Shao and Lo, 2003) to represent the solid body can create very large unphysical boundary layers and the particle boundary force method (Monaghan and Kajtar, 2009) is only well suited for the simulations with high viscosity. Here, using repulsive forces (Monaghan and Kos, 1999 and Rogers *et al.*, 2008) was found to be easy for implementing the complex boundaries and particle feedback interactions in comparison with the ghost particles method and stationary water particles. However, the use of normals is not satisfactory for problems where the normals should intersect. There are some new techniques presented recently, such as the zero-consistent 2-D boundary condition (Vacondio *et al.*, 2009), an improved ghost particles method (Colagrossi *et al.*, 2009) and semi-analytical boundary conditions (Ferrand *et al.*, 2010), Also, the enhanced dynamic boundary conditions of SPHysics V.2.0 based on the correction of Hughes and Graham (2010) could be tried as these were not available until the end of this work; the approach would probably improve the problems with the repulsive boundary conditions.

Simulating multiple floating bodies of the Manchester Bobber

A simulation of the float of the Manchester Bobber in a focused wave group has been shown with one degree of freedom. It is recommended that arrays of floating objects in linear and non-linear waves should be simulated. It is also recommended that the full dynamics of the problem (with six degrees of freedom) should be solved in order to simulate the actual movement of the Bobber. For future work, it is recommended that the results for the Manchester Bobber should be compared with the incompressible SPH code (e.g. Incompressible SPHysics) and standard SPH (Spartacus 3-D). There is still an open question to identify the fastest response time in an SPH fluid related to speed of sound i.e. compressibility.

Using Graphics Processing Units (GPUs)

In order to obtain more accurate results using SPH, finer resolution is required which needs an extremely large number of particles, which is difficult and time consuming. As used in this thesis, using parallel codes are an option for dealing with a large number of particles but with expensive maintenance costs and complexities (e.g conditioning costs, etc.). It is highly recommended to use Graphics Processing Units (GPUs), which are highly efficient in terms of computational and maintenance costs, especially for the problems which need a huge number of particles. Modelling SPH problems with GPUs has been proven to be a stable tool and accurate enough to deal with wave interactions with structures (Crespo *et al.*, 2010), however, the issue of computational precision of GPUs has not yet been addressed due to hardware limitations.

Alternatives for pre-processing

One of the advantages of the SPH method, in comparison with the mesh-based methods, is that there is no need to construct mesh. However, at the moment, the particle initialisation is solved by a Fortran code, which can be used for creating a limited set of geometries and objects. Particle initialisation is therefore can be time consuming for 3-D problems which need a large number of particles. Recently, some studies have been conducted (See Mayrhofer *et al.*, 2010 and Crespo *et al.*, 2010) to combine the Fortran files with CAD files which allows the creation of arbitrary set-up and consequently reduces the CPU cost involved with the particle initialisation. This can also improve the difficulties with the introducing the neighbourhoods for boundary particles in order to calculate normals for the repulsive boundary conditions.

Appendix A

Detecting free-surface particles

Several attempts have been proposed for detecting the free-surface particles. For instance, Marrone *et al.* (2009) presented a fast algorithm for free-surface particle detection for 2-D and 3-D simulations. This algorithm is based on two steps, first particles next to free surface are detected using the properties of the renormalisation matrix and second the particles located at the free surface and their local normals are calculated. This algorithm cannot identify bubbles with a diameter greater than $2h$.

Here, based on Gómez-Gesteira and Dalrymple (2004) approach, we use the idea of a vertically descending density probe line to detect any particles at the free surface on a regular grid using the kernel definition by using a threshold for density

$$\rho = \sum_j m_j W_{ij}. \tag{A.1}$$

where the surface position, $\eta_{surface}$, is defined when the estimated density, $\rho_{estimate}$, first exceeds $\frac{1}{2}\rho$ with a step size of $0.01h$. Obviously, these positions are not necessarily the position of single particles.

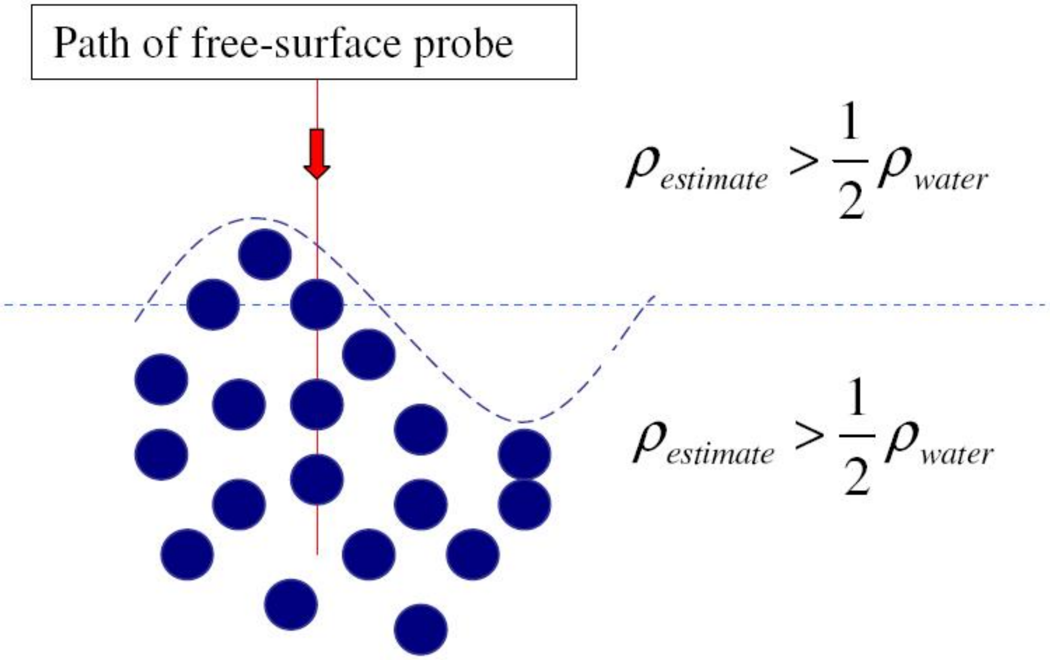

Figure A.1: Surface detection using a vertically descending density probe, free surface defined at $\rho_{estimate} = \frac{1}{2}\rho_{water}$

Bibliography

[1] Arefmanesh, A., Najafi, M., and Abdi, H. (2005), "A meshless local Petrov–Galerkin method for fluid dynamics and heat transfer applications". *Journal of Fluids Engineering*, **127**(4): 647-655.

[2] Atluri, S. N. and Zhu, T. (1998), "A new meshless local Petrov-Galerkin (MLPG) approach in computational mechanics", *Computational Mechanics*, **22:** 117-127.

[3] Barba, L. A., Leonard, A. and Allen, C. B. (2005), "Advances in viscous vortex methods-meshless spatial adaption based on radial basis function interpolation", *International Journal for Numerical Methods in Fluids*, **47**(5): 387–421.

[4] Batchelor, G. K. (1967), "*An introduction to fluid dynamics*". Cambridge University Press.

[5] Berczik, P. (2000), "Modeling the star formation in galaxies using the chemodynamical SPH code", *Astronomy and Astrophysics*, **360**: 76-84.

[6] Benz, W. (1988), "Applications of Smoothed Particle Hydrodynamics (SPH) to astrophysical problems", *Computer Physics Communications*, **48**: 130-139.

[7] Benz, W. (1990), "Smoothed Particle Hydrodynamics: a review" *Numerical modelling of nonlinear stellar pulsations: Problems and Prospects, Kluwer Academic Boston Publication*; Netherlands: 269–288.

[8] Benz, W. and Asphaug, E. (1994), "Impact simulations with fracture. I. Methods and tests*", International Journal of Solar System Studies*, **107**: 98-116.

[9] Bonet, J. and Lok, T. S. L. (1999), "Variational and momentum preservation aspects of Smoothed Particle Hydrodynamics formulations", *Computer Methods in Applied Mechanics and Engineering*, **180**: 97-115.

[10] Bonet, J. and Kulasegaram, S. (2000), "Corrections and stabilzation of Smooth Particle Hydrodynamics methods with applications in metal forming simulations", *International Journal for Numerical Methods in Engineering*, **47**: 1189-1214.

[11] Bonet, J. and Rodriguez-Paz, M. X. (2005), "Hamiltonian formulation of the variable-h SPH equations". *Journal of Computational Physics*, **209**: 541-558.

[12] Bretschneider, C. L. (1968), "*Significant waves and wave spectrum*", Ocean Industry.

[13] Campbell, J. C. and Vignjevic, R. (2009), " Modelling extreme wave loading of offshore structures", *Proceeding of 4th International SPHERIC Workshop*; France: 310-315.

[14] Cha, S. H. and Whitworth, A. P. (2003), "Implementations and tests of Godunov-type particle hydrodynamics", *Monthly Notice of the Royal Astronomical Society*, **340**(1): 73-90.

[15] Chen, J. K., Beraun, J. E. and Carney, T. C. (1999), "A corrective Smoothed Particle method for boundary value problems in heat conduction", *Computer Methods in Applied Mechanics and Engineering*, **46**: 231-252.

[16] Chorin, A. J. (1973), "Numerical study of slightly viscous flow". *Journal of Fluid Mechanics*, **57**: 785-796.

[17] Chorin, A. J. (1978), "Vortex sheet approximation of boundary layers", *Journal of Computational Physics*, **27**: 428-442.

[18] Colagrossi, A. and Landrini, M. (2003), "Numerical simulation of interfacial flows by smoothed particle hydrodynamics", *Journal of Computational Physics*, **191**: 448-475.

[19] Colagrossi, A., Antuono, M. and Marrone, S. (2009), "A 2D+t SPH model with enhanced solid boundary treatment", *Proceeding of 4th International SPHERIC Workshop*; France: 158-165.

[20] Coveney, P. V. and Novik, K. E. (1997), "Computer simulations of domain growth and phase separation in two-dimensional binary immiscible fluids using dissipative particle dynamics", *Physical review*, **54**: 5134-5141.

[21] Crespo, A .J. C., Gómez-Gesteira, M. and Dalrymple, R. A. (2007), "3D SPH simulation of large waves mitigation with a dike", *Journal of Hydraulic Research*, **45**: 631-642.

[22] Crespo, A .J. C., Gómez-Gesteira, M. and Dalrymple, R. A. (2008), "Modeling dam break behavior over a wet bed by a SPH technique", *Journal of Waterway, Port, Coastal, and Ocean Engineering*, **134**(6): 313-320.

[23] Crespo, A .J. C., Dominguez, J. M., Barreiro, A. and Gómez-Gesteira, M. (2010), "Development of a Dual CPU-GPU SPH model", *Proceeding of 5th International SPHERIC Workshop*; UK: 401-407.

[24] Cummins, S. J. and Rudman, M. (1999), "An SPH projection method", *Journal Computational Physics*, **152**: 584–607.

[25] Dalrymple, R. A. and Rogers, B. D. (2006), "Numerical modeling of water waves with the SPH method", *Coastal Engineering*, **53**: 141-147.

[26] De Leffe, M., Le Touze, D. and Alessandrini, B. (2009), "Normal flux method at the boundary for SPH", *Proceeding of 4th International SPHERIC Workshop*; France: 150-157.

[27] Dean, R. G. and Dalrymple, R. A. (2000), "*Water wave mechanics for engineers and scientists*", World Scientific.

[28] Delorme, L., Celigueta, M. A., Oñate, E. and Souto-Iglesias, A. (2007), "Pressure measurement in 2D sloshing simulations with SPH" *Proceeding of 2nd International SPHERIC Workshop*; Spain: 55-58.

[29] Dixon, A. G., Salter, S. H. and Greated, C. A. (1979), "Wave forces on partially submerged cylinders", *Journal of the Waterway Port, Coastal and Ocean Division*, **105**: 421-438.

[30] Doring, M., Oger, G., Ferrant, P. and Alessandrini, B. (2004), "SPH simulations of floating bodies in waves", *Proceeding of OMAE.*

[31] Drake, K., Taylor, R. E., Taylor, P. H. and Bai, W. (2009), "On the hydrodynamics of bobbing cones", *Ocean Engineering*, **36**: 1270-1277.

[32] Durisen, R. H., Gingold, R. A. and Boss, A. P. (1986), "Dynamic fission instabilities in rapidly rotating n=3/2 polytropes: A comparison of results from

Finite-difference and Smoothed Particle Hydrodynamics codes", *Astronomical Journal*, **305**: 281-308.

[33] Dutta, P. K. (1988), "*Discrete vortex method for separated and free shear flows*", Ph.D. Thesis, Indian Institute of Science, Bangalore.

[34] Ellero, M., Kroger, M. and Hess, S. (2002), "Viscoelastic flows studied by smoothed particle dynamics", *Journal of Non-Newtonian Fluid Mechanics*, **105**: 35-51.

[35] Español, P. (1997), "Dissipative particle dynamics with energy conservation" *Europhysics Letters*, **40**(6): 631-636.

[36] Feldman, J. and Bonet, J. (2007), "Dynamic refinement and boundary contact forces in SPH with applications in fluid flow problems", *International Journal for Numerical Methods in Engineering*, **72**: 295-324.

[37] Ferrand, M., Laurence, D., Rogers, B. D and Violeau, D. (2010), "Improved time scheme integration approach for dealing with semi analytical boundary conditions in SPARTACUS2D", *Proceeding of 5th International SPHERIC Workshop*; UK: 98-105.

[38] Gingold, R. A. and Monaghan, J. J. (1977), "Smoothed Particle Hydrodynamics", *Monthly Notices of the Royal Astronomical Society*, **235**: 911-934.

[39] Gingold, R. A. and Monaghan, J. J. (1982), "Kernel estimates as a basis for general particle methods in hydrodynamics", *Journal Computational Physics*, **46**: 429-453.

[40] Gómez-Gesteira, M. and Dalrymple, R. A. (2004), "Using a 3D SPH method for wave impact on a tall structure", *Journal of the Waterway Port, Coastal and Ocean Division*, **130**(2): 63-69.

[41] Gómez-Gesteira, M., Cerqueiro, D., Crespo, A. J. C. and Dalrymple, R. A. (2005), "Green water overtopping analyzed with an SPH model", *Ocean Engineering*, **32**(2): 223-238.

[42] Gómez-Gesteira, M., Rogers, B. D., Dalrymple, R. A., Crespo, A. J. C. and Narayanaswamy, M. (2009), "User guide for the SPHysics code v2.0", *http://wiki.manchester.ac.uk/sphysics*.

[43] Gómez-Gesteira, M., Rogers, B. D., Dalrymple, R. A.and Crespo, A. J. C. (2010), "State-of-the-art of classical SPH for free-surface flows", *Journal of Hydraulic Research*; **48**: 6-27.

[44] Gotoh, H. and Sakai, T. (1999), "Lagrangian simulation of breaking waves using particle method", *Coastal Engineering Journal,* **41**: 303-326.

[45] Gotoh, H., Shibihara, T. and Sakai, T. (2001), "Sub-particle-scale model for the MPS method-Lagrangian flow model for hydraulic engineering", *Journal of Computational Fluid Dynamics*, **9**(4): 339-347.

[46] Gotoh, H., Ikari, H., Memita, T. and Sakai, T. (2005), "Lagrangian particle method for simulation of wave overtopping on a vertical seawall", *Coastal Engineering Journal*, **47**: 157-181.

[47] Gu, Y. T. and Liu, G. R. (2001), "A meshless local Petrov-Galerkin (MLPG) method for free and forced vibration analyses for solids", *Computational Mechanics*, **27**(3): 188-198.

[48] Guilcher, P. M., Ducorzet, G., Alessandrini, B. and Ferrant, P. (2007), "Water wave propagation using SPH models", *Proceeding. of 2nd International SPHERIC Workshop*; Spain :119-124.

[49] Hirsch, C. (1998), "*Numerical computation of internal and external flows.* John Wiley and Sons.

[50] Ho, S. L., Yang, S., Wong, H. C., Lo, E. W. C. and Ni, G. (2005), "Refinement computations of electromagnetic fields using FE and meshless methods," *IEEE Transactions on Magnetics*, **41**: 1456-1459.

[51] Hoogerbrugge, P. J. and Koelman, J. M. V. A. (1992), "Simulating microscopic hydrodynamic phenomena with Dissipative Particle Dynamics", *Europhysics Letters*, **19**: 155-160.

[52] Hughes, J. P. and Graham, D. I. (2010), "Comparison of incompressible and weakly-compressible SPH models for free-surface water flows", *Journal of Hydraulic Research*, **48**: 105-117.

[53] Hunt-Raby, A., Borthwick, A. G. L., Stansby, P. K. and Taylor, P. H. (2010), "Experimental measurement of solitary and wave group overtopping", *Submitted for publication.*

[54] Idelsohn, S. R. and Oñate, E. (2005), "To mesh or not to mesh. That is the question", *Computer Methods in Applied Mechanics and Engineering*, **195**: 4681-4696.

[55] Idelsohn, S. R., Oñate, E., Calvo, N. and Del Pin, F. (2003), "The meshless finite element method", *International Journal for Numerical Methods in Engineering*, **58**(6): 893-912.

[56] Idelsohn, S. R., Oñate, E. and Del Pin, F. (2003), "A Lagrangian meshless finite element method applied to fluid–structure interaction problems", C*omputers and Structures*, **81**: 655-671.

[57] Issa, R. (2005), "*Numerical assessment of the smoothed particle hydrodynamics gridless method for incompressible flows and its extension to turbulent flows*", Ph.D. Thesis, University of Manchester, UK.

[58] Johnson, G. R. and Beissel, S. R. (1996), "Normalized smoothing functions for impact computations", *International Journal for Numerical Methods in Engineering*, **39**: 2725-2741.

[59] Johnson, G. R., Stryk, R. A. and Beissel, S. R. (1996), "SPH for high velocity impact computations", *Computer Methods in Applied Mechanics and Engineering*, **139**: 347-373.

[60] Kajtar, B. and Monaghan, J. J. (2009), "SPH particle boundary forces for arbitrary boundaries", *Computer Physics Communications*, **180**: 1811-1820.

[61] Khayyer, A., Gotoh, H. and Shao, S. D. (2008), "Corrected incompressible SPH method for accurate water-surface tracking in breaking waves", *Coastal Engineering*, **55**(3): 236-250.

[62] Khayyer, A. and Gotoh, H. (2009), "Modified Moving Particle Semi-implicit methods for the prediction of 2D wave impact pressure", *Coastal Engineering Journal*, **59**: 419-440.

[63] Koelman, J. M. V. A. and Hoogerbrugge, P. J. (1993), "Dynamic simulation of hard-sphere suspensions under steady shear", *Europhysics Letters*, **21**: 363-368.

[64] Koshizuka, S., Tamako, H. and Oka, Y. (1995), "A particle method for incompressible viscous flow with fluid fragmentation", *Computational Fluid Dynamics*, **4**(1): 29-46.

[65] Koshizuka, S. and Oka, Y. (1996), "Moving particle semi-implicit method for fragmentation of incompressible fluid", *Nuclear Science and Engineering*, **123**: 421-434.

[66] Koshizuka, S., Chikazawa, Y. and Oka, Y. (2001), "A particle method for elastic and visco-plastic structures and fluid-structure interactions", C*omputational Mechanics*, **27**: 97-106.

[67] Kuhnert, J. and Tiwari, S. (2007), "Modeling of two-phase flows with surface tension by finite pointset method (FPM)", *Journal of Computational and Applied Mathematics*, **203**(2): 376-386.

[68] Larsen, J. and Dancy, H. (1983), "Open boundaries in short wave simulations-A new approach" *Journal of Coastal Engineering*, **7**: 285-297.

[69] Lastiwka, M., Quinlan, N. and Basa, M. (2005), "Adaptive particle distribution for Smoothed Particle Hydrodynamics", *International Journal for Numerical Methods in Fluids,* **47**: 1403-1409.

[70] Laverty, S. M. (2003), "*Experimental hydrodynamics of spherical projectiles impacting on a free surface using high speed imaging techniques*", MS. thesis, MIT, USA.

[71] LeBlond, P. H. and Mysak, L. A. (1978), "*Waves in ocean*", Elsevier, Amsterdam.

[72] Lee, E-S. (2007), "*Truly incompressible approach for computing incompressible ow in SPH and comparisons with the traditional weakly compressible approach*", Ph.D. Thesis, University of Manchester, UK.

[73] Lee, E-S., Moulinec, C., Xu, R., Violeau, D., Laurence, D. R. P. and Stansby, P. K. (2008), "Comparisons of weakly compressible and truly incompressible algorithms for the SPH mesh free simulation with polyhedral meshes". *Journal of Computational Physics*, **227**: 8417-8436.

[74] Leimkuhler, B. J., Reich, S. and Skeel, R. D. (1997), "*Integration methods for molecular dynamic IMA volume in mathematics and its application*", Springer.

[75] Li, S. and Liu, W.K. (2000), "Numerical simulations of strain localization in inelastic solids using mesh-free methods", *International Journal for Numerical Methods in Engineering*, **48**: 1285-1309.

[76] Libersky, L. D. and Petscheck, A. G. (1991), "Smoothed Particle Hydrodynamics with strength of materials", *Proceeding of the Next Free Lagrange Conference*, **395**: 248-257.

[77] Libersky, L. D. and Petscheck, A. G. (1993), "High strain Lagrangian hydrodynamics a three dimensional SPH code for dynamic material response", *Journal of Computational Physics*, **109**: 67-75.

[78] Lin, G. and Lin, M. (2003), "*A meshfree particle method*", World Scientific.

[79] Lin, H. and Atluri, S. N. (2001), "The meshless local Petrov-Galerkin (MLPG) method for solving incompressible Navier-Stokes equations", *Computer Modeling in Engineering and Sciences*, **2**(2): 117-142.

[80] Liu, W. K., Jun, S. and Zhang, Y. F. (1995), "Reproducing kernel particle methods", *International Journal for Numerical Methods in Fluids*, **20**: 1081-1106.

[81] Lo, E. and Shao, S. (2002), "Simulation of near-shore solitary wave mechanics by an incompressible SPH method", *Applied Ocean Research*, **24**: 275–286.

[82] Lucy, L. B. (1977), "A numerical approach to the testing of fusion process", *Astronomical Journal*, **88**: 1013-1024.

[83] Ma, Q. W. (2005), "Meshless local Petrov–Galerkin next term method for two-dimensional nonlinear water wave problems", *Journal of Computational Physics*, **205**: 611-625.

[84] Manenti, S., Panizzo, A., Ruol, P. and Martinelli, L. (2008), "SPH simulation of a floating body forced by regular waves. *Proceeding of 3rd International SPHERIC Workshop*; Switzerland: 38-41.

[85] Marongiu, J. C., Leboeuf, F. and Parkinson, E. (2008), "Riemann Solvers and efficient boundary treatments: an hybrid SPH-finite volume numerical method", *Proceeding of 3rd International SPHERIC Workshop*; Switzerland: 101-108.

[86] Marongiu, J. C., Leboeuf, F., Caro, J. and Parkinson, E. (2009), "Low Mach number numerical schemes for the SPH-ALE method. Application in free-surface flows in Pelton turbines", *Proceeding of 4th International SPHERIC Workshop*; France: 324-331.

[87] Maruzewski, P., Le Touzé, D., Oger, G. and Avellan, F. (2010), "SPH high-performance computing simulations of rigid solids impacting the free-surface", *Journal of Hydraulic Research*; **47**: 126-134.

[88] Mayrhofer, A., Gómez-Gesteira, M., Crespo, A .J. C. and Rogers, B. D. (2010), "Advanced pre-processing for SPHysics", *Proceeding of 5th International SPHERIC Workshop*; UK: 201-208.

[89] Monaghan, J. J. (1988), " An introduction to SPH", *Computer Physics Communication,* **48**: 89-96.

[90] Monaghan, J. J. (1989), "On the Problem of penetration in particle methods", *Journal Computational Physics*, **82**: 1-15.

[91] Monaghan, J. J. (1990), "Modeling the universe". *Proceeding of the Astronomical Society of Australia*, **18**: 233-237.

[92] Monaghan, J. J. (1992), "Smoothed Particle Hydrodynamics", *Annual Review of Astronomy and Astrophysics*, **30**: 543-574.

[93] Monaghan, J. J. (1994), "Simulating free surface flows with SPH", *Journal Computational Physics*, **110**: 399-406.

[94] Monaghan, J. J. (2000), "SPH without a tensile instability", *Journal of Computational Physics*, **159**: 290-311.

[95] Monaghan, J. J. (2005), "Smoothed Particle Hydrodynamics", *Reports on Progress in Physics*, **68**: 1703-1759.

[96] Monaghan, J. J. and Kocharyan A. (1995), "SPH simulation of multi-phase flow", *Computer Physics Communication,* **87**: 225-235.

[97] Monaghan, J. J. and Kos, A. (1999), "Solitary waves on a Creatan beach". *Journal of Waterway, Port, Coastal and Ocean Engineering*, **125**: 145-154.

[98] Monaghan, J. J. and Kos, A. (2000), "Scott Russell's wave generator", *Physics of Fluids*, **12**(3): 622-630.

[99] Monaghan, J. J., Kos, A. and Issa, N. (2003), "Fluid motion generated by impact", *Journal of the Waterway Port, Coastal and Ocean Division*, **129**(6): 250-259.

[100] Monaghan, J. J. and Lattanzio, J. C. (1991), "A simulation of the collapse and fragmentation of cooling molecular clouds", *Astrophysical Journal*, **375**: 177-189.

[101] Morris, J. P., Fox, P. J. and Zhu, Y. (1997), "Modelling low Reynolds number incompressible flows using SPH", *Journal Computational Physics*, **136**: 214-226.

[102] Narayanaswamy, M. S. (2008), "*A Hybrid Boussinesq-SPH wave propagation model with applications to forced waves in rectangular tanks*", Ph.D. Thesis, Johns Hopkins University, USA.

[103] Nayroles, B., Touzot, G. and Villon, P. (1992), "Generalizing the finite element method: diffuse approximation and diffuse elements", *Computational Mechanics*, **10**: 307-318.

[104] Nelson, R. P. and Papaloizou, J. C. B. (1994), "Variable smoothing lengths and energy conservation in Smoothed Particle Hydrodynamics", *Monthly Notices of the Royal Astronomical Society*, **270**: 1-20.

[105] Novik, K. E. and Coveney, P. V. (1997), "Using dissipative particle dynamics to model binary immiscible fluids", *International Journal of Modern Physics*, **8**: 909-918.

[106] O'Connor, J. E. and Costa, J. E. (2004), "The world's largest floods, past and present - their causes and magnitudes", US *Geological Survey Study of Oceanic Circulation*, **1254**: 1-13.

[107] Oger, G., Doring, M., Alessandrini, B. and Ferrant, P. (2006), "Two-Dimensional SPH simulations of wedge water entries", *Journal of Computational Physics*, **213**: 803-822.

[108] Omidvar, P., Stansby, P. K. and Rogers, B. D. (2010), "Wave body interaction in 2D using Smoothed Particle Hydrodynamics (SPH) including variable particle mass", *Accepted for publication.*

[109] Oñate, E., Idelsohn, S. R., Zienkiewicz, O. C. and Taylor, R. L. (1996), "A finite point method in computational mechanics: Applications to convective transport and fluid flow", *International Journal for Numerical Methods in Engineering*, **39**(22): 3839-3886.

[110] Oñate, E., Idelsohn, S. R., Zienkiewicz, O. C., Taylor, R. L. and Sacco, C. (1996), "A stabilized finite point method for analysis of fluid mechanics problems", *Computer Methods in Applied Mechanics and Engineering*, **39**: 315-346.

[111] Panizzo, A. (2004), "*Physical and numerical modelling of subaerial landslide generated waves*", Ph.D. Thesis, Universita Degli Studi di L'Aquila, Italy.

[112] Panizzo, A. and Dalrymple, R. A. (2004), "SPH modelling of underwater landslide generated waves", *Proceeding 29th International Conference on Coastal Engineering*; Portugal: 1147-1159.

[113] Parshikov, A. N., Medin, S. A., Loukashenko, I. I. and Milekhin, V. A. (2000), "Improvements in SPH method by means of interparticle contact algorithm and analysis of perforation tests at moderate projectile velocities", *International Journal of Impact Engineering*, **24**: 779-796.

[114] Peregrine, D. H. (1972), " Flow due to vertical moving in a channel", *Unpublished.*

[115] Petterson, R., Xu, L. and Troesch, A. W. (1998), "Asymmetric hydrodynamic impact and dynamic response of vessels", *Proceeding of 17th International Conference on Offshore and Mechanics and Arctic Engineering*: 98-320.

[116] Phillips, O. M. (1977), "*Dynamics of the upper ocean*", 2nd edition, Cambridge University Press.

[117] Quinlan, N. J., Basa, M., and Lastiwka, M. (2006), "Truncation error in meshfree particle methods", *International Journal for Numerical Methods in Engineering*, **66**: 2064-2085.

[118] Robinson, M., Monaghan, J. J. and Mansour, J. (2007), "DNS SPH simulation of 2D wall-bounded turbulence", *Proceeding of 2nd International SPHERIC Workshop*; Spain: 107-110.

[119] Robinson, M., Cleary, P. and Monaghan, J.J. (2008), "Analysis of mixing in a Twin Cam mixer using Smoothed Particle Hydrodynamics", *American Institute of Chemical Engineers Journal*; **54**: 1987-1998.

[120] Rogers, B. D. (2001), "*Refined localised modelling of coastal flow features using adaptive quadtree grids*", D.Phil. Thesis, University of Oxford, UK.

[121] Rogers, B. D. and Dalrymple, R. A. (2008), "SPH modelling of tsunami waves". *Advances in Coastal and Ocean Engineering 2008*, **10**: World Scientific.

[122] Rogers, B. D., Dalrymple, R. A. and Stansby, P. K. (2008), "SPH modeling of floating bodies in the surf zone", *Proceeding* of *31st International Conference on Coastal Engineering (ICCE)*; Germany: 204-215.

[123] Rogers, B. D., Dalrymple, R. A. and Stansby, P. K. (2010), "Simulation of Caisson Breakwater movement using 2-D SPH", *Journal of Hydraulic Research*; **48**: 135-141.

[124] Sarpkaya, T. (1989), "Computational methods with vortices", *Journal of Fluid Mechanics*, **111**: 5-52.

[125] Schwaiger, H. F. (2007), "*An implementation of Smoothed Particle Hydrodynamics for large deformation, history dependent geomaterials with applications to tectonic deformation*", Ph.D. Thesis, University of Washington, USA.

[126] Sims, J. S. and Martys, N. S. (2004), "Simulation of sheared suspensions with a parallel implementation of QDPD", *Journal of Research of the National Institute of Standards and Technology*, **109**(2): 267-277.

[127] Smith, P. A. and Stansby, P. K. (1988), "Impulsively started flow around a circular cylinder by the vortex method", *Journal of Fluid Mechanics*, **194**: 45-77.

[128] Shao, S., Changming, J., Graham, D. I., Reeveb, D. E., James, P. W. and Chadwick, A. J. (2006), "Simulation of wave overtopping by an incompressible SPH model", *Coastal Engineering*, **53**: 723-735.

[129] Shao, S. and Lo, E. Y. M. (2003), "Incompressible SPH method for simulating Newtonian and non-Newtonian flows with a free surface," Advances in Water Resources, **26**: 787-800.

[130] Stallard, T., Stansby, P. K., Weller, S. D. and Williamson, A. C. (2009), "Float design to limit displacement in severe seas", *8th European Wave and Tidal Energy Conference*; Sweden.

[131] Stoker, J. J. (1957), "*Water waves*", John Wiley & Sons.

[132] Swegle, J. W. and Attaway, S. (1995), "On the feasibility of using Smoothed Particle Hydrodynamics of underwater explotion calculation", *Computational Mechanics*, **17**: 151-168.

[133] Taylor, P. H. and Williams, B. A. (2004), "Wave statistics for intermediate depth water-NewWaves and symmetry", *Journal of Offshore Mechanics and Arctic Engineering*, **126**: 54-59.

[134] Tiwari, S. and Kuhnert, J. (2003), "Finite pointset method based on the projection method for simulations of the incompressible Navier-Stokes equations", *Lecture Notes in Computational and Applied Mathematics*, **26**: 373-388.

[135] Toro, F. (1997), "*Riemann solvers and numerical methods for fluid dynamics: a practical introduction*", Springer.

[136] Toro, F. (2001), "*Shock-capturing methods for free-surface shallow flows*", John Wiley & Sons.

[137] Tromans, P. S., Anatuak ,A. and Hagermeijer, P. (1991), "A new model for kinematics of large ocean waves - application as a design wave", *Proceeding of 1st Offshore and Polar Engineering Conference*; UK.

[138] Vacondio, R. and Mignosa, P. (2009), "Incompressible finite pointset method for free surface flow", *Proceeding of 4th International SPHERIC Workshop*, France; 201-208.

[139] Vacondio, R., Rogers, B. D. and Stansby, P. K. (2009), "Smoothed Particle Hydrodynamics: approximate zero-consistent 2-D boundary conditions and still shallow water test", *In press.*

[140] Vaughan, G. L., Healy, T. R., Bryan, K. R., Sneyd, A. D. and Gorman, R. M. (2008), "Completeness, conservation and error in SPH for fluids", *International Journal for Numerical Methods in Engineering*, **56**: 37-62.

[141] Vila, J. P. (1999), "On particle weighted methods and Smoothed Particle Hydrodynamics", *Mathematical Models and Methods in Applied Sciences*, **9**: 161-209.

[142] Westphalen, J., Greaves, D. M., Williams, C. K., Taylor, P. H., Causon, D. M., Mingham, C. G., Hu, Z. Z., Stansby, P. K., Rogers, B.D. and Omidvar, P. (2009), "Extreme wave loading on offshore wave energy devices using CFD: a

hierarchical team approach", *8th European Wave and Tidal Energy Conference*; Sweden.

[143] Westphalen, J., Greaves, D. M., Hunt-Raby, R., Williams, C. K., Taylor, P. H., Hu, Z. Z., Omidvar, P., Causon, D. M., Mingham, C. G., Stansby, P. K. Rogers, B. D. (2010), "Numerical simulation of wave energy converters using Eulerian and Lagrangian CFD methods", *20th International Society of Offshore and Polar Engineers Conference*; China.

[144] Westphalen, J., Greaves, D. M., Hu, Z. Z., Omidvar, P. and Causon, D M. (2010), "Numerical simulation of wave-structure interaction wave energy conversion applications using Eulerian and Lagrangian CFD methods", *3rd International Conference and Exhibition on Ocean energy*; Spain.

[145] Wu, Y. L., Liu, G. R. and Gu, Y. T. (2005), "Application of Meshless Local Petrov-Galerkin (MLPG) approach to simulation of incompressible flow", *An International Journal of Computation and Methodology*, **48**(5): 459-475.

[146] Xu, R., Stansby, P. K. and Laurence, D. R. P. (2009), "Accuracy and stability in projection based method incompressible SPH (ISPH) and a new approach", *Journal of Computational Physics*, **228**(18): 6703-6725.

[147] Xu, R. (2009), "An improved incompressible Smoothed Particle Hydrodynamics method and its application in free-surface simulations", Ph.D. Thesis, University of Manchester, UK.

[148] Xuan, L., Zeng, Z., Shanker, B. and Udpa, L. (2004), "Element-free Galerkin method for static and quasi-static electromagnetic field computation," *IEEE Transactions on Magnetics*, **40**: 12–20.

[149] Yu, Y. S. and Ursell, F. (1961), "Surface wave generated by an oscillating circular cylinder on water of finite depth: theory and experiment", *Journal of Fluid Mechanics*, **11**: 529-551.

[150] Zhou, J., Causon, D., Mingahm, C. and Ingram, D. (2001), "The surface gradient method for the treatment of source terms in the shallow water equations", *Journal of Computational Physics*, **168**: 1-25.

[151] The Manchester Bobber, http://www.manchesterbobber.com.

[152] SPHysics code v2.0, http://wiki.manchester.ac.uk/sphysics.